SHEAR-INDUCED CRYSTALLIZATION OF NUCLEATED POLYMERS

Jen Shueng Tiang

Doctoral of Philosophy
Department of Chemical Engineering
McGill University
Montreal, Quebec, Canada

February 2010

A thesis submitted to McGill University in partial fulfillment
of the requirements of the degree of Doctor of Philosophy

To my parents

献给我的父母

丁国才 梁九妹

Abstract

Crystallization that occurs during or after a strong shear is important in polymer processing due to its strong effect on product properties and production rate. This study addresses several major gaps in our knowledge of this phenomenon by investigating shear-induced crystallization of nucleated isotactic polypropylenes by simultaneous measurement of light intensity and rheology using a sliding plate rheometer at high, uniform shear rates. An optical fiber probe was devised for the light intensity measurement. For the conditions studied, both measurements were found equally able to detect nascent crystalline structures, but light intensity is more suitable for monitoring changes during the early stages, whereas rheology is more useful for tracking the late kinetics. The relative influence of a melt-insensitive nucleating agent, molecular weight, shear rate, and strain were studied under isothermal, low-supercooling conditions following brief shearing. In contrast to that in quiescent crystallization, the nucleation pathway of nucleated polymers after strong shear was found to be governed not by the nucleating agent but by the molecular weight. The primary effect of shear was confirmed to be in inducing nucleation and is much weaker in changing growth kinetics. Shear and nucleating agent both shorten the induction time, but the effects were found not to be additive. With increasing shear rate or strain, crystallization was found to first accelerate as a result of the increase in the number of point-like nuclei, then saturate due to either slip or consumption of high-molecular weight components for the creation of nuclei, and finally accelerate again at the onset of the transition from spherulitic to highly oriented morphology. Both a critical shear rate and a critical strain are necessary to initiate this morphological transition. The product of shear rate and strain was found useful for describing the acceleration in crystallization associated with the increase in point-like nuclei. Specific work and the Weissenberg number are inadequate for characterizing kinetic and morphological changes. The complex interplay between nucleating agent, shearing conditions and molecular weight can lead to segregation of crystalline structures, resulting in non-uniformity in the bulk samples.

Résumé

La cristallisation sous ou après un cisaillement fort est importante dans les procédés de mise en forme des polymères dus à ses effets significatifs sur les propriétés du produit et sur le taux de production. Cette étude traite de plusieurs importantes lacunes dans notre connaissance de ce phénomène en étudiant la cristallisation induite par cisaillement des polypropylènes isotactiques contenant un agent nucléant par une mesure simultanée de l'intensité lumineuse et de la rhéologie en utilisant un rhéomètre à plaques parallèles à des taux de cisaillement élevés et homogènes. Une sonde à fibres optiques a été conçue pour mesurer l'intensité lumineuse. Pour les conditions étudiées, ces deux mesures se sont avérées être aussi bien en mesure de détecter des structures cristallines naissantes, mais l'intensité lumineuse est mieux adaptée pour surveiller les changements au cours des premiers stades de la cristallisation, considérant que la rhéologie est plus utile pour en suivre les derniers stades. L'influence relative d'un agent nucléant ne réagissant pas à la fusion, le poids moléculaire, le taux et la déformation du cisaillement ont été étudiés en conditions isothermes avec faible surfusion après un cisaillement bref. Si on la compare à une cristallisation en condition statique, la voie de la germination des polymères nucléés suite à un fort cisaillement est apparue être régie non pas par l'agent nucléant, mais par le poids moléculaire. Le principal effet du cisaillement a été confirmé être présent durant la germination induite et est beaucoup plus faible en changeant la cinétique de croissance. Le cisaillement et l’agent nucléant ont à la fois réduit le temps d’induction, mais les effets se sont révélés ne pas être cumulatifs. Avec l'augmentation du taux de cisaillement ou de la déformation, la cristallisation s’est avérée tout d'abord accélérée comme une conséquence de l'augmentation du nombre de germes en forme de points, pour ensuite se saturer à cause du glissement de la paroi ou de la consommation de composants de poids moléculaire plus élevé pour la création des germes, et finalement pour accélérer encore au début de la transition des sphérolites vers des structures fortement orientées. À la fois un taux de cisaillement seuil et une déformation seuil sont nécessaires afin d’initier une transition morphologique. Le produit du taux de cisaillement et de la déformation s’est

avéré être utile pour décrire l’augmentation des cinétiques de cristallisation associée avec l’augmentation du nombre de germes en forme de points. Le travail spécifique et le nombre de Weissenberg sont inadéquats pour caractériser des changements cinétiques et morphologiques. L'interaction complexe entre l’agent nucléant, l’intensité du cisaillement et le poids moléculaire peut mener à une ségrégation des structures cristallines, provoquant une non-uniformité des échantillons en vrac.

Acknowledgments

I would like to extend my greatest appreciation to my advisor Prof. John M. Dealy for his professional guidance, constant support, and invaluable advice. I have learned many things other than rheology from him, especially during the time when we shared an office. I greatly appreciate his understanding and patience with the mistakes that I made. I also would like to thank him for the many opportunities that he provided, *e.g.*, funding to attend conferences, meeting and initiating the contacts with the relevant experts.

I am grateful to Prof. Phillip Servio for being my co-supervisor. I appreciate his assistance during my study.

I would like to specially thank my third thesis advisory committee member and my colleague Hee Eon Park for the training he provided with the sliding plate rheometer and his assistance with many problems in the lab. I would not be able to complete this project without his dedication and patience with my shortcomings.

Thanks also to my other committee members, Prof. Pierre Carreau at École Polytechnique, Prof. Paula Wood-Adams at Concordia University, Prof. Gerrit Peters at Eindhoven University of Technology, and Prof. Musa Kamal for taking the time to read my thesis. I would also like to acknowledge Prof. Kamal's direct help in this project by allowing me to use the DSC and the optical microscope in his lab.

I would like to thank several individuals at Dow Chemical for getting this project started, particularly Hoang Pham for providing several samples, Anne Leugers for donating an optical fiber probe for use in a preliminary study, and Willem deGroot for establishing contacts with the company's specialists.

I benefitted a lot from some useful advice as well as the draft of a new book kindly provided by Prof. Hermann Janeschitz-Kriegl at Linz, Austria. I also obtained helpful information about the construction of an optical fiber probe from Anthony Bur at NIST. Prof. Julia Kornfield at Caltech provided crucial suggestions to include turbidity measurement at the inception of this study. I also received valuable insights from meeting her during a conference.

Charles Dolan and Alain Gagnon at the machine shop have helped me a lot with the repairs and fabrication of parts. Their assistance is greatly appreciated.

My graduate experience at McGill has been enriched by some great people that I met in the rheology group: Hee Eon Park, Michelle Si Wan Li, Junke Xu, Chunxia He, Stéphane Costeux, Siripon Anantawaraskul, Sung Taek Lim, Fabricio Smilllo and Matthew Campell. I appreciate their help, advice, support and friendship.

Finally, I am grateful to my parents, brothers and sister for their endless love, care, support and understanding.

Table of Contents

Appendices

List of Figures

Chapter 1: Introduction

Chapter 2: Experimental

Chapter 3: Rheological Characterization

Chapter 4: Quiescent Crystallization

Chapter 5: Shear-Induced Crystallization - High Shear Rates with Nucleating Agent

Chapter 6: Parameters Characterizing Shear-Induced Crystallization

Appendices

List of Tables

Chapter 1: Introduction

Chapter 2: Experimental

Chapter 3: Rheological Characterization

Chapter 4: Quiescent Crystallization

Chapter 5: Shear-Induced Crystallization - High Shear Rates with Nucleating Agent

Chapter 6: Parameters Characterizing Shear-Induced Crystallization

Appendices

Chapter 1: Introduction

1.1 Motivation

Synthetic polymers, including polyethylene and polypropylene, are ubiquitous and indispensable in our everyday life. Owing to their modest cost and many advantageous properties, *e.g.*, lightweight, superior durability, corrosion resistant, reasonable strength, low thermal and electrical conductivities, polymers have become the materials of choice for myriads of applications such as food packaging, household appliances, furniture, textile goods, building materials, medical devices, and automotive parts, to name a few [1]. They are also exceptionally versatile, due not only to our ability to tailor their molecular structures using advanced polymerization techniques and catalysts [2] but also to the possibility of enhancing their performance and processability by blending and the addition of fillers and additives [3]. Another asset is their relative ease of forming, typically in the molten state, into complex shapes via processes such as extrusion, injection molding, blow molding, film blowing, and fiber spinning [4].

Products fabricated from these processes are often semicrystalline solids consisting of three-dimensional crystalline structures interspersed with disordered amorphous regions, whereas a perfectly crystalline polymer is not possible because of the connectivity of long chain molecules [5, 6]. Understanding the crystallization process, *viz.*, how segments of chains organize from a topologically entangled melt with mobility restricted by neighboring chains into crystalline structures over multiple length scales, has been a key subject in polymer studies [6-11]. The process is complex, as it depends on a number of variables: molecular structure (*e.g.*, stereoregularity, molecular weight distribution, branching), foreign matter (*e.g.*, nucleating agents, non-molten additives, catalyst residues, dust particles), thermal history (*e.g.*, degree of supercooling, cooling rate, temperature gradient), flow history (*e.g.*, shear, extensional, mixed flow, strain magnitude and rate), and pressure [6-10]. Further complications may arise from the subtle yet potentially important interplay among the variables.

Flow occurs in all plastics forming operations. Thus, crystallization that occurs during or after flow, commonly known as flow-induced crystallization[*], is of particular industrial relevance. Thanks to the ability of flow to orient and stretch chains in a preferred direction, highly oriented products such as fibers of high strength and stiffness can be produced from rigid- and flexible-chain polymers by extensional processes such as fiber spinning [12]. Although less effective in stretching chains than extensional flow [13], shear flow has long been known capable of accelerating crystallization and altering morphology [14, 15], and these effects influence both production rate and solid-state properties ranging from optical attributes to mechanical performance. Hence, a quantitative understanding of the resin properties and processing conditions controlling shear-induced crystallization is a requisite not only for the development of accurate predictive models for the forming processes but also for optimization of the product properties.

Early work on shear-induced crystallization of polymer melts dates back to the 60s [16-19] and 70s [20-28] (see review [29]), but the past decade has seen a resurgence of interest in the subject (see more recent reviews [10, 30, 31]). Useful insights into the molecular and processing parameters governing this phenomenon have recently been gained from well-controlled experiments that made use of novel or refined flow devices and in situ measurement techniques in conjunction with judicious choice of experimental materials and conditions [32-118]. Many of these efforts have been directed towards examining such issues as the creation and the relaxation dynamics of precursors (oriented threadlike structures induced by flow at the very early stage, particularly in the formation of shish-kebabs) [37, 41, 56, 64, 70, 97, 104], the role of long chains and molecular weight distribution [33, 39, 46, 48, 51, 58, 88, 103, 112, 113], and the parameters to be used to characterize kinetic and morphological changes [32, 35, 38, 47, 49, 56, 60, 61, 65, 68, 117, 118].

---

[*] "Stress-induced crystallization" and "strain-induced crystallization" are also used, but mostly for semi-rigid chain and cross-linked polymers. "Flow-induced crystallization", "orientation-induced" and "flow-enhanced crystallization" are commonly found in the literature of flexible-chain polymers.

Yet, a number of areas remain understudied. Very little work has been done on crystallization after shearing at either high stresses or high rates, i.e., above 100 s^{-1}, in a spatially homogeneous flow in which the shear rate, strain, and stress are all uniform throughout the sample [19, 34, 72, 107]. The importance of high shear rates cannot be overemphasized, as they are dominant in industrial processing. Secondly, while changes in optical and rheological properties have been exploited for probing crystallization kinetics, there have only been a few reports of the simultaneous use of these techniques in a single experiment [19, 26, 28, 77, 82]. Thirdly, nucleating agents of various types are commonly added to commercial resins [119-121], but nearly all previous studies of nucleated polymers were conducted at low shear rates (see Chapter 5, Table 5.1). Thus, the interplay between high shear rates and nucleating agents merits further investigation.

The aim of this experimental work was to fill the above knowledge gaps. In short, shear-induced crystallization of nucleated isotactic polypropylenes was studied at high shear rates using a sliding plate rheometer by means of simultaneous measurement of light intensity and rheology.

1.2 Isotactic Polypropylene and Morphology

Isotactic polypropylene[*] is used to make most of the polypropylene products on the market. The process for making this stereoregular polyolefin from its monomer propylene was discovered by Giulio Natta in 1954 [125], using an organometallic catalyst similar to that discovered earlier by Karl Ziegler [126] for the synthesis of polyethylene; and the first commercial production was by Montecatini in Italy in 1957 [122].

This homopolymer has been the subject of many shear-induced crystallization studies for several reasons: its commercial importance (about 45 million tons consumed globally in 2007 [1], second only to polyethylene), broad experimental window (due to relatively slow quiescent growth kinetics compared to polyethylene [7]), and intriguing

---

[*] Comprehensive information about polypropylene can be found in several handbooks [122-124].

polymorphic nature [122] (i.e., more than one crystal phase). Additionally, among the many nucleated polymers used in quiescent crystallization studies, iPP is the most popular [119-121, 127].

One of the most important molecular characteristics of polypropylene is its stereoregularity, as determined by the sequence of the methyl groups attached to the asymmetric carbon along the main chain. Stereoregularity is a prerequisite for crystallization. Atactic polypropylene with random placements of its methyl groups on the main chain does not crystallize, whereas stereoregular isotactic and syndiotactic polypropylenes do crystallize. An ideal iPP has all of its methyl groups attached to the same side of its backbone; but, microstructural defects (stereodefects and regiodefects), whose amounts and distribution depend strongly on the polymerization catalyst (Ziegler-Natta or metallocene), suppress the degree of stereoregularity (isotacticity) in commercial iPP resins [128]. Isotacticity influences crystallinity (fraction of crystalline material), overall crystallization and growth kinetics, melting behavior, and morphology (lamellar crystal thickness, density of lamellar branching) [129-131].

The morphology of iPP, like those of other semicrystalline polymers, is complex and typically characterized by a hierarchy of structures with sizes ranging from angstroms to millimeters [132]. Kinetics plays a crucial role, as polymer crystals are regarded as metastable [133]. This follows Ostwald's stage rule [134], wherein the structure that forms is not necessarily the one with the lowest free energy (i.e., extended chain crystals) as would be dictated by equilibrium thermodynamics [133]. Figure 1.1 is a schematic illustration of the typical structures found at various length scales in an injection molded product. The skin-core morphology shown [122] is usually characterized by two supermolecular structures[*]: spherulites (roughly spherical clusters consisting of lamellar crystals splayed from a common center, *i.e.*, nucleus) at the core where shear is minimum, and row or highly oriented structures (*e.g.*, shish-kebabs, which consist of

---

[*] Other structures, including a transcrystalline zone, are described elsewhere [135].

platelet-like structures termed “kebabs” molecularly connected or unconnected to the fibrous structures called “shishes” [14]) in the skin where shear is maximum. On a smaller scale, within each lamella of nanometer thickness, chains fold back and forth repeatedly in a phenomenon called chain folding [136, 137]. Between the stacks of chain-folded lamellae are amorphous chain segments. On the crystallographic scale, segments of neighboring chains, which adopt a certain conformation (*i.e.*, 3_1 helical for iPP), are confined in unit cells with specific dimensions and symmetry. Also listed in Fig. 1.1 are the techniques typically used to characterize the various structures.

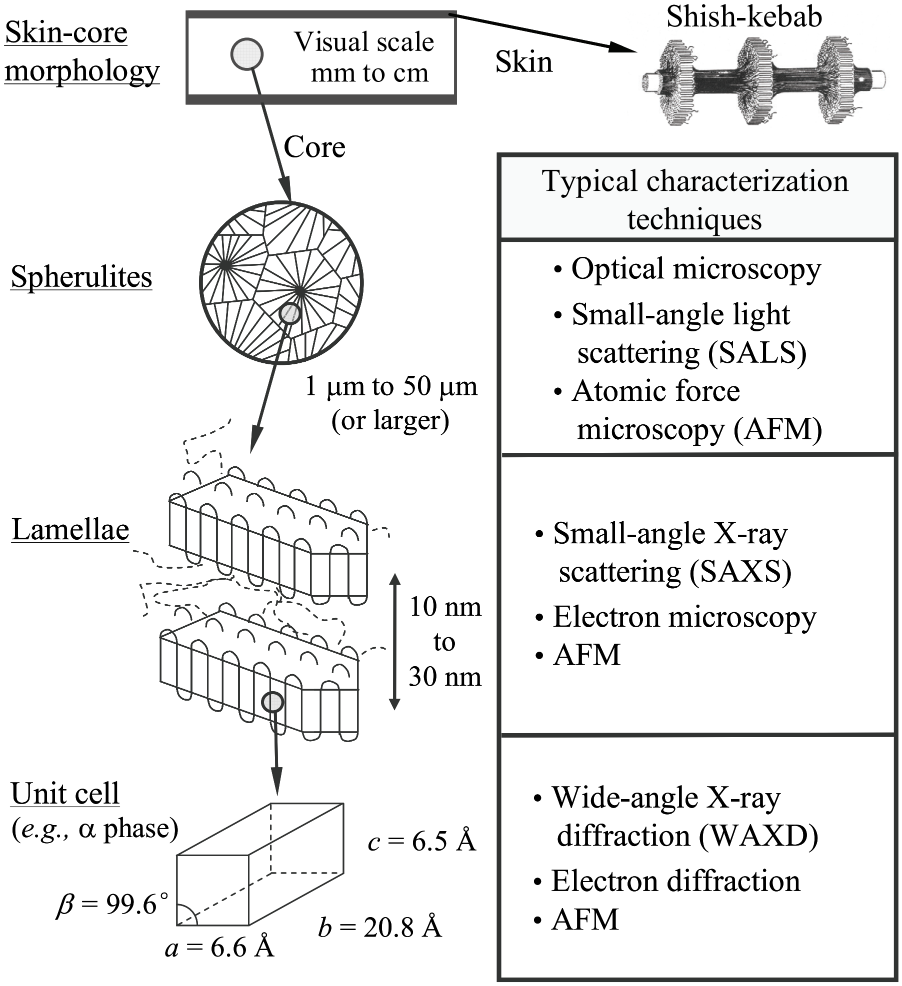

Figure 1.1. Hierarchy of crystalline structures of an injection molded isotactic polypropylene and several typical characterization techniques (adapted from [122, 14]).

Isotactic polypropylene can crystallize into three types of unit cell or polymorph: α (monoclinic), β (trigonal, formally identified as being hexagonal) and γ (orthorhombic) [122]. It can also exist in a smectic or mesomorphic phase, which has a degree of order intermediate between the crystalline and amorphous states. In brief [122], the α phase[*] is the most common and stable, the β phase forms under certain conditions (*e.g.*, high shear, in the presence of a β phase nucleating agent, in a temperature gradient, within a certain range of temperatures), the γ phase also develops under specific conditions (*e.g.*, high pressure, very low molecular weight, high contents of microstructural defects, small amounts of comonomer), and the mesomorphic phase results from rapid quenching. Depending strongly on the processing variables, simultaneous formation of all three polymorphs has been reported under industrial conditions [138]. Accordingly, the final properties depend on the composition of the polymorphs ultimately formed [124].

1.3 Quiescent Crystallization

The simplest polymer crystallization occurs in the absence of flow, i.e., under quiescent conditions following a change in a thermodynamic variable, most often a decrease in temperature below the equilibrium melting temperature[†]. In the classical view, quiescent crystallization of polymers, like the first-order phase transition of many other materials [140], involves nucleation and growth [8]. Starting with a supercooled, amorphous melt, nucleation involves the formation of stable crystal nuclei above a critical size, as determined by the free energy barrier for forming an interface between the new crystal phase and the melt phase, through statistical thermal fluctuations of chain conformations [7, 8]. Nuclei smaller than the critical size are unstable, *i.e.*, failure to overcome the activation energy barrier, and dissolve back into the melt phase. The term "primary nucleation" is used to describe this process. The subsequent growth of the stable nuclei

---

[*] "Phase", "form", and "modification" are used interchangeably in the literature.

[†] The equilibrium melting temperature T_m^o is the melting temperature of a perfect crystal formed by infinite molecular weight chains [139]. The exact value of this ideal property remains controversial for iPP. It ranges from 180 °C to 220 °C [122], which is higher than the nominal melting peak by at least 15 °C.

into lamellar crystals and spherulites is often called “secondary nucleation”, and the kinetics is often analyzed using the Hoffman-Lauritzen model [141, 142].

Nucleation is generally divided into homogenous nucleation and heterogeneous nucleation. The former occurs when nuclei form in an impurity-free environment, whereas the latter takes place at either the surface of foreign matter or a wall. Since commercial polymers are never devoid of foreign matter (dust particles, catalyst residues, additives, *etc.*), heterogeneous nucleation is the prevalent mechanism.

Two new theories that challenge the two-step nucleation and growth mechanism have recently been proposed: the spinodal-assisted crystallization theory [143, 144] based on the concept of spinodal decomposition (*i.e.*, phase separation without energy barrier), and the multi-step model [145], which involves the transformation from melt to lamellar crystals via two intermediate steps, a mesomorphic phase and a granular layer of crystals. These theories have received much support as well as some criticism [146-149].

1.4 Nucleating Agents

A nucleating agent (or nucleant or nucleator) is a substance added to a commercial polymer to promote heterogeneous nucleation. It has a low energy surface that reduces the interfacial free energy for nucleation [120, 121]. Although foreign materials such as dust particles, catalyst residues and non-molten additives also provide sites for heterogeneous nucleation, their effect is far less effective and less predictable than commercial nucleating agents, which have high nucleation efficiency owing to certain characteristics (crystalline substances, contain both an organic group and a polar or condensed aromatic group, insoluble in polymer melt or crystallize before polymer starts to crystallize, *etc.* [119-121]).

Not only can a nucleating agent significantly decrease the induction time for nucleation, it can also reduce crystal size as a result of a substantial increase in the number of nuclei

[119]. Because of these strong effects on both crystallization kinetics and crystalline morphology, nucleating agents are normally dispersed in small amounts (less than 1 % concentration [150]) in commercial resins to shorten processing time and improve product properties [151]. The term “clarifying agent” is also widely used, but it implies an additive that can also enhance transparency or clarity [119]. For enhancing toughness and impact strength, nucleating agents capable of inducing the β phase, instead of the commonly encountered α phase, are also in common use [152].

The mechanism by which a commercial nucleating agent acts can be either physical or chemical, but the latter is only applicable to certain reactive polymers [153, 154]. In this study, only physical nucleating agents are considered, and they can be generally divided into two categories based on melting temperature [119, 122]: melt-sensitive (melting temperature below or near typical polymer processing temperature), and melt-insensitive (melting temperature much higher than polymer processing temperature). Table 1.1 summarizes their differences, and of particular importance is the way nucleation takes place [122]: the former dissolves in the molten polymer during processing and phase separates upon cooling to form a physical gel [155, 156], whereas the latter is insoluble and acts as a single nucleation site. Nonetheless, both types of nucleating agent are thought to facilitate crystallization via the epitaxial mechanism [157, 158], which involves geometrical matching of the unit cell of the polymer crystal to the lattice of the nucleating agent at the contact planes.

The nucleating agent used here was sodium 2,2'-methylenebis(4,6-di-*tert*-butylphenyl)phosphate, a melt-insensitive additive patented by Asahi Denka Kogyo (now Adeka, Japan) for use with polyolefins [159]. This organophosphate salt is commonly known by its trade name IRGASTAB® NA 11 (Ciba Specialty Chemicals, Switzerland) or ADK STAB NA-11 (Adeka, Japan). Its structural formula is shown in Fig. 1.2. Further information about this compound is given in Section 5.2.

Table 1.1. Melt-sensitive and melt-insensitive nucleating agents for polypropylene.

	Melt-sensitive	Melt-insensitive
Melting temperature	Below or near processing temperature	Significantly higher than processing temperature
Nucleation mode	Dissolve in molten polymer during processing and form a gel network	Do not melt during processing and act as single point nucleation sites
Typical compounds*	Sorbitol derivatives: ▪ DBS or 1,3:2,4-dibenzylidenesorbitol (CAS number: 32647-67-9) ▪ MDBS or 1,3:2,4-bis(p-methyl-dibenzylidene)sorbitol (CAS number: 81541-12-0) ▪ MDBS or bis(3,4-dimethyl-benzylidene)sorbitol (CAS number: 135861-56-2)	Talc, benzoate salts, organic dicarboxylic acid salts, organic phosphate salts: ▪ IRGASTAB® NA 11 or sodium 2,2'-methylene-bis-(4,6-di-tert-butyl-phenyl)phosphate (CAS number: 85209-91-2) ▪ Hyperform® HPN-68L or cis-endo-bicyclo[2.2.1]heptane-2,3-carboxylate disodium salt (CAS number: 351870-33-2)
Disadvantages	Thermal decomposition at high temperatures, potential solubility problems, plate-out issues	Effectiveness highly dependent on degree of dispersion

* Included here are those to be discussed in Chapter 5, other compounds are given elsewhere [119]. The most common names and/or trade names are provided. Alternative names can be found from the CAS Registry using the given CAS number.

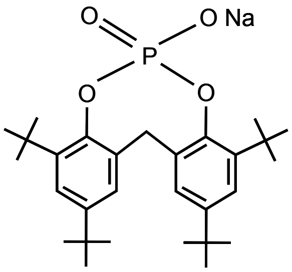

Figure 1.2. Structural formula of nucleating agent sodium 2,2'-methylenebis(4,6-di-*tert*-butylphenyl) phosphate.

1.5 Shear-Induced Crystallization

In contrast to crystallization under quiescent conditions, that after a strong shear deformation is generally characterized by a significant enhancement in kinetics, a marked increase in the number of nuclei, and a morphological transition from relatively isotropic structures such as spherulites to highly oriented structures such as shish-kebabs. While these effects undoubtedly originate from changes in chain conformation (*i.e.*, chains being oriented to the flow direction), the underlying molecular events are complex, and most theories are still lacking in some aspects.

For example, the thermodynamic justification for acceleration in shear-induced crystallization based on the increase in supercooling or melting temperature as a result of a reduction in entropy, derived from Flory's early work [160] on extensional flow-induced crystallization of cross-linked polymers, was found unsatisfactory [161]. Keller [14] explained the formation of shish-kebab in extensional flow in terms of a coil-stretch transition (*i.e.*, chains initially in coiled conformations are stretched to form threadlike shish), and this idea was used by Hsiao and coworkers [51, 56] to describe the development of shish-kebab in shear flow. But the effectiveness of shear to induce chain stretch is somewhat questionable. Also, Keller's model [14] requires a critical molecular weight M^* for shish to form, but a recent study [41] concluded that both long chains and short chains (*i.e.*, less than M^*) are involved in the creation of shish.

In his new book [10], Janeschitz-Kriegl provides an alternative explanation. He assumes that poorly ordered aggregates of chains resembling fringed micelles, termed "local alignments", are available in large quantity in quiescent melt at low supercooling. These local alignments are dormant and only become activated as athermal nuclei (*i.e.*, start to grow at a certain temperature at the same time) when they are oriented by flow; as a result, shearing leads to an increase in the number density of nuclei (often described as point-like). Due to association with other molecules, the length of these nuclei increases, and this leads to the transition to threadlike precursors. He also recommends specific work to describe the effect of flow on kinetic and morphological changes. An evaluation of this parameter is provided in Chapter 6.

Salient information about the flow devices, shearing protocols, and measurement techniques most commonly used in shear-induced crystallization investigations is given below. These three experimental aspects have important implications for comparison of findings from various studies. A short review on nucleated polymers and high shear rates is provided in Chapter 5.

1.5.1 Flow Devices

Drag flow (*i.e.*, generated by moving one surface relative to another, stationary surface) and pressure flow (*i.e.*, flow in a closed channel due to a pressure drop) can be used to shear a supercooled melt; and among the most popular devices are: rotational (*e.g.*, [27, 28, 50, 77, 78, 82, 87, 89, 162-165]), sliding plate (*e.g.*, [19, 24, 34, 72, 107]), fiber pullout (*e.g.*, [95, 112, 113, 166]), and pressure flow devices (slit, capillary or duct [32, 90, 167, 168]).

As shown in Table 1.2, which provides a summary of these four devices, only the sliding plate device is capable of generating a uniform shear rate higher than 100 s^{-1}. High shear rates are desirable because of their relevance to industrial processing and their strong effect on crystallization. Furthermore, it is at high shear rates that polymers manifest their nonlinear viscoelastic properties. The main drawback of a sliding plate device is that the total strain is constrained by the instrument dimensions. Little information is available on the use of this kind of device to measure rheological behavior during shear-induced crystallization at high shear rates.

Table 1.2. Four flow devices commonly used in shear-induced crystallization studies.

	Schematic	Parameter	Equations and Remarks
Rotational	**a) Cone-plate** 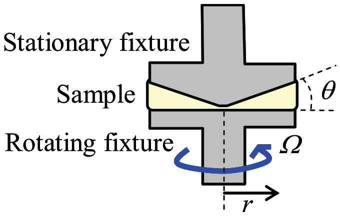 **b) Parallel-plate** 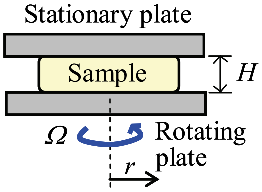 	Ω	**a) Cone and plate in rotational rheometer** Shear rate: $\dot{\gamma} = \frac{\Omega}{\tan\theta} \approx \frac{\Omega}{\theta}$ (1.1) - Uniform but low shear rates and difficult sample loading **b) Parallel plates in Linkam shearing system or parallel disks in rotational rheometer** Shear rate: $\dot{\gamma}(r) = \frac{r\Omega}{h}$ (1.2) - Easy to use, but non-uniform and low shear rates Ω : angular velocity, θ : cone angle, H : gap between moving and stationary surfaces, r : radial distance from axis of rotation
Sliding plate	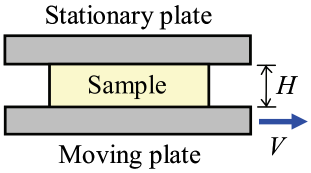 	V	Shear rate: $\dot{\gamma} = \frac{V}{H}$ (1.3) - High and uniform rates, but limited strains V : velocity of moving plate, H : gap between moving and stationary plates
Fiber pullout	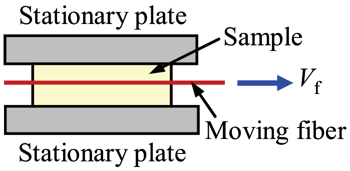 	V_f	Shear rate*: $\dot{\gamma}(r) = \frac{dV_f}{dr}$ (1.4) - Easy to use and moderate shear rates, but non-uniform shear rates V_f : fiber velocity, r : radial distance from fiber axis. *A constituitive equation must be used.
Pressure flow	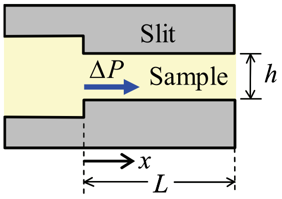 For circular channel, see [169].	ΔP	Wall shear stress: $\sigma_w = -\frac{\Delta P}{L}\frac{h}{2}$ (1.5) Wall shear rate [169]: $\dot{\gamma}_w = \frac{\dot{\gamma}_a}{3}\left(2 + \frac{d(\log\dot{\gamma}_a)}{d(\log\sigma_w)}\right), \dot{\gamma}_a = \frac{6Q}{h^2W}$ (1.6) - High shear rates, but non-uniform flow, and pressure and stress are not independent ΔP : pressure drop, L : slit length, h : slit thickness, W : slid width, Q : volumetric flow rate, $\dot{\gamma}_a$: apparent wall shear rate

With flow fields resembling somewhat those occurring in polymer processing, pressure flow has been widely used for viscosity measurement at high shear rates. However, for crystallization studies, two complications arise. First, pressure is coupled to shear stress, one cannot determine the effect of each variable independently. This is important because pressure itself has considerable influence on quiescent crystallization, notably in shifting the equilibrium melting temperature and favoring the formation of a particular polymorph [106, 170-172]. Second, neither the shear stress nor the shear rate is uniform, which causes some difficulties in the interpretation of kinetic and morphological observations. Instead of a uniform distribution, the resulting crystalline structures vary in size and type with the distance from the wall, *i.e.*, large spherulites at the core and highly oriented structures in the skin. Kinetic data obtained from *in situ* measurement of an optical property (*e.g.*, light intensity) cannot be associated with a single flow quantity. This is because the optical axis always passes through the sample thickness or diameter, so the data reflect optical changes in a crystallizing sample in which there is a gradient in the shear stress, and the signal is mostly affected by crystallization near the wall. A recent study [43] showed that this problem can be overcome by means of a real-time depth sectioning technique. Additionally, a seemingly trivial but unaddressed question is whether the presence of a flow gradient may alter the way crystallization takes place.

Rotational rheometers with cone-plate fixtures can generate a uniform shear rate, but sample loading is difficult, and high shear rates are inaccessible. On the other hand, a rotational device equipped with a pair of parallel disks or plates (either a rheometer or an optical shearing system manufactured by Linkam Scientific Instruments, Surrey, UK) has been popular among researchers due to its ease of use. The shear rate is a function of radial position: maximum at the sample edge and zero at the center. Issues related to spatial variation in shear rates, as noted earlier for the pressure flow devices, are less critical because the optical axis passes through the plates and the sample in which the local shear rate is uniform. Of course, the measured properties (*e.g.*, optical, rheological) must be correctly correlated to the appropriate local shear rate.

In the fiber pullout technique, shearing is generated by a moving glass fiber embedded in melt. Moderate shear rates are achievable, but the flow field is not well-defined.

Other shearing devices include Couette or Searle flow between two coaxial cylinders [20, 22, 26, 90, 173, 174], a biconical rotational rheometer [25], and the multipass rheometer (pressure flow driven by two moving pistons) [66, 175].

1.5.2 Shearing Protocol

Two shearing protocols are frequently used (Fig. 1.3). Mostly used in early studies [18-28], the continuous shearing protocol involves the application of a constant shear rate (or shear stress σ) over the entire duration of the experiment. The short-term shearing protocol proposed by Janeschitz-Kriegl and coworkers [32] subjects the sample to a very brief period of shearing (t_s ~ seconds or less) at a constant σ or $\dot{\gamma}$. Used in the present work and many recent studies, this method is especially useful for separating the effect of shearing on nucleation from that on growth in low-supercooling experiments when the shearing time is much shorter than the quiescent induction time.

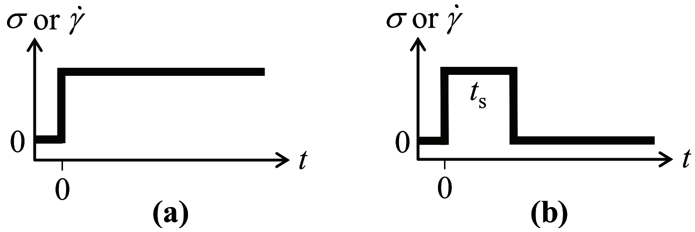

Figure 1.3. Shearing protocols: a) Continuous shearing, b) Short-term shearing.

1.5.3 Measurement Techniques

As crystallization is a first-order phase transition [139], sharp changes in polymer properties during the process can be used to infer rates of nucleation, growth or overall crystallization. The commonly used measurement techniques are:

- dilatometry, which measures volume change,
- differential scanning calorimetry (DSC) or differential thermal analysis (DTA), which detects liberation of the heat of fusion,

- optical and X-ray techniques, which probe the evolution of structures of varying length scales: light intensity, birefringence, dichroism, wide-angle or small-angle X-ray scattering or diffraction (WAXS, WAXD, SAXS; especially using synchrotron source), small-angle light scattering (SALS), optical microscopy, and
- rheometry, which monitors flow behavior from measurement of stress and deformation.

Because of the difference in the property probed, differences in sensitivity among the techniques are inevitable, and correlation between two or more measurements obtained from separate experiments is subject to error. An effective solution to this problem is the simultaneous application of several techniques in a single flow device during a single experiment. Rheo-optical instruments capable of doing so are frequently used in rheological characterization of polymer melts or solutions [176], but few research groups have combined rheometry (mostly using continuous shearing protocol) with other techniques for studying shear-induced crystallization. As summarized in Table 1.3, the shear rates investigated in these studies were quite low (< 15 s^{-1}).

Table 1.3. Summary of previous work using rheometry and a second measurement technique simultaneously for shear-induced crystallization study.

Second technique	**Flow device**	**Max. σ or $\dot{\gamma}$**	**Authors**
Optical (polarized light microscopy)	Sliding plate	438 kPa	Haas and Maxwell [19]
	Rotational (parallel disks)	12 s^{-1}	Wolkowicz [28]
Optical (birefringence)	Coutte (cylinders)	0.4 s^{-1}	Andersen and Carr [26]
Optical (turbidity, birefringence and dichroism)	Rotational (parallel disks)	1.8 kPa	Floudas *et al.* [77]
		0.36 s^{-1}	Chaari *et al.* [82]
Dilatometry	Coutte (cylinders)	10 s^{-1}	Krueger and Yeh [22]
Differential scanning calorimetry	Rotational (parallel disks)	0.8 s^{-1}	Kiewiet *et al.* [165]
Differential thermal analysis	Rotational (parallel disks)	0.2 s^{-1}	Nagatake *et al.* [105]

Rheometry has been used for crystallization studies in three ways. By performing successive periods of small-amplitude oscillatory shear within a certain range of frequency, several groups [44, 177, 178] have determined the gel time, a characteristic time based on the concept that crystallization is a physical gelation process. In the second method, a constant shear rate or stress is applied continuously (Fig. 1.3a), and an abrupt increase in the measured shear stress or strain is used to determine the onset of crystallization [19, 24, 25, 89, 90]. In the third method, which was used in the present study, a small-amplitude oscillatory shear is applied continuously at a constant frequency, and the time evolution of the rheological data yields information about crystallization kinetics. Some studies reported that this technique is more advantageous than DSC [179] and optical microscopy [65].

The light intensity measurement used in this study works on the principle that the transmission of a beam of unpolarized light through a crystallizing sample attenuates as a result of scattering by the evolving crystals. It is one of the simplest optical techniques but has several advantages over the more complex small-angle light scattering measurement, e.g., higher sensitivity, angular range of the detector is not a concern, data are not affected by multiple scattering, and intensity fluctuation of the light source can be corrected for [180]. This technique has also been reported to be more sensitive than dilatometry, calorimetry and X-ray scattering [181]. Note that this measurement is different from that of depolarized light intensity [182, 183], where the signal increases at the onset of crystallization.

1.6 Scope and Objectives

The following major gaps in our knowledge of shear-induced crystallization have been identified: a lack of data for high and uniform shear rates, rare use of simultaneous rheometry and optical measurements, and an inadequate understanding of the interplay between nucleating agent and high shear rate. The objective of the present work was to extend our understanding of these three issues, and the specific tasks were:

1. To develop a technique for simultaneous measurement of light intensity and rheology to monitor crystallization kinetics at high shear rates in a sliding plate rheometer.
2. To investigate the relative influence of melt-insensitive nucleating agent, molecular weight, shear rate, and strain using nucleated and non-nucleated isotactic polypropylenes under isothermal, low-supercooling conditions.
3. To use experimental data to evaluate parameters characterizing kinetic and morphological changes.

1.7 Organization of Thesis

Chapter 2 describes the experimental technique developed for studying shear-induced crystallization by light intensity and rheology. Included are details about the sliding plate rheometer, the optical system incorporating an optical fiber probe, the characteristics of the four isotactic polypropylenes used, and the experimental protocol.

Chapter 3 presents the rheological data obtained from linear and nonlinear viscoelastic measurements, with emphasis on the determination of the relaxation times and the analysis of the stress growth data.

Chapter 4 discusses the light intensity and oscillatory shear results obtained for quiescent crystallization and elucidates the four key events observed during the experiment, namely the induction time, the early stages, and the late stages of crystallization, as well as slip. Results obtained from differential scanning calorimetry are presented to aid comparison of the crystallization behavior among samples.

Chapter 5 highlights important issues in shear-induced crystallization of nucleated polymers at high shear rates, compares results with those obtained in quasi-quiescent crystallization, and examines the relative influence of the nucleating agent, molecular weight, shear rate, and strain. The morphology and uniformity of the solidified samples are also discussed.

Chapter 6 evaluates several parameters characterizing kinetic and morphological changes in shear-induced crystallization, namely the product of shear rate and strain, the multiplication of this product by a characteristic relaxation time, specific work, and the Weissenberg number.

Finally, conclusions and original contributions to knowledge are provided in Chapters 7 and 8.

1.8 References

1. Defosse, M. *Modern Plastics World Encyclopedia* (Canon Communications, Los Angeles, 2008).
2. Hustad, P.D. "Frontiers in olefin polymerization: Reinventing the world's most common synthetic polymers" *Science* (2009) **325**, 704-707.
3. Zweifel, H., Maier, R.D., and Schiller, M. *Plastics Additives Handbook*, 6th ed. (Hanser Publishers, Munich, 2009).
4. Tadmor, Z. and Gogos, C.G. *Principles of Polymer Processing*, 2nd ed. (Wiley-Interscience, Hoboken, N.J., 2006).
5. Wunderlich, B. *Macromolecular Physics, Vol. 1: Crystal Structure, Morphology, Defects* (Academic Press, New York, 1973).
6. Van Krevelen, D.W. *Properties of Polymers. Their Correlation with Chemical Structure; Their Numerical Estimation and Prediction from Additive Group Contributions*, 3rd ed. (Elsevier, Amsterdam, 1990).
7. Wunderlich, B. *Macromolecular Physics. Vol. 2: Crystal Nucleation, Growth and Annealing* (Academic Press, New York, 1976).
8. Mandelkern, L. *Crystallization of Polymers. Vol. 2: Kinetics and Mechanisms*, 2nd ed. (Cambridge University Press, Cambridge, 2004).
9. Schultz, J.M. *Polymer Crystallization: The Development of Crystalline Order in Thermoplastic Polymers* (Oxford University Press, New York, 2001).

10. Janeschitz-Kriegl, H. *Crystallization Modalities in Polymer Melt Processing: Fundamental Aspects of Structure Formation* (SpringerWienNewYork, Germany, 2010).
11. Strobl, G. “Crystallization and melting of bulk polymers: New observations, conclusions and a thermodynamic scheme” *Prog. Polym. Sci.* (2006) **31**, 398-442.
12. Barham, P.J. “Structure and morphology of oriented polymers”, in *Structure and Properties of Oriented Polymers*, I. M. Ward, Ed., (Chapman & Hall, New York, 1997).
13. Dealy, J.M. and Larson, R.G. *Structure and Rheology of Molten Polymers: From Structure to Flow Behavior and Back Again* (Hanser Publishers, Munich, 2006).
14. Keller, A. and Kolnaar, H.W.H. “Flow-induced orientation and structure formation”, in *Materials Science and Technology: A Comprehensive Treatment*, R. W. Cahn, P. Haasen, E. J. Kramer, Eds., Vol. 18, (Wiley-VCH, Weinheim, 1997), 189-268.
15. Eder, G. and Janeschitz-Kriegl, H. “Crystallization”, in *Materials Science and Technology: A Comprehensive Treatment*, R. W. Cahn, P. Haasen, E. J. Kramer, Eds., Vol. 18, (Wiley-VCH, Weinheim, 1997), 269-342.
16. Binsbergen, F.L. “Orientation-induced nucleation in polymer crystallization” *Nature* (1966) **211**, 516-517.
17. Williamson, R.B. and Busse, W.F. “Intercluster links. Mechanism for flow-induced crystallization of polymer melts” *J. Appl. Phys.* (1967) **38**, 4187-4196.
18. Kawai, T., Matsumoto, T., Kato, M., and Maeda, H. “Crystallization of polyethylene in steady-state flow” *Kolloid-Z. u. Z. Polymere* (1968) **222**, 1-10.
19. Haas, T.W. and Maxwell, B. “Effects of shear stress on the crystallization of linear polyethylene and poly-1-butene” *Polym. Eng. Sci.* (1969) **9**, 225-241.
20. Kobayashi, K. and Nagasawa, T. “Crystallization of sheared polymer melts” *J. Macromol. Sci., Phys.* (1970) **4**, 331-345.
21. Wereta, A., Jr. and Gogos, C.G. “Crystallization studies on deformed polybutene-1 melts” *Polym. Eng. Sci.* (1971) **11**, 19-27.
22. Krueger, D. and Yeh, G.S.Y. “Morphology of high-strength transparent polyethylene prepared under controlled conditions” *J. Appl. Phys.* (1972) **43**, 4339-4343.
23. Fritzsche, A.K. and Price, F.P. “Crystallization of polyethylene oxide under shear” *Polym. Eng. Sci.* (1974) **14**, 401-412.
24. Lagasse, R.R. and Maxwell, B. “An experimental study of the kinetics of polymer crystallization during shear flow” *Polym. Eng. Sci.* (1976) **16**, 189-199.

25. Tan, V. and Gogos, C.G. “Flow-induced crystallization of linear polyethylene above its normal melting point” *Polym. Eng. Sci.* (1976) **16**, 512-525.
26. Andersen, P.G. and Carr, S.H. “Crystal nucleation in sheared polymer melts” *Polym. Eng. Sci.* (1978) **18**, 215-221.
27. Sherwood, C.H., Price, F.P., and Stein, R.S. “Effect of shear on the crystallization kinetics of poly(ethylene oxide) and poly(ε-caprolactone) melts” *J. Polym. Sci., Polym. Symp.* (1978) **63**, 77-94.
28. Wolkowicz, M.D. “Nucleation and crystal growth in sheared poly(1-butene) melts” *J. Polym. Sci., Polym. Symp.* (1978) **63**, 365-382.
29. Eder, G., Janeschitz-Kriegl, H., and Liedauer, S. “Crystallization processes in quiescent and moving polymer melts under heat transfer conditions” *Prog. Polym. Sci.* (1990) **15**, 629-714.
30. Kumaraswamy, G. “Crystallization of polymers from stressed melts” *J. Macromol. Sci., Polym. Rev.* (2005) **45**, 375-397.
31. Kornfield, J.A., Kumaraswamy, G., and Issaian, A.M. “Recent advances in understanding flow effects on polymer crystallization” *Ind. Eng. Chem. Res.* (2002) **41**, 6383-6392.
32. Liedauer, S., Eder, G., Janeschitz-Kriegl, H., Jerschow, P., Geymayer, W., and Ingolic, E. “On the kinetics of shear-induced crystallization in polypropylene” *Int. Polym. Process.* (1993) **8**, 236-244.
33. Jerschow, P. and Janeschitz-Kriegl, H. “The role of long molecules and nucleating agents in shear induced crystallization of isotactic polypropylenes” *Int. Polym. Process.* (1997) **12**, 72-77.
34. Janeschitz-Kriegl, H., Ratajski, E., and Stadlbauer, M. “Flow as an effective promotor of nucleation in polymer melts: A quantitative evaluation” *Rheol. Acta* (2003) **42**, 355-364.
35. Janeschitz-Kriegl, H. and Ratajski, E. “Kinetics of polymer crystallization under processing conditions: Transformation of dormant nuclei by the action of flow” *Polymer* (2005) **46**, 3856-3870.
36. Janeschitz-Kriegl, H. “Phases of flow-induced crystallization of i-PP: How remote pieces of the puzzle appear to fit” *Macromolecules* (2006) **39**, 4448-4454.
37. Janeschitz-Kriegl, H. and Eder, G. “Shear induced crystallization, a relaxation phenomenon in polymer melts: A re-collection” *J. Macromol. Sci., Part B: Phys.* (2007) **46 B**, 591-601.

38. Kumaraswamy, G., Issaian, A.M., and Kornfield, J.A. "Shear-enhanced crystallization in isotactic polypropylene. 1. Correspondence between in situ rheo-optics and ex situ structure determination" *Macromolecules* (1999) **32**, 7537-7547.
39. Seki, M., Thurman, D.W., Oberhauser, J.P., and Kornfield, J.A. "Shear-mediated crystallization of isotactic polypropylene: The role of long chain-long chain overlap" *Macromolecules* (2002) **35**, 2583-2594.
40. Kumaraswamy, G., Verma, R.K., Kornfield, J.A., Yeh, F., and Hsiao, B.S. "Shear-enhanced crystallization in isotactic polypropylene. In-situ synchrotron SAXS and WAXD" *Macromolecules* (2004) **37**, 9005-9017.
41. Kimata, S., Sakurai, T., Nozue, Y., Kasahara, T., Yamaguchi, N., Karino, T., Shibayama, M., and Kornfield, J.A. "Molecular basis of the shish-kebab morphology in polymer crystallization" *Science* (2007) **316**, 1014-1017.
42. Fernandez-Ballester, L., Gough, T., Meneau, F., Bras, W., Ania, F., Balta-Calleja, F.J., and Kornfield, J.A. "Simultaneous birefringence, small- and wide-angle X-ray scattering to detect precursors and characterize morphology development during flow-induced crystallization of polymers" *J. Synchrotron Radiat.* (2008) **15**, 185-190.
43. Fernandez-Ballester, L., Thurman, D.W., and Kornfield, J.A. "Real-time depth sectioning: Isolating the effect of stress on structure development in pressure-driven flow" *J. Rheol.* (2009) **53**, 1229-1254.
44. Pogodina, N.V., Lavrenko, V.P., Srinivas, S., and Winter, H.H. "Rheology and structure of isotactic polypropylene near the gel point: Quiescent and shear-induced crystallization" *Polymer* (2001) **42**, 9031-9043.
45. Somani, R.H., Yang, L., Sics, I., Hsiao, B.S., Pogodina, N.V., Winter, H.H., Agarwal, P., Fruitwala, H., and Tsou, A. "Orientation-induced crystallization in isotactic polypropylene melt by shear deformation" *Macromol. Symp.* (2002) **185**, 105-117.
46. Acierno, S., Palomba, B., Winter, H.H., and Grizzuti, N. "Effect of molecular weight on the flow-induced crystallization of isotactic poly(1-butene)" *Rheol. Acta* (2003) **42**, 243-250.
47. Elmoumni, A., Winter, H.H., Waddon, A.J., and Fruitwala, H. "Correlation of material and processing time scales with structure development in isotactic polypropylene crystallization" *Macromolecules* (2003) **36**, 6453-6461.
48. Elmoumni, A., Gonzalez-Ruiz, R.A., Coughlin, E.B., and Winter, H.H. "Isotactic poly(propylene) crystallization: Role of small fractions of high or low molecular weight polymer" *Macromol. Chem. Phys.* (2005) **206**, 125-134.

49. Elmoumni, A. and Winter, H.H. “Large strain requirements for shear-induced crystallization of isotactic polypropylene” *Rheol. Acta* (2006) **45**, 793-801.
50. Somani, R.H., Hsiao, B.S., Nogales, A., Srinivas, S., Tsou, A.H., Sics, I., Balta-Calleja, F.J., and Ezquerra, T.A. “Structure development during shear flow-induced crystallization of i-PP: In-situ small-angle X-ray scattering study” *Macromolecules* (2000) **33**, 9385-9394.
51. Nogales, A., Hsiao, B.S., Somani, R.H., Srinivas, S., Tsou, A.H., Balta-Calleja, F.J., and Ezquerra, T.A. “Shear-induced crystallization of isotactic polypropylene with different molecular weight distributions: In situ small- and wide-angle X-ray scattering studies” *Polymer* (2001) **42**, 5247-5256.
52. Somani, R.H., Hsiao, B.S., Nogales, A., Fruitwala, H., Srinivas, S., and Tsou, A.H. “Structure development during shear flow induced crystallization of i-PP: In situ wide-angle X-ray diffraction study” *Macromolecules* (2001) **34**, 5902-5909.
53. Somani, R.H., Yang, L., Hsiao, B.S., Agarwal, P.K., Fruitwala, H.A., and Tsou, A.H. “Shear-induced precursor structures in isotactic polypropylene melt by in-situ rheo-SAXS and rheo-WAXD studies” *Macromolecules* (2002) **35**, 9096-9104.
54. Agarwal, P.K., Somani, R.H., Weng, W., Mehta, A., Yang, L., Ran, S., Liu, L., and Hsiao, B.S. “Shear-induced crystallization in novel long chain branched polypropylenes by in situ rheo-SAXS and -WAXD” *Macromolecules* (2003) **36**, 5226-5235.
55. Hsiao, B.S., Yang, L., Somani, R.H., Avila-Orta, C.A., and Zhu, L. “Unexpected shish-kebab structure in a sheared polyethylene melt” *Phys. Rev. Lett.* (2005) **94**, 117802.
56. Somani, R.H., Yang, L., Zhu, L., and Hsiao, B.S. “Flow-induced shish-kebab precursor structures in entangled polymer melts” *Polymer* (2005) **46**, 8587-8623.
57. Somani, R.H., Yang, L., Hsiao, B.S., Sun, T., Pogodina, N.V., and Lustiger, A. “Shear-induced molecular orientation and crystallization in isotactic polypropylene: Effects of the deformation rate and strain” *Macromolecules* (2005) **38**, 1244-1255.
58. Somani, R.H., Yang, L., and Hsiao, B.S. “Effects of high molecular weight species on shear-induced orientation and crystallization of isotactic polypropylene” *Polymer* (2006) **47**, 5657-5668.
59. Keum, J.K., Zuo, F., and Hsiao, B.S. “Formation and stability of shear-induced shish-kebab structure in highly entangled melts of UHMWPE/HDPE blends” *Macromolecules* (2008) **41**, 4766-4776.

60. van Meerveld, J., Peters, G.W.M., and Hütter, M. “Towards a rheological classification of flow induced crystallization experiments of polymer melts” *Rheol. Acta* (2004) **44**, 119-134.
61. Van der Beek, M.H.E., Peters, G.W.M., and Meijer, H.E.H. “Classifying the combined influence of shear rate, temperature, and pressure on crystalline morphology and specific volume of isotactic (poly)propylene” *Macromolecules* (2006) **39**, 9278-9284.
62. Balzano, L., Kukalyekar, N., Rastogi, S., Peters, G.W.M., and Chadwick, J.C. “Crystallization and dissolution of flow-induced precursors” *Phys. Rev. Lett.* (2008) **100**, 048302.
63. Balzano, L., Rastogi, S., and Peters, G.W.M. “Flow induced crystallization in isotactic polypropylene-1,3:2,4-bis(3,4-dimethylbenzylidene)sorbitol blends: Implications on morphology of shear and phase separation” *Macromolecules* (2008) **41**, 399-408.
64. Balzano, L., Rastogi, S., and Peters, G.W.M. “Crystallization and precursors during fast short-term shear” *Macromolecules* (2009) **42**, 2088-2092.
65. Housmans, J.-W., Steenbakkers, R.J.A., Roozemond, P.C., Peters, G.W.M., and Meijer, H.E.H. “Saturation of pointlike nuclei and the transition to oriented structures in flow-induced crystallization of isotactic polypropylene” *Macromolecules* (2009) **42**, 5728-5740.
66. Mackley, M.R., Moggridge, G.D., and Saquet, O. “Direct experimental evidence for flow induced fibrous polymer crystallization occurring at a solid/melt interface” *J. Mater. Sci.* (2000) **35**, 5247-5253.
67. Hassell, D.G. and Mackley, M.R. “Localised flow-induced crystallisation of a polyethylene melt” *Rheol. Acta* (2008) **47**, 435-446.
68. Scelsi, L., Mackley, M.R., Klein, H., Olmsted, P.D., Graham, R.S., Harlen, O.G., and McLeish, T.C.B. “Experimental observations and matching viscoelastic specific work predictions of flow-induced crystallization for molten polyethylene within two flow geometries” *J. Rheol.* (2009) **53**, 859-876.
69. Azzurri, F. and Alfonso, G.C. “Lifetime of shear-induced crystal nucleation precursors” *Macromolecules* (2005) **38**, 1723-1728.
70. Azzurri, F. and Alfonso, G.C. “Insights into formation and relaxation of shear-induced nucleation precursors in isotactic polystyrene” *Macromolecules* (2008) **41**, 1377-1383.
71. Baert, J. and Van Puyvelde, P. “Effect of molecular and processing parameters on the flow-induced crystallization of poly-1-butene. Part 1: Kinetics and morphology” *Polymer* (2006) **47**, 5871-5879.

72. Baert, J., Van Puyvelde, P., and Langouche, F. “Flow-induced crystallization of PB-1: From the low shear rate region up to processing rates” *Macromolecules* (2006) **39**, 9215-9222.
73. Koscher, E. and Fulchiron, R. “Influence of shear on polypropylene crystallization: Morphology development and kinetics” *Polymer* (2002) **43**, 6931-6942.
74. Bustos, F., Cassagnau, P., and Fulchiron, R. “Effect of molecular architecture on quiescent and shear-induced crystallization of polyethylene” *J. Polym. Sci., Part B: Polym. Phys.* (2006) **44**, 1597-1607.
75. Naudy, S., David, L., Rochas, C., and Fulchiron, R. “Shear induced crystallization of poly(m-xylylene adipamide) with and without nucleating additives” *Polymer* (2007) **48**, 3273-3285.
76. Byelov, D., Panine, P., Remerie, K., Biemond, E., Alfonso, G.C., and de Jeu, W.H. “Crystallization under shear in isotactic polypropylene containing nucleators” *Polymer* (2008) **49**, 3076-3083.
77. Floudas, G., Hilliou, L., Lellinger, D., and Alig, I. “Shear-induced crystallization of poly(ε-caprolactone). 2. Evolution of birefringence and dichroism” *Macromolecules* (2000) **33**, 6466-6472.
78. Lellinger, D., Floudas, G., and Alig, I. “Shear induced crystallization in poly(ε-caprolactone): Effect of shear rate” *Polymer* (2003) **44**, 5759-5769.
79. Pople, J.A., Mitchell, G.R., and Chai, C.K. “In-situ time-resolving wide-angle X-ray scattering study of crystallization from sheared polyethylene melts” *Polymer* (1996) **37**, 4187-4191.
80. Pople, J.A., Mitchell, G.R., Sutton, S.J., Vaughan, A.S., and Chai, C.K. “The development of organized structures in polyethylene crystallized from a sheared melt, analyzed by WAXS and TEM” *Polymer* (1999) **40**, 2769-2777.
81. Chai, C.K., Auzoux, Q., Randrianatoandro, H., Navard, P., and Haudin, J.M. “Influence of pre-shearing on the crystallisation of conventional and metallocene polyethylenes” *Polymer* (2003) **44**, 773-782.
82. Chaari, F., Chaouche, M., Benyahia, L., and Tassin, J.F. “Investigation of the crystallization of m(LLDPE) under shear flow using rheo-optical techniques” *Polymer* (2006) **47**, 1689-1695.
83. Li, L. and de Jeu, W.H. “Shear-induced smectic ordering and crystallisation of isotactic polypropylene” *Faraday Discuss.* (2005) **128**, 299-319.
84. Byelov, D., Panine, P., and de Jeu, W.H. “Shear-induced smectic order in isotactic polypropylene revisited” *Macromolecules* (2007) **40**, 288-289.

85. Na, B., Wang, Y., Zhang, Q., and Fu, Q. "Shish and its relaxation dependence of re-crystallization of isotactic polypropylene from an oriented melt in the blends with high-density polyethylene" *Polymer* (2004) **45**, 6245-6260.
86. Coppola, S., Grizzuti, N., and Maffettone, P.L. "Microrheological modeling of flow-induced crystallization" *Macromolecules* (2001) **34**, 5030-5036.
87. Coppola, S., Balzano, L., Gioffredi, E., Maffettone, P.L., and Grizzuti, N. "Effects of the degree of undercooling on flow induced crystallization in polymer melts" *Polymer* (2004) **45**, 3249-3256.
88. Acierno, S., Coppola, S., and Grizzuti, N. "Effects of molecular weight distribution on the flow-enhanced crystallization of poly(1-butene)" *J. Rheol.* (2008) **52**, 551-566.
89. Hadinata, C., Gabriel, C., Ruellman, M., and Laun, H.M. "Comparison of shear-induced crystallization behavior of PB-1 samples with different molecular weight distribution" *J. Rheol.* (2005) **49**, 327-349.
90. Hadinata, C., Gabriel, C., Ruellmann, M., Kao, N., and Laun, H.M. "Shear-induced crystallization of PB-1 up to processing-relevant shear rates" *Rheol. Acta* (2006) **45**, 539-546.
91. Zhang, C., Hu, H., Wang, D., Yan, S., and Han, C.C. "In situ optical microscope study of the shear-induced crystallization of isotactic polypropylene" *Polymer* (2005) **46**, 8157-8161.
92. An, Y., Holt, J.J., Mitchell, G.R., and Vaughan, A.S. "Influence of molecular composition on the development of microstructure from sheared polyethylene melts: Molecular and lamellar templating" *Polymer* (2006) **47**, 5643-5656.
93. Martins, J.A., Zhang, W., and Brito, A.M. "Saturation of shear-induced isothermal crystallization of polymers at the steady state and the entanglement-disentanglement transition" *Macromolecules* (2006) **39**, 7626-7634.
94. Heeley, E.L., Fernyhough, C.M., Graham, R.S., Olmsted, P.D., Inkson, N.J., Embery, J., Groves, D.J., McLeish, T.C.B., Morgovan, A.C., Meneau, F., Bras, W., and Ryan, A.J. "Shear-induced crystallization in blends of model linear and long-chain branched hydrogenated polybutadienes" *Macromolecules* (2006) **39**, 5058-5071.
95. Lee, O. and Kamal, M.R. "Experimental study of post-shear crystallization of polypropylene melts" *Polym. Eng. Sci.* (1999) **39**, 236-248.
96. Tavichai, O., Feng, L., and Kamal, M.R. "Crystalline spherulitic growth kinetics during shear for linear low-density polyethylene" *Polym. Eng. Sci.* (2006) **46**, 1468-1475.

97. Yamazaki, S., Watanabe, K., Okada, K., Yamada, K., Tagashira, K., Toda, A., and Hikosaka, M. "Formation mechanism of shish in the oriented melt (I) - Bundle nucleus becomes to shish" *Polymer* (2005) **46**, 1675-1684.
98. Yamazaki, S., Watanabe, K., Okada, K., Yamada, K., Tagashira, K., Toda, A., and Hikosaka, M. "Formation mechanism of shish in the oriented melt (II) - Two different growth mechanisms along and perpendicular to the flow direction" *Polymer* (2005) **46**, 1685-1692.
99. Watanabe, K., Okada, K., Toda, A., Yamazaki, S., Taniguchi, T., Koyama, K., Yamada, K., and Hikosaka, M. "Acceleration mechanism of growth rates under shear flow due to the oriented melt-the novel morphology of spiral crystal (spiralite)" *Macromolecules* (2006) **39**, 1515-1524.
100. Fukushima, H., Ogino, Y., Matsuba, G., Nishida, K., and Kanaya, T. "Crystallization of polyethylene under shear flow as studied by time resolved depolarized light scattering. Effects of shear rate and shear strain" *Polymer* (2005) **46**, 1878-1885.
101. Ogino, Y., Fukushima, H., Takahashi, N., Matsuba, G., Nishida, K., and Kanaya, T. "Crystallization of isotactic polypropylene under shear flow observed in a wide spatial scale" *Macromolecules* (2006) **39**, 7617-7625.
102. Kanaya, T., Matsuba, G., Ogino, Y., Nishida, K., Shimizu, H.M., Shinohara, T., Oku, T., Suzuki, J., and Otomo, T. "Hierarchic structure of shish-kebab by neutron scattering in a wide Q range" *Macromolecules* (2007) **40**, 3650-3654.
103. Matsuba, G., Sakamoto, S., Ogino, Y., Nishida, K., and Kanaya, T. "Crystallization of polyethylene blends under shear flow. Effects of crystallization temperature and ultrahigh molecular weight component" *Macromolecules* (2007) **40**, 7270-7275.
104. Hayashi, Y., Matsuba, G., Zhao, Y., Nishida, K., and Kanaya, T. "Precursor of shish-kebab in isotactic polystyrene under shear flow" *Polymer* (2009) **50**, 2095-2103.
105. Nagatake, W., Takahashi, T., Masubuchi, Y., Takimoto, J.I., and Koyama, K. "Development of shear flow thermal rheometer for direct measurement of crystallization fraction of polymer melts under shear deformation" *Polymer* (2000) **41**, 523-531.
106. Watanabe, K., Suzuki, T., Masubuchi, Y., Taniguchi, T., Takimoto, J.I., and Koyama, K. "Crystallization kinetics of polypropylene under high pressure and steady shear flow" *Polymer* (2003) **44**, 5843-5849.
107. Langouche, F. "Orientation development during shear flow-induced crystallization of i-PP" *Macromolecules* (2006) **39**, 2568-2573.

108. An, H., Zhao, B., Zhe, M., Shao, C., Wang, X., Fang, Y., Li, A., and Li, Z. "Shear-induced conformational ordering in the melt of isotactic polypropylene" *Macromolecules* (2007) **40**, 4740-4743.
109. Nogales, A., Mitchell, G.R., and Vaughan, A.S. "Anisotropic crystallization in polypropylene induced by deformation of a nucleating agent network" *Macromolecules* (2003) **36**, 4898-4906.
110. Nogales, A. and Mitchell, G.R. "Development of highly oriented polymer crystals from row assemblies" *Polymer* (2005) **46**, 5615-5620.
111. Tribout, C., Monasse, B., and Haudin, J.M. "Experimental study of shear-induced crystallization of an impact polypropylene copolymer" *Colloid Polym. Sci.* (1996) **274**, 197-208.
112. Jay, F., Haudin, J.M., and Monasse, B. "Shear-induced crystallization of polypropylenes: Effect of molecular weight" *J. Mater. Sci.* (1999) **34**, 2089-2102.
113. Duplay, C., Monasse, B., Haudin, J.M., and Costa, J.L. "Shear-induced crystallization of polypropylene: Influence of molecular weight" *J. Mater. Sci.* (2000) **35**, 6093-6103.
114. Haudin, J.M., Duplay, C., Monasse, B., and Costa, J.L. "Shear-induced crystallization of polypropylene. Growth enhancement and rheology in the crystallization range" *Macromol. Symp.* (2002) **185**, 119-133.
115. Devaux, N., Monasse, B., Haudin, J.M., Moldenaers, P., and Vermant, J. "Rheooptical study of the early stages of flow enhanced crystallization in isotactic polypropylene" *Rheol. Acta* (2004) **43**, 210-222.
116. Coccorullo, I., Pantani, R., and Titomanlio, G. "Spherulitic nucleation and growth rates in an iPP under continuous shear flow" *Macromolecules* (2008) **41**, 9214-9223.
117. Mykhaylyk, O.O., Chambon, P., Graham, R.S., Fairclough, J.P.A., Olmsted, P.D., and Ryan, A.J. "The specific work of flow as a criterion for orientation in polymer crystallization" *Macromolecules* (2008) **41**, 1901-1904.
118. Yan, T., Zhao, B., Cong, Y., Fang, Y., Cheng, S., Li, L., Pan, G., Wang, Z., Li, X., and Bian, F. "Critical strain for shish-kebab formation" *Macromolecules* (2010) **43**, 602-605.
119. Kurja, J. and Mehl, N. "Nucleating agents for semi-crystalline polymers", in *Plastics Additives Handbook*, H. Zweifel, R. D. Maier, M. Schiller, Eds., (Hanser Publishers, Munich, 2009), 967-990.
120. Beck, H.N. "Heterogeneous nucleating agents for polypropylene crystallization" *J. Appl. Polym. Sci.* (1967) **11**, 673-685.

121. Binsbergen, F.L. "Heterogeneous nucleation in the crystallization of polyolefins. 1. Chemical and physical nature of nucleating agents" *Polymer* (1970) **11**, 253-267.
122. Pasquini, N. *Polypropylene Handbook*, 2nd ed. (Hanser Publishers, Munich, 2005).
123. Karger-Kocsis, J. *Polypropylene: Structure, Blends and Composites. Vol 1: Structure and Morphology* (Chapman & Hall, New York, 1995).
124. Karger-Kocsis, J. *Polypropylene: An A-Z Reference* (Kluwer Academic Publishers, Dordrecht, The Netherlands, 1998).
125. Natta, G., Pino, P., Corradini, P., Danusso, F., Mantica, E., Mazzanti, G., and Moraglio, G. "Crystalline high polymers of α-olefins" *J. Am. Chem. Soc.* (1955) **77**, 1708-1710.
126. Ziegler, K., Holzkamp, E., Breil, H., and Martin, H. "Das Mülheimer Normaldruck-Polyäthylen-Verfahren" *Angew. Chem.* (1955) **67**, 541-547.
127. Binsbergen, F.L. and De Lange, B.G.M. "Heterogeneous nucleation in the crystallization of polyolefins. 2. Kinetics of crystallization of nucleated polypropylene" *Polymer* (1970) **11**, 309-326.
128. Busico, V. and Cipullo, R. "Microstructure of polypropylene" *Prog. Polym. Sci.* (2001) **26**, 443-533.
129. Cheng, S.Z.D., Janimak, J.J., Zhang, A., and Hsieh, E.T. "Isotacticity effect on crystallization and melting in polypropylene fractions. 1. Crystalline structures and thermodynamic property changes" *Polymer* (1991) **32**, 648-655.
130. Janimak, J.J., Cheng, S.Z.D., Giusti, P.A., and Hsieh, E.T. "Isotacticity effect on crystallization and melting in poly(propylene) fractions. 2. Linear crystal growth rate and morphology study" *Macromolecules* (1991) **24**, 2253-2260.
131. Janimak, J.J., Cheng, S.Z.D., Zhang, A., and Hsieh, E.T. "Isotacticity effect on crystallization and melting in polypropylene fractions. 3. Overall crystallization and melting behavior" *Polymer* (1992) **33**, 728-735.
132. Bassett, D.C. *Principles of Polymer Morphology* (Cambridge University Press, New York, 1981).
133. Cheng, S.Z.D. *Phase Transitions in Polymers: The Role of Metastable States* (Elsevier, Boston, 2008).
134. Ostwald, W. "Studien über die Bildung und Umwandlung fester Körper" *Z. Phys. Chem.* (1897) **22**, 289-302.
135. Varga, J. "Supermolecular structure of isotactic polypropylene" *J. Mater. Sci.* (1992) **27**, 2557-2579.
136. Keller, A. "Polymer crystals" *Rep. Prog. Phys.* (1968) **31**, 623-704.

137. Phillips, P.J. “Polymer crystals” *Rep. Prog. Phys.* (1990) **53**, 549-604.

138. Kalay, G. and Bevis, M.J. “Processing and physical property relationships in injection-molded isotactic polypropylene. 2. Morphology and crystallinity” *J. Polym. Sci., Part B: Polym. Phys.* (1997) **35**, 265-291.

139. Mandelkern, L. *Crystallization of Polymers. Vol. 1: Equilibrium Concepts*, 2nd ed. (Cambridge University Press, Cambridge, 2002).

140. Oxtoby, D.W. “Nucleation of first-order phase transitions” *Acc. Chem. Res.* (1998) **31**, 91-97.

141. Hoffman, J.D. and Lauritzen Jr., J.I. “Crystallization of bulk polymers with chain folding: Theory of growth lamellar spherulites” *J. Res. Natl. Bur. Stand. Sect. A* (1961) **65**, 297-336.

142. Hoffman, J.D. and Miller, R.L. “Kinetics of crystallization from the melt and chain folding in polyethylene fractions revisited: Theory and experiment” *Polymer* (1997) **38**, 3151-3212.

143. Olmsted, P.D., Poon, W.C.K., McLeish, T.C.B., Terrill, N.J., and Ryan, A.J. “Spinodal-assisted crystallization in polymer melts” *Phys. Rev. Lett.* (1998) **81**, 373-376.

144. Kaji, K., Nishida, K., Kanaya, T., Matsuba, G., Konishi, T., and Imai, M. “Spinodal crystallization of polymers: Crystallization from the unstable melt” *Adv. Polym. Sci.* (2005) **191**, 187-240.

145. Strobl, G. “From the melt via mesomorphic and granular crystalline layers to lamellar crystallites: A major route followed in polymer crystallization?” *Eur. Phys. J. E* (2000) **3**, 165-183.

146. Gee, R.H., Lacevic, N., and Fried, L.E. “Atomistic simulations of spinodal phase separation preceding polymer crystallization” *Nat. Mater.* (2006) **5**, 39-43.

147. Muthukumar, M. “Commentary on theories of polymer crystallization” *Eur. Phys. J. E* (2000) **3**, 199-202.

148. Lotz, B. “What can polymer crystal structure tell about polymer crystallization processes?” *Eur. Phys. J. E* (2000) **3**, 185-194.

149. Cheng, S.Z.D., Li, C.Y., and Zhu, L. “Commentary on polymer crystallization: selection rules in different length scales of a nucleation process” *Eur. Phys. J. E* (2000) **3**, 195-197.

150. Fillon, B., Lotz, B., Thierry, A., and Wittmann, J.C. “Self-nucleation and enhanced nucleation of polymers. Definition of a convenient calorimetric "efficiency scale" and evaluation of nucleating additives in isotactic polypropylene (α phase)” *J. Polym. Sci., Part B: Polym. Phys.* (1993) **31**, 1395-1405.

151. Fujiyama, M. and Wakino, T. "Structures and properties of injection moldings of crystallization nucleator-added polypropylenes. I. Structure-property relationships" *J. Appl. Polym. Sci.* (1991) **42**, 2739-2747.
152. Varga, J. "β-modification of isotactic polypropylene: Preparation, structure, processing, properties, and application" *J. Macromol. Sci., Part B: Phys.* (2002) **41 B**, 1121-1171.
153. Legras, R., Mercier, J.P., and Nield, E. "Polymer crystallization by chemical nucleation" *Nature* (1983) **304**, 432-434.
154. Mercier, J.P. "Nucleation in polymer crystallization. A physical or a chemical mechanism?" *Polym. Eng. Sci.* (1990) **30**, 270-278.
155. Kristiansen, M., Werner, M., Tervoort, T., Smith, P., Blomenhofer, M., and Schmidt, H.W. "The binary system isotactic polypropylene/bis(3,4-dimethylbenzylidene)sorbitol: Phase behavior, nucleation, and optical properties" *Macromolecules* (2003) **36**, 5150-5156.
156. Balzano, L., Portale, G., Peters, G.W.M., and Rastogi, S. "Thermoreversible DMDBS phase separation in iPP: The effects of flow on the morphology" *Macromolecules* (2008) **41**, 5350-5355.
157. Thierry, A., Straupe, C., Wittmann, J.C., and Lotz, B. "Organogelators and polymer crystallisation" *Macromol. Symp.* (2006) **241**, 103-110.
158. Wittmann, J.C. and Lotz, B. "Epitaxial crystallization of polymers on organic and polymeric substrates" *Prog. Polym. Sci.* (1990) **15**, 909-948.
159. Nakahara, Y., Akutsu, M., Haruna, T., and Takahashi, M. "Bis-phenol phosphates as clarifiers for polyolefin resins", *US Patent*, 4,463,113 (1984).
160. Flory, P.J. "Thermodynamics of crystallization in high polymers. I. Crystallization induced by stretching" *J. Chem. Phys.* (1947) **15**, 397-408.
161. McHugh, A.J. "Flow-induced crystallization in polymers", in *Rheo-physics of Multiphase Polymer Systems: Characterization by Rheo-optical Techniques*, K. Søndergaard, J. Lyngaae-Jørgensen, Eds., (Technomic Publishing Company, Lancaster, Pennsylvania, 1995).
162. Vleeshouwers, S. and Meijer, H.E.H. "A rheological study of shear induced crystallization" *Rheol. Acta* (1996) **35**, 391-399.
163. Nobile, M.R., Bove, L., Somma, E., Kruszelnicka, I., and Sterzynski, T. "Rheological and structure investigation of shear-induced crystallization of isotactic polypropylene" *Polym. Eng. Sci.* (2005) **45**, 153-162.
164. Pogodina, N.V., Winter, H.H., and Srinivas, S. "Strain effects on physical gelation of crystallizing isotactic polypropylene" *J. Polym. Sci., Part B: Polym. Phys.* (1999) **37**, 3512-3519.

165. Kiewiet, S., Janssens, V., Miltner, H.E., Van Assche, G., Van Puyvelde, P., and Van Mele, B. "RheoDSC: A hyphenated technique for the simultaneous measurement of calorimetric and rheological evolutions" *Rev. Sci. Instrum.* (2008) **79**, 023905.

166. Varga, J. and Karger-Kocsis, J. "Rules of supermolecular structure formation in sheared isotactic polypropylene melts" *J. Polym. Sci., Part B: Polym. Phys.* (1996) **34**, 657-670.

167. Kumaraswamy, G., Verma, R.K., and Kornfield, J.A. "Novel flow apparatus for investigating shear-enhanced crystallization and structure development in semicrystalline polymers" *Rev. Sci. Instrum.* (1999) **70**, 2097-2104.

168. Titomanlio, G. and Marrucci, G. "Capillary experiments of flow induced crystallization of HDPE" *AIChE J.* (1990) **36**, 13-18.

169. Dealy, J.M. and Wissbrun, K.F. *Melt Rheology and Its Role in Plastics Processing. Theory and Applications.* (Springer, Berlin, 1999).

170. He, J. and Zoller, P. "Crystallization of polypropylene, nylon-66 and poly (ethylene terephthalate) at pressures to 200 MPa: Kinetics and characterization of products" *J. Polym. Sci., Part B: Polym. Phys.* (1994) **32**, 1049-1067.

171. Mezghani, K. and Phillips, P.J. "The γ-phase of high molecular weight isotactic polypropylene: III. The equilibrium melting point and the phase diagram" *Polymer* (1998) **39**, 3735-3744.

172. Angelloz, C., Fulchiron, R., Douillard, A., Chabert, B., Fillit, R., Vautrin, A., and David, L. "Crystallization of isotactic polypropylene under high pressure (γ phase)" *Macromolecules* (2000) **33**, 4138-4145.

173. Hsiue, E.S., Robertson, R.E., and Yeh, G.S.Y. "Effects of shearing conditions on crystalline orientation and relaxation in polyethylene" *Polym. Eng. Sci.* (1983) **23**, 75-79.

174. Van der Beek, M.H.E., Peters, G.W.M., and Meijer, H.E.H. "Influence of shear flow on the specific volume and the crystalline morphology of isotactic polypropylene" *Macromolecules* (2006) **39**, 1805-1814.

175. Scelsi, L. and Mackley, M.R. "Rheo-optic flow-induced crystallisation of polypropylene and polyethylene within confined entry-exit flow geometries" *Rheol. Acta* (2008) **47**, 895-908.

176. Fuller, G.G. "Optical rheometry" *Annu. Rev. Fluid Mech.* (1990) **22**, 387-417.

177. Hadinata, C., Gabriel, C., Ruellmann, M., Kao, N., and Laun, H.M. “Correlation between the gel time and quiescent/quasi-quiescent crystallization onset time of poly(butene-1) as determined from rheological methods” *Rheol. Acta* (2006) **45**, 631-639.
178. Coppola, S., Acierno, S., Grizzuti, N., and Vlassopoulos, D. “Viscoelastic behavior of semicrystalline thermoplastic polymers during the early stages of crystallization” *Macromolecules* (2006) **39**, 1507-1514.
179. Khanna, Y. “Rheological mechanism and overview of nucleated crystallization kinetics” *Macromolecules* (1993) **26**, 3639-3643.
180. Heck, B., Kawai, T., and Strobl, G. “Time dependent light attenuation measurements used in studies of the kinetics of polymer crystallization” *Polymer* (2006) **47**, 5538-5543.
181. Deltu, R., Stille, W., and Strobl, G. “Depression of the zero growth temperature by counits observed for s-polypropylene in light attenuation experiments” *Macromolecules* (2010) **43**, 1035-1040.
182. Magill, J.H. “A new technique for following rapid rates of crystallization” *Nature* (1960) **187**, 770-771.
183. Magill, J.H. “A new technique for following rapid rates of crystallization. II. Isotactic polypropylene” *Polymer* (1962) **3**, 35-42.

Chapter 2: Experimental

2.1 Introduction

A variety of flow devices have been used to study shear-induced crystallization (Section 1.5.1). In essence, it is desirable to use a device that can generate high shear rates, as such flow conditions are of direct relevance to industrial processing and have a pronounced effect on crystallization behavior. Additionally, it is preferable to deform the sample at a uniform shear rate to avoid complications associated with an inhomogeneous flow field. An instrument that meets these two criteria is a sliding plate device.

In such a device, the sample is sandwiched between two parallel plates, and a rectilinear simple shear is generated by moving one of the plates relative to the other, stationary plate. While rectilinear shearing avoids some complex issues encountered in rotational and pressure flows, it is not as widely used as the latter in both rheological and shear-induced crystallization experiments. This is mainly due to several technical difficulties: fluctuations in the plate gap, instrument friction, end and edge effects, shear wave propagation due to inertia, and uncertainty of the wetted area of the sample [1]. But unlike other devices, the sliding plate rheometer (SPR) used in this study, developed at McGill University by Dealy and Giacomin [2-4], was designed to overcome these challenges. Equipped with a unique transducer for the direct measurement of shear stress, this device has been successfully used in the past for investigating wall slip and nonlinear viscoelasticity of polymer melts [5-8]. A commercial version of this instrument, known as the True Shear Rheometer, was available from EnduraTEC Systems Corporation (Minnetonka, MN), but is no longer manufactured.

Likewise, a wide range of measurement techniques have been employed to probe crystallization kinetics (Section 1.5.3). Due to the inherent limitations associated with each technique, it is a common practice to use two or more techniques in the hope of extracting complementary information that is either inaccessible or less sensitive from a single set of measurement. To be effective, the techniques should be employed simultaneously in the same device in a single experiment. As identical test conditions are involved in both techniques, the data obtained this way allow direct and unambiguous correlation. In contrast, data collected otherwise from separate experiments are affected by uncertainties that arise from not only the differences in the sensitivity of the measuring devices but also the inevitable changes in the test conditions between experiments (*e.g.*, sample size, heat transfer conditions, repeatability error).

While the use of rheo-optical instruments for simultaneous rheometry, polarimetry and scattering measurements is fairly popular in the studies of polymer melts and solutions [9, 10], it has not been extended to study the phenomenon of shear-induced crystallization in a sliding plate device at high shear rates. To enable tracking of crystallization kinetics by simultaneous rheometry and light intensity measurement, the present work capitalized on the advantages of the SPR shear stress transducer and added an optical system incorporating a bifurcated optical fiber probe.

2.2 Materials

Four isotactic polypropylene samples were used in this study, and Table 2.1 summarizes their key characteristics. The nucleated samples iPP1 and iPP2, produced using a Ziegler-Natta catalyst by The Dow Chemical Company, are highly isotactic with an isotactic pentad content of more than 96 %. Both iPP3 and iPP4 are commercial resins obtained from Sigma-Aldrich Corporation, St. Louis, MO. While samples iPP1 and iPP3 have a similar weight-average molecular weight M_w, iPP2 has a M_w that is approximately half that of iPP1, and iPP4 has the largest M_w. The polydispersity indexes $M_\mathrm{w}/M_\mathrm{n}$ of the four samples are in the range of 3.5 to 5.6. Figure 2.1 shows the molecular weight distributions of iPP1 and iPP2, which are similar in shape and indicate no high-molecular weight tails.

Table 2.1. Characteristics of isotactic polypropylene samples used in this study.

Sample name	**iPP1**	**iPP2**	**iPP3**	**iPP4**
Supplier	Dow Chemical	Dow Chemical	Sigma-Aldrich	Sigma-Aldrich
Isotacticity[a]				
% pentad [mmmm]	96.87	97.74	Not available	Not available
% triad [mm]	98.45	98.59		
Molecular weight distribution				
M_w /(kg/mol)	384[b] 323[c]	160[b] 162[c]	340[d]	580[d]
M_w / M_n	5.4[b] 4.7[c]	5.2[b] 5.6[c]	3.5[d]	3.5[d]
Melt flow index[e]				
MFI /(g/10 min)	3.9	57.2	4.0	0.5
Additives (by mass %)	• 0.08 % IRGASTAB® NA 11 • 0.2 % IRGANOX® B 225 • 0.04 % DHT 4A		No nucleating agent	

[a] Determined by carbon-13 nuclear magnetic resonance spectroscopy.

[b] Determined by high-temperature gel permeation chromatography (GPC) equipped with a refractive index detector and a viscometer at 160 °C. Samples were prepared at concentration of 0.1 g of polymer in 50 mL of 1,2,4-trichlorobenzene. Injection volume was 100 μL and flow rate was 1.0 mL/min. These data were used for comparison with those of non-nucleated samples in the following chapters.

[c] Same as above, in addition to a light scattering detector.

[d] Typical values reported by the supplier.

[e] Determined in accordance with ASTM D1238 at 230 °C and 2.16 kg load.

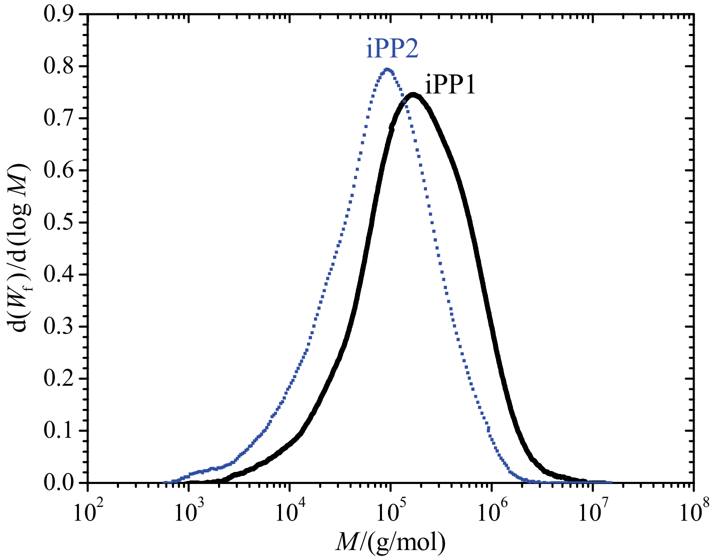

Figure 2.1. Molecular weight distributions of iPP1 and iPP2 determined by gel permeation chromatography with a light scattering detector.

Both iPP1 and iPP2 contain 0.08 % of nucleating agent IRGASTAB® NA 11 from Ciba Specialty Chemicals, Switzerland (see Sections 1.4 and 5.2 for further information). Other additives in these two samples are 0.2 % of antioxidant IRGANOX® B 225* (Ciba Specialty Chemicals, Switzerland) and 0.04 % of hydrotalcite DHT-4A† (Kyowa Chemical Industry, Japan). Little information regarding their composition is available for iPP3 and iPP4, but these resins contain no nucleating agent.

2.3 Instrument Description

An overview of the experimental setup is shown schematically in Fig. 2.2. The sliding plate rheometer, which consists of a shear fixture and a shear stress transducer, is installed inside an oven and mounted to a stiff, servo-hydraulic load frame. For light intensity measurement, an optical system incorporating a specially designed bifurcated optical fiber probe was assembled. A detailed description of the various components of the instrument is given below (see Appendix A for further specifications).

2.3.1 Shear Fixture

Figure 2.3 shows the main components of the SPR shear fixture. Both the moving and stationary plates are flat, smooth, rectangular plates made of stainless steel (AISI 420, 63 microinch surface finish). The moving plate, fitted with a pair of Teflon® siderails to suppress secondary flow due to normal stress gradient, is bolted to a precision linear bearing table. The assembly is coupled to a stainless steel support frame, which has a support shaft vertically mounted at its top end to a load frame. The stationary plate has hinges at its bottom end that enable it to swing open for sample loading and cleaning. Along its left and right edges, the plate has a total of eight tapped holes used for fastening to the support frame with shoulder screws and nuts.

---

[*] According to the manufacturer, IRGANOX® B 225 is a synergistic 50:50 blend of two antioxidants: IRGAFOS® 168 and IRGANOX® 1010. The former is an organophosphate that prevents oxidation during processing, whereas the latter is a hindered phenolic stabilizer that protects a polymer from thermo-oxidative degradation over its long-term service life.

[†] According to the manufacturer, DHT-4A is a magnesium/aluminum-hydrotalcite co-stabilizer and acts as an acid scavenger by neutralizing acids liberated by residual catalysts or other degrading compounds.

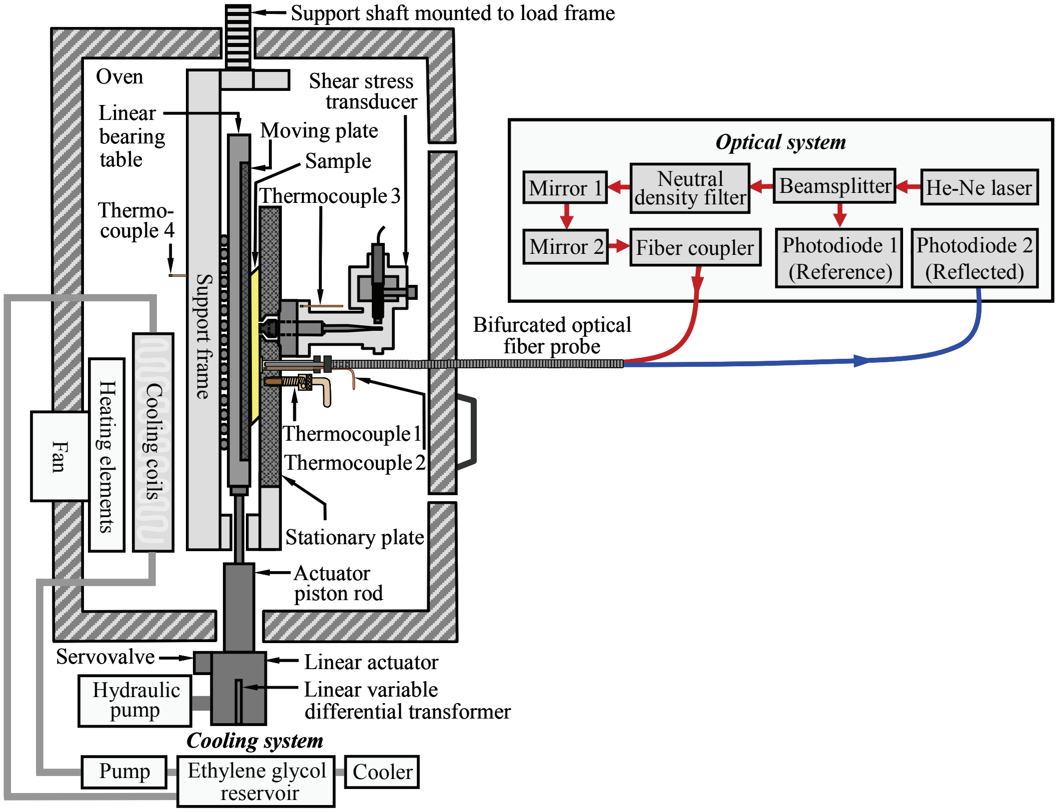

Figure 2.2. Overview of experimental setup illustrating the sliding plate rheometer, optical system, and temperature measurement and control system.

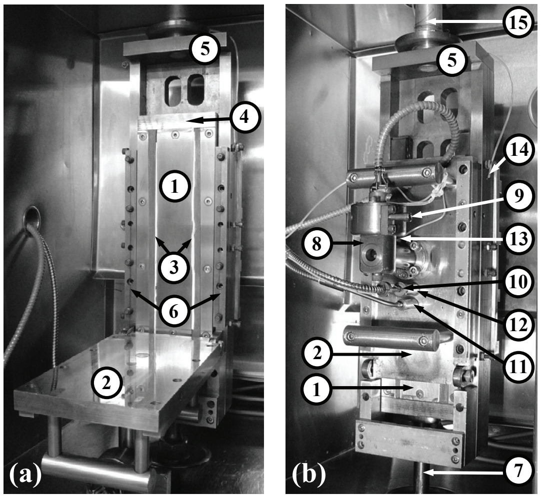

Figure 2.3. Front-view photographs of SPR inside an oven. (a) Stationary plate open. (b) Stationary plate fastened. Legends: 1: moving plate, 2: stationary plate, 3: Teflon® rails, 4: linear bearing table, 5: support frame, 6: gap spacers, 7: actuator piston rod, 8: shear stress transducer, 9: screw adjustor, 10: bifurcated optical fiber probe, 11: thermocouple 1, 12: thermocouple 2, 13: thermocouple 3, 14: thermocouple 4, 15: support shaft mounted to load frame.

Rectilinear shearing is achieved by displacing the moving plate up and down using a linear actuator, which is connected to the bottom of the linear bearing table via the actuator piston rod. The actuator is controlled by a precision servovalve and driven by a heavy-duty hydraulic pump. These two devices enable a precise translation of the moving plate by a large force that far exceeds the friction, inertia and the sample resistance. The linear bearing table, equipped with high-temperature grease-lubricated roller bearings, provides smooth, low-friction displacement. A linear variable differential transformer (LVDT) mounted on the actuator is used to measure the displacement. The LVDT output signal serves as a feedback signal for control of the position of the moving plate.

A pair of stainless steel spacers, available in various thicknesses (0.2 mm to 1.5 mm, machined to tolerances of ± 0.005 mm), are placed between the moving and stationary plates to provide the desired gap H. A gap of 1.0 mm was used throughout this study. The displacement x and the velocity V of the moving plate are used to determine the shear strain γ and the shear rate $\dot{\gamma}$ imposed on the sample:

$$\gamma = x/H \tag{2.1}$$

$$\dot{\gamma} \equiv \frac{d\gamma}{dt} = V/H \tag{2.2}$$

The length of the plates limits the maximum displacement (140 mm) and strain. The maximum shear rate is approximately 500 s^{-1}.

2.3.2 Shear Stress Transducer

A distinctive feature of the SPR over other sliding plate devices is its unique shear stress transducer (SST) [2], which provides a direct measurement of the shear stress, instead of the less accurate way of estimating it from the total force (which includes friction) required to displace the moving plate. Installed in the center of the stationary plate, the SST provides local measurement of the true shear stress in the sample over a small surface area that is well far away from the free surfaces. This not only eliminates the need for determining the exact wetted area of the sample but also circumvents issues associated with flow irregularities at the edges and ends. Another advantage of positioning the transducer in the center is that it minimizes potential errors contributed by sample degradation, which is less severe at the center than at the edges and ends that are exposed to the ambient air.

The SST was designed based on the principle of beam deflection. Several versions have been developed over the years, and the one used in this study was a disk spring SST. As shown in Fig. 2.4, the left end of the SST is called the active face, a small circular surface designed to be mounted flush with the surface of the stationary plate and in contact with the sample. The active face is bolted to a rigid beam, which is supported by a thin stainless steel disk spring (elastic diaphragm). The beam deflects in response to the stress acting tangentially on the active face, and the amount of deflection at the other end, *i.e.*, the target, is detected by a capacitance proximity probe. Secured to the transducer housing, the probe is placed axially perpendicular to the beam target. The probe and its electronic components produce a voltage signal V_s that is proportional to the gap between the target and the probe tip*. Shear stress is related to V_s using the calibration method described below.

---

* The conductive surface of the probe tip and that of the beam target, which is electrically connected to the ground, form a parallel-plate capacitor with its capacitive reactance given by: $X_\mathrm{cr} = V_\mathrm{p} / I_\mathrm{p} = d / (2\pi f \varepsilon A_\mathrm{c})$, where I_p is the peak excitation current, V_p is the peak measured voltage, d is the gap between the two surfaces, f is the excitation current frequency, ε is the permittivity of air, and A_c is the capacitor area. The beam deflection or the gap d is thus linearly proportional to V_p. The probe electronics has an alternating-current (AC), constant current source that supplies an excitation signal I_p at a fixed frequency of 15 kHz to the probe. It also has a low-capacitance voltage preamplifier, a synchronous detector, a low-pass filter at a cut-off frequency of 200 Hz, and a linearization circuit for converting the measured AC voltage V_p into an average direct-current voltage V_s with an output range of 0 V to 10 V.

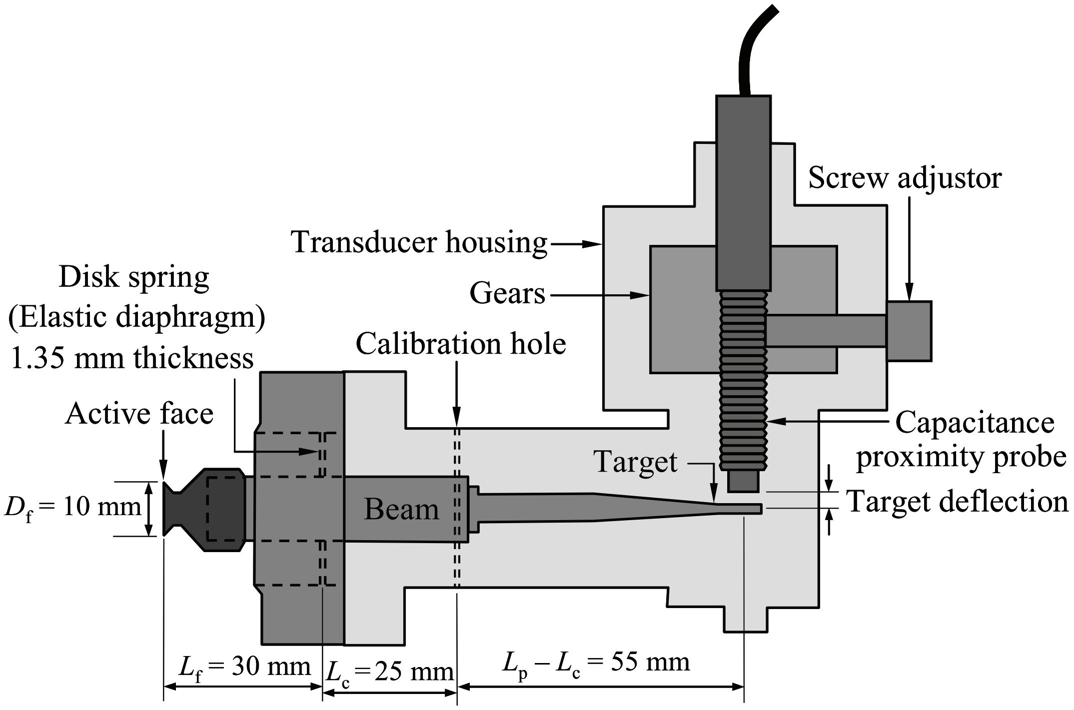

Figure 2.4. Cross-sectional side-view schematic of shear stress transducer.

As shown in Fig 2.5a, by suspending a weight of W_c (in kg) at the calibration hole with the aid of a steel wire and a series of pulleys, the shear stress σ (in kPa) acting on the active face can be determined by the following equation:

$$\sigma = \frac{F_f}{A_f} = \frac{W_c g \frac{L_c}{L_f}}{\pi (D_f / 2)^2} = 104.087 W_c \tag{2.3}$$

where F_f is the tangential force at the active face, A_f is the active face area, L_c is the calibrating lever length (25 mm, see Fig. 2.4), L_f is the active face lever length (30 mm), D_f is the active face diameter (10 mm), and g is the acceleration of gravity (9.81 m/s^2). The linear relationship $V_s \propto W_c \propto \sigma$ shown in the calibration results in Fig. 2.5b confirms linearity of the transducer over its operating range at the experimental temperature.

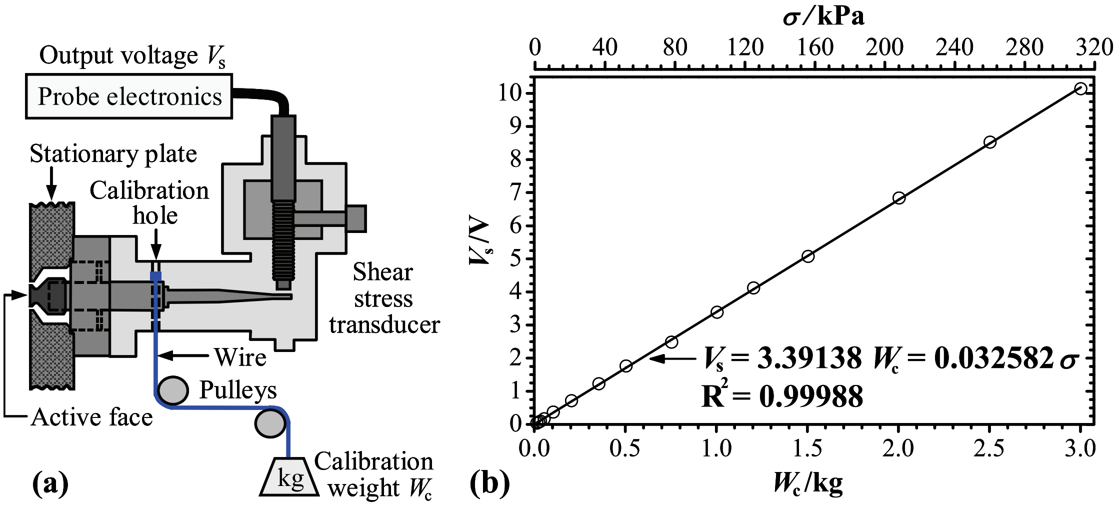

Figure 2.5. Calibration of the shear stress transducer. (a) Side-view schematic of the calibration setup. (b) As indicated by a coefficient of determination close to unity, the calibration results confirm the transducer linearity at 155.5 °C.

Due to the effect of thermal expansion or contraction, the gap between the beam target and the probe tip is very sensitive to changes in temperature. The transducer is therefore limited to stress measurements under isothermal conditions only, i.e., constant-cooling crystallization experiments are unfeasible. Accordingly, calibration must be performed isothermally at the experimental temperature. Additionally, for a satisfactory operation of the transducer, the gap must be kept within the narrow linear range of the capacitance probe (0.508 mm) and the output voltage at the initial probe position should be set to zero prior to an experiment. It is thus important to be able to manually adjust the probe position at the operating temperature to compensate for the thermal effects. For this purpose, the transducer housing has a screw adjustor that is connected laterally to the probe by several gears (Fig. 2.4). By means of a screw driver, the screw adjustor can be turned from outside the oven to move the probe toward or away from the beam target, thus allowing the setting of the gap just before the start of the experiment.

The active face is flush with the stationary plate surface but has a narrow gap of about 0.1 mm around its rim (Fig. 2.5a) so that a small deflection is possible during shearing. A very small quantity of the polymer can flow through the gap into the transducer housing.

For short rheological tests with melts, the sample has a negligible damping effect on the dynamic response of the transducer (except at high frequency) [7, 11]. In contrast, in crystallization experiments where an oscillatory shear is applied over an extended period of time, the accumulating, crystallizing sample with increasing stiffness can affect the stress measurements. This effect, however, is manifested only at the very late stages of crystallization, i.e., during which the viscosity of the sample is very high.

Two transducers with different stress ranges (300 kPa and 600 kPa) are available. For a more sensitive measurement, the SST with a maximum nominal stress of 300 kPa was used here. It provides a satisfactory signal-to-noise ratio for a stress above 2 kPa.

2.3.3 Optical System

A light intensity measurement typically involves directing a light beam through an optical window and the sample and detecting the transmitted intensity after passing through a second window. The installation of a second window on the SPR moving plate for measuring the transmitted intensity, however, would require some major retrofitting of the instrument. An alternative is to use a bifurcated optical fiber probe, also commonly known as a reflection or backscattering probe, which is capable of not only carrying the excitation light from a source to the sample but also returning the reflected light from the sample to a detector. Bur and Thomas [12, 13] have demonstrated the use of such an apparatus for monitoring the crystallization process during injection molding[*].

The key components of the optical system are shown in Fig. 2.6. A 5-milliwatt helium-neon laser with random polarization at a wavelength of 632.8 nm is used as the light source. Two amplified silicon photodiodes with adjustable gain settings, which provide voltage signals proportional to the measured light intensities, are used as detectors. A non-polarizing beam splitter cube with a split ratio of 50:50 is used to split the red laser into two beams. One of the beams serves as a reference of which the stability of its

---

[*] If crystallization does not take place, for example in the injection molding of amorphous polystyrene, there will be no attenuation in light intensity (see Fig. 6 in [14]).

intensity (< 2 % fluctuation over 12 hours) is monitored by one of the two photodiodes (photodiode 1), whereas the other beam passes a neutral density filter and two dielectric mirrors before being coupled to the optical fiber probe. The neutral density filter, with a variable optical density range of 0 to 4.0, provides an adjustable setting of the desired light intensity. A fiber coupler with a focusing lens is used to facilitate the alignment and coupling of the incident light into the fibers. The optical components are mounted on a breadboard and contained in an enclosure with a black interior.

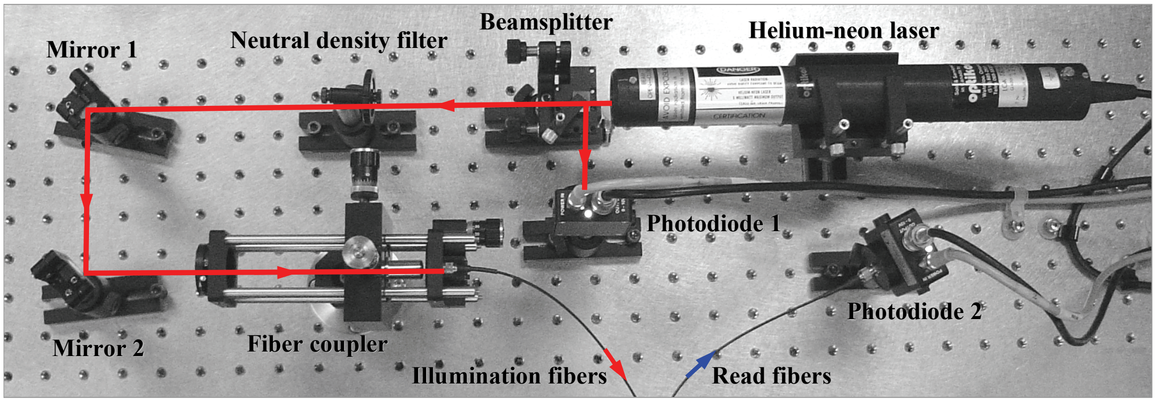

Figure 2.6. Top-view photograph of the optical components mounted on a breadboard.

Figure 2.7 shows the principal features of the homemade bifurcated optical fiber probe, which consists of nineteen 200-micrometer fused silica fibers. The fibers transmit light in the wavelength range of 200 nm to 800 nm and are multimode, step-indexed and buffered with polyimide for high-temperature operation. They are bifurcated into two bundles: the twelve fibers at the periphery are the illumination fibers for delivering the excitation light from the light source via the fiber coupler to the sample, while the remaining seven situated at the center serve as the read fibers for sending the reflected light from the sample to photodiode 2 for measurement. At the probe tip, both the illumination and read fibers are tightly held in place within Teflon$^{®}$ tubing and glued using a high-temperature epoxy to a stainless steel sleeve of 10 cm length and 4.76 cm diameter. The other ends of the fibers, terminated with standard SMA905 connectors, were clamped inside a flexible stainless steel jacket for stress relief and protection against damage under tight bending.

To enhance light propagation, the fiber ends at both the probe tip and the connectors were polished using aluminum oxide lapping films. The probe was designed for safe operation at temperatures as high as 250 °C.

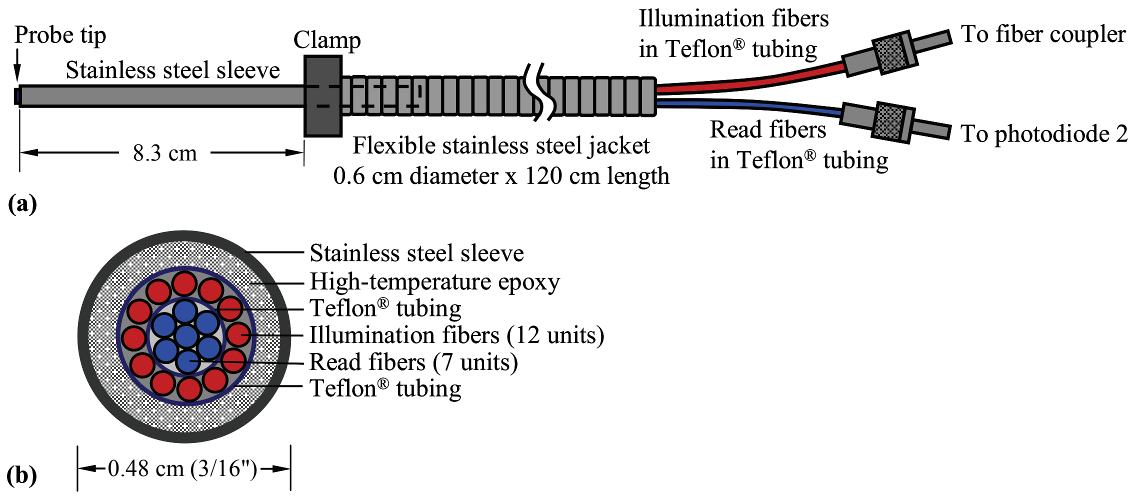

Figure 2.7. Bifurcated optical fiber probe. (a) Side-view schematic. (b) Cross-section of probe tip.

A sapphire window with a diameter of 15 mm and a thickness of 2 mm was mounted flush with the stationary plate using a high-temperature epoxy. Sapphire was used because of its broad transmission range, exceptional hardness, durability and scratch resistance, thermal conductivity comparable to stainless steel, high tolerance to thermal and mechanical shocks, and excellent chemical resistance. The window is located about 3.6 cm below the center of the SST active face (see Fig. 2.8). A 3.2 cm long stainless steel cylindrical holder mounted on the stationary plate facilitates insertion of the probe into a 0.635 cm diameter hole drilled axially parallel to the window. The probe is held in place to the holder with a clamp, and there is small gap of about 0.5 mm between the probe tip and the window.

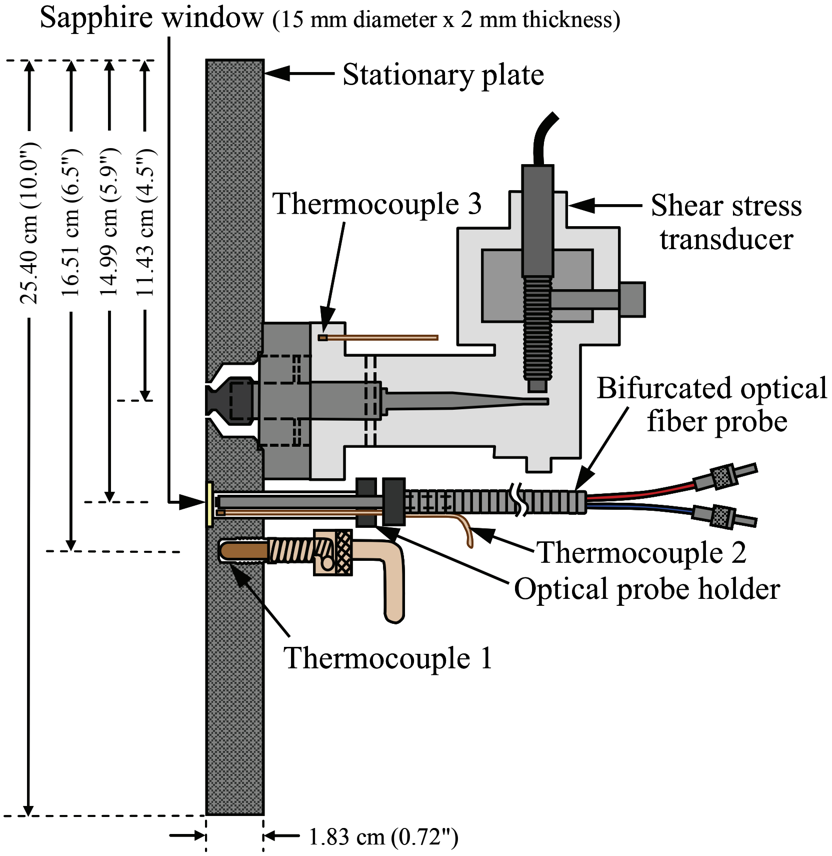

Figure 2.8. Side-view schematic showing locations of the sapphire window, shear stress transducer, and thermocouples 1, 2 and 3 on the stationary plate.

2.3.4 Temperature Measurement and Control

Primarily used in the past for polymer melt experiments at isothermal conditions, the SPR forced convection oven was equipped with a fan and two electrical finned-strip heating elements. For crystallization studies, a cooling system had to be added. A series of copper cooling coils were thus installed inside the oven, and cooling was aided by circulating a solution of ethylene glycol and water at a volume ratio of 30:70 to these coils via a pump from a reservoir maintained at a temperature of about -15 °C (Fig. 2.2). A cooling rate of about 5 °C/min is achievable with this cooling system, in comparison to only 2 °C/min obtained by just cutting the heat and opening the oven door. Because of the large thermal mass of the shear fixture, it would be difficult to further improve the cooling rate by means of convection. Although 5 °C/min is low compared to rates used in industrial processing conditions, the present cooling rate is comparable to those used in other flow devices and in commercial dilatometers [15-18].

For better monitoring of the temperature gradients and transients during cooling, two additional chromel-constantan type E thermocouples with very fine wires for fast response were installed. One is attached laterally to the optical probe tip and placed adjacent to the optical window (thermocouple 2), while the other (thermocouple 3) is inserted into an aperture in the SST housing (Figs. 2.3 and 2.8). In contrast, the previous experimental setup used only two thermocouples: one embedded in a hole drilled about half way into the stationary plate (thermocouple 1), and the other attached to the support frame for measuring the oven air temperature (thermocouple 4). The thermocouples were calibrated using a class A resistance temperature detector (RTD), and their accuracies were found to be accurate to ± 0.3 °C.

The digital temperature controller used in the past for polymer melt experiments only provided temperature readout but had no data logging capability. For crystallization experiments, however, the thermal history is needed for data analysis. It was thus necessary to upgrade the temperature data acquisition system so that real-time data could be stored and analyzed in a computer. These changes are discussed in the following section.

2.3.5 Data Acquisition and Instrument Control

The computer program for operating the SPR is WinTest®, developed by Bose Corporation – EnduraTEC Systems Group, Minnetonka, MN. Used in combination with the manufacturer's peripheral component interconnect (PCI) series controller and a 16-bit PCI data acquisition board in a desktop computer, the program allows measurements of the shear stress and displacement as well as control of the moving plate via a hydraulic servovalve. By entering the relevant experimental parameters (command position, velocity, ramp time, dwell time, waveform type, oscillation amplitude and frequency, *etc.*), a variety of shear histories (*e.g.*, start-up of steady simple shear, step strain, oscillatory shear) can be imposed on the sample in either stress-controlled or strain-controlled mode. Only strain-controlled deformations were used in this study.

As it was not feasible to incorporate the optical and temperature measurements into WinTest®, it was necessary to retrofit the data acquisition software and hardware. Figure 2.9 shows a block diagram of the principal components and signal connections of the retrofitted data acquisition and instrument control system. A graphical user interface program based on LabVIEW™ (National Instruments, Austin, TX) for acquiring, processing, displaying, and storing the input signals from various sensors was developed (see Appendix B). The program is implemented on a separate desktop computer. A 16-bit PCI data acquisition board was installed in this computer for digitizing the conditioned analog voltage signals generated by the two photodiodes and the capacitance proximity probe through a connector block housing a series of portable signal conditioning modules (low-pass filter, amplifier and attenuator).

A 24-bit USB-based temperature conditioning module is used to digitize and convert the voltage signals from the thermocouples into temperature readings in the LabVIEW™ program. In addition, instead of using the digital temperature controller, a proportional-integral-differential (PID) feedback control algorithm was integrated into the program to provide more efficient control of the oven temperature. The control algorithm was configured to use the oven air temperature measured by thermocouple 4 as the process variable for manipulating the voltage signal sent to the heating elements via a power controller.

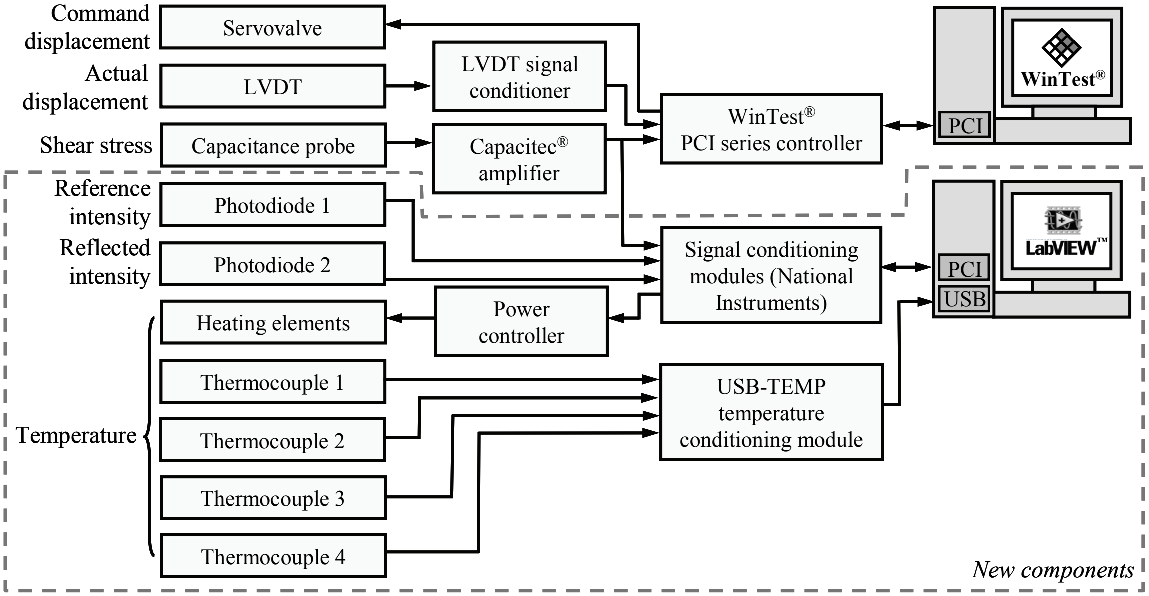

Figure 2.9. Block diagram illustrating the key components and signal connections in the retrofitted data acquisition and instrument control system.

The LabVIEW^{TM} program is run in parallel with WinTest® during experiments. In the LabVIEW^{TM} program, a sampling rate of 100 samples/s was used for the input signals from the photodiodes, while a rate of 1 sample/s was used for the temperature signals. A greater time resolution, however, was required for the shear stress and displacement measurements, as the timescales of these signals are very short for experiments at high shear rates. Moreover, in oscillatory shear, an adequate sampling rate must be used to avoid aliasing. Hence, a minimum sampling rate[*] of 2048 samples per 10 seconds was used for acquiring these signals in the WinTest® program.

---

[*] 2048 was used because conversion of data from time domain into frequency domain, by means of a fast Fourier transform algorithm, is facilitated when the sampling rate is a power of 2. To obtain a good resolution of the stress signal for very short transient stress measurement (*i.e.*, fractions of a second for tests at high shear rates), higher sampling rates (*e.g.*, 2048 samples per 3 seconds, 2048 samples/s) were also used. Not all measurements were acquired at such high sampling rates, particularly those involving an experimental time of several hours, as file storage and processing become a problem due to the large files (of gigabytes size) generated.

2.4 Sample Preparation

Rectangular samples of approximately 1.1 mm thickness, 42 mm width, and 115 mm length were prepared by compression molding 5 g of as-received polymer pellets in an aluminum mold using a temperature-controlled, manual, hydraulic press (Carver, Wabash, IN). The mold was placed between two smooth metal plates, each covered by a clean sheet of Mylar® polyester film. The films serve to prevent sample contamination when in contact with the metal plates as well as ease sample removal after molding. The polymer pellets, which had been kept in vacuum at 50 °C for a minimum of six hours to remove any trace of volatiles, were heated in the press at 185 °C for 20 min. A load of 49 kN (5 tons force) was applied for the first 5 min, and this was increased to 78 kN (8 tons force) during the remaining 15 min. The samples were then quenched to room temperature with cold water. This method was effective in producing bubble-free samples for use in the SPR.

2.5 Experimental Protocol

Shear-induced crystallization experiments were performed at isothermal conditions in the SPR by subjecting the sample to a constant shear rate $\dot{\gamma}_s$ for a brief duration t_s (short-term shearing [19], Section 1.5.2), then allowing it to rest for 30 s for stress relaxation measurement, and subsequently applying a small-amplitude oscillatory shear[*] (SAOS) over the course of the experiment for monitoring its crystallization kinetics (Fig. 2.10a). The largest $\dot{\gamma}_s$ studied was 500 s^{-1}, and the largest strain γ_s was 50.

Figure 2.10b shows the thermal history applied to the sample. The SPR oven is initially preheated to about 230 °C from room temperature for at least three hours. The oven is then opened, and the sample is quickly loaded onto the stationary plate. After sample loading, the stationary plate is fastened to the support frame, and the molten sample is reheated to 214 °C. As in typical crystallization studies of isotactic polypropylene, the

---

[*] Background information about small-amplitude oscillatory shear is given in Chapter 3.

melt is kept at a temperature above 210 °C for a minimum period of 5 min to erase its previous thermal history[*]. The melt is then cooled at a cooling rate of approximately 5 °C/min and equilibrated to the crystallization temperature of 155.5 °C ± 0.5 °C. The total cooling and equilibration time to reach a steady, isothermal condition is 60 min. As shown in Fig. 2.10a, the shearing protocol is then applied to the supercooled melt at this isothermal condition. At the same time that the shear stress $\sigma(t)$ is being measured the reflected light intensity $I(t)$ from the optical probe is recorded[†]. The experiment is ended when crystallization has progressed to a point that the sample begins to slip, as indicated by a drop in the oscillatory shear stress amplitude. The oven is then opened to cool the sample to room temperature. The solidified sample is carefully removed for analysis.

The rationales for performing the experiments at the conditions specified above are explained below. Foremost among the parameters that affect crystallization is the experimental temperature, which is often a value in between the equilibrium melting temperature and the glass transition temperature. If it is too low, crystallization might occur during cooling, before the desired isothermal condition is even reached, thereby compromising data analysis. Also, to allow an effective determination of the effect of shear on nucleation kinetics by means of the short-term shearing protocol, the temperature must be sufficiently high that the quiescent crystallization time is significantly longer than the shearing time. Moreover, given the low cooling rate attainable with the present instrument, experiments at large supercooling are impractical. On the other hand, a too high temperature adversely accelerates thermal degradation, although it allows for a long induction time for measurements. With the heat transfer limitation of the instrument taken into account, it was found that 155.5 °C would be a suitable temperature for revealing differences in the shear-induced crystallization behavior between the nucleated and non-nucleated samples.

---

[*] Despite this thermal treatment, the nucleated samples are not completely molten since the melting temperature of the nucleating agent is above 400 °C.

[†] Because of the rest time, the oscillatory shear measurement lags that of light intensity by 30 s. This small difference, however, has negligible effect on the correlation between the two data.

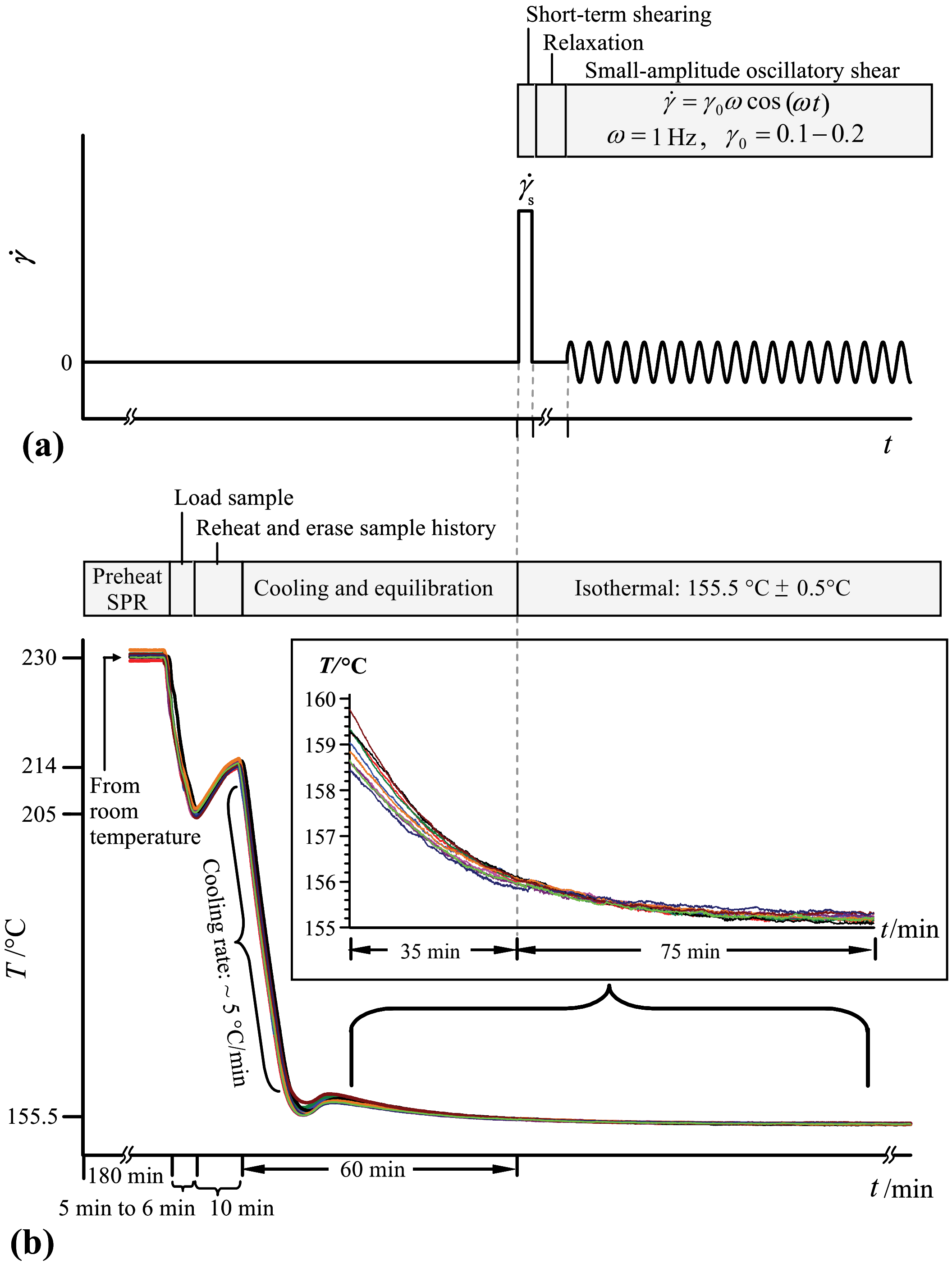

Figure 2.10. Protocol for shear-induced crystallization experiment. (a) Sample is sheared at a constant shear rate for a short period, then allowed to relax for 30 s, and is subsequently subjected to a small-amplitude oscillatory shear at 155.5 °C. (b) Thermal history applied to the sample based on temperatures recorded by thermocouple 1. The inset shows a magnification of the measurements during cooling and thermal equilibration. Data shown are for ten experiments.

The temperature of the sample was not measured directly, and that measured by thermocouple 1, which was fitted to the stationary plate, was used as the experimental temperature. As shown in Fig. 2.11, this temperature was in very good agreement with thermocouple 2, and was slightly lower than thermocouple 3, which is situated close to edge of the transducer flange at a temperature closer to that of the oven air. Considering the instrument size, this small temperature difference is deemed acceptable. The inset in Fig. 2.11 indicates that a period of 60 min was required for the sample to cool and equilibrate to 155.5 °C. It is important to note that despite this rather long equilibration time, crystallization was not detected by light intensity during this period. More importantly, the data in Fig. 2.11 confirm a good repeatability (less than ± 0.15 °C at 155.5 °C) of the thermal history under well-controlled conditions and indicate negligible undershoots during the cooling process. A temperature undershoot is particularly undesirable since it could trigger an early onset of crystallization.

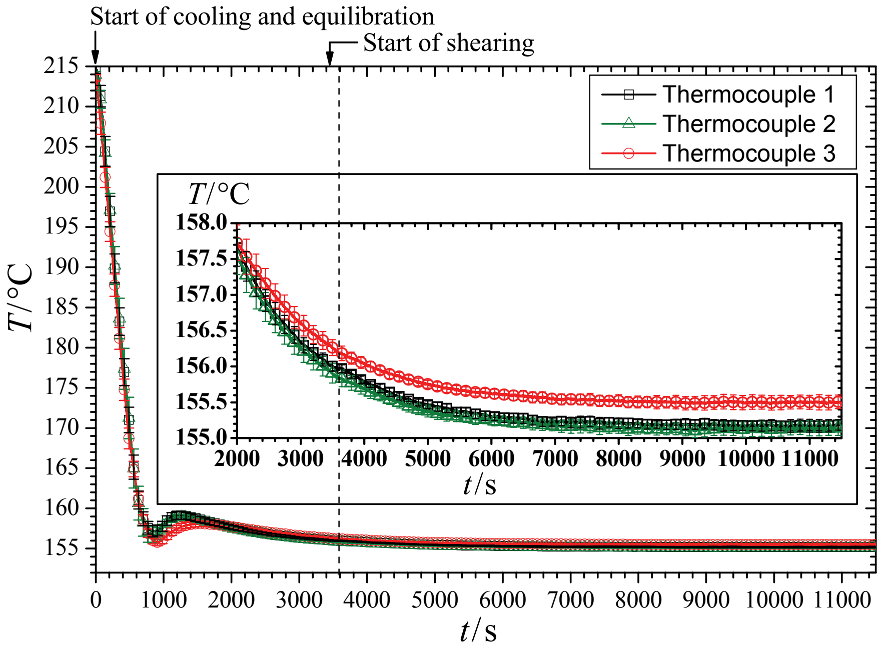

Figure 2.11. Temperatures measured by thermocouples 1 (embedded in a hole drilled into the stationary plate), 2 (attached to the optical probe tip), and 3 (inserted into the shear stress transducer housing) during cooling and thermal equilibration. The inset shows a magnification of the measurements after *t* = 2000 s. Shearing starts at *t* = 3600 s when the temperatures reach 155.5 °C ± 0.5 °C (based on thermocouples 1 and 2). Data are averages and standard deviations for ten runs.

The purpose of subjecting the sample to SAOS is to probe its crystallization kinetics. It is thus important to use the appropriate oscillation frequency ω and strain amplitude γ_0 so that they do not alter the kinetics. A sample exhibits a relatively more elastic behavior at high frequencies than at low frequencies, so measurements at high frequencies would be less sensitive to changes in the sample crystallinity than those at low frequencies[*]. Conversely, too low a frequency is not effective as a probe due to the long time required to complete one oscillation cycle. A frequency of 1 Hz was found to offer a good balance of effectiveness and sensitivity.

The strain amplitude γ_0 should be kept as small as possible. A small strain is also desirable for keeping the stress response within the range of linear viscoelasticity[†]. However, the strain must be large enough to yield a stress signal with an acceptable signal-to-noise ratio. Moreover, because the SPR was originally devised for use at high shear rates, shear strains as small as those available in commercial rotational rheometers are not possible. From the strain sweep test results at ω = 1 Hz (Appendix C.1), a proper value of γ_0 for samples iPP1, iPP2 and iPP3 was found to be 20 %, and that for iPP4 was 10 %. To verify that the parameters ω and γ_0 had been appropriately selected, a comparison of the light intensity measurements from three crystallization experiments was made. In the first experiment, no SAOS was applied. A continuous SAOS was imposed in the second experiment. In a third experiment, brief periods (20 cycles) of SAOS were introduced intermittently at equally spaced time intervals of 20 min. As corroborated by the results presented in Fig. 2.12, which shows time evolution of the

---

[*] Further evidence is provided by the results of a gel time study (see Fig. 4 in [20]), which showed that changes in the dynamic moduli with time due to crystallization can be several orders of magnitude larger at low frequency than those at high frequency.

[†] While linear viscoelasticity is ensured for the supercooled melt at the beginning, it may not be maintained over the course of the test. This happens as the sample crystallinity and its stress increase significantly during the late stages of crystallization. A way to overcome this problem is to constantly reduce the magnitude of γ_0 during the test to achieve a linear stress response. This can be done easily in commercial rheometers equipped with the auto-strain feature, but WinTest® does not have this feature, and thus a constant γ_0 was used over the entire test duration.

light intensity $I(t)$ normalized to its initial value $I(0)$ at the start of the experiment, an oscillatory shear applied either continuously or intermittently under the prescribed conditions had a minimal effect on the early crystallization kinetics.

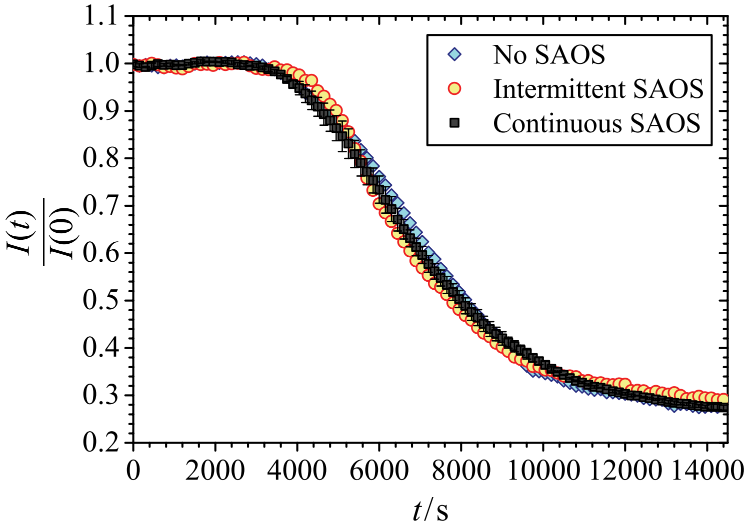

Figure 2.12. Comparison of normalized light intensity measurements for three types of experiments, namely no SAOS, intermittent SAOS, and continuous SAOS, to verify that the chosen oscillatory shear conditions have a minimal influence on the early crystallization kinetics of iPP1 at 155.5 °C. Data for continuous SAOS are averages and ranges for three runs.

If $\dot{\gamma}_s$ is sufficiently large, the test sequences of a short-term shearing and a rest time essentially become a step-strain experiment, from which the nonlinear shear stress relaxation modulus $G(t,\gamma)$ can be determined. A rest time of 30 s is adequate for measuring this material function, because the decaying stress signal has already fallen below the resolution limit of the transducer within this period. This, however, does not mean that the sheared sample will have fully relaxed within 30 s. In addition, the shear stress growth coefficient $\eta^+(t,\dot{\gamma})$ is another nonlinear material function that can be obtained. Thus, the shearing protocol adopted here provides not only a probe for tracking shear-induced crystallization, but also two nonlinear viscoelastic properties that are useful for understanding the polymer rheological behavior (see Chapter 3).

2.6 Summary

A technique for tracking crystallization kinetics by simultaneous measurement of light intensity and rheology was developed for use in a sliding plate rheometer at high shear rates. An optical system incorporating a bifurcated optical fiber probe was devised and implemented. In addition, a temperature measurement and control system as well as a new data acquisition system were designed and assembled. Finally, an optimal test protocol was established following a judicious selection of experimental conditions within the limitations of the instrument.

2.7 References

1. Dealy, J.M. and Giacomin, A.J. "Sliding plate and sliding cylinder rheometers", in *Rheological Measurement*, A. A. Collyer, D. W. Clegg, Eds., (Chapman & Hall, London, 1998), 237-259.
2. Dealy, J.M. "Method and apparatus for measuring shear stress", *US Patent*, 4,464,928 (1984).
3. Giacomin, A.J. "A sliding plate melt rheometer incorporating a shear stress transducer" *Doctoral Thesis*, McGill University, Montreal (1987).
4. Giacomin, A.J., Samurkas, T., and Dealy, J.M. "A novel sliding plate rheometer for molten plastics" *Polym. Eng. Sci.* (1989) **29**, 499-504.
5. Hatzikiriakos, S.G. and Dealy, J.M. "Wall slip of molten high density polyethylene. I. Sliding plate rheometer studies" *J. Rheol.* (1991) **35**, 497-523.
6. Koran, F. "Anomalous wall slip behavior of linear low density polyethylenes" *Master's Thesis*, McGill University, Montreal (1994).
7. Park, H.E., Lim, S.T., Smillo, F., Dealy, J.M., and Robertson, C.G. "Wall slip and spurt flow of polybutadiene" *J. Rheol.* (2008) **52**, 1201-1239.
8. Xu, J., Costeux, S., Dealy, J.M., and De Decker, M.N. "Use of a sliding plate rheometer to measure the first normal stress difference at high shear rates" *Rheol. Acta* (2007) **46**, 815-824.
9. Fuller, G.G. "Optical rheometry" *Annu. Rev. Fluid Mech.* (1990) **22**, 387-417.
10. Søndergaard, K. and Lyngaae-Jørgensen, J. *Rheo-Physics of Multiphase Polymer Systems: Characterization by Rheo-Optical Techniques* (Technomic Publishing, Lancaster, Pennsylvania, 1995).
11. Dealy, J.M. and Jeyaseelan, R.S. "Frequency response of a shear stress transducer installed in a sliding plate rheometer" *J. Rheol.* (1998) **42**, 833-841.

12. Bur, A.J. and Thomas, C.L. "Method and apparatus for monitoring resin crystallization and shrinkage during polymer molding", *US Patent*, 5,519,211 (1996).
13. Thomas, C.L. and Bur, A.J. "Optical monitoring of polypropylene injection molding" *Polym. Eng. Sci.* (1999) **39**, 1291-1302.
14. Marinelli, A.L., Farah, M., and Bretas, R.E.S. "Optical monitoring of polyesters injection molding" *J. Appl. Polym. Sci.* (2006) **99**, 563-579.
15. Kimata, S., Sakurai, T., Nozue, Y., Kasahara, T., Yamaguchi, N., Karino, T., Shibayama, M., and Kornfield, J.A. "Molecular basis of the shish-kebab morphology in polymer crystallization" *Science* (2007) **316**, 1014-1017.
16. Hadinata, C., Gabriel, C., Ruellmann, M., Kao, N., and Laun, H.M. "Shear-induced crystallization of PB-1 up to processing-relevant shear rates" *Rheol. Acta* (2006) **45**, 539-546.
17. Scelsi, L. and Mackley, M.R. "Rheo-optic flow-induced crystallisation of polypropylene and polyethylene within confined entry-exit flow geometries" *Rheol. Acta* (2008) **47**, 895-908.
18. He, J. and Zoller, P. "Crystallization of polypropylene, nylon-66 and poly (ethylene terephthalate) at pressures to 200 MPa: Kinetics and characterization of products" *J. Polym. Sci., Part B: Polym. Phys.* (1994) **32**, 1049-1067.
19. Liedauer, S., Eder, G., Janeschitz-Kriegl, H., Jerschow, P., Geymayer, W., and Ingolic, E. "On the kinetics of shear-induced crystallization in polypropylene" *Int. Polym. Process.* (1993) **8**, 236-244.
20. Pogodina, N.V. and Winter, H.H. "Polypropylene crystallization as a physical gelation process" *Macromolecules* (1998) **31**, 8164-8172.

Chapter 3: Rheological Characterization

3.1 Introduction

Two types of rheological measurement are of chief interest in this study: linear viscoelastic (LVE) data that provide information about the relaxation times of the samples, and nonlinear viscoelastic (NLVE) data that describe the evolution of shear stress during start-up of steady simple shear. As will be shown in Chapters 5 and 6, these results are useful for understanding shear-induced crystallization, specifically in terms of explaining saturation in crystallization kinetics (based on observations of slip), and evaluating the parameters characterizing kinetic and morphological changes.

As its name implies, linear viscoelasticity entails a linear relationship between the stress response and the applied deformation, which is observed when the deformation rate is very low or the deformation is very small [1]. Under such conditions, the chain conformations are only negligibly perturbed from their equilibrium state. Viscoelastic properties obtained from this kind of measurement, in combination with molecular models (e.g. tube models [2-4]), have long been exploited to extract information about the relaxation dynamics of polymer melts [1, 5]. In contrast, under fast and large deformations, the response is nonlinear, due to the substantial orientation and possibly stretching of the chains in the flow direction. It is in this flow regime that the profound effect of shear on crystallization is observed.

In this work, LVE properties were measured using a rotational rheometer by small-amplitude oscillatory shear (SAOS), whereas measurements in the NLVE regime were obtained by means of a sliding plate rheometer according to the shearing protocol described in Section 2.5. The emphasis of this chapter is on determining the relaxation times from the LVE data and presenting the transient stress responses, particularly as evidence of slip, measured during start-up flow at high shear rates. In addition, some other interesting rheological observations are discussed.

3.2 Linear Viscoelasticity

3.2.1 Small-Amplitude Oscillatory Shear

Usually performed in strain-controlled mode, a SAOS test subjects a sample to a sinusoidal shear strain $\gamma(t)$ with a strain amplitude γ_0 and frequency ω:

$$\gamma(t) = \gamma_0 \sin(\omega t) \tag{3.1}$$

Accordingly, the shear rate $\dot{\gamma}(t)$ is given by:

$$\dot{\gamma}(t) = \gamma_0 \omega \cos(\omega t) = \dot{\gamma}_0 \cos(\omega t) \tag{3.2}$$

where $\dot{\gamma}_0$ is the shear rate amplitude. If γ_0 is small, the measured shear stress response $\sigma(t)$ is within the LVE regime and can be described by the sinusoidal function below:

$$\sigma(t) = \sigma_0 \sin(\omega t + \delta) \tag{3.3}$$

where σ_0 is the shear stress amplitude, and δ is the mechanical loss angle or phase shift between the stress response and the applied strain.

The following equations relate $\sigma(t)$, $\dot{\gamma}(t)$ and $\gamma(t)$ to several commonly used frequency-dependent functions [1]:

$$\sigma(t) = \dot{\gamma}_0 \left[\eta'(\omega)\cos(\omega t) + \eta''(\omega)\sin(\omega t)\right] \tag{3.5}$$

$$|G^*| \equiv \sigma_0/\gamma_0 = \sqrt{(G')^2 + (G'')^2} \tag{3.6}$$

$$|\eta^*| \equiv |G^*|/\omega = \sqrt{(\eta')^2 + (\eta'')^2} \tag{3.7}$$

$$\tan\delta = G''/G' \tag{3.8}$$

where $G'(\omega)$ is the storage modulus representing the stored elastic energy, $G''(\omega)$ is the loss modulus representing the viscous dissipated energy, $|G^*|$ is the magnitude of the complex modulus, $|\eta^*|$ is the magnitude of the complex viscosity, $\eta'(\omega)$ is the dynamic viscosity, $\eta''(\omega)$ is the out-of-phase component of the complex viscosity, and $\tan\delta$ is the loss tangent.

At low ω, $G'' \propto \omega$ and $G' \propto \omega^2$. Two important material constants can be extracted from the data in this terminal region: the zero-shear viscosity η_0 and the steady-state compliance J_s^0. The determination of these properties by means of SAOS experiments can sometimes be difficult due to the very small signal-to-noise ratio at low frequencies or the inability of the instrument to reach low enough frequencies*.

At higher ω , the non-Newtonian fluid behavior or solid-like elastic characteristic becomes more apparent. The transition from a more liquid-like to a more solid-like behavior occurs when $G' = G''$, i.e., at the crossover frequency ω_c.

For monodisperse melts, a further increase in ω leads to a plateau zone, in which G' becomes nearly independent of frequency. This region is characterized by G_N^0, but a flat plateau is not observed for polydisperse melts. Several methods for estimating G_N^0 have been suggested [6], and the value estimated by Eckstein et al. [7], based on integration of the loss modulus data extrapolated to high frequencies, was assumed for all the samples used in this study. The justification for this assumption is given later.

3.2.2 Time-Temperature Superposition

It is a common practice to perform SAOS measurements over a range of frequencies at several temperatures, and to shift the data so that they superpose onto a single master curve at a selected reference temperature T_0 by means of time-temperature superposition [1, 5]. The data at various temperatures can be horizontally shifted along the logarithmic frequency axis and vertically shifted along the logarithmic stress-related axis. It works on the basis that varying the temperature affects all of the relaxation times by a constant shift factor a_T and all of the stress-related quantities by another constant factor b_T. The

---

* These material constants can also be determined by creep and creep recovery experiments, which, however, are more difficult to perform.

resulting master curve is thus a plot of the reduced modulus $b_{\mathrm{T}}G'$ or $b_{\mathrm{T}}G''$ versus the reduced frequency ωa_{T}.

The vertical shift factor is a function of the melt density ρ [1, 5]:

$$b_{\mathrm{T}} = \frac{T_0 \rho_0}{T \rho} \tag{3.9}$$

where the subscript 0 refers to the reference temperature. Taking into consideration the sample densities and the narrow range of the temperatures studied here, the influence of b_{T} is weak, and it is reasonable to assume $b_{\mathrm{T}} = 1$, *i.e.*, no vertical shift.

Horizontal shift can be done either manually by judging the goodness of the superposed data by the human eye or more systematically using an optimization algorithm. The latter method, in which the sum of square differences between the dynamic moduli at T and those at T_0 is minimized, was used here to determine a_{T}. For $T_{\mathrm{g}} < T < T_{\mathrm{g}} + 100\,\mathrm{K}$, the dependence of a_{T} on temperature is usually described by the Arrhenius equation [1, 8]:

$$\ln a_{\mathrm{T}} = \frac{E_{\mathrm{a}}}{R}\left(\frac{1}{T} - \frac{1}{T_0}\right) \tag{3.10}$$

where T_{g} is the glass transition temperature, E_{a} is the activation energy for flow, and R is the universal gas constant.

3.2.3 Characteristic Relaxation Times

Listed below are equations for calculating several characteristic relaxation times:

$$\tau_{\mathrm{n}} = \eta_0 / G_{\mathrm{N}}^0 \tag{3.11}$$

$$\tau_{\mathrm{w}} = \eta_0 J_{\mathrm{s}}^0 \tag{3.12}$$

$$\tau_{\mathrm{c}} = \omega_{\mathrm{c}}^{-1} \tag{3.13}$$

$$\tau_{\mathrm{d}} = \frac{12}{\pi^2}\frac{\eta_0}{G_{\mathrm{N}}^0} \tag{3.14}$$

where τ_{n} is the number-average terminal relaxation time [9, 10], τ_{w} is the weight-average terminal relaxation time [9, 10], τ_{c} is the inverse of the frequency at which the storage and loss moduli cross, and τ_{d} is the reptation time [5]. The ratio of $\tau_{\mathrm{w}}/\tau_{\mathrm{n}}$ is a measure of the breadth of the terminal relaxation time distribution.

The reptation time is derived from the tube model formulated by Doi and Edwards [2] based on Edwards's mean-field idea of a "tube" [11] and de Gennes' concept of "reptation" [12, 13]. In brief, reptation is the primary means by which an entangled chain (modeled as a freely-jointed chain [14]) relaxes through snake-like sliding diffusion along an effective tube formed by the surrounding chains. The other relaxation time reported to be useful in shear-induced crystallization studies is the stretch relaxation time τ_{s} [15], but there is no clear definition for this time for a polydisperse melt.

3.2.4 Relaxation Spectrum

LVE data are often represented by a discrete or continuous relaxation spectrum [1]:

$$\text{Discrete:} \quad G(t) = \sum_{i=1}^{N} G_i\, e^{-t/\tau_i} \tag{3.15}$$

$$\text{Continuous:} \quad G(t) = \int_{-\infty}^{\infty} H(\tau)\, e^{-t/\tau}\, \mathrm{d}\ln\tau \tag{3.16}$$

where G_i is a relaxation strength, τ_i is the corresponding relaxation time constant, and $H(\tau)\,\mathrm{d}\ln\tau$ is the contribution to the modulus in the time interval between $\ln\tau$ and $\ln\tau + \mathrm{d}\ln\tau$.

Defined as the ratio of shear stress to strain in stress relaxation, the relaxation modulus $G(t)$ can be obtained from a step-strain experiment, although it is rarely measured. This material function is usually determined by calculating the relaxation spectrum from the dynamic moduli using the following equations:

$$G'(\omega)=\sum_{i=1}^{N}\frac{G_i\,\omega^2\tau_i^{\ 2}}{1+\omega^2\tau_i^{\ 2}}=\int_{-\infty}^{\infty}\frac{H(\tau)\,\omega^2\tau^2}{1+\omega^2\tau^2}\,\mathrm{d}\ln\tau \tag{3.17a}$$

$$G''(\omega)=\sum_{i=1}^{N}\frac{G_i\,\omega\tau_i}{1+\omega^2\tau_i^{\ 2}}=\int_{-\infty}^{\infty}\frac{H(\tau)\,\omega\tau}{1+\omega^2\tau^2}\,\mathrm{d}\ln\tau \tag{3.17b}$$

Conversion of $G'(\omega)$ and $G''(\omega)$ to a relaxation spectrum is an ill-posed mathematical problem due to the unavailability of data at all frequencies from $-\infty$ to ∞. Several numerical techniques have been used to address this problem, *e.g.*, linear regression [16], nonlinear regression [17], and nonlinear regularization [18]. In this study, a computer program (NLREG version 2929, Freiburg Materials Research Center, Germany) based on a nonlinear regularization algorithm by Honerkamp and Weese [18] was used to calculate the continuous spectrum with 200 elements and the discrete spectrum with eight elements.

From the relaxation spectrum, η_0, J_s^0, and the linear shear stress growth coefficient $\eta^+(t)$ can be calculated using Eqs. 3.18-3.20. The latter quantity and $G(t)$ are used as bases for comparing nonlinear data from step-strain and start-up tests.

$$\eta_0=\sum_{i=1}^{N}G_i\tau_i=\int_{-\infty}^{\infty}\tau\,H(\tau)\,\mathrm{d}\ln\tau \tag{3.18}$$

$$J_s^0=\left(\sum_{i=1}^{N}G_i\tau_i^2\right)\Bigg/\left(\sum_{i=1}^{N}G_i\tau_i\right)^2=\left(\int_{-\infty}^{\infty}\tau^2H(\tau)\,\mathrm{d}\ln\tau\right)\Bigg/\left(\int_{-\infty}^{\infty}\tau\,H(\tau)\,\mathrm{d}\ln\tau\right)^2 \tag{3.19}$$

$$\eta^+(t)=\sum_{i}^{N}G_i\tau_i(1-e^{-t/\tau_i})=\int_{0}^{t}\tau\,H(\tau)\,\mathrm{d}\ln\tau \tag{3.20}$$

3.3 Nonlinear Viscoelasticity

3.3.1 Start-up of Steady Simple Shear

The measured stress $\sigma^+(t,\dot{\gamma})$ during start-up flow at a steady shear rate $\dot{\gamma}$ is usually reported in term of the nonlinear shear stress growth coefficient $\eta^+(t,\dot{\gamma})$:

$$\eta^{+}(t,\dot{\gamma}) = \frac{\sigma^{+}(t,\dot{\gamma})}{\dot{\gamma}} \tag{3.21}$$

3.3.2 Cessation of Steady Simple Shear

If $\dot{\gamma}$ is large, the measured stress decay $\sigma^{-}(t,\dot{\gamma})$ following cessation of shearing gives the nonlinear relaxation modulus $G(t,\gamma)$:

$$G(t,\gamma) = \frac{\sigma(t,\gamma)}{\gamma} \tag{3.22}$$

where $\gamma = t\dot{\gamma}$, $\sigma(t,\gamma) = \sigma^{-}(t,\dot{\gamma})$.

Time-strain separability [5] is often used to analyze $G(t,\gamma)$:

$$G(t,\gamma) = G(t)\,h(\gamma) \tag{3.23}$$

where $G(t)$ is given by Eq. 3.16, and $h(\gamma)$ is called the damping function, which can be categorized into several types [19] and represented by various equations [20].

3.4 Experimental Details[*]

A strain-controlled rotational rheometer ARES (Advanced Rheometric Expansion System, made by Rheometric Scientific, now made by TA Instruments), equipped with a spring torque transducer (2K Bendix) with a range of 1.96 x 10^{-4} N m to 0.196 N m (2 g_f cm to 2000 g_f cm), was used for the SAOS experiments. Parallel disk fixtures with a diameter of 25 mm were used with a nominal gap of 1 mm. Prior to performing the measurements, the transducer was calibrated according to the manufacturer's instructions by suspending weights on a calibration fixture mounted on the transducer.

Cylindrical samples of 1 mm in thickness and 25 mm in diameter were prepared by the same compression molding method described in Section 2.4. The only difference is that a stainless steel mold plate with circular holes was used in place of a rectangular mold.

---

[*] Information about the experimental materials and NLVE measurements can be found in Chapter 2.

The test fixtures were preheated in the ARES oven with a gap of approximately 1 mm at the test temperature for at least 2 h to ensure uniform temperature in the fixtures. The gap was then zeroed by lowering the upper fixture to touch the bottom fixture. The temperature was then increased and maintained at 200 °C for 15 min. The upper fixture was then raised about 15 mm to allow for sample loading onto the lower fixture. The sample was allowed to stabilize at 200 °C for about 5 min before the upper fixture was lowered to squeeze the sample to a nominal thickness of 1.015 mm. The oven was opened, and the sample was trimmed flush with the edges of the fixtures. The temperature[*] was set to the desired test temperature, and the sample was allowed to stabilize for about five minutes before the gap was reduced to its final value of 1 mm. The small initial excess of 0.015 mm was to ensure that the sample would bulge slightly around its edge. The test was started when the sample was relaxed, as indicated by a normal force reading below 1 N.

Frequency sweep measurements were carried out in the range of 0.01 rad/s to 500 rad/s with strain amplitudes that were within the LVE regime. These amplitudes were determined by means of strain sweeps over the full range of frequencies used (see Appendix D). Thermal stability of the samples over the test duration was verified from repeat measurements in reverse test sequences in frequency sweeps. Measurements were performed with a fresh sample each time for a total of three runs at several temperatures[†] between 155.5 °C and 200 °C. A nitrogen environment was used during the test to minimize thermo-oxidative degradation. Typical variation between runs, evaluated based on the range of the data, was found to be less than ± 2.5 %.

---

[*] Gap setting was performed at the desired test temperature, whereas a higher temperature of 200 °C was used only for sample loading. Particularly for low test temperatures, this loading procedure ensures complete melting of the sample before the desired temperature is set.

[†] Crystallization can affect rheological measurements involving extended test times at low temperatures, especially at 155.5 °C, but repeat tests in reverse frequency sweeps verified that the data collected over the chosen test durations were not influenced by crystallization.

3.5 Results and Discussion

3.5.1 Applicability of Time-Temperature Superposition

Figures 3.1a and b show master curves of G', G'' and $|\eta^*|$ on double logarithmic plots for iPP1 and iPP2. The good superposition of the data confirms the applicability of time-temperature superposition for these linear polymers. The values of the activation energy for flow, as obtained from the horizontal shift factor data fitted to the Arrhenius equation in Fig. 3.2, are (40.1 ± 0.4) kJ/mol and (43.4 ± 0.2) kJ/mol for iPP1 and iPP2, respectively. These are within the range of literature values between 36.8 kJ/mol and 44.0 kJ/mol [7, 21-24]. Because of the small magnitudes of the activation energy and the narrow range of measurement temperatures, time-temperature superposition was not able to extend the experimental frequency fully into the terminal zone.

3.5.2 Plot of Loss Angle versus Magnitude of Complex Modulus

Figure 3.3 is a semi-log plot of δ versus $|G^*|$, often called a van Gurp-Palmen plot [25]. For a thermorheologically simple polymer, data obtained at several temperatures should superpose on such a plot if a vertical shift is unnecessary. Reasonably good superposition is observed not only over the range of temperatures studied but also for the four samples with differences in the degree of tacticity, molecular weight, and polydispersities. Based on a similar plot using $|G^*|/G_N^0$ for various types of polymer, Trinkle and Friedrich [26] concluded that the curve shape is very sensitive to polydispersity while it is largely independent of the chemical nature, tacticity, and composition of copolymers, as normalization using G_N^0 seems to cancel out these differences. This is somewhat different from the results shown in Fig. 3.3, where a variation in the polydispersity index by more than a factor of 1.5 seems to have little influence on the shape of the superposed data.

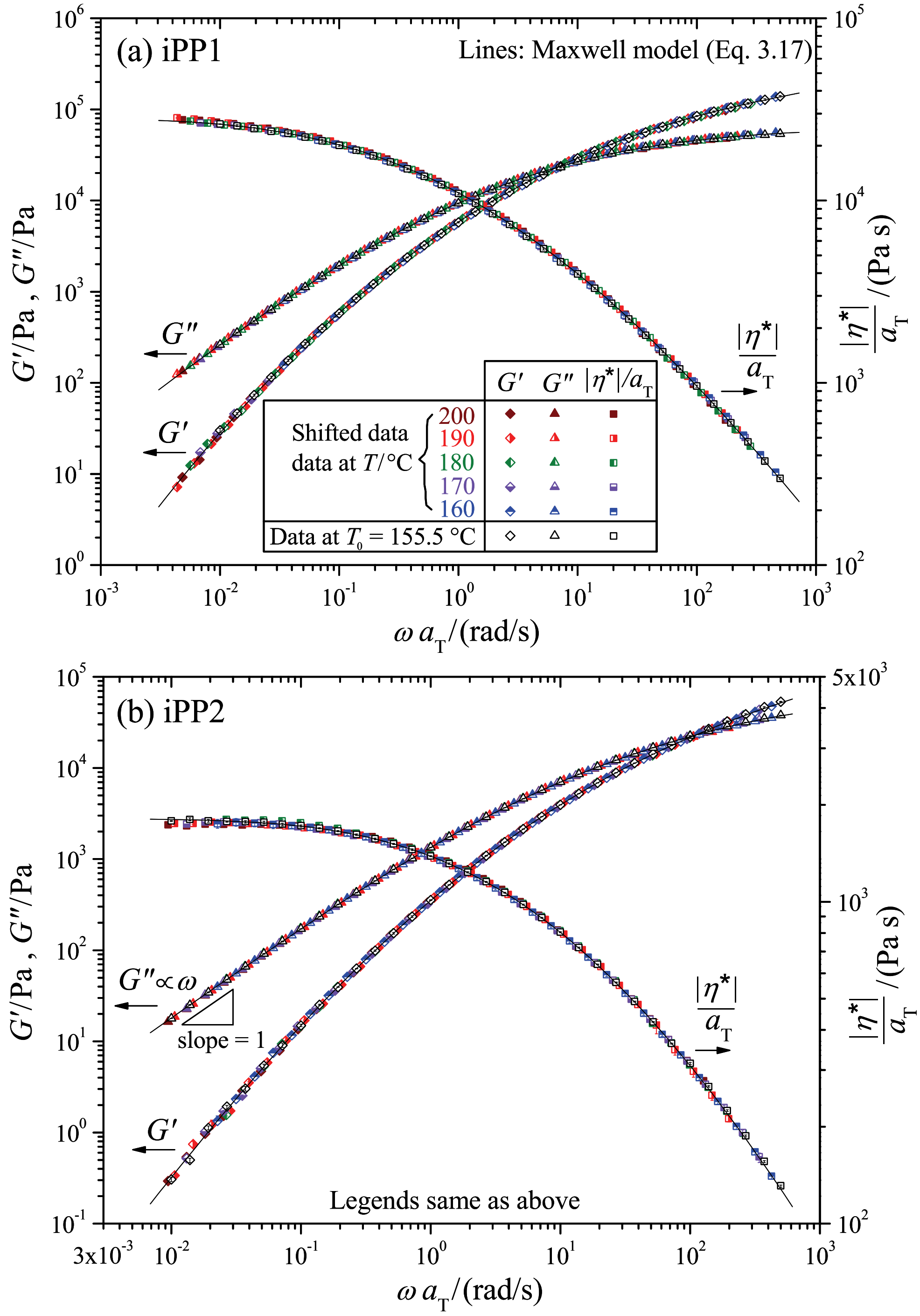

Figure 3.1. Master curves of the magnitude of the complex viscosity, storage and loss moduli at 155.5 °C for (a) iPP1, and (b) iPP2. The terminal zones extend to frequencies much lower than those investigated here. Predictions based on a Maxwell model with continuous relaxation spectrum are indicated. Data shown are averages and ranges for three runs.

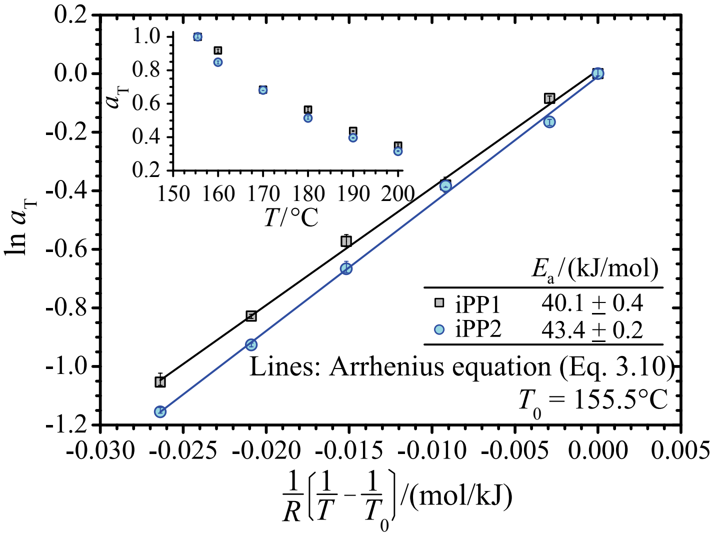

Figure 3.2. Temperature dependence of the horizontal shift factors for iPP1 and iPP2. Flow activation energy was determined by fitting using the Arrhenius equation. The inset shows the data on a linear scale. Data shown are averages and ranges for three runs.

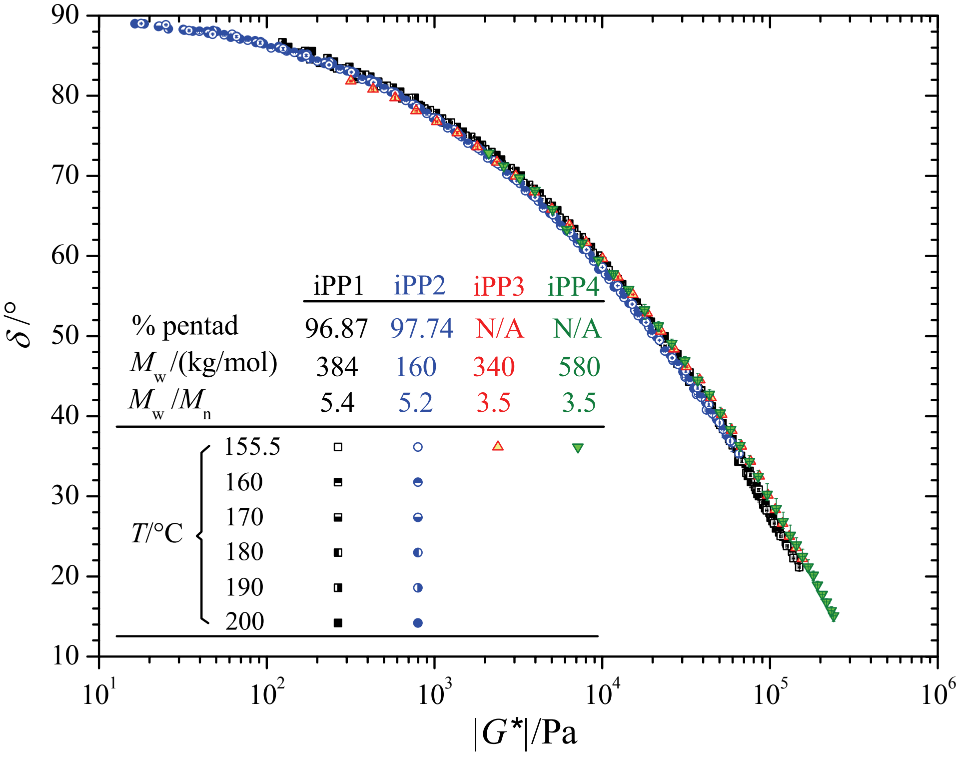

Figure 3.3. Loss angle versus the magnitude of the complex modulus for the four samples studied at various temperatures. Differences in the degree of tacticity, molecular weight and polydispersity do not affect superposition of the data. Data shown are averages and ranges for three runs.

This leads to an interesting question: Do the superposed data actually represent a unique, characteristic curve for all linear isotactic polypropylenes? To answer this, a comparison is made with some literature data. As seen in Fig. 3.4, about half of the data sets [23, 27-29] are found to overlap each other, whereas deviations are also evident for the other half [7, 23, 24, 27]. Neither M_w nor $M_\mathrm{w}/M_\mathrm{n}$ appears to contribute to the deviations. Information about the degree of tacticity, however, was unavailable for most samples, including iPP3 and iPP4. Interestingly, except for those from one study [24], all the data seem to come together at small values of δ, where $|G^*|$ is expected to approach G_N^0. This implies that the values of G_N^0 are probably the same for the samples considered here. To sum up, although a general conclusion cannot be made with regard to the uniqueness of the plot of δ versus $|G^*|$ for isotactic polypropylene, the four samples used in this study are thought to be stereoregularly similar, since G_N^0 is dependent on tacticity [7].

3.5.3 Comparison of Linear Viscoelastic Properties

Figure 3.5 compares the LVE properties of the four samples. Relationships between these properties and molecular weight typically reported for linear polymers are observed here. As shown by $|\eta^*|$ and G' (Figs. 3.5a and b), the flow resistance and elasticity increase with M_w, despite the fact that there are small differences in $M_\mathrm{w}/M_\mathrm{n}$. As expected, differences between the samples increase as we approach the terminal zone. As seen from the plot of δ in Fig. 3.5c, the crossover frequency increases as M_w decreases. In other words, for a given range of frequencies, the low-molecular weight sample iPP2 behaves more liquid-like over most frequencies when compared to the other three high-molecular weight samples. The terminal zone was not quite reached at the lowest frequency. However, reasonably good estimates of η_0 and J_s^0 could be made using Eqs. 3.19 and 3.20, and small extrapolations to the terminal zone using the Maxwell model are shown in Fig. 3.1 for iPP1 and iPP2. Table 3.1 lists their values and the relaxation times.

	This study				He [27]			Eckstein *et al.* [7]	Auhl *et al.* [28]	Laun [24]		Hingmann & Marczinke [29]	Wasserman & Graessley [23]	
Symbol	⬒	⬓	◧	◨	◉	◓	◐	▽	★	⬠	⬟	△	◆	◇
% triad	98.5	98.6	N/A	N/A	N/A	N/A	N/A	98.7	N/A	N/A	N/A	N/A	N/A	N/A
M_w/(kg/mol)	384	160	340	580	210	179	375	871	669	256	211	910	360	410
M_w/M_n	5.4	5.2	3.5	3.5	5.9	3.6	7.3	2.4	4.2	5.4	4.5	4.2	4.7-5.6	5.7-7.9
T/°C	155.5	210	155.5	155.5	180	180	180	190	180	190	190	175	190	190
Superposed?	Yes	Yes	Yes	Yes	Yes	No	No	No	Yes	No	No	Yes	Yes	No

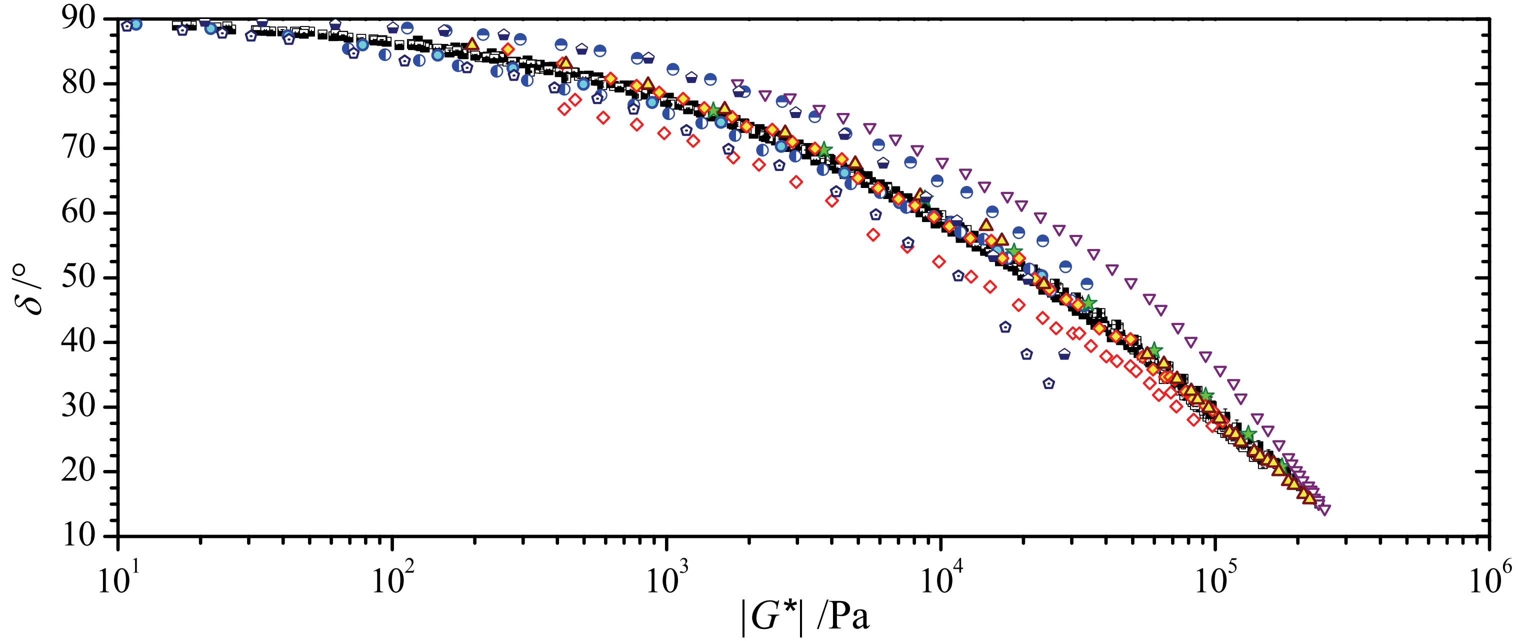

Figure 3.5. Comparison of the data from various studies of linear isotactic polypropylenes on a plot of loss angle versus the magnitude of the complex modulus. While some data [23, 27-29] appear to overlap with those in this study, several deviations are also found [7, 23, 24, 27]. Except for one study [24], all data seem to come together at low values of δ as $|G^*|$ approaches G_N^0. This suggests that these polymers have the same value of G_N^0 and likely to be structurally similar in terms of tacticity.

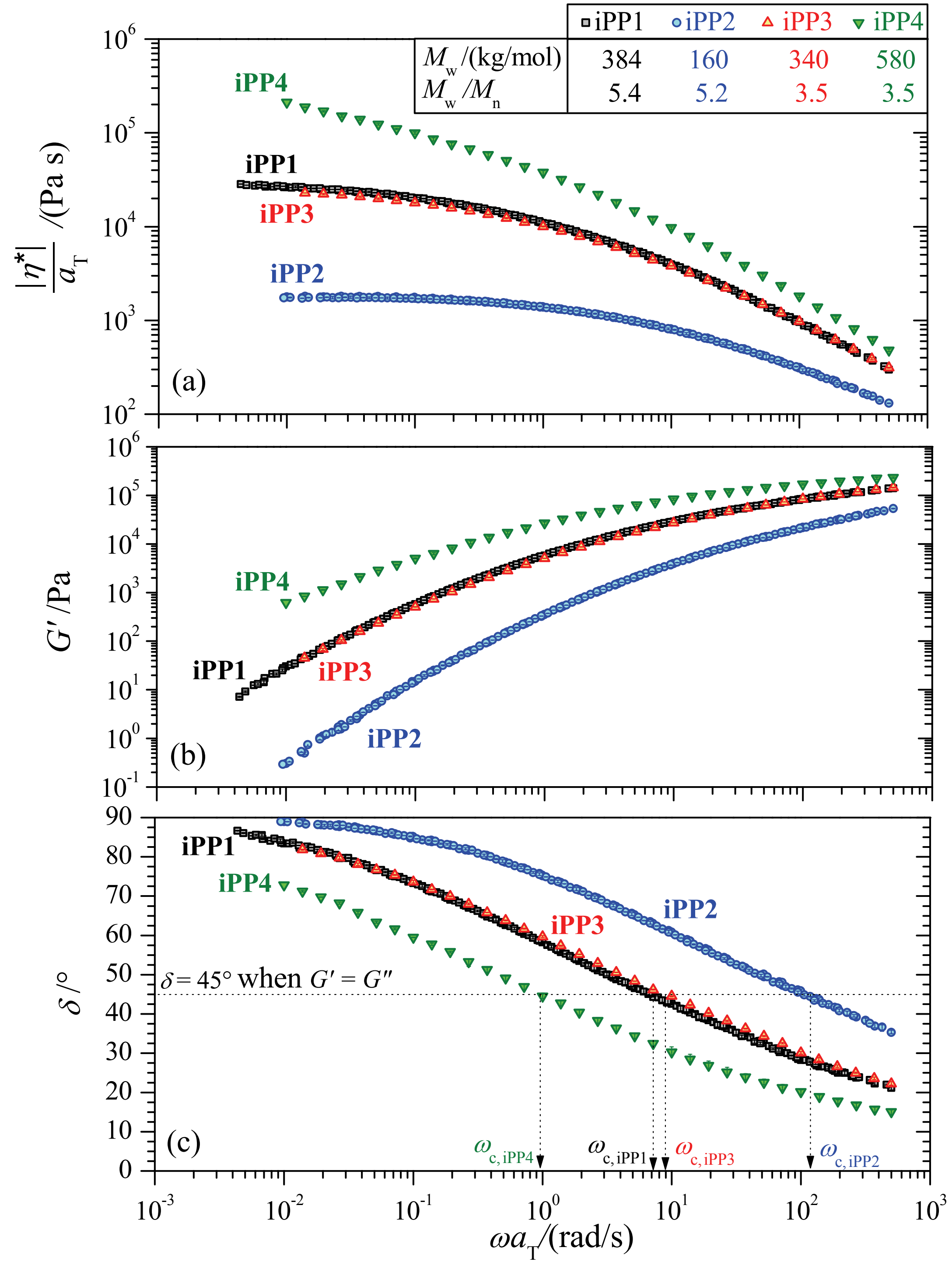

Figure 3.5. Comparison of the linear viscoelastic properties at 155.5 °C: (a) magnitude of the complex viscosity, (b) storage modulus, (c) loss angle and crossover frequency. Data for iPP1 and iPP2 include those shifted from other temperatures. Data are averages and ranges for three runs.

Table 3.1. Viscoelastic properties and characteristic relaxation times at 155.5 °C.

	iPP1	**iPP2**	**iPP3**	**iPP4**
η_0 /Pa s (Eq. 3.18)	28 060	1810	26 340	282 800
J_s^0 /Pa^{-1} (Eq. 3.19)	0.856 x 10^{-3}	1.440 x 10^{-3}	1.706 x 10^{-3}	0.609 x 10^{-3}
τ_n /s (Eq. 3.11)	0.0657	0.00424	0.0617	0.662
τ_w /s (Eq. 3.12)	24.0	2.61	44.9	172.2
τ_c /s (Eq. 3.13)	0.141	0.00971	0.116	1.11
τ_d /s (Eq. 3.14)	0.0799	0.00516	0.0750	0.805

3.5.4 Maxwell Relaxation Spectrum

The discrete and continuous relaxation spectra are presented in Fig. 3.6. In comparison to the continuous spectrum, the discrete spectrum with only eight relaxation modes is particularly inadequate to describe the behavior of the high-molecular weight sample iPP4. As expected, as the molecular weight increases, the spectrum shifts to longer relaxation times, as shown in both the conventional (Fig. 3.6a) and normalized time-weighted plots (Fig. 3.6b). Due to its much larger molecular weight, iPP4 has a distribution that is markedly different from the other three samples. While iPP1 and iPP3 appear to have very similar rheological behavior (Fig. 3.5), there is some difference between their relaxation spectra (Fig. 3.6b). The breadth of the normalized time-weighted spectrum is an indication of the degree of polydispersity. Both iPP1 and iPP2 have almost the same spectrum breadth; in fact, the spectrum of iPP2 can be shifted by a constant multiplication factor to superpose on that of iPP1. This observation corroborates well with the molecular weight distributions shown in Fig. 2.1.

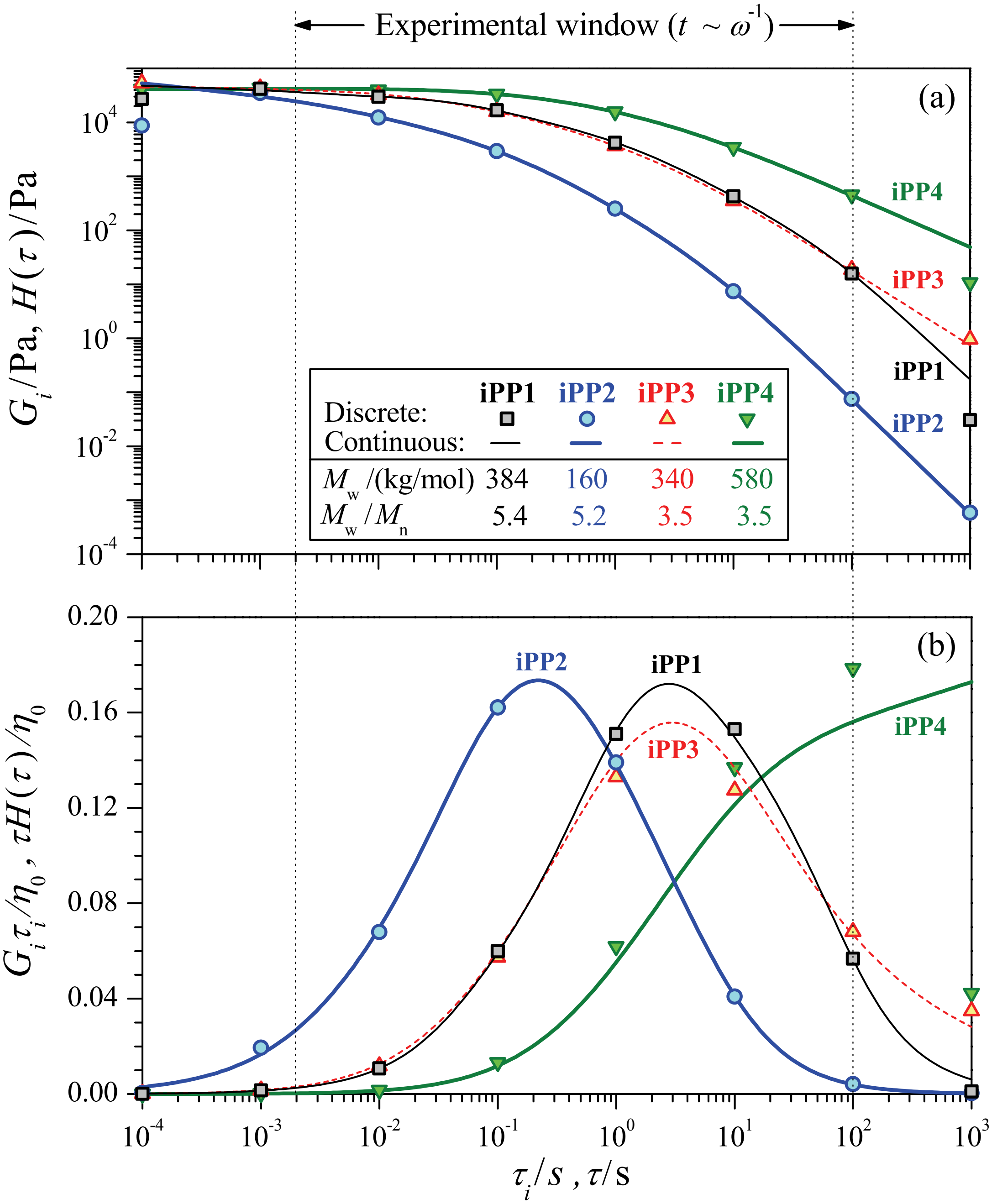

Figure 3.6. Comparison of the discrete (8 elements) and continuous relaxation spectra (200 elements) at 155.5 °C. (a) Relaxation strength versus relaxation time constant. (b) Time-weighted relaxation spectrum normalized using the zero-shear viscosity. The approximate time scale that corresponds to the experimental window is marked with dash line.

3.5.5 Characteristic Relaxation Times

The plateau modulus is needed for the calculation of characteristic relaxation times, but the samples did not exhibit well-defined plateaus in G' at high frequency (Fig. 3.5b). However, as concluded in Section 3.5.2, G_{N}^{0} for all the samples is expected to be of the same as that of the other samples presented in Fig. 3.4, and it is thought reasonable to use the value of 427 kPa reported by Eckstein et al. [7], which has been widely accepted [30].

As shown in Table 3.1, the values of τ_{w} are more than two orders of magnitude larger than those of τ_{n}, τ_{d} and τ_{c}. More simply put, $\tau_{\mathrm{w}} >> \tau_{\mathrm{c}} \sim 2\tau_{\mathrm{n}}$ and $\tau_{\mathrm{d}} = 1.21\,\tau_{\mathrm{n}}$. Regardless of which relaxation time is used, that of iPP4 is an order of magnitude larger than those of iPP1 and iPP3, whereas the latter two polymers have relaxation times that are an order of magnitude larger than that of iPP2.

3.5.6 Start-up of Steady Simple Shear

Start-up test data recorded using the sliding plate rheometer need to be corrected for the lag in the start time due to the inertia of the moving plate and the sample, and imperfections of the rheometer control system. As shown in Fig. 3.7, which compares the actual and the command strain histories for two pairs of shear rates and strains, the offset t_{off} was about 10 ms at low shear rates (10 s^{-1} in the insets of Figs. 3.7a and b) and was much shorter, about 4 ms, albeit more obvious, at high shear rates (500 s^{-1} in Figs. 3.7c and d). And for the latter, the actual shear rates were lower than the command rate of 500 s^{-1}, and this deviation is evidently larger at a lower strain (or a shorter shearing time). Because the actual shear rate was not constant but varied with time (see the insets of Figs. 3.7c and d), an average value was used to denote the shear rate for these tests.

Figure 3.8a is a plot of $\eta^{+}(t,\dot{\gamma})$, after the t_{off} correction, at shear rates of 1 s^{-1}, 10 s^{-1} and 50 s^{-1} for iPP1. The nonlinear data are expected to superpose on the linear $\eta^{+}(t)$ envelope at small strains or short times, and this is demonstrated for the sliding plate rheometer data at strains less than unity (*i.e.*, $t < 1$ s for 1 s^{-1}, and $t < 0.1$ s for 10 s^{-1}). Slight deviations due to imperfections of the instrument are found at very short times, *i.e.*, $t < 0.03$ s. The deviations were much longer in other studies ($t < 0.5$ s [16], $t < 1$ s [31]). Included in the figure for comparison are data obtained using an ARES rheometer with parallel disk fixtures[*]. Disregarding the much larger deviations from the linear response at short times ($t < 0.1$ s) for this rheometer, both the SPR and ARES data are in good agreement at a shear rate of 1 s^{-1}. Compared to the SPR data, those of the rotational rheometer are affected by edge instability[†] at high shear rates [32], as evidenced in a fall in stress at 10 s^{-1} for $t > 1$ s and a much lower steady-state value.

Particularly at high shear rates, *i.e.*, 200 s^{-1} and 500 s^{-1}, where the polymer chains can be effectively oriented, stress overshoots are observed, as shown in the linear plot of shear stress versus strain in Fig. 3.8b. The strain corresponding to the peak stress, which is not as sharp as expected, is slightly greater than two at low shear rates (≤ 10 s^{-1}) and increases at higher shear rates. These results are consistent with those reported for polymer solutions [33]. The data shown are for strains up to 20, before the occurrence of wall slip.

Figure 3.9 shows some evidence of slip during stress growth, *i.e.*, before stress relaxation that occurs following cessation of shear. As shown in Figs. 3.9b and c, an unexpected drop in stress suggestive of slip was found at nominal strains of 30 and 50 for shear rates of 200 s^{-1} and 500 s^{-1}. Especially at a strain of 50, the stress signals were irreproducible following the onset of slip. As wall slip is known to occur above a critical stress [34, 35], data shown in Fig. 3.9a for a shear rate of 50 s^{-1}, *i.e.*, a lower stress, did not show any sign of slip, and a steady-state value was reached.

---

[*] Cone-and-plate is the preferred geometry for NLVE measurements. Because of ease of sample loading, parallel disk fixtures with a diameter of 25 mm at a nominal gap of 1 mm were used.

[†] Edge fracture was also confirmed by visual observation during the experiment.

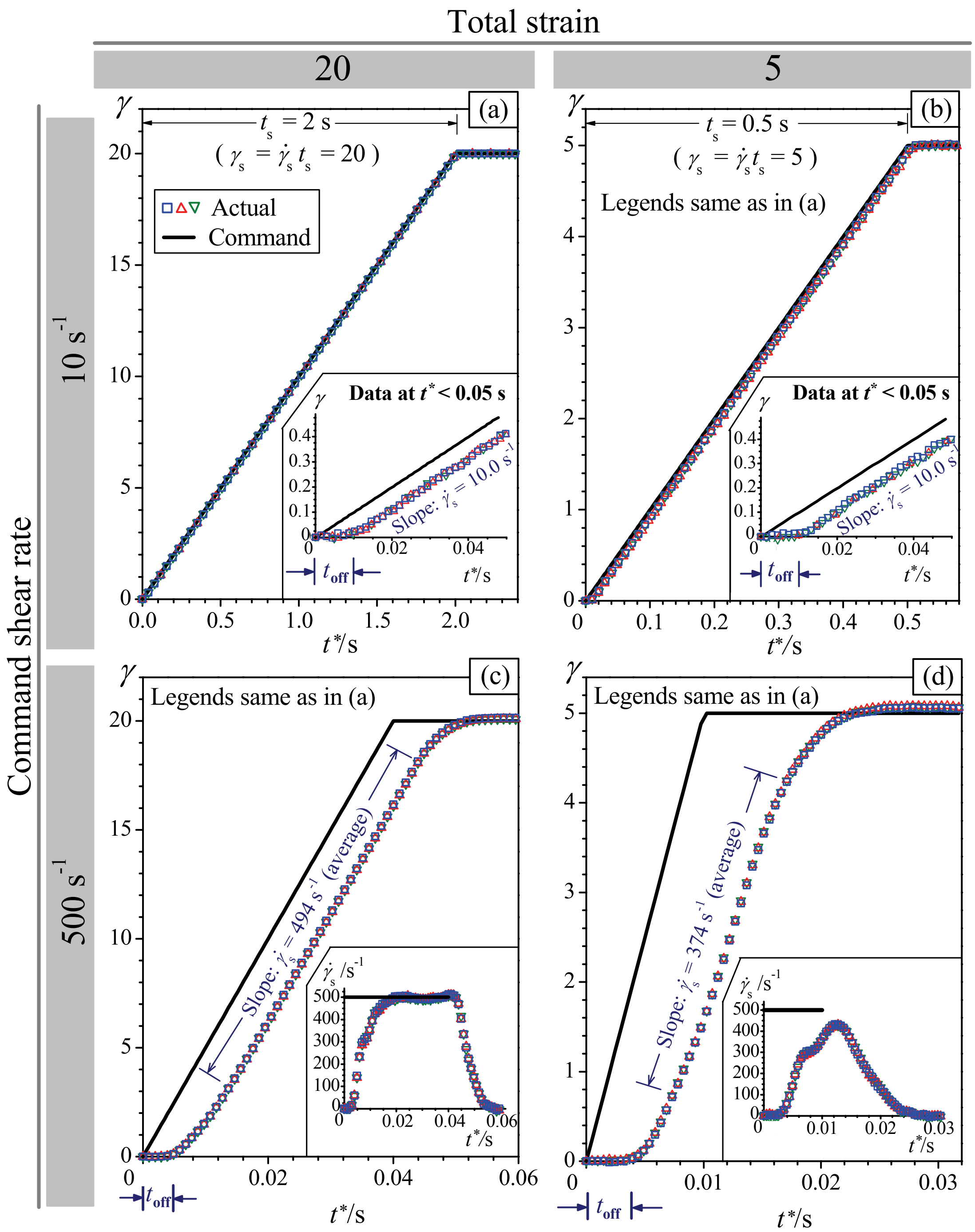

Figure 3.7. Test imperfections indicated by the actual and command strain histories in start-up of steady simple shear using the sliding plate rheometer at various command shear rates and strains: (a) 10 s^{-1}, 20; (b) 10 s^{-1}, 5; (c) 500 s^{-1}, 20; (d) 500 s^{-1}, 5. The insets in (a) and (b) show the time offset at the beginning of the test. The insets in (c) and (d) show variations in the actual shear rate with time. Data shown are for three measurements with iPP1 at 155.5 °C.

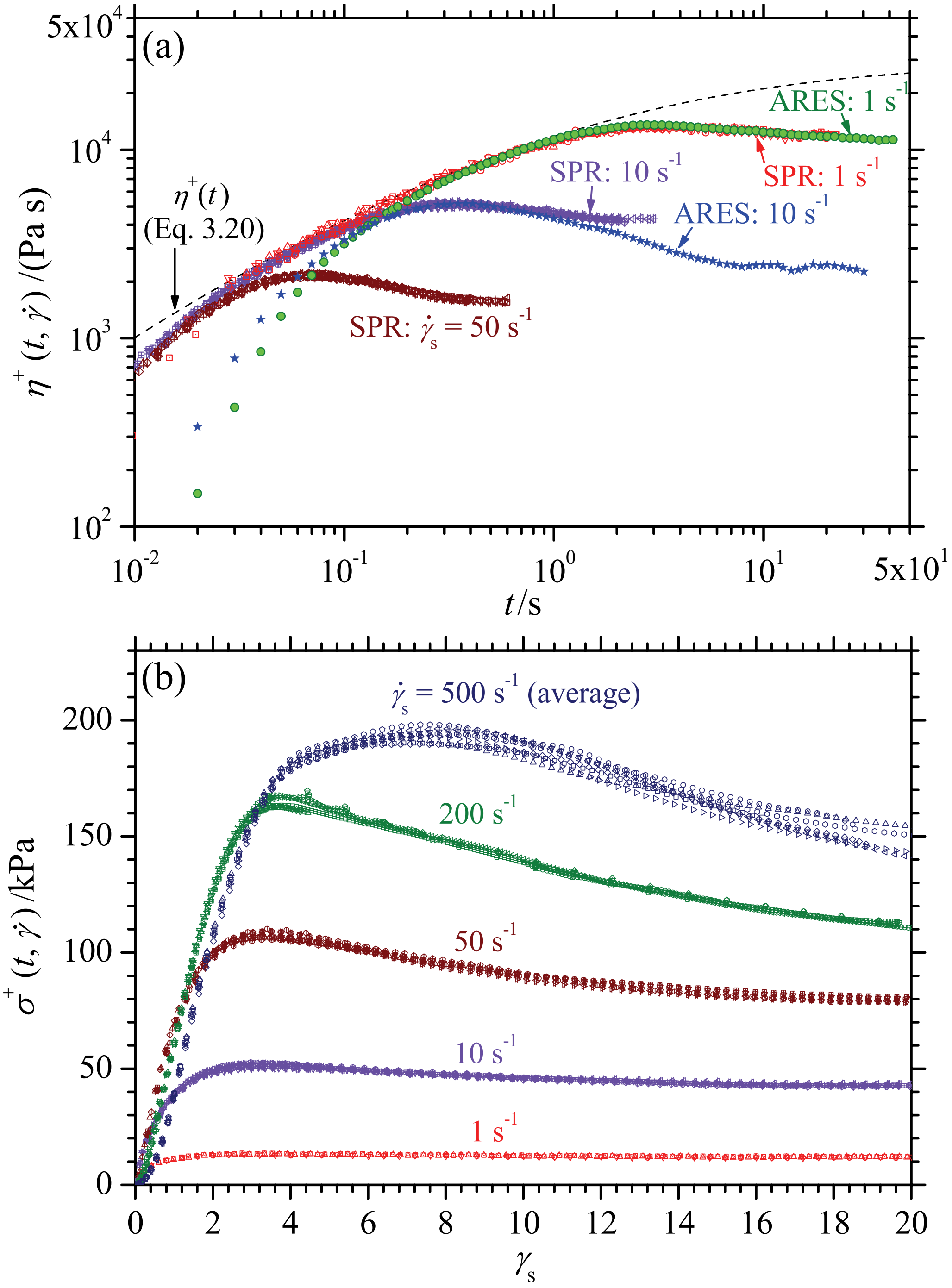

Figure 3.8. Start-up of steady shear results. (a) Comparison of nonlinear shear stress growth coefficients obtained using the SPR at various shear rates with the linear response and with those obtained using an ARES rotational rheometer. The SPR data superpose on the linear response at short times. Both the SPR and ARES yielded similar results at 1 s^{-1}, but edge instability was found for the ARES data at 10 s^{-1}. (b) SPR data for various shear rates on a plot of shear stress versus strain indicate transient overshoot. The strain corresponding to the peak stress increases with increasing shear rate. Data shown are for four to nine measurements for iPP1 at 155.5 °C.

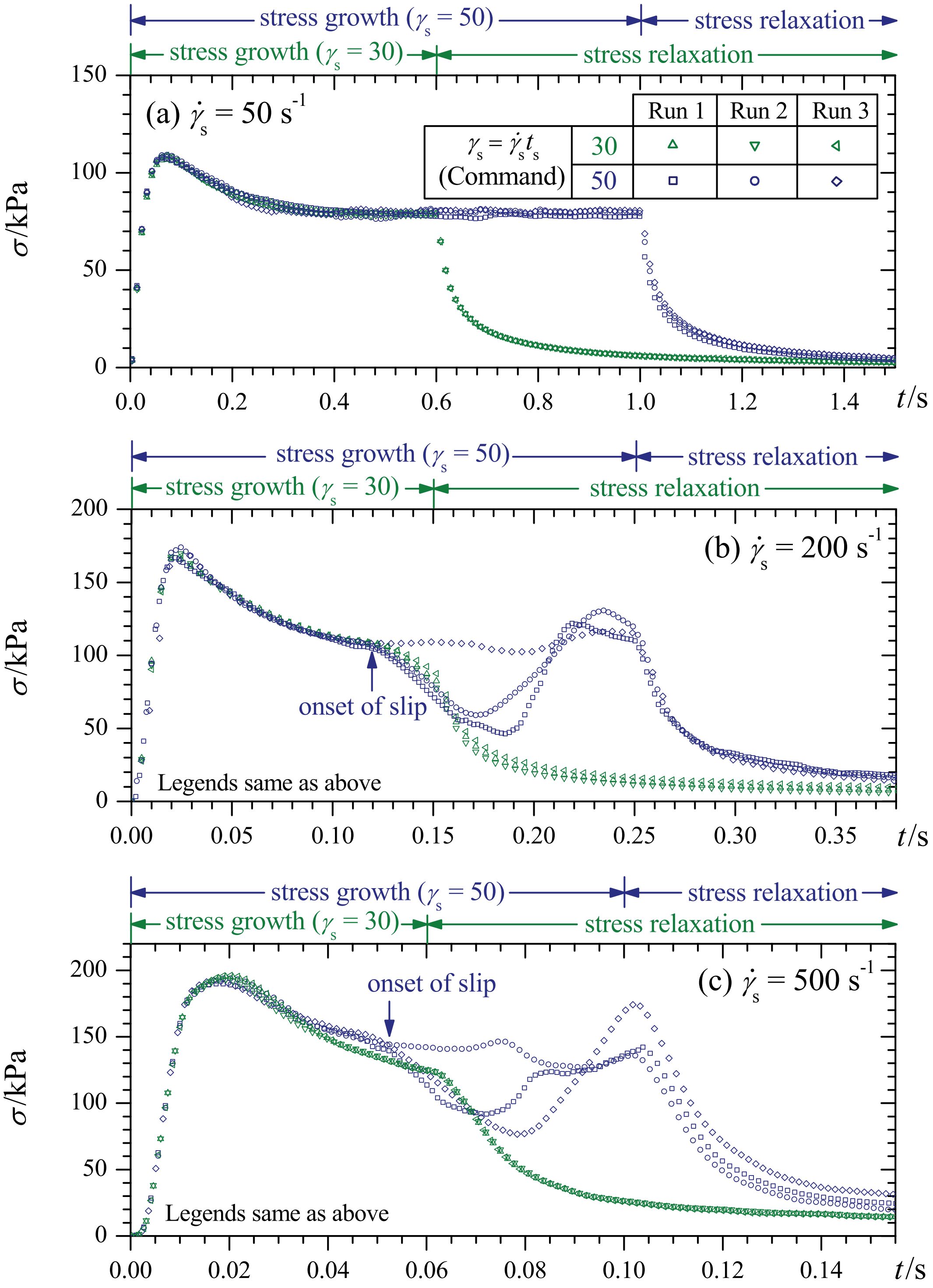

Figure 3.9. Stress growth and relaxation at strains of 30 and 50 for various shear rates. (a) At 50 s^{-1}, no slip and a steady stress were found. (b) At 200 s^{-1}, a fall in stress due to slip was observed, and the stress signals with a strain of 50 were irreproducible after the onset of slip. (c) At 500 s^{-1}, similar observations of slip were found. Data shown are for three measurements for iPP1 at 155.5 °C.

3.5.7 Nonlinear Relaxation Modulus

In the determination of $G(t,\gamma)$ using the SPR at the largest command shear rate, *i.e.*, 500 s^{-1}, to generate the desired strain, it is necessary to correct the data for both the offset time t_{off} and the rise time t_{rise}. This procedure is illustrated in Fig. 3.10, wherein the time at which stress relaxation begins is corrected for using: $t = t^* - t_{\text{off}} - t_{\text{rise}}$, where t^* is the raw time. As shown in Fig. 3.11, for strains in the range of 5 to 50, t_{rise} was found to vary from 0.0175 s to 0.102 s. Compared to the much larger value of 0.17 s recorded using a rotational rheometer for much lower strains (from 0.05 to 0.5), the rise time of the SPR is deemed acceptable.

Figure 3.12a compares $G(t,\gamma)$ data for iPP1 obtained using the SPR for various strains with the linear response $G(t)$ and the ARES data using much smaller strains. Only strains smaller than 20 were shown because higher values resulted in slip. As expected, the low strain data from ARES fall on the linear $G(t)$ envelope, and the SPR data at large strains reveal time-strain separability. Figure 3.12b compares the values of $h(t,\gamma)$ obtained based on the data shown in Fig. 3.12a with those of Stadler *et al.* (linear polypropylene, Fig. 2 in [36]) and the predictions of the Doi-Edwards model with independent alignment assumption [20]. Deviations from the model are somewhat expected [5], and the results here follow Osaki's description of type B behavior [19], i.e., data fall above the model prediction. The large difference between the present results and those of Stadler *et al.* [36] is rather surprising. It should be mentioned that most past studies [19, 20] were limited to strains much lower than 20, whereas Stadler *et al.* [36] applied a strain up to 100 for linear and branched polyolefins. Their results for three linear polypropylene samples suggested that $h(t,\gamma)$ is insensitive to molecular weight (406 kg/mol $\leq M_{\text{w}} \leq$ 669 kg/mol) and polydispersity ($2 \leq M_{\text{w}}/M_{\text{n}} \leq 6$), and so differences in these properties can be ruled out as the cause of the discrepancy. However, they used a rotational rheometer, and this is the main concern, as this instrument is less satisfactory for step-strain measurements.

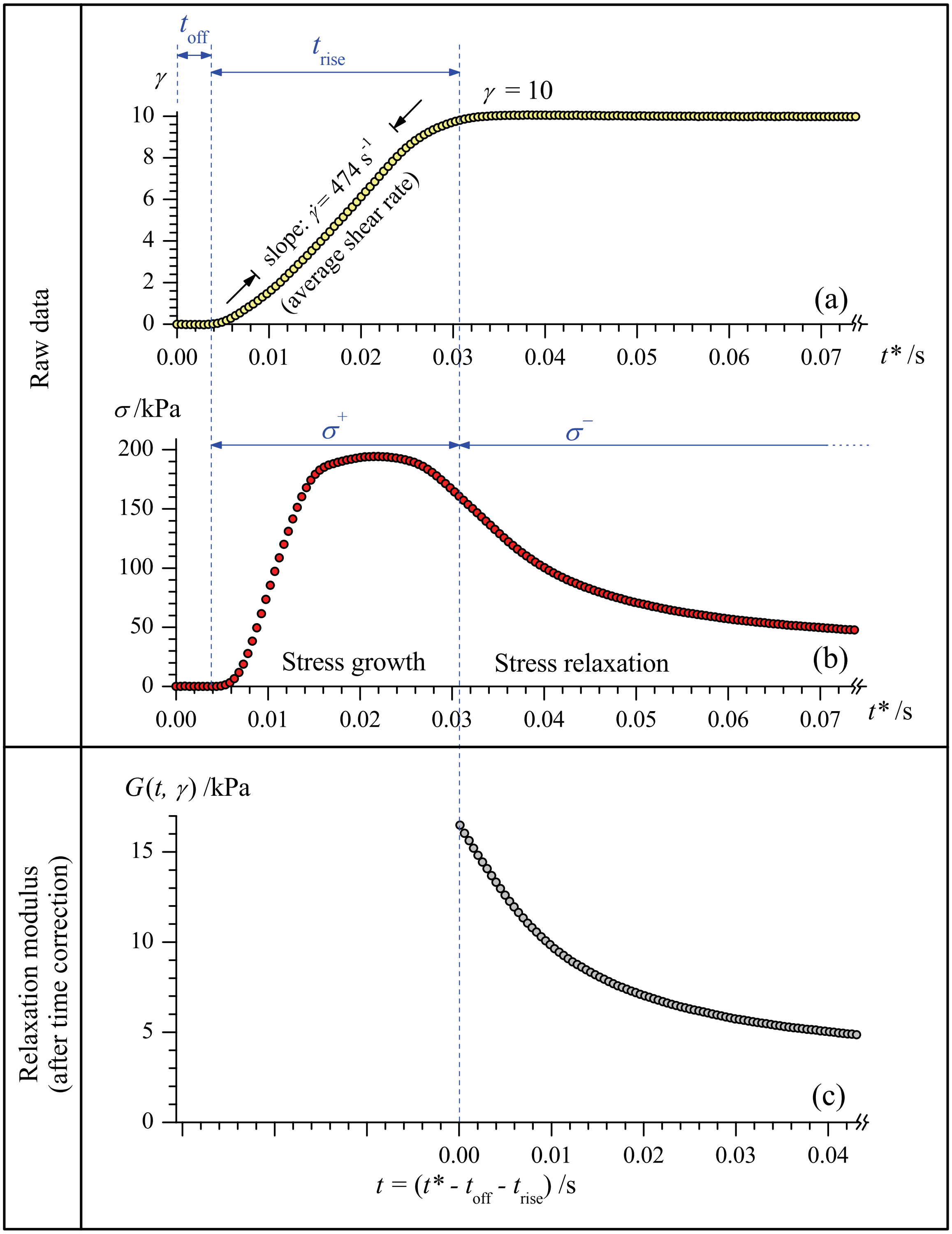

Figure 3.10. Correction for the offset and rise times in the determination of relaxation modulus based on the data obtained at an average shear rate of 474 s^{-1} (command: 500 s^{-1}) and a strain of 10 for iPP1 at 155.5 °C. (a) Raw strain data. (b) Raw stress data. (c) Relaxation modulus after time correction.

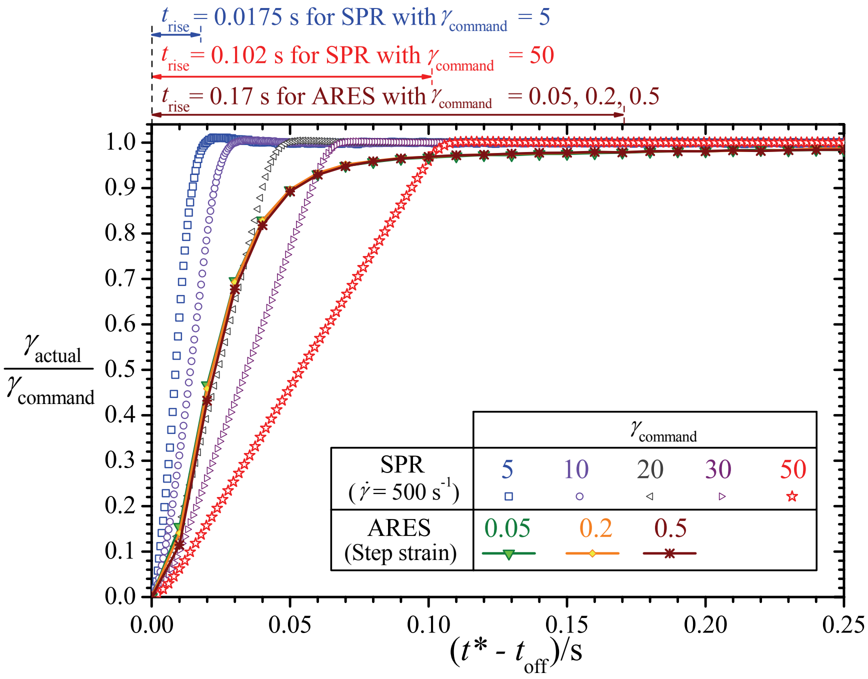

Figure 3.11. Comparison of the SPR rise times after a command shear rate of 500 s^{-1} at various strains with those for an ARES rotational rheometer after a step strain on a plot of the actual strain normalized by the command strain versus the corrected time. The rise time is defined as that at which the normalized strain is 0.98. Data shown were for iPP1 at 155.5 °C.

3.6 Conclusions

The relaxation times of supercooled melts were determined using small-amplitude oscillatory shear measurements and a Maxwell model. The terminal zone was not quite reached, but the results obtained are adequate for qualitative comparison as the relaxation times differ by two orders of magnitude between the high- and the low-molecular weight samples. Slip was observed at high shear rates (200 s^{-1} and 500 s^{-1}) and large strains (30 and 50). The data for the four samples investigated, as well as those from several other studies, were found to superpose on a plot of the loss angle versus the magnitude of the complex modulus. The damping function was found to be higher than that predicted by the Doi-Edwards model with independent alignment assumption. Compared to the sliding plate rheometer, the rotational rheometer is less satisfactory for step-strain and start-up of steady shear tests at high shear rates, because the measurements are affected by the relatively long rise time and the occurrence of edge instability.

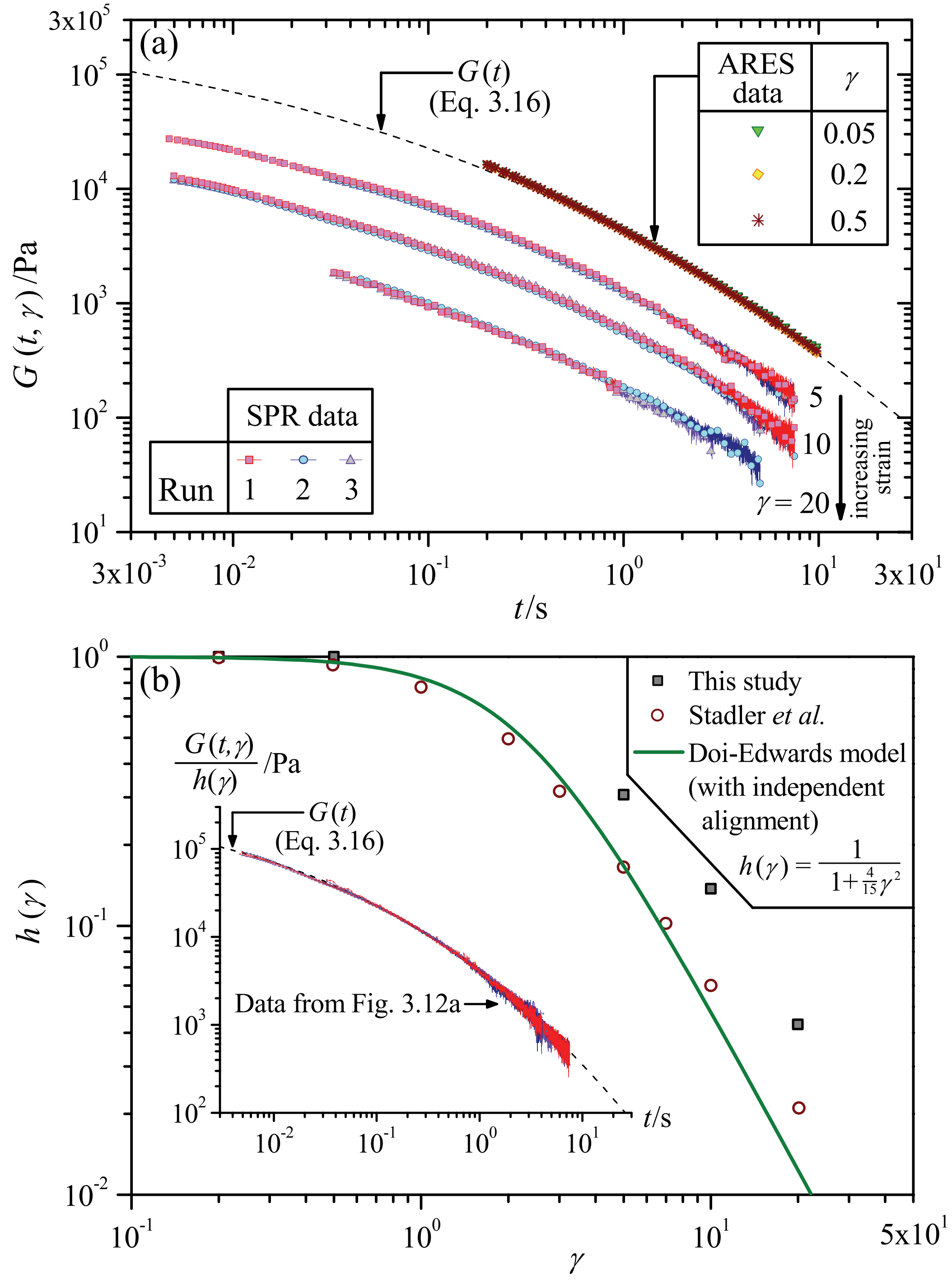

Figure 3.12. Step-strain results. (a) Comparison of the nonlinear relaxation modulus obtained using the SPR at various strains with the ARES data at low strains and the linear response. The data indicate time-strain separability. (b) Comparison of the damping function with the data of Stadler *et al.* [36] and predictions of the Doi-Edwards model with independent-alignment assumption. The inset shows the normalized nonlinear relaxation modulus. Data are averages and ranges for three measurements for iPP1 at 155.5 °C.

3.7 References

1. Ferry, J.D. *Viscoelastic Properties of Polymers*, 3rd ed. (John Wiley & Sons, New York, 1980).
2. Doi, M. and Edwards, S.F. *The Theory of Polymer Dynamics* (Clarendon, Oxford, 1986).
3. Watanabe, H. "Viscoelasticity and dynamics of entangled polymers" *Prog. Polym. Sci.* (1999) **24**, 1253-1403.
4. McLeish, T.C.B. "Tube theory of entangled polymer dynamics" *Adv. Phys.* (2002) **51**, 1379-1527.
5. Dealy, J.M. and Larson, R.G. *Structure and Rheology of Molten Polymers: From Structure to Flow Behavior and Back Again* (Hanser Publishers, Munich, 2006).
6. Liu, C., He, J., Ruymbeke, E.v., Keunings, R., and Bailly, C. "Evaluation of different methods for the determination of the plateau modulus and the entanglement molecular weight" *Polymer* (2006) **47**, 4461-4479.
7. Eckstein, A., Suhm, J., Friedrich, C., Maier, R.D., Sassmannshausen, J., Bochmann, M., and Mülhaupt, R. "Determination of plateau moduli and entanglement molecular weights of isotactic, syndiotactic, and atactic polypropylenes synthesized with metallocene catalysts" *Macromolecules* (1998) **31**, 1335-1340.
8. Dealy, J.M. and Wissbrun, K.F. *Melt Rheology and Its Role in Plastics Processing. Theory and Applications.* (Springer, Berlin, 1999).
9. Graessley, W.W. "The entanglement concept in polymer rheology" *Adv. Polym. Sci.* (1974) **16**, 1-179.
10. Graessley, W.W. *Polymeric Liquids and Networks: Dynamics and Rheology* (Garland Science, New York, 2008).
11. Edwards, S.F. "The statistical mechanics of polymerized material" *Proc. Phys. Soc.* (1967) **92**, 9-16.
12. de Gennes, P.G. *Scaling Concepts in Polymer Physics* (Cornell University Press, Ithaca, New York, 1979).
13. de Gennes, P.G. "Reptation of a polymer chain in the presence of fixed obstacles" *J. Chem. Phys.* (1971) **55**, 572-579.
14. Rouse, P.E., Jr. "A theory of the linear viscoelastic properties of dilute solutions of coiling polymers" *J. Chem. Phys.* (1953) **21**, 1329-1334.
15. van Meerveld, J., Peters, G.W.M., and Hütter, M. "Towards a rheological classification of flow induced crystallization experiments of polymer melts" *Rheol. Acta* (2004) **44**, 119-134.

16. Laun, H.M. “Description of the non-linear shear behaviour of a low density polyethylene melt by means of an experimentally determined strain dependent memory function” *Rheol. Acta* (1978) **17**, 1-15.
17. Baumgaertel, M. and Winter, H.H. “Determination of discrete relaxation and retardation time spectra from dynamic mechanical data” *Rheol. Acta* (1989) **28**, 511-519.
18. Honerkamp, J. and Weese, J. “A nonlinear regularization method for the calculation of relaxation spectra” *Rheol. Acta* (1993) **32**, 65-73.
19. Osaki, K. “On the damping function of shear relaxation modulus for entangled polymers” *Rheol. Acta* (1993) **32**, 429-437.
20. Rolón-Garrido, V.H. and Wagner, M.H. “The damping function in rheology” *Rheol. Acta* (2009) **48**, 245-284.
21. Mavridis, H. and Shroff, R.N. “Temperature dependence of polyolefin melt rheology” *Polym. Eng. Sci.* (1992) **32**, 1778-1791.
22. Eckstein, A., Friedrich, C., Lobbrecht, A., and Spitz, R. “Comparison of the viscoelastic properties of syndio- and isotactic polypropylenes” *Acta Polym.* (1997) **48**, 41-46.
23. Wasserman, S.H. and Graessley, W.W. “Prediction of linear viscoelastic response for entangled polyolefin melts from molecular weight distribution” *Polym. Eng. Sci.* (1996) **36**, 852-861.
24. Laun, H.M. “Orientation of macromolecules and elastic deformations in polymer melts. Influence of molecular structure on the reptation of molecules” *Prog. Colloid Polym. Sci.* (1987) **75**, 111-136.
25. van Gurp, M. and Palmen, J. “Time-temperature superposition for polymeric blends” *Rheology Bulletin* (1998) **67**, 5-8.
26. Trinkle, S. and Friedrich, C. “Van Gurp-Palmen-plot: a way to characterize polydispersity of linear polymers” *Rheol. Acta* (2001) **40**, 322-328.
27. He, C. “Shear flow behavior and molecular structure of high melt strength polypropylenes” *Doctoral Thesis*, McGill University, Montreal (2003).
28. Auhl, D., Stange, J., Münstedt, H., Krause, B., Voigt, D., Lederer, A., Lappan, U., and Lunkwitz, K. “Long-chain branched polypropylenes by electron beam irradiation and their rheological properties” *Macromolecules* (2004) **37**, 9465-9472.
29. Hingmann, R. and Marczinke, B.L. “Shear and elongational flow properties of polypropylene melts” *J. Rheol.* (1994) **38**, 573-587.

30. Fetters, L.J., Lohse, D.J., and Colby, R.H. “Chain dimensions and entanglement spacings”, in *Physical Properties of Polymer Handbook*, J. E. Mark, Ed., (Springer-Verlag, New York, 2006).
31. Meissner, J. “Modifications of the Weissenberg rheogoniometer for measurement of transient rheological properties of molten polyethylene under shear. Comparison with tensile data” *J. Appl. Polym. Sci.* (1972) **16**, 2877-2899.
32. Larson, R.G. “Instabilities in viscoelastic flows” *Rheol. Acta* (1992) **31**, 213-263.
33. Menezes, E.V. and Graessley, W.W. “Nonlinear rheological behavior of polymer systems for several shear-flow histories” *J. Polym. Sci., Polym. Phys. Ed.* (1982) **20**, 1817-1833.
34. Denn, M.M. “Extrusion instabilities and wall slip” *Annu. Rev. Fluid Mech.* (2001) **33**, 265-287.
35. Park, H.E., Lim, S.T., Smillo, F., Dealy, J.M., and Robertson, C.G. “Wall slip and spurt flow of polybutadiene” *J. Rheol.* (2008) **52**, 1201-1239.
36. Stadler, F.J., Auhl, D., and Münstedt, H. “Influence of the molecular structure of polyolefins on the damping function in shear” *Macromolecules* (2008) **41**, 3720-3726.

Chapter 4: Quiescent Crystallization

4.1 Introduction

Our extensive knowledge of polymer crystallization stems from the vast experimental and theoretical results on quiescent studies. And to learn more about shear-induced crystallization, it is apt to first understand how the samples used here crystallize under quiescent conditions, and then use the data as the basis for analysis and comparison. To this end, quiescent crystallization kinetics at isothermal conditions was investigated by means of the same measurement techniques used in shear-induced crystallization experiments, *i.e.*, light intensity and oscillatory shear. As noted in Chapter 2, because these two techniques were simultaneously applied in a single experiment, it allows for an unambiguous correlation between both measurements at different stages during crystallization. The four key events observed during the experiment, namely the induction time, the early stages, and the late stages of crystallization, as well as slip, will be explained in detail.

For practical applications, it is advantageous to convert the above data into a standard measure such as the volume or mass fraction of material crystallized, *i.e.*, crystallinity (although its meaning is disputable [1]). As will be discussed later, the conversion is by no means straightforward due to the influence of the crystal characteristics. Rather surprisingly, this issue is not given proper attention in the literature.

By contrast, differential scanning calorimetry (DSC) is an established technique for measuring crystallinity and crystallization kinetics. The calorimetric data also provide information about crystal size distribution, which is essential for the analysis of light intensity and rheological data. As with these two sets of data, the DSC measurements provide overall crystallization kinetics, whereas information about nucleation and growth behavior can only be deduced using appropriate assumptions.

4.2 Theoretical Considerations

For convenience, results obtained from overall crystallization kinetics studies are typically expressed in terms of the time evolution of volume crystallinity, *i.e.*, the fraction of space filled by the crystallized material. Except for dilatometry, which measures the actual volume change, all the other techniques use models to relate the measured properties to crystallinity. Generally, it is implicitly or explicitly assumed that a direct relationship exists between the two quantities, and that characteristics of the crystalline structures (*e.g.*, size, shape) are irrelevant. In reality, however, the influence of the latter aspect cannot be ignored in some cases, as is revealed later in the discussion.

Equations typically used for converting light intensity and rheological data into relative crystallinity ϕ or absolute crystallinity X are reviewed below. Note that ϕ is defined as the ratio of the volume of the material that has crystallized after an elapsed time to that at the end of the experiment, whereas X is a relative measure of the volume of the material crystallized with respect to an ideal, fully crystalline state.

4.2.1 Relating Light Intensity to Crystallinity

It was demonstrated decades ago [2, 3] that the intensity measurement of an unpolarized light beam transmitted through a crystallizing polymer is related to the development of crystalline structure. However, a quantitative relationship between this measurement and crystallinity has not been established for use in kinetic analysis. Indeed, many reports [4-7] only presented raw data and not crystallinity. The problem is that the measured intensity depends not only on the crystallized volume but also on other variables, *e.g.*, the distributions of the number, size, and shape of the crystalline structures, as well as the refractive index difference between the crystalline and amorphous components [8]. This necessitates the use of an appropriate model.

It is important that the model takes into consideration the details of the optical setup used. In this study the intensity measured by the optical fiber probe was that of the backscattered or reflected light, unlike the conventional setup in which the transmitted light intensity is recorded by a detector placed at a certain angle to or in line with the incident light. Although this kind of bifurcated probe is in widespread use in the pharmaceutical and specialty chemical industries for monitoring commercial-scale crystallization [9], the measurement is used solely as a qualitative indicator of the presence of crystals for process control. In principle, one can obtain both the crystal size* and crystallinity if the probe is appropriately calibrated and used with a spectrophotometer. However, in the present study, a monochromatic light source was used. Accordingly, the equations given below disregard the effect of crystal size and assume a monodisperse system of spherulites.

Thomas and Bur [12] formulated a simple model for an optical setup similar to the one used here. Their model assumes that the attenuation in the light intensity is a result of scattering by both spherulites and microcrystals within the spherulites. Scattering by the spherulites is represented by an attenuation coefficient α_s based on the scattering theory of Stein et al. [13, 14], whereas that by the microcrystals is accounted for by another attenuation coefficient β_s using the Lambert-Beer law [8]. Because their experiment involved non-isothermal crystallization in an injection molding machine, crystallinity was a function of both time and the position of the crystallizing front. For the case of isothermal crystallization, the model is as follows:

$$\frac{I(t)}{I(0)} = \exp\{-2D[\alpha_s + \beta_s]\} = \exp\{-2D[A(\varphi - \varphi^2) + CX]\} \tag{4.1}$$

where $I(t)/I(0)$ is the light intensity at time t normalized to that at the start of the experiment, D is the sample thickness, φ is the volume fraction of spherulites, A is an amplitude factor, and C is a fitting parameter. The minimum and the final values of $I(t)$

---

* Debye and Bueche [10] developed an equation that relates light intensity to the size of the scattering objects. Their equation was used in other studies [3, 11], which found that the scattering crystalline structures are a few nanometers in dimensions and smaller than spherulites.

can be used to estimate A and C. Due to the quadratic function $\alpha_s = A(\varphi - \varphi^2)$ in Eq. 4.1, a non-monotonic $I(t)$ with a minimum is expected. This minimum has indeed long been experimentally observed [2, 3], and is associated with the maximum in scattering when the volume fraction of the spherulites is approximately one half. A major assumption must be made to relate φ to X. The authors assumed $X = 0.5\varphi$ at all times, which is somewhat unrealistic, as this limits the maximum value of X to 0.5 (since $0 \le \varphi \le 1$). Following this assumption, X can be determined by the following equation:

$$X = \frac{1}{8A}\left\{(2A+C) \pm \sqrt{(2A+C)^2 + \frac{8A}{D}\ln\frac{I(t)}{I(0)}}\right\} \tag{4.2}$$

A more straightforward set of equations is that of Ding and Spruiell [15] for their improvised depolarized light intensity or microscopy technique*. Although they used a polarized light, which differs from the unpolarized laser used in this study, what they recorded as the transmitted intensity $I_O(t)$ without an analyzer (or overall light intenisty) is qualitatively comparable to the quantity $I(t)$ measured here. Their equations are as follows:

$$\phi(t) = \frac{R(t) - R(0)}{R(\infty) - R(0)} \tag{4.3}$$

$$R(t) = \frac{I_D(t) - I_c}{I_O(t)} \tag{4.4}$$

where I_c is a calibration constant, $R(0)$, $R(\infty)$, and $R(t)$ are the relative light intensities at the start of the experiment, at the end of the experiment, and at intermediate times, respectively. The above equations, however, also require the depolarized intensity with a crossed polarizer $I_D(t)$, which was not measured in the present work.

---

* The original setup for the depolarized light intensity technique [16, 17] measures only $I_D(t)$, which, with some assumptions, is positively correlated with crystallinity: $I_D(t) \propto \phi(t)$. By contrast, the unpolarized light intensity measurement in this study decreases at the onset of crystallization.

Lamberti *et al.* [18] used Ding and Spruiell's technique and developed a model that follows that of Thomas and Bur [12]. With some modifications, they assumed that the overall light intensity $I_{\mathrm{O}}(t)$, which is denoted as $I(t)$ here, is affected by three phenomena: scattering by the spherulites (*i.e.*, α_{s} in Eq. 4.1, without β_{s}), absorption by the crystalline structures, and absorption by the amorphous melt. The model is given by the following equations:

$$\ln I(t) = -LA_0(\phi - \phi^2) + \phi \ln I(\infty) + (1-\phi)\ln I(0) \tag{4.5}$$

$$\phi(t) = \frac{1}{2LA_0}\left\{LA_0 + \ln\frac{I(0)}{I(\infty)} \pm \sqrt{\ln\frac{I(\infty)}{I(0)} + LA_0\{LA_0 - 2[\ln I(0) + \ln I(\infty)] + 4\ln I(t)\}}\right\} \tag{4.6}$$

$$\phi_{\min} = \left[\ln\frac{I(\infty)}{I(0)}\right]^{-1}\left[\ln\frac{I_{\min}}{I(0)} + \sqrt{\ln\frac{I(\infty)}{I_{\min}}\ln\frac{I(0)}{I_{\min}}}\right] \tag{4.7}$$

$$A_0 = \frac{1}{L(2\phi_{\min} - 1)}\ln\frac{I(0)}{I(\infty)} \tag{4.8}$$

where $I(0)$, $I(\infty)$, $I(t)$ and $I_{\min}$ are the light intensities at the start, at the end, at intermediate times, and its minimum value, respectively, L is the light path length, A_0 is the scattering coefficient, and $\phi_{\min}$ is the relative crystallinity at the minimum intensity. In fact, Eq. 4.5 is similar to Eq. 4.1. A main flaw in the above derivation is the inclusion of absorption, which is negligible for most experimental conditions.

The term turbidity Λ, which represents the loss in energy due to scattering by the crystalline structures at all angles [3], is sometimes used. For a non-absorbing sample, turbidity is defined as follows [8]:

$$\Lambda = -\frac{1}{L}\ln\frac{I(t)}{I(0)} \tag{4.9}$$

Instead of relating Λ to crystallinity, Strobl recently highlighted in a review article [19] the possibility of using this quantity, also termed the linear attenuation coefficient, to study the early stage of crystallization. According to Strobl *et al.* [20-22], Λ is more sensitive than many conventional measurements (DSC, dilatometry and X-ray), and its time dependence can be described by a power law $\Lambda \sim t^{\nu}$, in which ν provides information about the growth process of the evolving spherulites. The typical value of ν is 4, but there are still many questions concerning the interpretation of this parameter, which depends on temperature and varies from 2 to 8 [20, 21].

4.2.2 Relating Rheological Data to Crystallinity

Similar to light intensity, a universal relationship between crystallinity and rheological measurements is not possible, due to the strong dependence of the latter on the crystal characteristics. Nonetheless, some equations have been widely used for converting the storage modulus G' or the magnitude of the complex viscosity $|\eta^*|$ to relative crystallinity. Equation 4.10, which assumes a linear scale for the normalization of the storage modulus, has been the most popular choice [23-28]:

$$\phi_{G',\mathrm{lin}}(t) = \frac{G'(t) - G'(0)}{G'(\infty) - G'(0)} \tag{4.10}$$

where $G'(0)$, $G'(\infty)$ and $G'(t)$ are the values of storage modulus measured at a prescribed frequency at the start of the experiment, at the end of crystallization, and at intermediate times, respectively.

Logarithmic scaling was proposed by Pogodina *et al.* [29] to analyze the gel behavior of crystallizing polymers. More recently, Peters *et al.* [30, 31] used this idea to define the following relative crystallinity:

$$\phi_{G',\log}(t) = \frac{\log G'(t) - \log G'(0)}{\log G'(\infty) - \log G'(0)} \tag{4.11}$$

Boutahar *et al.* [32] studied two crystallizing polyolefins having similar spherulitic morphologies but very different crystal sizes. They found that the nucleated polyethylene behaved rheologically like a colloid with aggregates of very fine crystals, whereas the non-nucleated polypropylene resembled a suspension of large crystals. They also reported that the former exhibited yield from the very early stages of crystallization, while the latter only demonstrated yield above a relative crystallinity of 0.4. The following empirical relations were found to work reasonably well for the two systems they studied:

$$\text{Suspension-like:} \quad \phi_{G',\mathrm{SL}}(t) \approx 1 - \frac{G'(0)}{G'(t)}, \qquad \text{for } \phi_{G',\mathrm{SL}}(t) \le 0.4 \tag{4.12}$$

$$\text{Colloid-like:} \quad \phi_{G',\mathrm{CL}}(t) = \left[\frac{G'(t) - G'(0)}{G'(\infty)}\right]^{1/3} \tag{4.13}$$

Many empirical relations or suspension models have also been used to relate $|\eta^*|$ to crystallinity (see recent reviews [33-35]).

4.2.3 Avrami Analysis

Despite its crude assumptions [36, 37], the Avrami equation [38-40], also sometimes called the Kolmogorov-Johnson-Mehl-Avrami equation, is the most widely used model for describing overall crystallization kinetics resulting from both nucleation and growth. It is commonly written in the following form:

$$\phi(t) = 1 - \exp(-kt^n) \tag{4.14}$$

where either $\phi(t)$ or $X(t)$ is used to denote the volume fraction of the material crystallized at time t, k is a temperature-dependent rate constant, n is the Avrami exponent, which depends on the mode of primary nucleation (homogeneous or heterogeneous) and the crystal growth geometry (one-, two-, or three-dimensional). Note that the value of n does not represent a unique set of nucleation mode and growth geometry [36, 37].

4.3 Experimental Details

Details about the materials and the experimental methodology for oscillatory shear and light intensity measurements can be found in Chapter 2. A truly quiescent crystallization experiment is not possible using the simultaneous measurement setup, as a small deformation is needed to probe the rheological properties. However, it was demonstrated in Section 2.5 (Fig. 2.12) that the small-amplitude oscillatory shear used here has little effect on the early crystallization kinetics. Thus, data obtained using oscillatory shear, hereafter referred to as quasi-quiescent, can be regarded as representative of behavior under quiescent conditions. The procedure used for converting the oscillatory waveform signals from time domain to frequency-domain properties is described in Appendix C.2.

4.3.1 Differential Scanning Calorimetry

A power compensation differential scanning calorimeter (DSC Pyris 1, PerkinElmer, Waltham, MA) equipped with an intracooler was used for thermal analysis. A sample was prepared by encapsulating either a whole, as-received pellet or a small piece cut from the pellet in a standard aluminum pan with a perforated lid (with pinholes) using a crimper press. A fresh sample with a mass between 4 mg and 6 mg, weighed to an accuracy of 0.1 μg by an ultra-microbalance (Sartorious Supermicro S4, Göttingen, Germany), was used for each run. An empty, crimped aluminum pan (26.5 mg to 27.0 mg, similar to that for encapsulating the sample) was used as the reference pan. Dry nitrogen at a flow rate of 20 mL/min was used as the purge gas. Data were acquired at a sampling rate of five data points per second. Temperature and enthalpy calibration was performed in accordance with standard procedures ([41], see Appendix E.1) using an indium standard with a purity of 99.999 %, a melting temperature of 156.60 °C and a heat of fusion of 28.45 J/g.

Three thermal protocols were used. Prior to running any of these protocols, the previous thermal history of each sample was erased by heating from 50 °C to 210 °C at 10 °C/min, and holding at that temperature for 5 min. In the first protocol, the sample was cooled from 210 °C to 50 °C at 10 °C/min, and then reheated to 210 °C at 10 °C/min. The resulting cooling exotherm and melting endotherm give the transition temperatures and heats of transitions.

The objective of the second protocol was to measure the isothermal crystallization kinetics at various temperatures. To avoid crystallization during the cooling step, a high cooling rate of 80 °C/min was applied to rapidly bring the sample to the desired crystallization temperature, which was in the range of 141.7 °C to 148.7 °C for the nucleated samples and 127.7 °C to 131.7 °C for the non-nucleated samples. These temperature limits were selected based on the instrument capability and the sample crystallization kinetics: too high a temperature yields an undetectable signal, whereas too low a temperature triggers early crystallization during the cooling step. To ensure an adequate duration for crystallization at the selected temperature, the sample was held for about five times the time at which the peak signal was detected.

The third protocol was designed to obtain data under a condition that could be qualitatively compared to the light intensity and rheological data. The sample was cooled from 210 °C to 155.5 °C at 5 °C/min, then held for a prescribed duration ($1\ \text{h} \le t_c \le 12\ \text{h}$) for isothermal crystallization, and finally reheated to 210 °C at 10 °C/min. Unlike the second protocol, the heat-flow rate at 155.5 °C was too small to be detected by the instrument to determine the amount of heat liberated during crystallization; therefore, crystallization kinetics was instead estimated based on the heat of fusion recorded in the final heating scan.

For data analysis (see Appendix E.2), the measured signals were first corrected using the calibration results, and then the zero line (*i.e.*, data obtained in every other run with empty sample pans) was subtracted. The analysis was done using a custom script routine in the DIAdem program (National Instruments, Austin, TX). Assuming that the crystallized mass is proportional to the measured heat change (given by the integration of the peak area using a linear baseline), the absolute crystallinity X_{w} and the relative crystallinity $\phi_{\mathrm{w}}(t)$, in mass fraction, can be calculated using the following equations, respectively:

$$X_{\mathrm{w}} = \frac{\Delta H_{\mathrm{m}}}{\Delta H_{\mathrm{m}}^{0}} \tag{4.15}$$

$$\phi_{\mathrm{w}}(t) = \frac{\Delta H_{\mathrm{c}}(t)}{\Delta H_{\mathrm{c}}(\infty)} \tag{4.16}$$

where $\Delta H_{\mathrm{m}} = \int_{0}^{\infty} \left(\mathrm{d}H_{\mathrm{m}}/\mathrm{d}t\right)\mathrm{d}t$ is the total heat change during melting, $\Delta H_{\mathrm{m}}^{0}$ is the equilibrium heat of fusion for the fully crystalline polymer (209 J/g for polypropylene [42]), $\Delta H_{\mathrm{c}}(t) = \int_{0}^{t} \left(\mathrm{d}H_{\mathrm{c}}/\mathrm{d}t\right)\mathrm{d}t$ and $\Delta H_{\mathrm{c}}(\infty) = \int_{0}^{\infty} \left(\mathrm{d}H_{\mathrm{c}}/\mathrm{d}t\right)\mathrm{d}t$ are the heat of crystallization released after an elapsed time t and that over the entire test duration, respectively.

The absolute crystallinity in mass fraction was converted into volume fraction using the following equation:

$$X = \frac{X_{\mathrm{w}}}{X_{\mathrm{w}} + (1 - X_{\mathrm{w}})\rho_{\mathrm{c}}/\rho_{\mathrm{a}}} \tag{4.17}$$

where ρ_{c} = 0.943 g/cm3 and ρ_{a} = 0.854 g/cm3 are the fully crystalline and amorphous densities [42], respectively. The same equation, with X_{w} and X replaced by $\phi_{\mathrm{w}}(t)$ and $\phi(t)$, respectively, was used for the relative crystallinity.

4.4 Results and Discussion

4.4.1 DSC: Melting and Crystallization Behavior at Constant Scanning Rate

Figure 4.1 compares the melting and crystallization characteristics of the nucleated (iPP1 and iPP2) and non-nucleated samples (iPP3 and iPP4) obtained at a constant scanning rate of 10 °C/min. The melting T_m and crystallization T_c temperatures, indicated on the figure correspond to the maxima and minima on the DSC thermograms, respectively. In agreement with results in the literature using the same organophosphate salt as nucleating agent [43], the nucleated samples show higher melting temperatures, greater degrees of crystallinity (by at least 10 % in X, Fig. 4.1a), and significantly higher crystallization temperatures (by more than 22 °C in T_c, Fig. 4.1b). The large elevation in T_c is an indicator of the high efficiency of the nucleating agent, which has been previously reported to be greater than many other additives [43].

It is common to observe multiple peaks in the melting endotherms, which have been attributed to various factors, *e.g.,* presence of a polymorph different than the α phase, difference in crystal size and perfection, reorganization, segregation and orientation effects [44]. These effects are strongly dependent not only on the molecular properties but also on the presence of a nucleating agent and the cooling history of the samples. As shown in Fig. 4.1a, only a single melting peak was evident for all the samples, except for a slight shoulder in the case of iPP2 at about 161 °C.

For the non-nucleated samples, the crystallization peak in Fig. 4.1b is slightly lower for the higher-molecular weight sample (iPP4) than for the lower-molecular weight sample (iPP3). By contrast, molecular weight has negligible influence on the nucleated samples, as iPP1 and iPP2 indicate little difference in their crystallization exotherms.

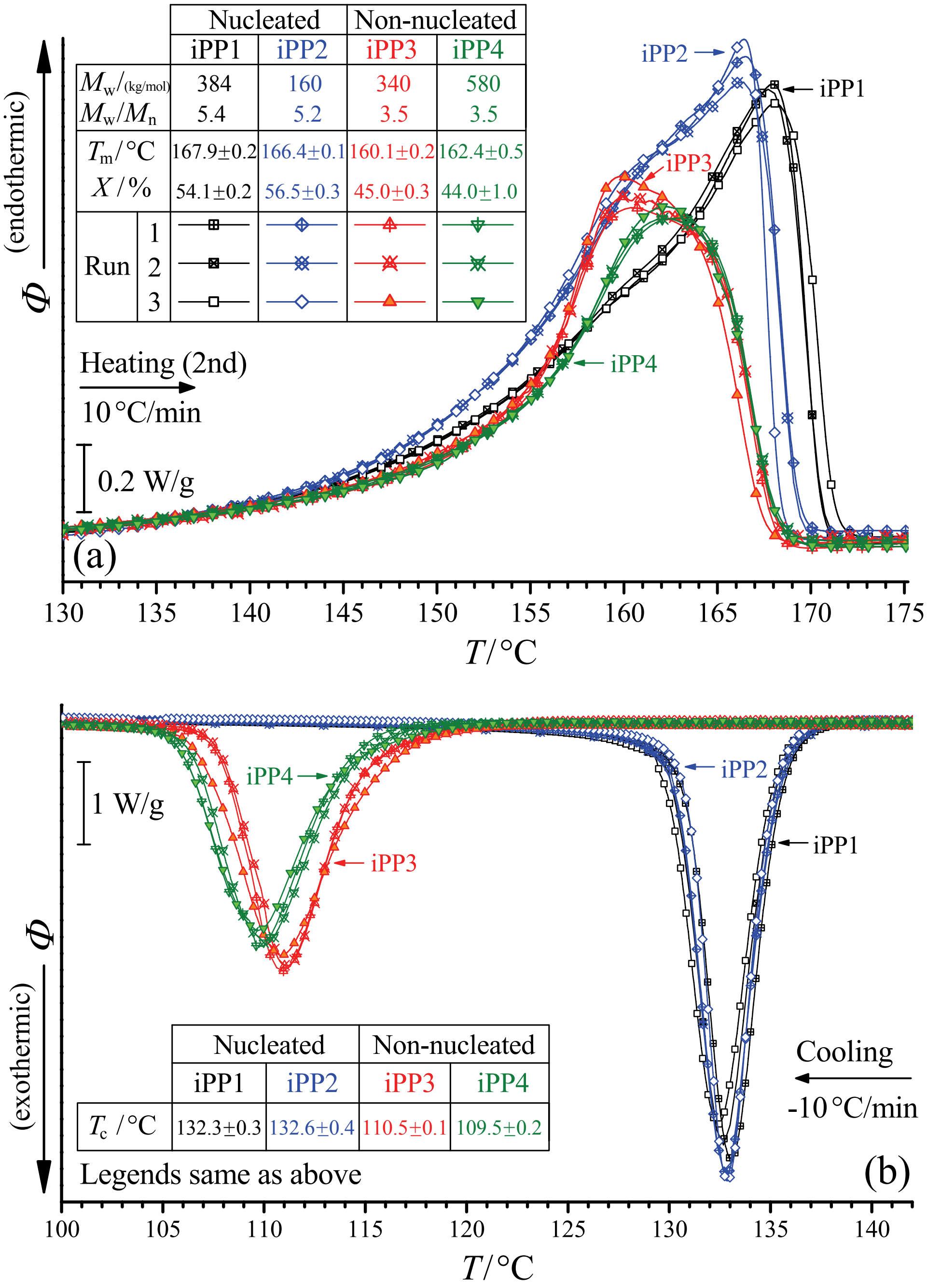

Figure 4.1. DSC heat-flow rate versus temperature at a scanning rate of 10 °C/min for the nucleated (iPP1 and iPP2) and non-nucleated samples (iPP3 and iPP4). (a) During the second heating scan, the nucleated samples indicate broader melting ranges and higher melting temperatures than those of the non-nucleated samples. (b) During the cooling scan, the nucleated samples indicate significantly higher crystallization temperatures than those of the non-nucleated samples. The tabulated T_m and T_c values are maxima on the melting endotherms and minima on the cooling exotherms, respectively. The curves indicate the data; symbols are distributed to mark different experiments. Data shown are for three measurements.

4.4.2 DSC: Isothermal Crystallization Kinetics

Figure 4.2a shows the time evolution of crystallinity X_c measured at several temperatures for the nucleated samples. Note that X_c refers to the crystallinity obtained in isothermal crystallization following cooling, which is usually smaller than the value of X as determined based on the melting endotherm. At all the temperatures studied, both samples have comparable kinetics up to a crystallinity of $X_c \approx 0.45$ (or $\phi \approx 0.90$ in iPP1 and $\phi \approx 0.85$ in iPP2). Above this value, more volume of material is crystallized in iPP2 than in iPP1, but this difference appears to decrease with increasing temperature. An excellent fit to the Avrami equation (Eg. 4.14), using a non-integer value of exponent n, was found for both samples up to $\phi \approx 0.877$ in Fig. 4.2c). An integer of $n = 3$ also gives an equally good fit, as shown in a double logarithmic plot of ϕ versus time in Fig. 4.2e. However, it is important to note that n is unable to represent a unique set of nucleation mode and growth, and its value also varies with the polymer type [36]. For isotactic polypropylene, literature values ranging from 2 to 4 have been reported [37, 45].

On the other hand, some peculiar behavior was observed for the non-nucleated samples, especially iPP4. Figures 4.2b, d and f show that iPP4 indicates a higher crystallinity than iPP3 at the beginning, but both have similar overall crystallization rates for $\phi > 0.362$. Interestingly, while the value of for iPP3 falls within the typical range of 2 to 4, that for iPP4 is lower at the beginning, *viz.*, $n = 1.6$ to 1.7, although the data approaches those of iPP3 with $n = 2.4$ for $\phi > 0.362$. Carfagna *et al.* [46] reported that the presence of residual unmelted material (from previous incomplete heating step), which serve as nuclei to initiate crystallization, can lead to a value of n as small as 0.5. A comparison of X_c and X in Table 4.1 provides further evidence for the remnants of unmelted crystals in iPP4. The tabulated values indicate that $X_c > X$ was observed for iPP4, whereas either $X_c < X$ or $X_c \approx X$ was found for the other three samples. This implies that the heating step intended to destroy all of the crystals was inadequate for iPP4, which has the highest molecular weight among the samples.

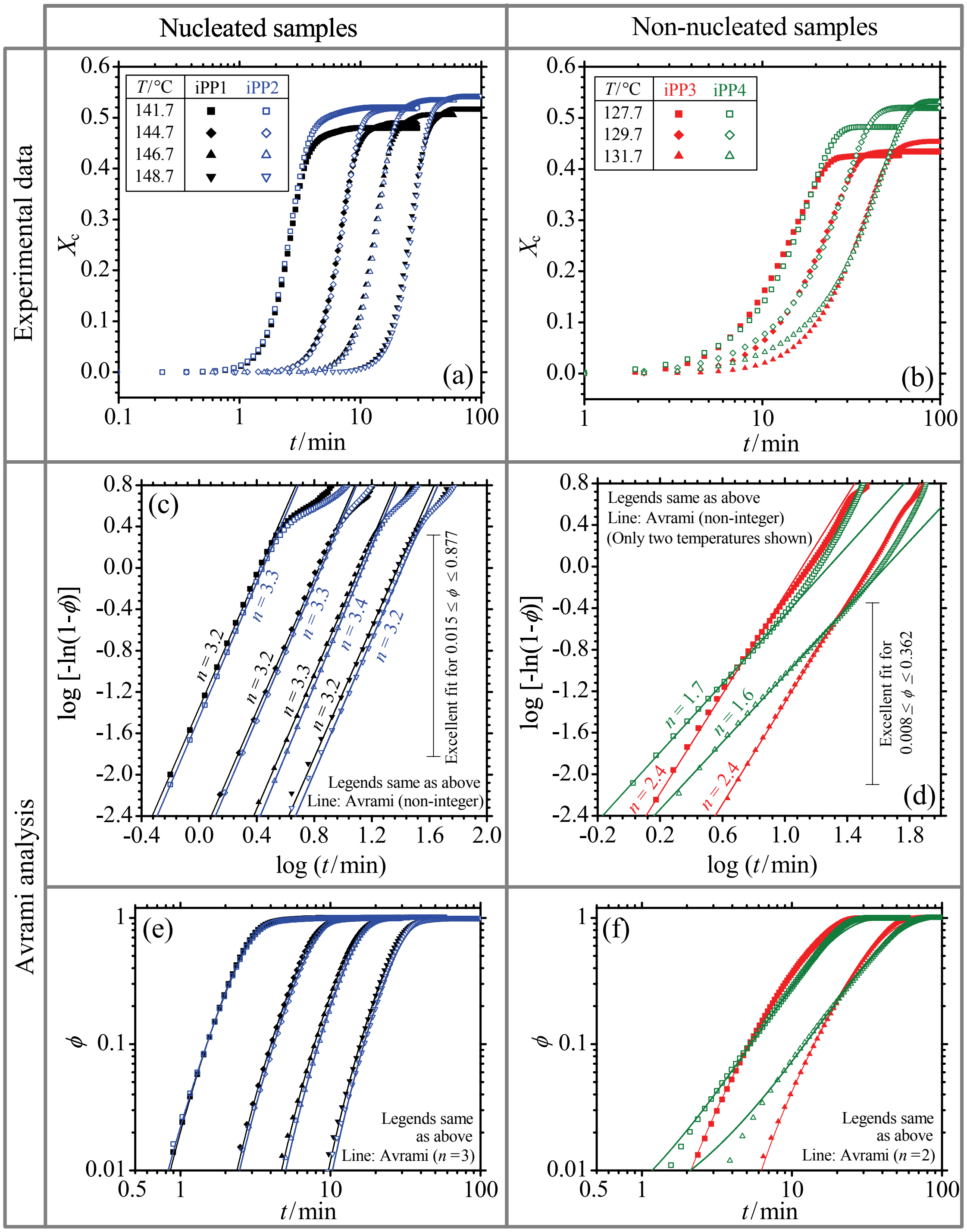

Figure 4.2. Isothermal crystallization kinetics at various temperatures obtained from DSC measurements. Time evolutions of crystallinity for (a) nucleated samples and (b) non-nucleated samples. Results from the Avrami analysis using non-integer *n* are given in (c) for nucleated samples, and in (d) for non-nucleated samples. Analysis based on integer values of *n* are given in (e) and (f).

Table 4.1. Crystallinities obtained from melting endotherms and in isothermal crystallization.

Crystallinity	iPP1		iPP2		iPP3		iPP4	
Melting endotherm[a] :								
X / %	54.1 ± 0.2		56.5 ± 0.3		45.0 ± 0.3		44.0 ± 1.0	
Isothermal crystallization[b] :								
X_c /%	48.0	51.8	52.0	54.3	42.7	54.3	48.2	53.1
at temperature	(141.7 °C)	(148.7 °C)	(141.7 °C)	(148.7 °C)	(127.7 °C)	(131.7 °C)	(127.7 °C)	(131.7 °C)

[a] Based on the heat of fusion recorded during heating at a scan rate of 10 °C/min, after the sample was crystallized at a constant cooling rate of 10 °C/min (see the inset table in Fig. 4.1a).

[b] Based on the heat liberated during isothermal crystallization following the second protocol described in Section 4.3.1. The reported values are the final plateaus shown in Figs. 4.2a and b.

Of particular interest for qualitative comparison[*] with the results obtained from the sliding plate rheometer is the crystallization kinetics at 155.5 °C. However, because this temperature was too high for recording a discernible DSC signal during crystallization, the third thermal protocol described in Section 4.3.1 was used. Figure 4.3 shows the melting endotherms at a heating rate of 10 °C/min for the four samples after they had been held isothermally at this temperature for various crystallization durations t_c. The nucleated samples indicate a progressive increase in crystallinity with t_c, as indicated by the increasing areas under the endothermic peaks (Figs. 4.3a and b), whereas a monotonic curve is observed for the non-nucleated samples (Figs. 4.3c and d). The absence of a peak in the latter two samples implies that they do not crystallize at 155.5 °C for a period as long as 12 h. The large differences between the nucleated and non-nucleated samples would be useful for revealing the effect of shear on crystallization in the next chapter.

---

[*] A direct comparison cannot be made because the sliding plate rheometer measurements included a cooling and equilibration time of 60 min (see Fig. 2.10b), whereas the DSC measurements followed the third protocol described in Section 4.3.1.

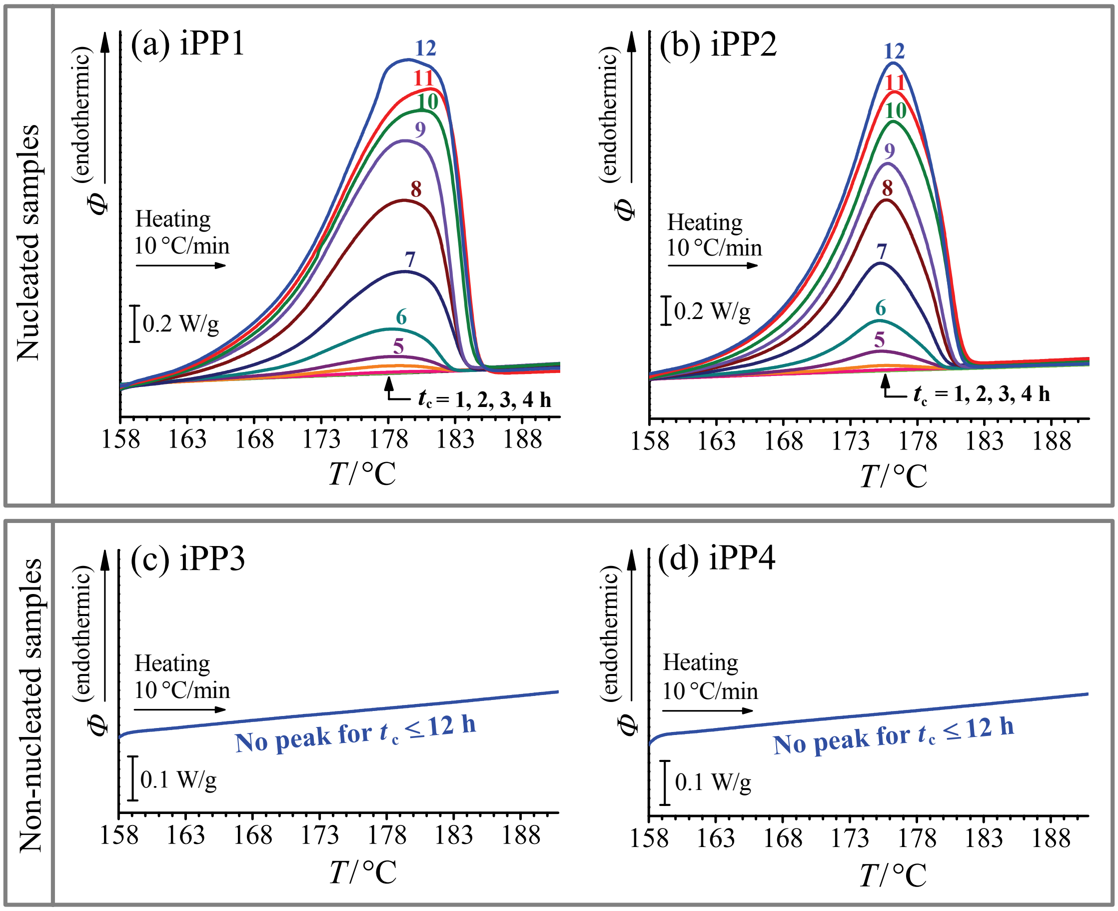

Figure 4.3. The DSC melting endotherms after the samples were held isothermally at 155.5 °C for various crystallization times (1 h ≤ t_c ≤ 12 h). As indicated by the area under the melting endotherm, an increasing crystallinity with t_c was found in (a) and (b) for the nucleated samples. The non-nucleated samples do not crystallize, as indicated by the absence of any peak in (c) and (d).

Figure 4.4a compares the time evolutions of crystallinity, estimated from the data given in Fig. 4.3, between the two nucleated samples. As shown in this figure, the two samples have similar overall crystallization kinetics, as was also observed earlier for isothermal crystallization at lower temperatures (Figs. 4.2a, c and e). They also behave similarly in non-isothermal crystallization at constant cooling rates (see Fig. 4.1b). But, rather surprisingly, the crystallization behavior inferred from the melting endotherms shown in Fig. 4.4b (selected data from Fig. 4.3) is clearly not the same for the two samples. It is well established that the melting temperature is proportional to the reciprocal of the lamellar thickness or crystal size[*], which is generally described by the Thomson-Gibbs equation [48]. Consequently, it can be inferred from the higher melting temperatures shown by the melting endotherms of iPP1 in Fig. 4.4b that this sample contains crystals larger than those in iPP2. Moreover, given the fact that both have a comparable volume of material crystallized at all times (Fig. 4.4a), the number of crystals must be greater for the sample with smaller crystals. Thus, these results reveal the crystallization behavior of these two samples; growth of larger and fewer crystals is favored for iPP1, whereas formation of smaller and more numerous crystals is preferred by iPP2.

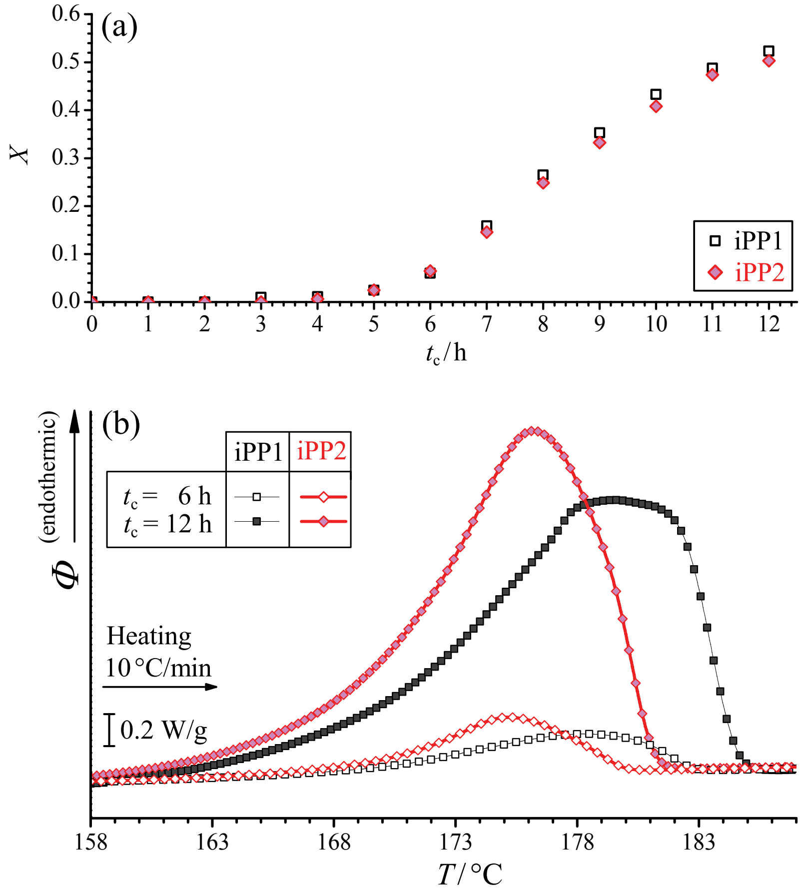

Figure 4.4. Comparison of the crystallization kinetics and behaviors of nucleated samples iPP1 and iPP2 under isothermal crystallization at 155.5 °C. (a) Both samples indicate comparable overall crystallization kinetics. (b) The higher melting temperatures on the melting endotherms (after crystallization times of 6 h and 12 h) shown by iPP1 suggest that this sample consists of larger crystals than those in iPP2.

---

[*] A more rigorous way of determining the crystal size distribution can be found elsewhere [47].

4.4.3 Light Intensity and Rheological Measurements

Figure 4.5 shows the time evolutions of the normalized light intensity, the magnitude of the complex viscosity, and the loss angle, measured simultaneously under isothermal, quasi-quiescent crystallization conditions at 155.5 °C for nucleated sample iPP1. To facilitate discussion, the results can be loosely classified into four periods: induction time, early and late stages of crystallization, and slip. This is not to be taken as a definitive classification, but simply a guide to help describe the sequence of events occurring during an experiment. Nonlinear viscoelasticity was also observed and is discussed in the section dealing with slip.

4.4.3.1 Induction Time

As shown in Fig. 4.5a, the normalized light intensity remains essentially constant at a value of unity (< 3 % change[*]) for $t < 3800$ s. This dormant period, commonly called the induction time, is required by the amorphous melt to form crystalline structures with sizes large enough to cause light attenuation. The value of this quantity depends strongly on the detection capability of the instrument [49, 50]. What happens during the induction time is particularly important and has been the subject of much debate in the past decade. It is widely accepted that both nucleation and growth take place during this time [49-52], but several recent experimental and numerical studies suggested other mechanisms, *e.g.*, spinodal decomposition [53-57], and the evolution of a mesomorphic phase via a multistage process [19, 58]. Much of this controversy comes from the unexpected observation in some studies [53, 54, 56, 59] that the induction time indicated by the small-angle X-ray scattering (SAXS) peak, which probes long-range ordering at lamellar dimensions, precedes that inferred from wide-angle X-ray diffraction (WAXD) crystalline peaks at unit cell length scales. However, it was reported in other studies [50, 60] that this puzzling observation was likely due to discrepancies in the detection limits of the SAXS and WAXD detectors.

---

[*] This detection limit was estimated based on the observations that the maximum fluctuation of the incident laser intensity over a period of 12 h was about 2 %.

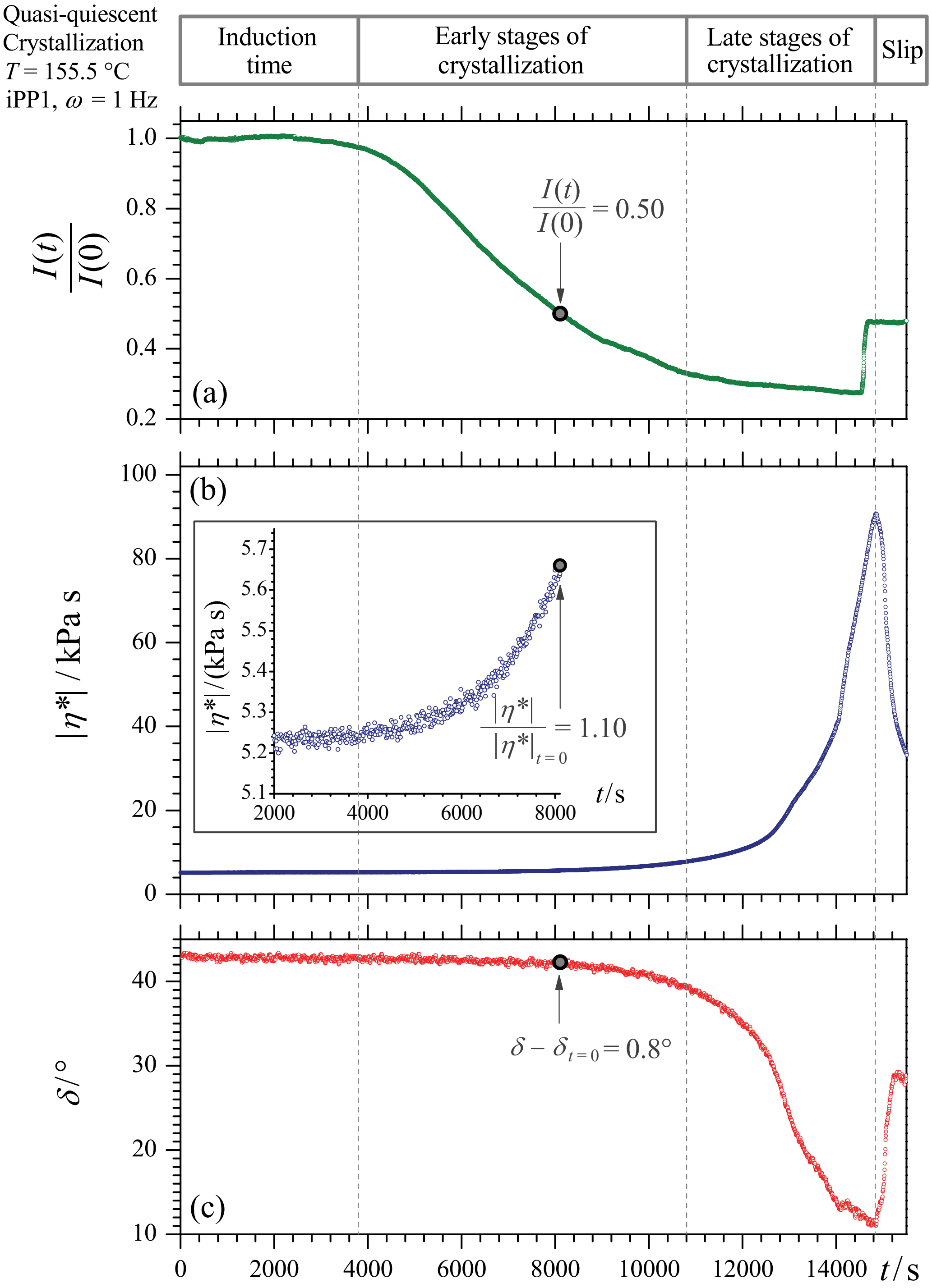

Figure 4.5. Time evolutions of (a) the normalized light intensity, (b) the magnitude of the complex viscosity, and (c) loss angle during isothermal, quasi-quiescent crystallization of iPP1 at 155.5 °C. The results can be divided into four events: induction time, early stages, and late stages of crystallization, as well as slip. The inset in (b) shows data between 2000 s ≤ *t* ≤ 8000 s.

Likewise, it is enlightening to compare induction times inferred from light intensity and rheological measurements. Interestingly, the induction time indicated by the fall in the normalized light intensity (Fig. 4.5a) matches closely the time when the magnitude of the complex viscosity begins to rise, as shown in the inset of Fig. 4.5b (albeit the onset is subject to some uncertainty due to noise). Indeed, the close correspondence between these two timescales is nontrivial; it implies that the crystalline structures initially formed at the end of the induction time can trigger concurrent changes in both light scattering and bulk flow behavior. The nascent structures that cause light attenuation within the Rayleigh-Debye-Gans scattering range [20, 21] are estimated to be smaller than the spherulites and have a size in the range of a few hundred nanometers [3, 11] (comparable to or smaller than the incident laser wavelength of 632.8 nm). It is noteworthy that both techniques demonstrate comparable capabilities in detecting these structures.

Because the early change in the magnitude of the complex viscosity is very small[*] (< 1 %, Fig. 4.5b), it is not surprising that the induction time is overestimated in most studies, particularly when rheological data are inappropriately plotted using a large range or a logarithmic scale. A few studies [25, 61-69] have explored the simultaneous use of rheometry with another technique, but none has made a proper comparison of the induction time. For example, based on continuous shearing measurements, Chaari *et al.* [67] concluded that the induction time given by the rheological response trailed that indicated by turbidity, birefringence and dichroism. They ascribed this observation to the imperfect, non-uniform flow conditions in their experimental setup, but the cause of the apparent delay likely lies in the inappropriate range used in plotting the data. Koyama *et al.* [25, 65] modified a rheometer for simultaneous rheometry and differential thermal analysis (DTA), and found differences between the two measurements, but the poor signal quality renders the comparison inconclusive. Similarly, Kiewiet *et al.* [68] developed an instrument that can simultaneously perform rheological and DSC measurements; but they only reported non-isothermal crystallization data, and a

---

[*] As mentioned in Section 2.5, a larger response or better sensitivity can be obtained if a lower frequency is used.

comparison of the induction times was not made. Hence, this study has conclusively demonstrated the usefulness of oscillatory shear for detecting the induction time, and benchmarked it against simultaneous light intensity measurement.

4.4.3.2 Early Stages of Crystallization

After the induction time, the early stages of crystallization (3800 s $< t <$ 10 800 s) are marked by a steep reduction in light intensity (Fig. 4.5a), a gradual increase in the magnitude of the complex viscosity (*i.e.*, increase in resistance to flow, Fig. 4.5b), and a marginal decrease in loss angle (*i.e.*, increase in elasticity, Fig. 4.5c). It is clear from these trends that the evolving structures have unequal effects on these properties; for example, at about 8100 s, while the light intensity has already fallen by 50 %, the magnitude of the complex viscosity has only increased by about 10 %, and the loss angle has dropped by only 0.8° (*i.e.*, a 3 % drop in the loss tangent). Intuitively, this large discrepancy is somewhat expected, since the presence of a low concentration of small crystalline structures is more likely to induce a substantial increase in light scattering than to cause an appreciable disturbance in the macroscopic flow behavior at moderate oscillation frequencies. The difference reflects clearly the higher sensitivity of the light intensity compared to oscillatory shear, and suggests that the former is more suitable than the latter for probing the early kinetics.

Winter et al. [29, 70-73] used the concept of physical gelation to describe the early stages of crystallization. Physical gelation is conceived as a network formation process that involves an increase in the connectivity of the polymer chains at a long distance called the correlation length. The time when this length diverges is defined as the gel time (or the gel point). The crystallinity at the gel time has been estimated to vary from as low as 1 % to 2 % [28, 71] to as high as 15 % to 17 % [70, 73]. While one study reported that clusters of about 1 μm in size were formed and impinged at the gel time [72], another found that spherulites as large as 100 μm were visible at this time [73]. The large discrepancies in these reports show that the actual amount of crystallinity and the size of the structure formed at the gel time are still not clear. Separate DSC and small-angle light scattering (SALS) experiments were conducted in these studies, which added some uncertainty in the analysis.

The salient question is: does the gel time fall within the early stages of crystallization? Gel time is rheologically* defined as the time when the loss tangent is independent of the frequency in cyclic frequency sweeps [70], which involve successive runs of small-amplitude oscillatory shear within a certain range of frequencies. It was shown in Fig. 4.5c that the change in the loss angle is the smallest output of all of the data, so loss tangent is not likely an effective indicator of early kinetics. This lack of sensitivity implies that the gel time probably occurs much later than the characteristic time indicated by either the magnitude of the complex viscosity or the storage modulus. Of course, in discussing the sensitivity of the gel time, the experimental frequency must not be ignored, as a lower frequency would give a higher loss tangent and thus a larger measurement range (or higher sensitivity). Since the frequency used here (1 Hz) was rather high compared to those commonly used in gel time studies (0.1 rad/s to 0.001 rad/s), one might argue that the data presented in Fig. 4.5c are unsuitable for direct comparison. Nonetheless, a survey of the literature data [29, 70-73, 75] indicates strong support for the present analysis. A good example is illustrated in the data of Hadinata *et al.* (Fig. 6 in [75]), which showed that the gel time is much longer than the time indicated by a 50 % increase in the magnitude of the complex viscosity. In fact, the data of Winter *et al.* [29, 70-73] also showed a significant increase in the storage modulus (*e.g.*, > 500 % at 0.025 rad/s [71]) before the gel time. In sum, this study provides convincing evidence, together with the survey results, that the gel point does not reflect the very early stages of crystallization but occurs at a much later time.

---

* At gel point the zero-shear viscosity diverges to infinity and the equilibrium modulus is zero [74].

4.4.3.3 Late Stages of Crystallization

As crystallization progresses, with more amorphous material being converted into crystals, the sample becomes more opaque, and the change in the normalized light intensity becomes very small due to the light scattering effect approaching its saturation or maximum (*e.g.*, at t > 10 800 s, Fig. 4.5a). As expected, the curve is non-monotonic, with a minimum intensity at about 14 500 s, and is accompanied by a rise to a new level at the end[*]. Stein *et al.* [14, 76] provided a plausible explanation and model for this observation based on the results obtained for spherulite formation in SALS experiments. In this experiment, the scattering patterns and intensities in both the cross-polarized mode (which depends on the orientation fluctuations associated with the anisotropy within the spherulite) and the parallel-polarized mode (which depends not only on orientation fluctuations but also on density fluctuations associated with average polarizability) were recorded. Although there are differences between their experiment and the one performed here, the physics is deemed similar. Briefly, the authors [14, 76] ascribed the minimum to a maximum in the scattering contributed by the fluctuations in the average polarizability. They estimated that it occurs when spherulites have occupied about one-half the sample volume, which, however, does not mean that the crystallinity is 50 %, as the spherulites also contain amorphous material. As the contribution by the average polarizability decreases after the minimum, the intensity then rises to a new level (Fig. 4.5a). Additionally, they found that the spherulite radius approaches a constant value, an indication of impingement between the spherulites, not long after the minimum. The spherulites at this time are then described as volume- or space-filling, where conversion of the amorphous material within the spherulites into crystalline material continues to take place. Because of this process, crystallinity can still develop even after the new level in the intensity indicates an apparent plateau [76].

In stark contrast to the small change in light intensity, the magnitude of the complex viscosity increases significantly, and the loss angle decreases markedly during this period

---

[*] Some studies [4, 5] only reported the intensity data up to the point at which a minimum was detected, without mentioning if a rise would follow after the minimum.

(Figs. 4.5b and c). These large changes are indicative of a transition in the stages of crystallization, albeit not accompanied by sharp changes in slope. In fact, a distinctly clear change of slope is not expected, since crystallization is a continuous process [36]. Physically, one can envisage that the number and size of crystalline structures, which were both too small to impart large changes to the bulk flow behavior during the early stages, have now grown to occupy a significant volume with length scales that can have a substantial effect on the rheological properties. From another perspective, the large increase in stress or viscosity in this period can be interpreted as due to a large quantity of chain segments being restricted to move only within the crystallized domains or structures into which they have been rearranged and ordered. In principle, each of these structures is made up of segments from different chains; therefore, a cooperative movement of a large number of chains is required for flow to occur. Consequently, it is unsurprising that the stress shows a large upturn when the incorporation of chain segments into the growing crystalline structures has entered a region in which the interactions between the chain segments or the structures become significant. It is tempting to suggest a critical value or parameter to characterize this change. The gel point appears to correspond to this event.

Like light intensity, rheological data also behave non-monotonically (Figs. 4.5b and c), although a monotonic increase in either the storage modulus or the magnitude of the complex viscosity is often reported in the literature [30, 32, 75, 77-80]. While some studies [30, 32, 77, 78, 81] demonstrated that the increase ultimately led to a plateau at the end of crystallization, there have also been reports [75, 79, 80] indicating difficulty in attaining a reproducible maximum or a plateau. One reason is that the stress can rise to a level that exceeds the measurement range of the rheometer transducer. Another possible cause is that the sample slips before the completion of crystallization. Indeed, this phenomenon was found in the present study to cause the non-monotonic behavior. This will be discussed later.

The large changes in rheological properties, with an increase of at least one order of magnitude in stress in contrast to only a marginal change in light intensity, mean that oscillatory shear is the more practical technique for tracking the late stages. This is opposite to what was mentioned earlier about these two measurements in regard to the early stages. Taken together, the results indicate that the two techniques offer complementary information about different events during crystallization.

The onset of the late stages, at about 10 800 s, is defined here as the time at which the magnitude of the complex viscosity has increased by 50 % of its initial value. Using this as a criterion, it is found that most previous studies have only made use of data in the late stages for analysis and inadvertently ignored the large segment of the data representing early kinetics. For instance, some studies [75, 82, 83] selected the time when the magnitude of the complex viscosity, or the steady-shear viscosity in continuous shearing tests, doubles its value as the crystallization onset time. If this criterion is applied to the data shown in Fig. 4.5b, the onset time would be about 11900 s, and this falls into the late stages. To better represent early kinetics, a much smaller increase in stress (*e.g.*, 1 % [69] or 5 % [78]) should be used. In other studies [27, 79, 80] the time corresponding to the intersection of the apparent initial plateau and the tangent line drawn to the large upturn in the storage modulus was used. Unfortunately, this method of analysis also results in a time that is actually within the late stages. Another approach is the half-time analysis [26, 30, 78], which uses the time when the storage modulus or the complex viscosity increases to one-half of the difference between its final and initial values (using either linear or logarithmic normalization). Evidently, this also only gives information about the late kinetics.

4.4.3.4 Slip

As noted earlier, both the fall in the magnitude of the complex viscosity and the rise in the loss angle at about 14 850 s in Figs. 4.5b and c are caused by wall slip. This occurs before the complete transition from melt to solid. Wall slip has often been observed in polymer melts, due to either adhesive or cohesive failure at a critical value of shear stress [84-87]. In most slip studies this critical stress is reached by increasing the shear rate, but here, the increase in stress arises from crystallization.

The marked decrease in the stress magnitude at time t_4 in Fig. 4.6a is a clear indication of slip. Prior to the onset of slip, the response to the oscillatory shear becomes nonlinear at t_3, as indicated by the normalized stress waveform shown in Fig. 4.6b and the stress-strain loops in Fig. 4.6c. At t_1 and t_2, the response is linear, as reflected by the sinusoidal waveforms and elliptical stress stress-strain loops. At t_3, however, the stress signal is not sinusoidal, and the loop is not an ellipse. If the strain amplitude were reduced as crystallization continued, the response could be kept in the linear regime. The stress-strain loop is still skew-symmetric at t_3, which is characteristic of nonlinearity but not of slip [85]. At t_5, however, the stress-strain loop is no longer skew-symmetric, and this is a hallmark of slip. The maximum stress amplitude of 0.11 MPa at t_4 shown in Fig. 4.6a is similar to the values of the critical stress for the onset of slip reported in the literature for polyethylene, which are in the range of 0.09 MPa to 0.14 MPa [84, 85]. Data obtained after the onset of slip are not included in subsequent discussions and figures[*].

These observations are somewhat novel, because most studies used commercial rheometers for which raw stress and strain waveforms are not readily available[†]. The possibility of slip has been mentioned [32], but a conclusive analysis cannot be made without the waveforms. It is noteworthy that both nonlinearity and slip can be avoided if the stress amplitude is sufficiently small; so these phenomena might not occur in studies using an auto-strain feature or extremely small strain amplitudes [30, 80].

---

[*] Strictly speaking, the complex viscosity and loss angle should not be used after the onset of nonlinear viscoelasticity. But, it is adequate for the purpose of the present study to display the nonlinear data using the linear properties up to the stress maximum, taking into account that the nonlinearity is small.

[†] Raw waveforms can be acquired using the output voltage connections in certain rheometers. Although this method is rather common in large-amplitude oscillatory shear studies, it has not been used in any crystallization study.

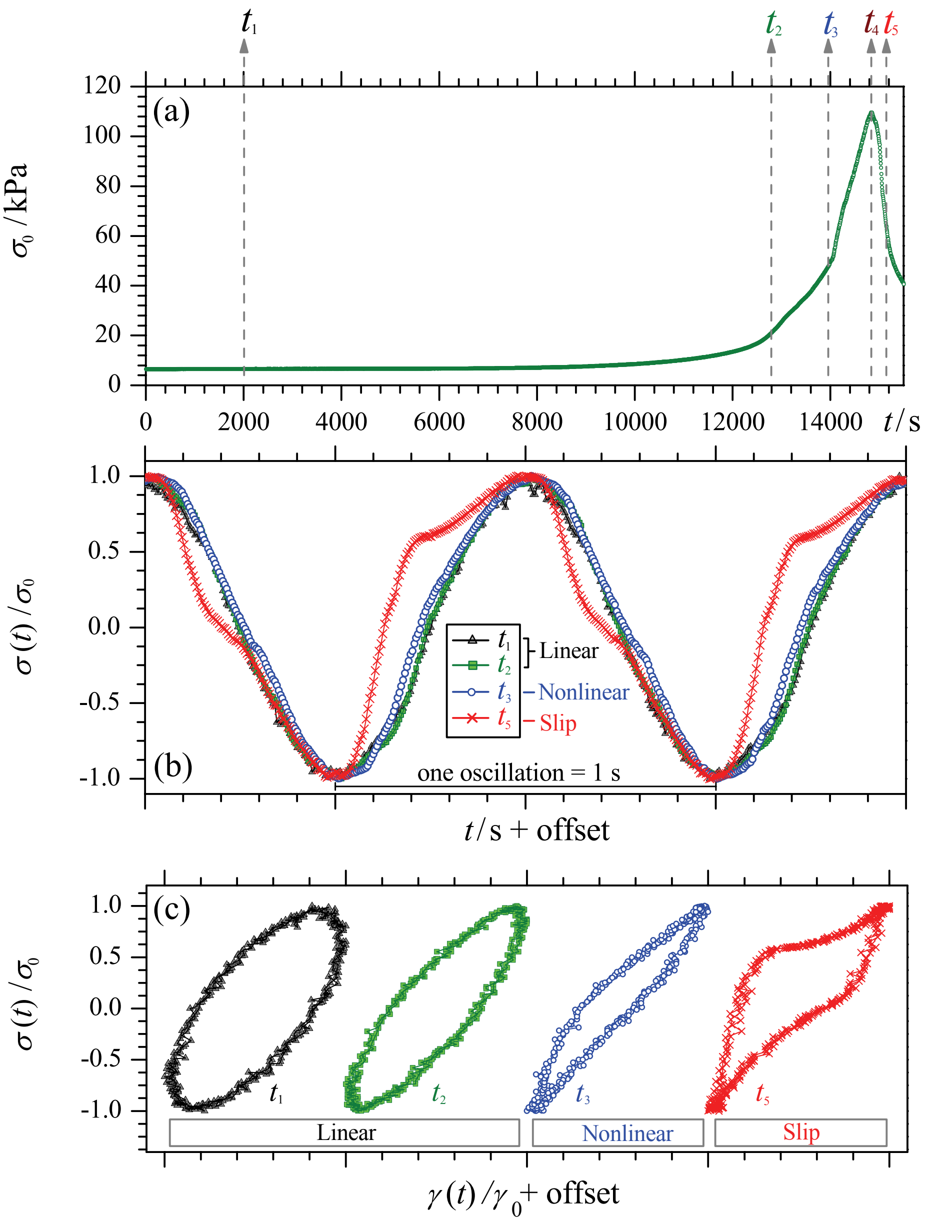

Figure 4.6. Observations of slip during quasi-quiescent crystallization of iPP1 at 155.5 °C. (a) Time evolution of the stress amplitude for the same data shown in Fig. 4.5. The fall in stress amplitude at time t_4 indicates slip. (b) Segments of the normalized stress waveform at ± one cycle of four selected times indicate changes in the rheological behavior: a sinusoidal waveform was observed for the linear response at t_1 and t_2, a non-sinusoidal waveform was observed for the nonlinear response at t_3, and a non-sinusoidal and highly distorted waveform was observed for slip at t_5. (c) Shape of stress-strain loops reflects changes in the rheological response: an ellipse indicates linear response at t_1 and t_2, a non-elliptical, skew-symmetrical shape indicates nonlinear response at t_3, and a non-elliptical, non-skew-symmetric shape indicates slip at t_5.

4.4.4 Comparison between Samples

Figure 4.7 compares data for the four samples under the same experimental conditions as shown in Fig. 4.5. For the non-nucleated samples (iPP3 and iPP4), the normalized light intensity (Fig. 4.7a) and the magnitude of the complex viscosity (Fig. 4.7b) remain approximately constant over the entire duration of the experiment. This agrees with the DSC measurements (Fig. 4.3c and d), which indicate that these samples do not crystallize at 155.5 °C even after 12 h.

On the other hand, the two nucleated samples have similar induction times during the initial fall in light intensity (3200 s to 3800 s, Fig. 4.7a). This is not surprising, as both samples are expected to exhibit similar nucleation kinetics considering that they contain similar concentrations of the same nucleating agent. More intriguing is the latter part of the curve, which shows that the subsequent decrease in light intensity is much steeper for iPP2 than for iPP1. This can be understood using the DSC results shown in Fig. 4.4b, which indicates that smaller and more numerous crystalline structures are found in iPP2 than in iPP1, although these samples exhibit little difference in the evolution of crystallinity at all times in Fig. 4.4a. It appears that the sample consisting of a larger number of smaller crystals attenuates more light compared to the one having crystals that are larger but smaller in quantity. This seems to contradict SALS measurement, in which the overall integrated scattering intensity is generally influenced more by crystal size than amount. A possible explanation is that SALS detects the scattering intensity at only one angle, whereas the measurement in this study is affected by scattering at all directions. Despite the differences, the minimum intensities shown by both samples are similar and qualitatively consistent with the DSC crystallinity results.

The inset in Fig. 4.7b shows the magnitude of the complex viscosity normalized by its initial value. Because of its significantly lower viscosity, the data for iPP2 are much noisier than those for iPP1. Despite this, their induction times appear to be similar, which agree with the light intensity results. From a comparison of the upturn in the complex viscosity in Fig. 4.7b, it seems that iPP2, which has more and smaller crystals, has a stronger effect on rheological properties during crystallization than iPP1, which has fewer and larger crystals.

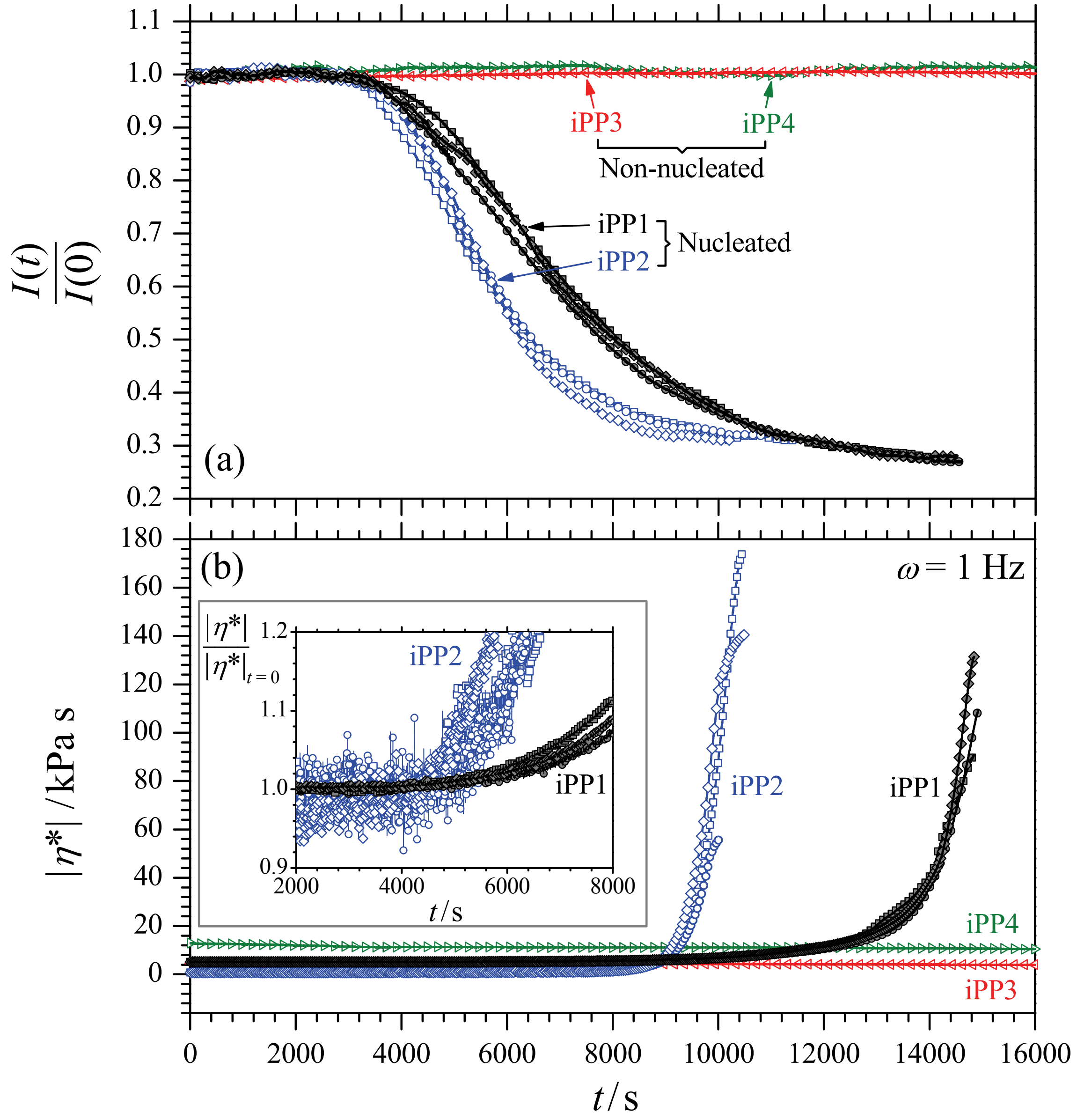

Figure 4.7. Comparison of the time evolutions of (a) the normalized intensity and (b) the magnitude of the complex viscosity between the nucleated (iPP1 and iPP2) and non-nucleated (iPP3 and iPP4) samples during quasi-quiescent crystallization at 155.5 °C. The inset in (b) shows data between 2000 s ≤ t ≤ 8000 s. Both iPP3 and iPP4 do not crystallize, whereas iPP1 and iPP2 indicate similar induction times. The differences between the latter two samples at later times are associated with their crystallization behaviors (see text). Data for iPP1 and iPP2 are for three measurements.

The above results clearly demonstrate the important influence of the crystal characteristics on both light scattering and flow behavior of two crystallizing samples having comparable crystallinities at all times during crystallization. Since the equations presented in Section 4.2 neglect this effect, none of them can describe the results reported here.

4.5 Conclusions

Simultaneous measurement of light intensity and rheology eliminates ambiguity in interpretation of the events occurring during isothermal, quasi-quiescent crystallization. Both techniques demonstrate comparable capabilities in detecting the nascent crystalline structures following an induction time, but they give complementary information; the former is more suitable for monitoring the changes occurring during the early stages, whereas the latter is more useful for tracking the late kinetics. The gel point is not reached during the very early times of crystallization but most likely around the onset of the late stages when the spherulites occupy about half of the sample volume. The occurrence of slip prevents the tracking of the final stages of crystallization. Despite differences in molecular weight, the two nucleated isotactic polypropylenes studied here showed similar evolutions of the crystallinity but marked differences in crystal size distribution, whereas the other two non-nucleated samples do not crystallize at 155.5 °C. Because of their strong dependence on the crystal characteristics, light intensity and rheological data cannot be used to determine crystallinity using equations that are available in the literature.

4.6 References

1. Van Krevelen, D.W. *Properties of Polymers. Their Correlation with Chemical Structure; Their Numerical Estimation and Prediction from Additive Group Contributions*, 3rd ed. (Elsevier, Amsterdam, 1990).
2. Hawkins, S.W. and Richards, R.B. “Light transmission and the formation and decay of spherulites in polythene” *J. Polym. Sci.* (1949) **4**, 515-522.

3. Keane, J. and Stein, R.S. "The scattering of light from thin polymer films. II. Scattering from polyethylene" *J. Polym. Sci.* (1956) **20**, 327-350.
4. Kumaraswamy, G., Issaian, A.M., and Kornfield, J.A. "Shear-enhanced crystallization in isotactic polypropylene. 1. Correspondence between in situ rheo-optics and ex situ structure determination" *Macromolecules* (1999) **32**, 7537-7547.
5. Elmoumni, A. and Winter, H.H. "Large strain requirements for shear-induced crystallization of isotactic polypropylene" *Rheol. Acta* (2006) **45**, 793-801.
6. Langouche, F. "Orientation development during shear flow-induced crystallization of i-PP" *Macromolecules* (2006) **39**, 2568-2573.
7. Janeschitz-Kriegl, H., Ratajski, E., and Stadlbauer, M. "Flow as an effective promotor of nucleation in polymer melts: A quantitative evaluation" *Rheol. Acta* (2003) **42**, 355-364.
8. Kerker, M. *The Scattering of Light and Other Electromagnetic Radiation* (Academic Press, New York, 1969).
9. Harner, R.S., Ressler, R.J., Briggs, R.L., Hitt, J.E., Larsen, P.A., and Frank, T.C. "Use of a fiber-optic turbidity probe to monitor and control commercial-scale unseeded batch crystallizations" *Org. Process Res. Dev.* (2009) **13**, 114-124.
10. Debye, P. and Bueche, A.M. "Scattering by an inhomogeneous solid" *J. Appl. Phys.* (1949) **20**, 518-525.
11. Starkweather, H.W., Jr. "Turbidity and structure of polytetrafluoroethylene films" *J. Polym. Sci., Polym. Lett.* (1964) **2**, 499-502.
12. Thomas, C.L. and Bur, A.J. "Optical monitoring of polypropylene injection molding" *Polym. Eng. Sci.* (1999) **39**, 1291-1302.
13. Stein, R.S. and Rhodes, M.B. "Photographic light scattering by polyethylene films" *J. Appl. Phys.* (1960) **31**, 1873-1884.
14. Yoon, D.Y. and Stein, R.S. "Effect of interference between anisotropic scattering entities on light scattering from polymer films. II. The correlation function approach" *J. Polym. Sci., Polym. Phys. Ed.* (1974) **12**, 735-761.
15. Ding, Z. and Spruiell, J.E. "An experimental method for studying nonisothermal crystallization of polymers at very high cooling rates" *J. Polym. Sci., Part B: Polym. Phys.* (1996) **34**, 2783-2804.
16. Magill, J.H. "A new technique for following rapid rates of crystallization" *Nature* (1960) **187**, 770-771.
17. Magill, J.H. "A new technique for following rapid rates of crystallization. II. Isotactic polypropylene" *Polymer* (1962) **3**, 35-42.

18. Lamberti, G., De Santis, F., Brucato, V., and Titomanlio, G. “Modeling the interactions between light and crystallizing polymer during fast cooling” *Appl. Phys. A: Mater. Sci. Process.* (2004) **78**, 895-901.
19. Strobl, G. “Crystallization and melting of bulk polymers: New observations, conclusions and a thermodynamic scheme” *Prog. Polym. Sci.* (2006) **31**, 398-442.
20. Fritsch, J., Stille, W., and Strobl, G. “Investigation of polymer crystallization kinetics with time dependent light attenuation” *Colloid Polym. Sci.* (2006) **284**, 620-626.
21. Heck, B., Kawai, T., and Strobl, G. “Time dependent light attenuation measurements used in studies of the kinetics of polymer crystallization” *Polymer* (2006) **47**, 5538-5543.
22. Deltu, R., Stille, W., and Strobl, G. “Depression of the zero growth temperature by counits observed for s-polypropylene in light attenuation experiments” *Macromolecules* (2010) **43**, 1035-1040.
23. Gauthier, C., Chailan, J.-F., and Chauchard, J. “Utilisation de l'analyse viscoélastique dynamique à l'étude de la cristallisation isotherme du poly(téréphtalate d'ethylène) amorphe. Application à des composites unidirectionnels avec fibres de verre” *Makro. Chem.* (1992) **193**, 1001-1009.
24. Khanna, Y. “Rheological mechanism and overview of nucleated crystallization kinetics” *Macromolecules* (1993) **26**, 3639-3643.
25. Nagatake, W., Takahashi, T., Masubuchi, Y., Takimoto, J.I., and Koyama, K. “Development of shear flow thermal rheometer for direct measurement of crystallization fraction of polymer melts under shear deformation” *Polymer* (2000) **41**, 523-531.
26. Kelarakis, A., Mai, S.M., Booth, C., and Ryan, A.J. “Can rheometry measure crystallization kinetics? A comparative study using block copolymers” *Polymer* (2005) **46**, 2739-2747.
27. Bustos, F., Cassagnau, P., and Fulchiron, R. “Effect of molecular architecture on quiescent and shear-induced crystallization of polyethylene” *J. Polym. Sci., Part B: Polym. Phys.* (2006) **44**, 1597-1607.
28. Coppola, S., Acierno, S., Grizzuti, N., and Vlassopoulos, D. “Viscoelastic behavior of semicrystalline thermoplastic polymers during the early stages of crystallization” *Macromolecules* (2006) **39**, 1507-1514.
29. Pogodina, N.V., Winter, H.H., and Srinivas, S. “Strain effects on physical gelation of crystallizing isotactic polypropylene” *J. Polym. Sci., Part B: Polym. Phys.* (1999) **37**, 3512-3519.

30. Housmans, J.-W., Steenbakkers, R.J.A., Roozemond, P.C., Peters, G.W.M., and Meijer, H.E.H. "Saturation of pointlike nuclei and the transition to oriented structures in flow-induced crystallization of isotactic polypropylene" *Macromolecules* (2009) **42**, 5728-5740.
31. Steenbakkers, R.J.A. and Peters, G.W.M. "Suspension-based rheological modeling of crystallizing polymer melts" *Rheol. Acta* (2008) **47**, 643-665.
32. Boutahar, K., Carrot, C., and Guillet, J. "Crystallization of polyolefins from rheological measurements - Relation between the transformed fraction and the dynamic moduli" *Macromolecules* (1998) **31**, 1921-1929.
33. Pantani, R., Coccorullo, I., Speranza, V., and Titomanlio, G. "Modeling of morphology evolution in the injection molding process of thermoplastic polymers" *Prog. Polym. Sci.* (2005) **30**, 1185-1222.
34. Lamberti, G., Peters, G.W.M., and Titomanlio, G. "Crystallinity and linear rheological properties of polymers" *Int. Polym. Process.* (2007) **22**, 303-310.
35. Tanner, R.I. "A suspension model for low shear rate polymer solidification" *J. Non-Newtonian Fluid Mech.* (2002) **102**, 397-408.
36. Mandelkern, L. *Crystallization of Polymers. Vol. 2: Kinetics and Mechanisms*, 2nd ed. (Cambridge University Press, Cambridge, 2004).
37. Wunderlich, B. *Macromolecular Physics. Vol. 2: Crystal Nucleation, Growth and Annealing* (Academic Press, New York, 1976).
38. Avrami, M. "Kinetics of phase change. I: General theory" *J. Chem. Phys.* (1939) **7**, 1103-1112.
39. Avrami, M. "Kinetics of phase change. II Transformation-time relations for random distribution of nuclei" *J. Chem. Phys.* (1940) **8**, 212-224.
40. Avrami, M. "Granulation, phase change, and microstructure. Kinetics of phase change. III" *J. Chem. Phys.* (1941) **9**, 177-184.
41. Della Gatta, G., Richardson, M.J., Sarge, S.M., and Stølen, S. "Standards, calibration, and guidelines in microcalorimetry. Part 2. Calibration for differential scanning calorimetry (IUPAC Technical Report)" *Pure Appl. Chem*. (2006) **78**, 1455-1476.
42. Bai, F., Li, F., Calhoun, B.H., Quirk, R.P., and Cheng, S.Z.D. "Physical constants of poly(propylene)", in Polymer Handbook, J. Brandrup, E. H. Immergut, E. A. Grulke, Eds., (John Wiley & Sons, New York, 1999).
43. Marco, C., Gómez, M.A., Ellis, G., and Arribas, J.M. "Highly efficient nucleating additive for isotactic polypropylene studied by differential scanning calorimetry" *J. Appl. Polym. Sci.* (2002) **84**, 1669-1679.
44. Pasquini, N. *Polypropylene Handbook*, 2nd ed. (Hanser Publishers, Munich, 2005).

45. Janimak, J.J., Cheng, S.Z.D., Zhang, A., and Hsieh, E.T. “Isotacticity effect on crystallization and melting in polypropylene fractions. 3. Overall crystallization and melting behavior” *Polymer* (1992) **33**, 728-735.
46. Carfagna, C., De Rosa, C., Guerra, G., and Petraccone, V. “Recrystallization kinetics of isotactic polypropylene (α–form)” *Polymer* (1984) **25**, 1462-1464.
47. Feng, L. and Kamal, M.R. “Distributions of crystal size from DSC melting traces for polyethylenes” *Can. J. Chem. Eng.* (2004) **82**, 1239-1251.
48. Mandelkern, L. *Crystallization of Polymers. Vol. 1: Equilibrium Concepts*, 2nd ed. (Cambridge University Press, Cambridge, 2002).
49. Mandelkern, L., Quinn, F.A., Jr., and Flory, P.J. “Crystallization kinetics in high polymers. I. Bulk polymers” *J. Appl. Phys.* (1954) **25**, 830-839.
50. Wang, Z.G., Hsiao, B.S., Sirota, E.B., Agarwal, P., and Srinivas, S. “Probing the early stages of melt crystallization in polypropylene by simultaneous small- and wide-angle X-ray scattering and laser light scattering” *Macromolecules* (2000) **33**, 978-989.
51. Hoffman, J.D. and Miller, R.L. “Kinetics of crystallization from the melt and chain folding in polyethylene fractions revisited: Theory and experiment” *Polymer* (1997) **38**, 3151-3212.
52. Muthukumar, M. and Welch, P. “Modeling polymer crystallization from solutions” *Polymer* (2000) **41**, 8833-8837.
53. Imai, M., Mori, K., Mizukami, T., Kaji, K., and Kanaya, T. “Structural formation of poly (ethylene terephthalate) during the induction period of crystallization: 1. Ordered structure appearing before crystal nucleation” *Polymer* (1992) **33**, 4451-4456.
54. Terrill, N.J., Fairclough, P.A., Towns-Andrews, E., Komanschek, B.U., Young, R.J., and Ryan, A.J. “Density fluctuations: The nucleation event in isotactic polypropylene crystallization” *Polymer* (1998) **39**, 2381-2385.
55. Olmsted, P.D., Poon, W.C.K., McLeish, T.C.B., Terrill, N.J., and Ryan, A.J. “Spinodal-assisted crystallization in polymer melts” *Phys. Rev. Lett.* (1998) **81**, 373-376.
56. Heeley, E.L., Maidens, A.V., Olmstead, P.D., Bras, W., Dolbnya, I.P., Fairclough, J.P.A., Terrill, N.J., and Ryan, A.J. “Early stages of crystallization in isotactic polypropylene” *Macromolecules* (2003) **36**, 3656-3665.
57. Gee, R.H., Lacevic, N., and Fried, L.E. “Atomistic simulations of spinodal phase separation preceding polymer crystallization” *Nat. Mater.* (2006) **5**, 39-43.

58. Strobl, G. “From the melt via mesomorphic and granular crystalline layers to lamellar crystallites: A major route followed in polymer crystallization?” *Eur. Phys. J. E* (2000) **3**, 165-183.
59. Katayama, K., Nakamura, K., and Amano, T. “Structural formation during melt spinning process” *Kolloid-Z. u. Z. Polymere* (1968) **226**, 125-134.
60. Panine, P., Di Cola, E., Sztucki, M., and Narayanan, T. “Early stages of polymer melt crystallization” *Polymer* (2008) **49**, 676-680.
61. Haas, T.W. and Maxwell, B. “Effects of shear stress on the crystallization of linear polyethylene and poly-1-butene” *Polym. Eng. Sci.* (1969) **9**, 225-241.
62. Wolkowicz, M.D. “Nucleation and crystal growth in sheared poly(1-butene) melts” *J. Polym. Sci., Polym. Symp.* (1978) **63**, 365-382.
63. Andersen, P.G. and Carr, S.H. “Crystal nucleation in sheared polymer melts” *Polym. Eng. Sci.* (1978) **18**, 215-221.
64. Floudas, G., Hilliou, L., Lellinger, D., and Alig, I. “Shear-induced crystallization of poly(ε-caprolactone). 2. Evolution of birefringence and dichroism” *Macromolecules* (2000) **33**, 6466-6472.
65. Masubuchi, Y., Watanabe, K., Nagatake, W., Takimoto, J.I., and Koyama, K. “Thermal analysis of shear induced crystallization by the shear flow thermal rheometer: Isothermal crystallization of polypropylene” *Polymer* (2001) **42**, 5023-5027.
66. Martins, J.A., Zhang, W., Brito, A.M., Infante, U., Romero, M., and Soares, F.O. “Isothermal and nonisothermal crystallization of polymers: Analysis with a shear differential thermal analyzer” *Rev. Sci. Instrum.* (2005) **76**, 105105.
67. Chaari, F., Chaouche, M., Benyahia, L., and Tassin, J.F. “Investigation of the crystallization of m(LLDPE) under shear flow using rheo-optical techniques” *Polymer* (2006) **47**, 1689-1695.
68. Kiewiet, S., Janssens, V., Miltner, H.E., Van Assche, G., Van Puyvelde, P., and Van Mele, B. “RheoDSC: A hyphenated technique for the simultaneous measurement of calorimetric and rheological evolutions” *Rev. Sci. Instrum.* (2008) **79**, 023905.
69. Krueger, D. and Yeh, G.S.Y. “Morphology of high-strength transparent polyethylene prepared under controlled conditions” *J. Appl. Phys.* (1972) **43**, 4339-4343.
70. Schwittay, C., Mours, M., and Winter, H.H. “Rheological expression of physical gelation in polymers” *Faraday Discuss.* (1995) **101**, 93-104.
71. Pogodina, N.V. and Winter, H.H. “Polypropylene crystallization as a physical gelation process” *Macromolecules* (1998) **31**, 8164-8172.

72. Pogodina, N.V., Siddiquee, S.K., Van Egmond, J.W., and Winter, H.H. “Correlation of rheology and light scattering in isotactic polypropylene during early stages of crystallization” *Macromolecules* (1999) **32**, 1167-1174.
73. Pogodina, N.V., Lavrenko, V.P., Srinivas, S., and Winter, H.H. “Rheology and structure of isotactic polypropylene near the gel point: Quiescent and shear-induced crystallization” *Polymer* (2001) **42**, 9031-9043.
74. Ferry, J.D. *Viscoelastic Properties of Polymers*, 3rd ed. (John Wiley & Sons, New York, 1980).
75. Hadinata, C., Gabriel, C., Ruellmann, M., Kao, N., and Laun, H.M. “Correlation between the gel time and quiescent/quasi-quiescent crystallization onset time of poly(butene-1) as determined from rheological methods” *Rheol. Acta* (2006) **45**, 631-639.
76. Akpalu, Y., Kielhorn, L., Hsiao, B.S., Stein, R.S., Russell, T.P., Van Egmond, J., and Muthukumar, M. “Structure development during crystallization of homogeneous copolymers of ethene and 1-octene: Time-resolved synchrotron X-ray and SALS measurements” *Macromolecules* (1999) **32**, 765-770.
77. Acierno, S. and Grizzuti, N. “Measurements of the rheological behavior of a crystallizing polymer by an "inverse quenching" technique” *J. Rheol.* (2003) **47**, 563-576.
78. Nobile, M.R., Bove, L., Somma, E., Kruszelnicka, I., and Sterzynski, T. “Rheological and structure investigation of shear-induced crystallization of isotactic polypropylene” *Polym. Eng. Sci.* (2005) **45**, 153-162.
79. Koscher, E. and Fulchiron, R. “Influence of shear on polypropylene crystallization: Morphology development and kinetics” *Polymer* (2002) **43**, 6931-6942.
80. Vleeshouwers, S. and Meijer, H.E.H. “A rheological study of shear induced crystallization” *Rheol. Acta* (1996) **35**, 391-399.
81. Carrot, C., Guillet, J., and Boutahar, K. “Rheological behavior of a semi-crystalline polymer during isothermal crystallization” *Rheol. Acta* (1993) **32**, 566-574.
82. Coppola, S., Balzano, L., Gioffredi, E., Maffettone, P.L., and Grizzuti, N. “Effects of the degree of undercooling on flow induced crystallization in polymer melts” *Polymer* (2004) **45**, 3249-3256.
83. Acierno, S., Coppola, S., and Grizzuti, N. “Effects of molecular weight distribution on the flow-enhanced crystallization of poly(1-butene)” *J. Rheol.* (2008) **52**, 551-566.
84. Ramamurthy, A.V. “Wall slip in viscous fluids and influence of materials of construction” *J. Rheol.* (1986) **30**, 337-357.

85. Hatzikiriakos, S.G. and Dealy, J.M. "Wall slip of molten high density polyethylene. I. Sliding plate rheometer studies" *J. Rheol.* (1991) **35**, 497-523.
86. Denn, M.M. "Extrusion instabilities and wall slip" *Annu. Rev. Fluid Mech.* (2001) **33**, 265-287.
87. Park, H.E., Lim, S.T., Smillo, F., Dealy, J.M., and Robertson, C.G. "Wall slip and spurt flow of polybutadiene" *J. Rheol.* (2008) **52**, 1201-1239.

Chapter 5: Shear-Induced Crystallization – High Shear Rates with Nucleating Agent

5.1 Introduction

Shear flow can accelerate crystallization and change morphology, and to some extent, so can a nucleating agent. When acting alone, each can shorten the induction time [1-4] and increase the number density of nuclei [3-6], but the mechanism by which these effects are achieved is quite different; flow induces nuclei from chains that have been distorted from their initial conformations, whereas nuclei activated by a nucleating agent, as a consequence of the reduction in the free-energy barrier to nucleation [7], come from chains undisturbed from their random-coil conformations at equilibrium. In the previous chapter, it was shown that compared to non-nucleated polypropylenes, the nucleated ones can readily crystallize under quiescent conditions at a temperature as much as 22 °C higher during constant cooling at 10 °C/min and in less than at least one tenth the time during isothermal crystallization at 155.5 °C.

Although the role and effects of nucleating agents have been well studied in the case of quiescent crystallization [7], this is not the case for shear-induced crystallization. What happens if nucleated polymers are subjected to high shear rates? After strong shear, will the nucleation pathway still be regulated by the nucleating agent? If not, what factors are at play? Also, how do the changes induced by flow in nucleated polymers differ from those in non-nucleated ones? The answer to the last question determines the extent to which our current knowledge of shear-induced crystallization, derived primarily from many studies of non-nucleated polymers (see reviews [8-12]), is readily applicable to the present work.

The above questions seem straightforward, but they remain largely open. At present, little is understood about the interplay between shear flow and nucleating agents in crystallization. Most often during polymer processing both factors are present at the same time [13, 14], and it is not clear how to separate their effects due to the complex thermal and flow histories in processing. Few studies [1, 15-22] have been conducted under well-defined conditions, and the findings are summarized in Table 5.1. It should be mentioned that shear-induced crystallization of nucleated polymers has been discussed recently, but less systematically than here, in a review by Kumaraswamy [11] and in a new book by Janeschitz-Kriegl [8]. Intriguingly, some of the findings in Table 5.1 are inconsistent. For example, in an early study, Lagasse and Maxwell [1] concluded that a nucleating agent has no effect on shear-induced crystallization, based on observations that induction times were similar for a pair of nucleated and non-nucleated polymers above a critical shear rate, under continuous shearing. Conversely, Jerschow and Janeschitz-Kriegl [15] reported that a nucleating agent is extremely effective in enhancing the formation of highly oriented structures in sheared samples. However, both groups overlooked the specific characteristics of the nucleating agent used when interpreting their results. Cumbersome as it may seem, it is only when properties of the nucleating agent, including melting temperature, concentration, shape, size, and dispersion, are considered together with the shearing conditions that the discrepancies among these studies can be explained.

What appears to account for most of the differences in Table 5.1 is the melting temperature of the nucleating agent, which determines whether it is melt-insensitive or melt-sensitive. In quiescent crystallization, a melt-insensitive agent acts simply as a single nucleation site, whereas the latter can self-assemble into a physical gel network of nanofibers (see Table 1.1). In shear-induced crystallization, it is the extent to which these two structurally dissimilar compounds, along with polymer chains, are oriented during flow that governs how much the ensuing crystallization process is changed relative to quiescent crystallization. For a melt-insensitive agent, the final crystalline orientation of a nucleated polymer containing talc has been shown [16] to be less than that of a non-nucleated one. In another study [17], the shape of the nucleating agent, as well as its concentration, was found to be important, where anisotropic particles (*e.g.*, elongated, platelet-like) was reported capable of inducing extra nuclei in the sheared samples. By contrast, interactions with flow are much stronger and more complicated for melt-sensitive agents made up of organogelator molecules, notably sorbitol derivatives. When sheared at certain temperatures, the nanofibrillar network structures of these molecules can be aligned parallel to the flow direction and template the development of highly oriented crystalline structures, notably shish-kebabs (*i.e.*, organogelator fibrils form shish on which polymer lamellae grow as kebabs) [18-21]. So in contrast to polymers containing melt-insensitive agents, the final morphology of those with melt-sensitive agents depends not only on shearing conditions but also on the organogelator phase separation behavior, as dictated by its concentration and the temperature at which flow is applied [18-21, 32]. In this study, the organophosphate salt added to the isotactic polypropylene samples is melt insensitive, thus making the analysis somewhat simpler. Accordingly, the discussion that follows is specific to melt-insensitive agents unless otherwise noted.

Intuitively it would seem difficult to observe the effect of flow on the crystallization of a nucleated polymer at low shear rates, as the sample itself already possesses a fair number of preferential nucleation sites. Particularly if the nucleating agent is extremely effective, the small effect of a weak shear can be masked. Useful data are therefore expected only at high shear rates. However, all the studies listed in Table 5.1 [1, 17-22], except for two [15, 16], involved shear rates well below 100 s^{-1}, while virtually all experiments that focused on strong shear used non-nucleated polymers [6, 33-37]. Even the two exceptions are lacking in some aspects. The shortcomings in the first study [15] include: non-uniform shearing in pressure flow, no quantitative data above wall shear rates of 51 s^{-1}, and inattention to the phase separation behavior of the melt-sensitive agent used. And the second study [16] did not use a homopolymer but a nucleated polymer blend with the matrix being a partially aromatic polyamide, which consists of semi-rigid chains that differ structurally from flexible-chain polymers. Clearly, the effect of a strong shear on the crystallization of nucleated polymers is far from well established; and this study is intended to fill this gap by providing data at shear rates up to 500 s^{-1}.

Table 5.1. Previous work on shear-induced crystallization of nucleated polymers*.

Polymers	Additives	Max $\dot{\gamma}_s$ /s^{-1}	Findings	Ref.
iPP EP	□ 0.003 % carbon black ⟐ Unspecified	4.2 ▼	⅄ iPP + CB: No effect on quiescent and SIC. ⅄ EP + unspecified agent: No effect on SIC kinetics above a critical shear rate (*i.e.*, same as non-nucleated EP).	[1]
iPP	⊙ 0.15 %, 0.2 % MDBS	132 ▲	★ MDBS enhances thickness of oriented morphology. ⅄ Crystallization characteristic time versus shearing time on log-log plot: slope = -1 or lower (nucleated, or new grade non-nucleated), -2 (degraded non-nucleated).	[15,23]
iPP	⭘ 0.05 % to 0.2 % HPN68L ⭘ 0.05 % to 0.2 % NA11UH ⭘ 0.1 % to 0.5 % talc	10 ▲	⅄ Shape of nucleating agent affects interaction with flow. ⅄ HPN68L (isotropic): No difference between quiescent and SIC kinetics due to high nucleation efficiency. ⅄ NA11UH (elongated) and talc (platelet-like): Interact with shear to create extra nuclei; concentration-dependent. ⅄ Flow is relevant only if its effect on nucleation is at least of same order of magnitude as that under quiescent.	[17]
iPP EP	⊙ 0.3 % to 20 % DBS	60 ▲	★ Oriented morphology in nucleated sample if sheared at some temperatures. DBS concentration affects orientation. ★ DBS fibrils aligned to flow direction and template growth of polymer lamellae.	[18,19]
iPP	⊙ 0.3 % to 1 % DMDBS	20 ▲	★ Similar findings as in [18, 19]. Oriented morphology if sheared at temperatures that DMDBS can phase separate to form percolated network of fibrils.	[20,21]
iPP	⭘ 0.05 % to 1 % β-phase NA	60 ▲	★ Low concentration: Increases β-iPP content with shearing up to a critical shear rate. ★ High concentration: Decreases β-iPP content with increasing shear rate.	[22]
PE	⭘ 3 % NA11	5 ▼	⅄ Negligible differences in nucleation rate and induction time between quiescent crystallization and SIC.	[24]
MXD6	⭘ 11 % PA 66 + 1 % talc	200 ▲	⅄ Non-nucleated MXD6 is more sensitive to shear with larger reduction in SIC time than MXD6 + PA66 + talc. ★ More orientation in non-nucleated than in nucleated sample.	[16]

⅄: kinetic changes ★: morphological changes □: foreign material ⟐: information not provided

⭘: melt-insensitive agent ⊙ : melt-sensitive agent ▼: continuous shearing ▲: short-term shearing

β-phase NA: nucleating agent made of lanthanum stearate and calcium carbonate; DBS: 1,3:2,4-dibenzylidenesorbitol; DMDBS: bis(3,4-dimethylbenzylidene)sorbitol; EP: ethylene-propylene copolymer; HPN68L: cis-endo-bicyclo[2,2,1] heptane 2,3-carboxylate disodium salt; iPP: isotactic polypropylene; MDBS: 1,3:2,4-bis(p-methyldibenzylidene) sorbitol; MXD6: poly(m-xylylene adipamide); NA11: sodium 2,2'-methylene-bis-(4,6-di-tert-butyl-phenyl)phosphate; NA11UH: ultrafine grade of NA11; PA 66: nylon 66; PE: polyethylene

* Excluded here are studies using complex experimental conditions (*e.g.*, injection molding, ill-defined history [13, 25, 26]) and fillers with nucleating capability but not used primarily as nucleating agents (*e.g.*, carbon nanotubes or nanofibers [27-29], colorants [30, 31]).

The central role of high molecular weight in shear-induced crystallization is well documented for non-nucleated polymers [1, 15, 38-43]. Presumably, the same should hold for nucleated ones, but not much has been done to verify this. Past studies often used only one polymer and tended to focus on such aspects as the presence or absence of a nucleating agent [1, 16, 17], and the variation in its concentration, shape or type [17-22]. The work of Jerschow and Janeschitz-Kriegl [15], already mentioned, is an exception, but they used a melt-sensitive agent and made no quantitative comparison. So the two nucleated isotactic polypropylenes studied here, which have the same type and amount of melt-insensitive agent as well as similar molecular weight distributions and tacticities, but distinctly different M_{w}, are well suited for confirming the above presumption. Included for comparison are two non-nucleated samples.

As in most recent studies, the short-term shearing protocol of Janeschitz-Kriegl *et al.* [33] was used in the present work. Under isothermal, low supercooling conditions, the sample was briefly sheared for a period several orders of magnitude shorter than the quiescent crystallization time. Following cessation of flow, crystallization kinetics was monitored simultaneously by light intensity and oscillatory shear measurements, which were shown in the previous chapter to be useful for understanding crystallization behavior under quasi-quiescent conditions. To complement the kinetic analysis, ex situ morphological characterization of the solidified samples was carried out by means of polarized optical microscopy. As will be shown, the results from this study not only help answer the questions put forth earlier but also address issues of direct relevance to industrial applications. For example, under what circumstances is a nucleating agent or shear flow most effective in accomplishing a desired crystallization behavior?

5.2 Characteristics of Nucleating Agent

The melt-insensitive nucleating agent used was sodium 2,2'-methylenebis(4,6-di-*tert*-butylphenyl)phosphate, identified by CAS number 85209-91-2, referred to hereafter as NA-11, its abbreviated trade name. With a melting temperature above 400 °C, NA-11 is an insoluble crystal in the polymer melt and has been shown to promote epitaxial crystallization of the α phase of isotactic polypropylene under quiescent conditions [44]. Previous studies [17, 45] have shown that this organophosphate salt is composed of anisotropic microparticles in a fairly broad distribution of aspect ratios, with most having an elongated shape. In the form of white powder, commercial-grade NA-11 particles have a typical size distribution as follows [46]: $d_{90} < 42\ \mu m$ (*i.e.*, 90% are less than $42\ \mu m$), $d_{50} < 16\ \mu m$, and $d_{10} < 5\ \mu m$.

In addition to size and shape, two other factors that may affect NA-11 particle-particle and particle-polymer interactions in shear-induced crystallization are concentration and dispersion. For the two nucleated samples studied, a mass fraction of NA-11 at 0.08 % was compounded with other stabilizers by the resin manufacturer (see Table 2.1), and this very low concentration has negligible influence on rheological properties. The dispersion of NA-11 in the polymer matrix was found to be macroscopically uniform, as is shown later by photographs of bulk samples crystallized under quasi-quiescent conditions.

5.3 Experimental Details

Details of the experimental materials and methodology can be found in Chapter 2. For ex situ morphological analysis, samples removed from the sliding plate rheometer at the end of an experiment (i.e., after solidification in cool air immediately following the detection of a fall in the stress amplitude in oscillatory shear measurement at the late stages of crystallization) were cut parallel to the flow direction into specimens with a thickness of about 5 μm by means of an ultra-microtome (Reichert UltraCut S, Leica Microsystems, Wetzlar, Germany) using a glass knife at room temperature. The specimens were examined under an optical microscope (BX50, Olympus, Center Valley, PA) between crossed polarizers equipped with a video camera (DXC-950/1, Sony, Tokyo, Japan) at a magnification of 20X. Images were captured and saved using Linksys 32 software (version 2.27, Linkam Scientific Instruments, Surrey, UK). To allow comparison of sample uniformity, photographs of bulk samples were taken using a digital camera.

5.4 Results and Discussion

5.4.1 Shear-Induced Crystallization versus Quasi-Quiescent Crystallization

To evaluate the effect of high shear rate on crystallization kinetics, data obtained after applying a shear rate $\dot{\gamma}_\mathrm{s}$ of 494 s^{-1} and a strain γ_s of 20 (i.e., a shearing time t_s of 0.04 s) are compared to those obtained under quasi-quiescent conditions. As explained in the previous chapter, light intensity and oscillatory shear measurements provide complementary information about early and late crystallization kinetics. In Figs. 5.1 and 5.2, the top plot provides information about the early kinetics, as given by the monotonically decreasing section of the time evolution of the normalized light intensity $I(t)/I(0)$, whereas the bottom plot shows the late kinetics, as given by the upturn in the time evolution of the normalized magnitude of the complex viscosity[*] $|\eta^*|(t)/|\eta^*|_{\mathrm{q0}}$. The latter quantity was obtained by normalization to the magnitude of the complex viscosity at the start of the quasi-quiescent crystallization experiment, denoted as $|\eta^*|_{\mathrm{q0}}$. Not included here is the subsequent rise in $I(t)/I(0)$, as it is irrelevant for early kinetic analysis. And owing to complications associated with nonlinear viscoelasticity and slip (see Section 4.4.3) not all of the $|\eta^*|(t)/|\eta^*|_{\mathrm{q0}}$ data are shown, but those provided are adequate for late kinetic analysis. The induction time t_{ind} is that at which $I(t)/I(0)$ drops to 97 %, and this characteristic time indicates when growth of the nascent crystalline structures following nucleation is first detectable (based on the incident laser intensity). Note that close to t_{ind}, $|\eta^*|(t)/|\eta^*|_{\mathrm{q0}}$ is about 1.005 – 1.03.

---

[*] Storage modulus can also be used, but the results are comparable to those presented here. This is because large changes in the loss angle, which partly contribute to the changes in the storage modulus according to $G' = (\sigma_0/\gamma_0)\cos\delta$, only occur at much later times (see Figs. 4.5c).

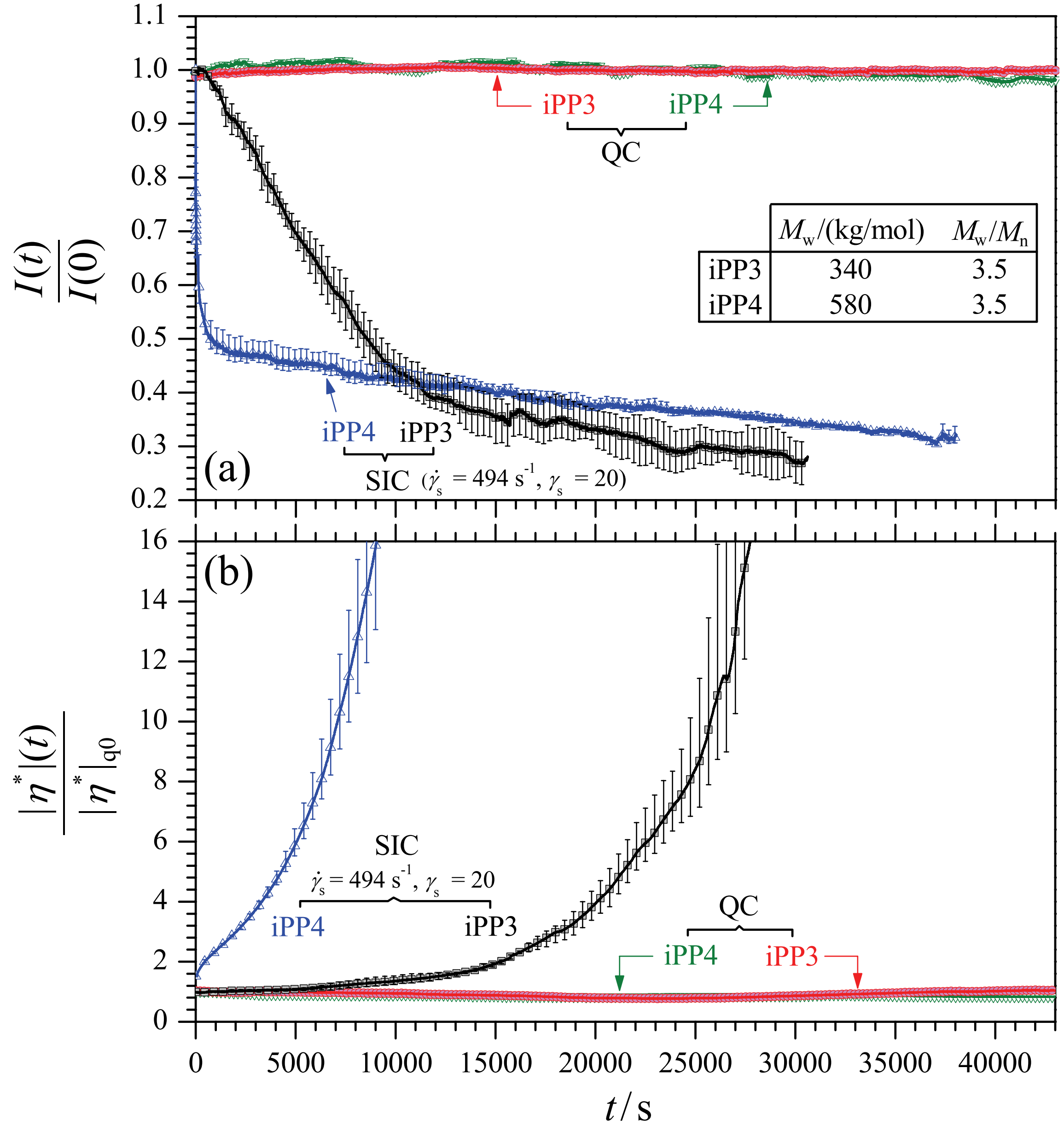

Figure 5.1. Comparison of shear-induced crystallization (SIC) and quasi-quiescent crystallization (QC) for non-nucleated samples iPP3 and iPP4 at different stages: (a) early kinetics in terms of normalized light intensity, and (b) late kinetics in terms of normalized magnitude of complex viscosity. The absence of measurable changes in both measurements suggests neither iPP3 nor iPP4 crystallizes in 12 h under quasi-quiescent conditions. A very brief flow at a shear rate of 494 s^{-1} and a strain of 20 readily induces crystallization. Data shown are averages and ranges for three measurements at 155.5 °C.

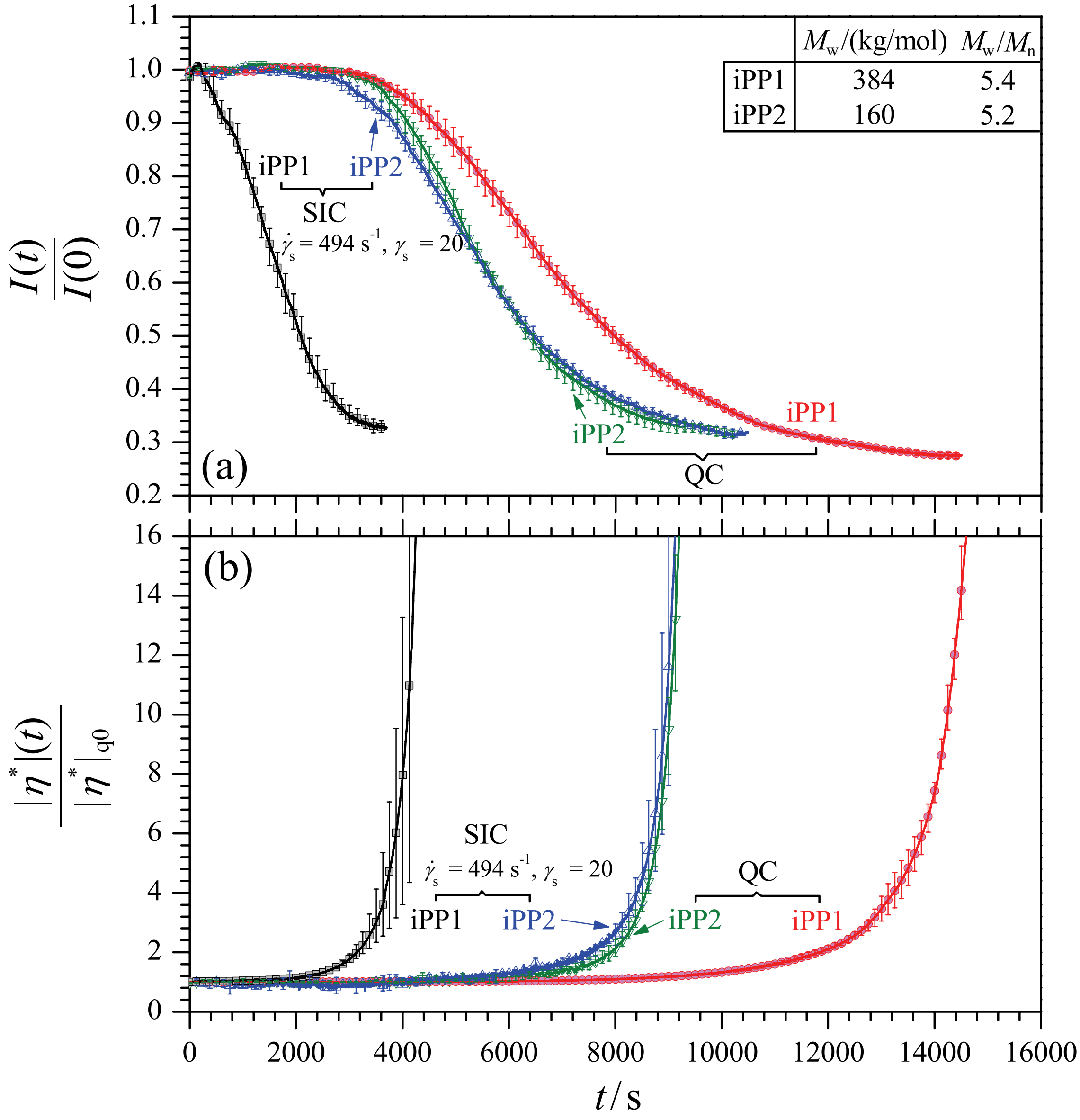

Figure 5.2. Comparison of shear-induced crystallization (SIC) and quasi-quiescent crystallization (QC) for nucleated samples iPP1 and iPP2 at different stages: (a) early kinetics in terms of normalized light intensity, and (b) late kinetics in terms of normalized magnitude of complex viscosity. Crystallization of iPP1 after being sheared at a shear rate of 494 s^{-1} and a strain of 20 is significantly accelerated compared to that under quasi-quiescent conditions, whereas iPP2 indicates only marginal differences between SIC and QC. Data shown are averages and ranges for three measurements at 155.5 °C.

5.4.1.1 Non-Nucleated Samples

As indicated by the absence of measurable changes in $I(t)/I(0)$ and $|\eta^*|(t)/|\eta^*|_{q0}$ in Figs. 5.1a and b, neither iPP3 nor iPP4 crystallizes under quasi-quiescent conditions during a 12-hour experiment. Crystallization is inhibited in these non-nucleated polymers because of the high free-energy barrier to nucleation at 155.5 °C, which is only 4.6 °C and 6.9 °C below the nominal melting temperatures of iPP3 and iPP4 respectively (or a supercooling of 56.5 °C, based on an equilibrium melting temperature of 212 °C [47]).

However, application of a very brief deformation at a high shear rate of 494 s-1 readily induces crystallization; the sheared iPP3 shows a very short t_{ind} of about 980 s (Fig. 5.1a), while iPP4 appears to crystallize instantaneously during flow with $t_{\text{ind}} < 0.1$ s, followed by both an abrupt drop in $I(t)/I(0)$, *i.e.*, to 60 % within 150 s (Fig. 5.1a), and a rapid rise in $|\eta^*|(t)/|\eta^*|_{q0}$, *i.e.*, by 200 % within 450 s (Fig. 5.1b). Relative to quasi-quiescent conditions, these results represent an acceleration in crystallization by at least two orders of magnitude for iPP3 (*i.e.*, 980 s relative to > 12 h) and by at least five orders of magnitude for iPP4 (*i.e.*, < 0.1 s relative to > 12 h).

That this enormous enhancement in crystallization kinetics was achieved by flow lasting only 0.04 s has significant implications. It underlines the effectiveness of the high shear rate in initiating a crystallization, which would otherwise be negligible under this low supercooling condition. And equally importantly it highlights the importance of including this big effect in a realistic model of industrial processes involving a strong flow field. The strong response observed here would not occur at the same shearing time using a conventional low-shear rate device. Few groups [1, 33, 34, 37] have made use of custom-built instruments that can apply high shear rates or stresses to produce similar results, and owing to instrumental limitations, most had to resort to much longer shearing time or continuous shearing. An early work of Haas and Maxwell [48] and a recent study of Baert *et al.* [36] reported interesting results using a shearing time of comparable magnitude to the one applied here, but the dependence of crystallization time on molecular weight is conflicting between the two reports, where a shorter time was found to correlate with a lower molecular weight in the first work [48] as opposed to the opposite relationship in the second study [36]. The latter correlation is the norm, and is addressed later.

5.4.1.2 Nucleated Samples

As in the case of non-nucleated samples, after shearing under the same conditions, crystallization of iPP1 is markedly changed, as reflected by the sheared sample having comparable values of $I(t)/I(0)$ and $|\eta^*|(t)/|\eta^*|_{q0}$ at shorter times than those exhibited in quasi-quiescent experiment (Figs. 5.2a and b). However, if the effect of flow on crystallization kinetics is evaluated on the basis of how much t_{ind} is reduced after shearing relative to quasi-quiescent conditions, it is evident that the nucleated sample iPP1 exhibits significantly less enhancement of kinetics than the two non-nucleated samples iPP3 and iPP4, as can be seen by the reduction of only one order of magnitude in t_{ind} for iPP1, *i.e.*, from 3800 s to 350 s (Fig. 5.2a), compared to that of several orders of magnitude for the latter two samples. Thus, in relative terms, the nucleating agent appears to decrease the effectiveness of shear (or the sensitivity to flow [16]) in enhancing crystallization kinetics. However, it is important to note that its presence does not limit the t_{ind} of the sheared sample to 350 s. As will be explained later in Section 5.4.2, the limiting factor is molecular weight.

Concurrent with the reduction in induction time, the number of nuclei in iPP1 is increased by shearing, as can be seen in the polarized optical micrographs of the solidified samples in Figs. 5.3c and a, wherein there are significantly more spherulites, which correspond to a markedly higher number density of nuclei in the sheared sample than in the quasi-quiescent sample. As expected, the size of the spherulites decreases in tandem with the increase in nucleation density, as illustrated by the sheared sample (Fig.

5.3c) having spherulites at least one order of magnitude smaller than those in the quasi-quiescent sample (about 50 μm, Fig. 5.3a). Despite displaying some differences from typical descriptions [49, 50], *viz.*, disks or polygonal shapes with lamellae or fibrils splaying from central nuclei, the fine spherulites with highly irregular shapes observed here resemble closely those described as densely packed textures in the literature [8, 51]. Previously, Janeschitz-Kriegl *et al.* [6] made use of optical micrographs to count the number of spherulites per unit surface, and then converted this quantity to the number of nuclei per unit volume. This technique appears to yield a reasonable estimate only when the nucleation density is low, *i.e.*, when the spherulites are not too crowded and their boundaries can be clearly delineated, but it is not possible to do this objectively from the micrographs in Figs. 5.3a and c in view of the densely packed textures. Nonetheless, these figures show that the number density of nuclei is certainly at least one order of magnitude greater in the sheared sample than in the quasi-quiescent one.

In contrast to the behavior of iPP1, the results for both shear-induced and quasi-quiescent crystallizations appear to be indistinguishable for iPP2, except for marginally faster kinetics in the former at very early times (Figs. 5.2a and b). The slightly shorter induction time in the sheared sample, *viz.*, a difference of about 500 s, however, does not lead to a steeper drop in $I(t)/I(0)$; instead, the sheared and quasi-quiescent samples display similar kinetics at later times. Again, compared to iPP1, the difference in the morphology between the sheared and quasi-quiescent samples for iPP2 was much less obvious, except that a slightly higher proportion of smaller spherulites were found in the sheared sample (Fig. 5.3d) than in the quasi-quiescent one (Fig. 5.3b). The disparate results in both the induction time and the spherulitic morphology between the two polymers can be attributed to the substantially lower molecular weight of iPP2 (M_w = 160 kg/mol compared to 384 kg/mol for iPP1). To yield crystallization behavior comparable to that of iPP1, a much higher shear rate is needed to effectively deform the shorter chains in iPP2. However, shear rates above 500 s^{-1} are inaccessible with the current experimental setup. These results lead to the following important conclusions: first, shear-induced crystallization is irrelevant or much less important for nucleated polymers of low molecular weight; and second, nucleating agents are more effective than flow to enhance crystallization kinetics and decrease the size of spherulites in low-molecular weight polymers.

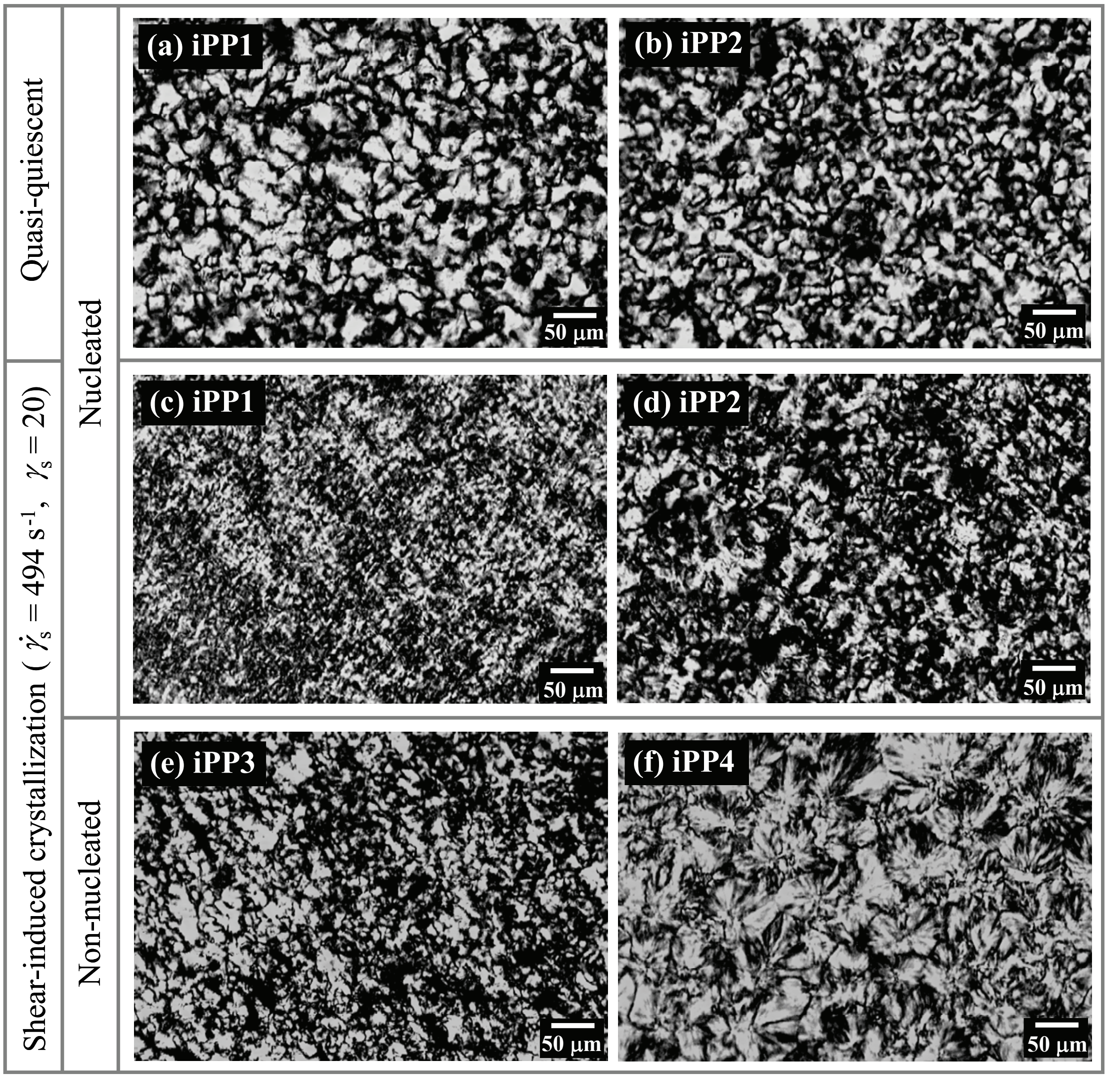

Figure 5.3. Cross-polarized optical micrographs of crystallized samples at 155.5 °C, after quasi-quiescent crystallization for (a) iPP1, (b) iPP2, and after shear-induced crystallization at a shear rate of 494 s^{-1} and a strain of 20 for (c) iPP1, (d) iPP2, (e) iPP3, and (f) iPP4.

5.4.2 Effect of Molecular Weight

To demonstrate the effect of molecular weight on shear-induced crystallization, a comparison of the data for nucleated and non-nucleated samples following shearing at $\dot{\gamma}_\mathrm{s}$ = 494 s^{-1} and γ_s = 20 is shown in Fig. 5.4. Arranged in increasing order of t_ind, the sequence in which evolving crystalline structures first appear in the sheared samples is as follows: iPP4, iPP1, iPP3, and iPP2. This sequence correlates well with the decreasing order of M_w for the four samples: iPP4 > iPP1 > iPP3 > iPP2. Unsurprisingly, this is consistent with the general notion from studies of non-nucleated polymers that shear-induced crystallization kinetics is positively correlated with molecular weight. Yet what is enlightening, and not mentioned in the literature, is that the correlation appears to hold even for comparisons involving nucleated and non-nucleated polymers, despite an apparent advantage of the former in having a fair quantity of preferential sites that are readily available for nucleation. In addition, the sensitivity of t_ind to M_w is extremely high, as shown in the inset of Fig. 5.4a, where an increase in M_w by a factor of only 3.6, *viz.*, from 160 kg/mol to 580 kg/mol, reduces t_ind by more than four orders of magnitude. It is also clear from the inset that the dependence of t_ind on M_w is particularly strong at large values of M_w, and much less so at small values of M_w.

On the basis of the above results, it is postulated that molecular weight is the dominant factor controlling nucleation kinetics after application of a high shear rate – so much so that even the normally strong influence of nucleating agent becomes vanishingly small. As a corollary, for a given polymer, the addition of nucleating agent should not change the induction time provided sufficiently strong shear is applied. This agrees well with the conclusion reached by Lagasse and Maxwell [1], despite several shortcomings in their study, *e.g.*, unspecified nucleating agent, continuous shear, and narrow data range. Indeed, it is surprising that their conclusion is in line with those of the present work, considering that fairly low shear rates ($\leq$ 4.2 s^{-1}) were used in their study, in sharp contrast to the strong emphasis on high shear rates in the present work. A likely explanation is that the effect of the nucleating agent itself was not that strong in their study, as evidenced by the reported small difference in the induction times (only 14 s, Fig. 14 in [1]) between the nucleated and non-nucleated polymers under quiescent crystallization. As a result, the effect of even a modest shear rate was adequate to override the relatively weak influence of the nucleating agent.

It is clear that both nucleating agent and molecular weight act to shorten the induction time in shear-induced crystallization, and an important question is whether these effects are additive at high shear rates. To answer this question, the data for shear-induced and quasi-quiescent crystallizations of iPP1 and iPP3 were compared. First, based on the data for iPP1 in Fig. 5.2a, if the sum of the two effects is simply additive, the latter effect alone should cause only a small decrease of 3450 s in t_{ind}, *viz.*, after the deduction of t_{ind} = 350 s in shear-induced crystallization from t_{ind} = 3800 s in quasi-quiescent condition (due exclusively to nucleating agent). Second, based on the data for iPP3 in Fig. 5.1a, the decrease in t_{ind} by 42 200 s, *viz.*, from quasi-quiescent crystallization (>12 h) to shear-induced crystallization (980 s), is clearly attributable solely to the effect of shear; and this implies that the effect of shear alone on iPP1 would contribute to a reduction of at least 42 200 s in t_{ind}, in view of the fact that iPP1 has a larger M_{w} and thus a larger effect on t_{ind} after being sheared compared to that of iPP3. Obviously, this time ($>$ 42 200 s) is at odds with that inferred from the first observation of 3450 s. Therefore, these observations imply that the interaction between nucleating agent and flow is not additive, and that molecular weight is most likely the limiting factor for the observed t_{ind} in shear-induced crystallization of iPP1 at high shear rates.

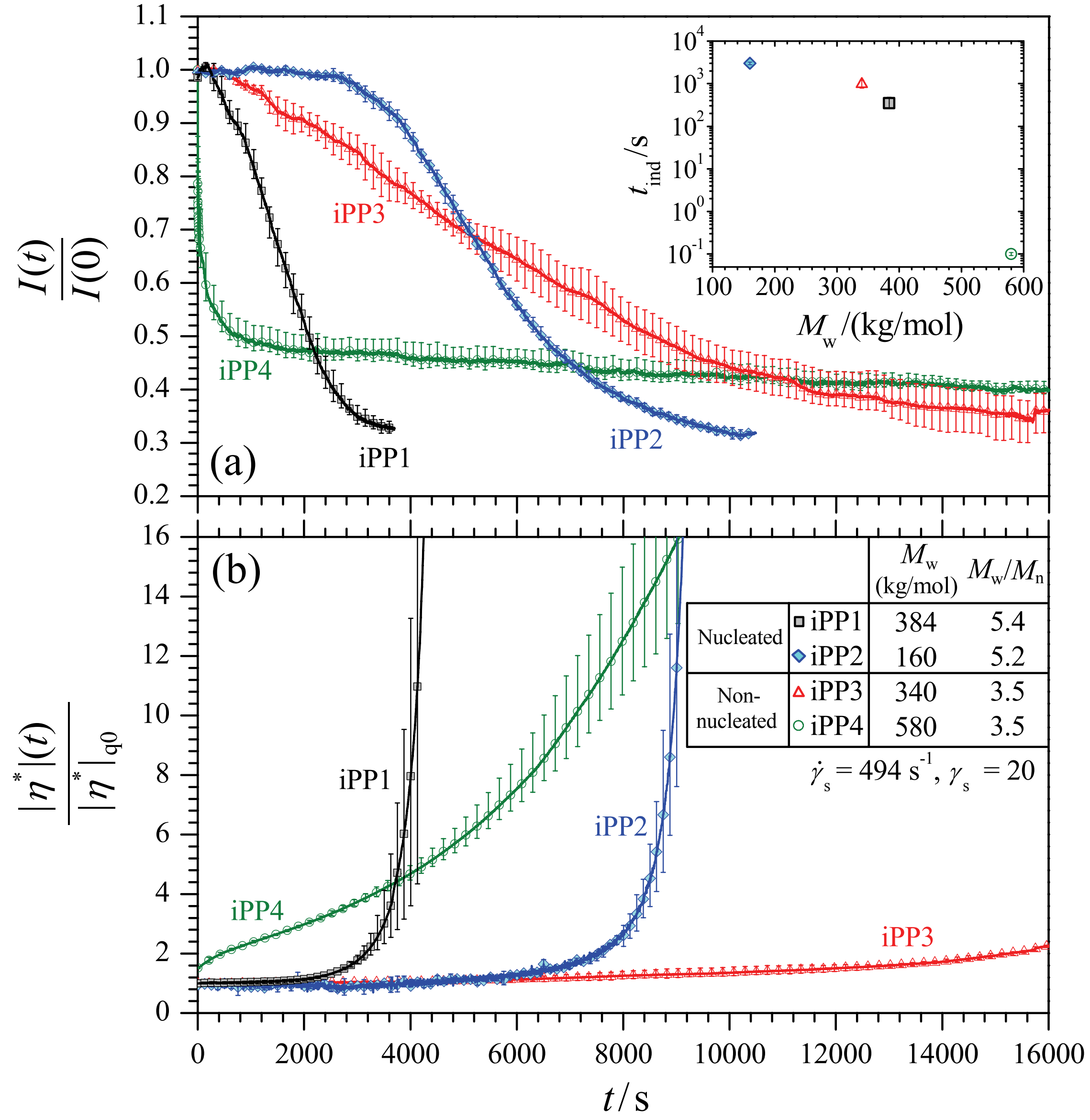

Figure 5.4. Comparison of nucleated (iPP1 and iPP2) and non-nucleated samples (iPP3 and iPP4) after being sheared at a shear rate of 494 s^{-1} and a strain of 20, as indicated by: (a) early kinetics in terms of normalized light intensity, and (b) late kinetics in terms of normalized magnitude of complex viscosity. At this high shear rate, the early kinetics is strongly correlated to the molecular weight, irrespective of the presence of a nucleating agent. The growth kinetics at later times is only modestly affected by flow, and is thus less dependent on molecular weight, and it follows closely the intrinsic kinetics shown in quiescent crystallization. The inset in (a) shows the strong dependence of induction time on the weight-average molecular weight. Data shown are averages and ranges for three measurements at 155.5 °C.

It was mentioned earlier that the number of nuclei is closely correlated to t_{ind} for the nucleated samples, and since t_{ind} decreases with increasing M_{w} (inset in Fig. 5.4a), it is probable that the nucleation density in the sheared samples is also governed by M_{w}. And consistent with this speculation, the optical micrographs of the sheared samples of iPP2, iPP3, and iPP1 (Figs. 5.3d, e, and c) show an increase in the number of spherulites (*i.e.*, number of nuclei) or a decrease in spherulite size with increasing M_{w}. The exception is iPP4, which has the largest M_{w}; rather than showing very fine spherulites, the micrograph of this polymer (Fig. 5.3f) indicates structures that are surprisingly different and much bigger than those of the other three samples (Figs. 5.3c, d, and e). Also dissimilar is its crystallization kinetics, which indicates that crystallization is initiated during shearing (Fig. 5.1a). Shearing a crystallizing polymer can result in the formation of threadlike structures. It has been shown in a previous study (see the crystal growth images obtained by *in situ* optical microscopy in Fig. 3 of [52]) that the growth of very large spherulites subsequent to the emergence of threadlike structures can obscure a direct correlation between the final morphology shown in an optical micrograph and the actual nucleation density. This means that the nucleation density cannot be inferred directly from the micrograph of the solidified sample iPP4 after a long crystallization time. As for the other three samples which do not contain any threadlike structures, the nucleation density inferred from spherulitic textures shown in Figs. 5.3d, e, and c is positively correlated with M_{w}, regardless of whether the polymers were nucleated or not.

In contrast to shear-induced crystallization, a poor correlation is found for quasi-quiescent crystallization of the four samples between M_{w} (decreasing order: iPP4 > iPP1 > iPP3 > iPP2) and t_{ind} (increasing order: iPP2 ~ iPP1 >> iPP3 ~ iPP4); this is somewhat expected, since the two non-nucleated polymers do not crystallize. The big difference in the dependence of t_{ind} on M_{w} between shear-induced and quasi-quiescent crystallizations implies that the primary factor regulating the nucleation pathway for the two phenomena is clearly not the same. Acierno *et al.* [41] reported similar findings for four non-nucleated poly(1-butene) samples having M_{w} in the range of 116 kg/mol to 398 kg/mol. They found that crystallization kinetics is independent of M_{w} in quiescent conditions but increases considerably with M_{w} . The present findings support the conclusion of Kumaraswamy *et al.* [10, 53] regarding the role of flow in opening a non-classical kinetic pathway to nucleation. Their conclusion was based on observations that the kinetics for the formation of shear-induced threadlike precursors is positively correlated with temperature, as opposed to the classical behavior in quiescent crystallization (*i.e.*, crystallization kinetics decreases as temperature increases). It should be mentioned that the same intriguing temperature dependence was reported much earlier by Haas and Maxwell [48] in continuous shearing experiments. Although the variables used are different, *i.e.*, M_{w} in the present study versus temperature in the work of Kumaraswamy *et al.* [10, 53], the conclusions that the nucleation pathway is altered after the application of a strong shear remain essentially the same.

The main caveat of the present analysis is that the comparison was made at a shear rate of 494 s^{-1} and a strain of 20; and under these conditions, the effect of molecular weight on crystallization kinetics outweighs that of nucleating agent. Obviously, at low shear rates the latter effect might prevail, which could lead to an outcome that is more similar to that observed in quiescent crystallization. This is likely to happen when the concentration of the nucleating agent is high; it has been shown in a recent study [17] that a small increase in the concentration of ultra-fine NA-11 from 0.05 % to 0.2 % can effectively reduce crystallization time by more than one order of magnitude under quiescent conditions and by nearly four-fold after shearing at a low shear rate (10 s^{-1}). Hence, if either the shearing conditions are weak or the nucleating agent is very effective, nucleation may not be controlled by molecular weight; and such cases are evident in studies [16, 17] that found that crystallization kinetics after shearing of a nucleated polymer was faster than that of a non-nucleated one.

The present analysis also relies on the premise that an appropriate characteristic time was used to make the comparison. Here, t_{ind} , which reflects the very early stage of crystallization, was chosen, and the outcome would be different if it were replaced by a later time, for example, the time corresponding to a 50 % drop in $I(t)/I(0)$, which is commonly used in the literature for kinetic analysis [34, 36, 54]. The rationale for selecting the characteristic time used here will become clear later.

Up to now, the discussion has been focused on the early kinetics. An accelerated nucleation with a shorter t_{ind} invariably enhances the overall crystallization rate, which, however, can be attenuated by sluggish growth. This is illustrated by the data at later times, *e.g.*, t > 9000 s, in Figs. 5.4a and b; despite having the shortest t_{ind}, iPP4 shows markedly slower late kinetics, *i.e.*, a much longer time for the decay of to a minimum and a more gradual upturn in $|\eta^*|(t)/|\eta^*|_{\mathrm{q0}}$, compared to the two nucleated samples iPP1 and iPP2, which both lag in t_{ind} but outpace iPP4 at later times owing to rapid growth. In other words, what slows down the overall kinetics in shear-induced crystallization of iPP4 in comparison to the nucleated samples seems to be its growth and not nucleation, and this is completely opposite to its quiescent crystallization behavior where the rate-limiting step is nucleation. Exhibiting similar behavior is the other non-nucleated sample, iPP3, as evidenced by its extremely sluggish overall kinetics (Fig. 5.4b), despite indicating a much shorter t_{ind} than that of iPP2 (Fig. 5.4a). As mentioned in the previous chapter, neither $I(t)/I(0)$ nor $|\eta^*|(t)/|\eta^*|_{\mathrm{q0}}$ can be converted directly into time evolution of crystallinity or overall growth rate; nonetheless, the slope of $|\eta^*|(t)/|\eta^*|_{\mathrm{q0}}$ at later times in Figs. 5.4b and 5.1b can serve as a relative measure of growth kinetics for qualitative comparisons. Evaluated at an arbitrarily chosen value of $|\eta^*|(t)/|\eta^*|_{\mathrm{q0}} \geq 3$, the slopes for the four samples follow this order: iPP1 ~ iPP2 > iPP4 > iPP3; and this is very different from the sequence mentioned earlier for M_{w} and t_{ind}.

Table 5.2. Correlation between molecular weight and crystallization kinetics.

Phenomenon	Parameter	Sequence
	M_w	Decreasing: iPP4 > iPP1 > iPP3 > iPP2
Early kinetics (Shear-induced crystallization)	t_{ind}	Increasing: iPP4 < iPP1 < iPP3 < iPP2
Growth kinetics (Shear-induced crystallization)	Slope of $\mid \eta^* \mid (t) / \mid \eta^* \mid_{q0}$ at $\mid \eta^* \mid (t) / \mid \eta^* \mid_{q0} \geq 3$	Decreasing: iPP1 ~ iPP2 > iPP4 > iPP3
Early kinetics (Quasi-quiescent crystallization)	t_{ind}	Increasing: iPP2 ~ iPP1 >> iPP3 ~ iPP4

It is clear from the above results that molecular weight is no longer the determining factor during the late stage in shear-induced crystallization, namely the growth process. Instead, the sequence of the growth kinetics appears to correlate well with the quiescent crystallization results presented in the previous chapter (DSC data, Fig. 4.2), with overall crystallization rates much steeper for nucleated than for the non-nucleated samples. Collectively, the results, as summarized in Table 5.2, can be interpreted as follows: (i) the influence of a brief, strong shear flow on overall crystallization kinetics is primarily in inducing nucleation, and this effect is manifested most strongly in high-molecular weight polymers and is independent of the presence of a nucleating agent; and (ii) the subsequent growth of crystalline structures is only modestly affected by flow and thus less dependent on the molecular weight. As a result, it follows closely the intrinsic kinetics observed under quiescent conditions. Again it is important to note that the applied shear must be sufficiently strong for the above points to be valid; otherwise, the nucleation and growth kinetics are both controlled by the nucleating agent.

As there is a dearth of information about the effect of molecular weight for nucleated polymers, a comparison with literature can only be made with work on non-nucleated polymers, and good qualitative agreement is found, with the preponderance of data [1, 2, 36, 39, 41, 42, 55-58] showing that the effect of flow on crystallization kinetics, particularly nucleation, is more pronounced with a non-nucleated sample having a higher M_w than with one having a lower M_w. However, there is less consistency in the literature [2, 4, 5, 38, 59-62] with regard to the importance of shear or M_w in growth kinetics, and the results of the present study are in favor of those [2, 5, 62] that found the effect was modest or insignificant.

Admittedly, polydisperse samples are not ideal for evaluating the effect of molecular weight, but the analysis based on M_w seems to work reasonably well here, as well as in the wealth of studies just mentioned of non-nucleated polymers. The general applicability of M_w may be due to the small difference in polydispersity and tacticity as well as the absence of very long chains in the samples studied. A pertinent question is whether only a few very long chains, which might not be detected by gel permeation chromatography, would affect the present analysis. Seki *et al.* [40] have shown that their presence, even at a concentration of less than 1 % in specially prepared bidisperse blends having a component with M_w of about five times of that of the other, can strongly induce highly oriented structures via the formation of threadlike precursors. The importance of these chains, which normally act cooperatively with neighboring short chains [63], however, appears to be relevant only in the formation of a highly oriented morphology, as the authors [40] also stressed that there is little connection between their concentration and the increase in the number of point-like nuclei, which would subsequently grow into spherulites. In this light, the role of very long chains, very small in number if present at all, is deemed minimal in the present analysis, because all the sheared samples, except for iPP4 which possibly contains some threadlike structures, have been shown to be morphologically affected only in terms of an increase in the density of the point-like nuclei (Fig. 5.3). Hence, despite being an average parameter, M_w remains a practical indicator of how a given polymer, whether nucleated or not, would behave in comparison with others of similar polydispersity and tacticity in terms of nucleation kinetics after being sheared, especially when the principal effect is only associated with the increase in the number of point-like nuclei.

The discussion so far has omitted the subjects of chain orientation and relaxation time, which are intimately linked to molecular weight. How these are connected to shear-induced crystallization is addressed in the subsequent chapter.

5.4.3 Effects of Shear Rate and Strain

Figure 5.5 shows $I(t)/I(0)$ and $|\eta^*|(t)/|\eta^*|_{q0}$ for iPP1 following shearing at various shear rates $\dot{\gamma}_\mathrm{s}$ with a constant strain of 20, whereas the data following various strains γ_s at a constant shear rate of 200 s^{-1} are shown in Fig. 5.6. To reach the desired γ_s at a given $\dot{\gamma}_\mathrm{s}$, the shearing time t_s was varied ($t_\mathrm{s} = \gamma_\mathrm{s} / \dot{\gamma}_\mathrm{s}$). Also included for comparison are quasi-quiescent crystallization data.

These figures show three important features. First, and also most widely reported, when either shear rate or strain is increased, faster crystallization is observed, *i.e.*, comparable changes in $I(t)/I(0)$ and $|\eta^*|(t)/|\eta^*|_{q0}$ occur at shorter times. This effect is especially pronounced in the induction time, and the relationship between acceleration in kinetics and shear rate or strain is highly nonlinear.

The other two more interesting features are depicted more clearly by the $I(t)/I(0)$ data in Fig. 5.6a. First, the data shown suggest saturation in crystallization kinetics as strain is increased towards 30, *i.e.*, $I(t)/I(0)$ at this nominal strain is only marginally shifted to shorter times from that at a smaller strain of 20. This implies that the number of nuclei is no longer effectively enhanced by increasing the strain at the applied shear rate of 200 s^{-1}. Note that 30 is the nominal strain as the actual strain is less than the command value due to slip (see Section 3.5.6).

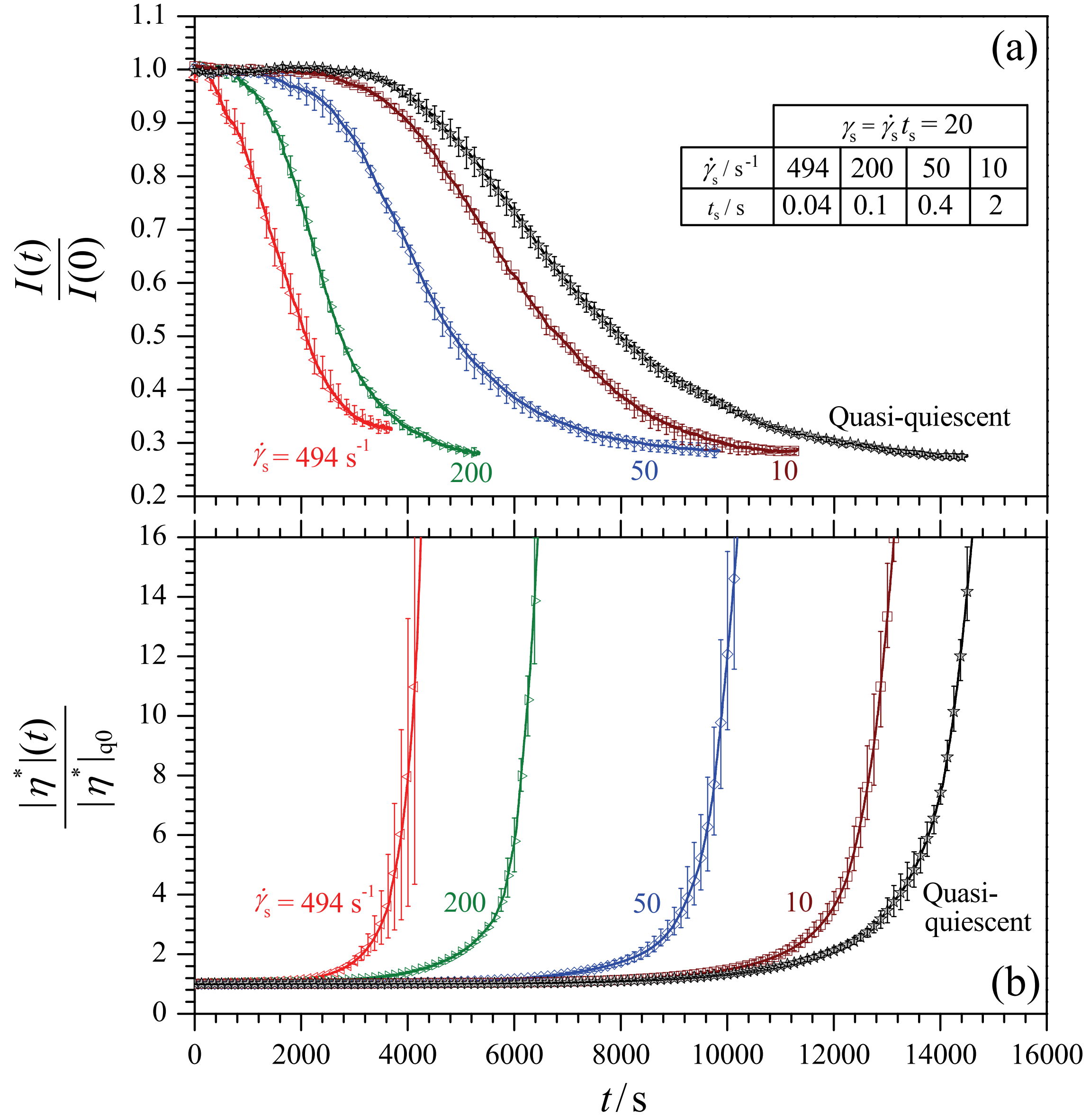

Figure 5.5. Effect of shear rate on crystallization of nucleated sample iPP1 after being sheared at a constant strain of 20, as indicated by: (a) early kinetics in terms of normalized light intensity, and (b) late kinetics in terms of normalized magnitude of complex viscosity. Crystallization time shortens as shear rate increases. Data shown are average and range of three measurements at 155.5 °C.

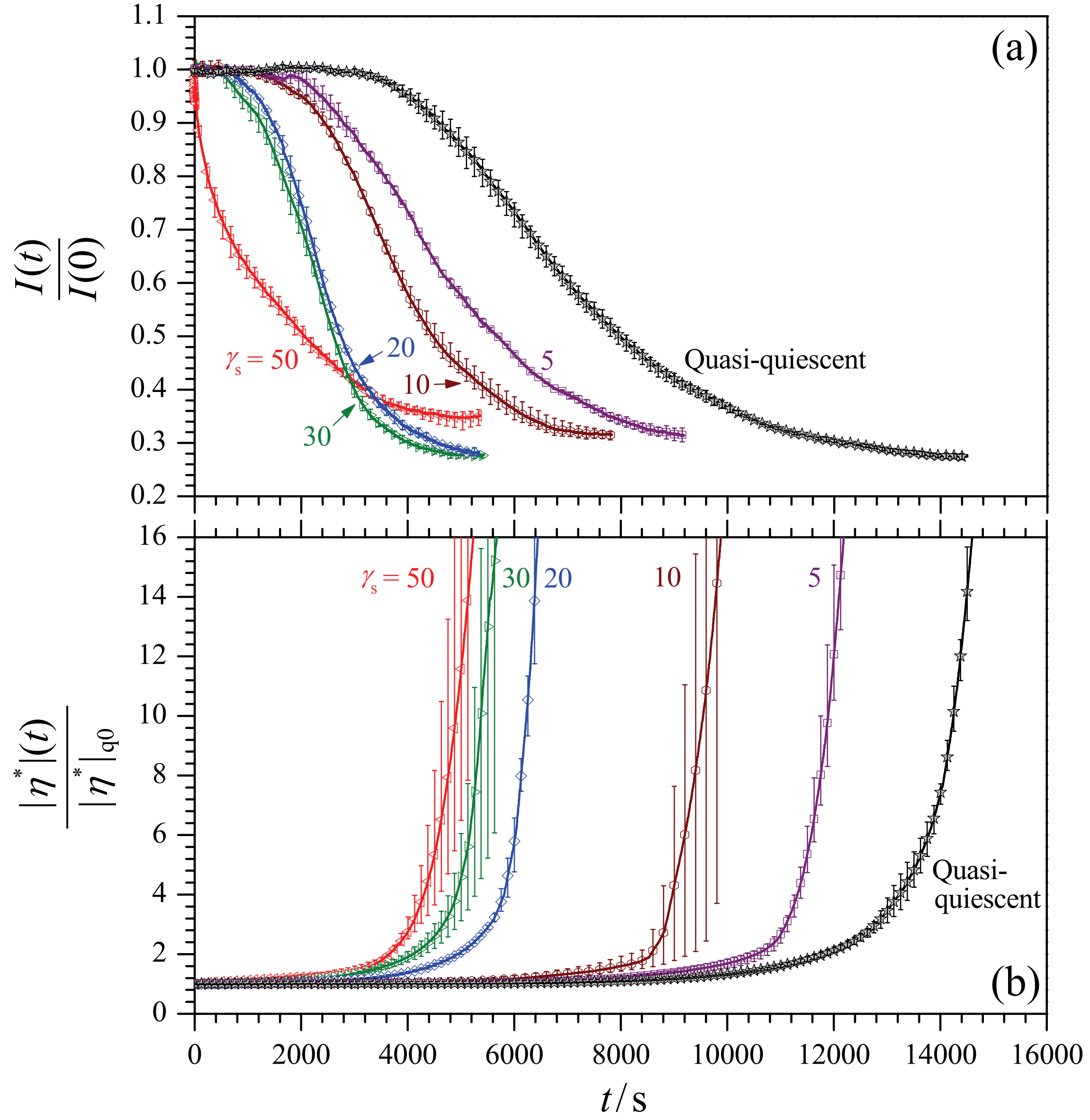

Figure 5.6. Effect of shear strain on crystallization of nucleated sample iPP1 after being sheared at a constant shear rate of 200 s^{-1}, as indicated by: (a) early kinetics in terms of normalized light intensity, and (b) late kinetics in terms of normalized magnitude of complex viscosity. Three important features are observed at different strains: an increase in crystallization kinetics with increasing strain, a saturation behavior, and the onset of a morphological transition (see text for details). Data shown are averages and ranges for three measurements at 155.5 °C.

There are two possible causes of saturation behavior. First, as a result of slip, the sample is not subjected to the command strain, which results in the chains being less distorted. This leads to an apparent saturation in kinetics, since distorted chains are responsible for accelerating crystallization. The second possibility is that distorted and incompletely relaxed chains, which are essential ingredients for inducing nuclei and which consist mostly of high-molecular weight chains (*i.e.*, on the right of the molecular weight distribution in Fig. 2.1) are available only in finite quantity; it is obvious that any further addition of nuclei would be restrained once these chains are completely consumed. The currently available information, however, is insufficient to ascertain which of these two causes plays the dominant role.

The third and most interesting feature in Fig. 5.6a is the $I(t)/I(0)$ data at a nominal strain of 50, which reveals clear departures from saturation behavior. More specifically, we see a much shorter induction time and a steeper initial fall, followed by a comparatively smaller slope, than at a strain of 30. The drastic reduction in induction time, by more than two orders of magnitude, is not associated with a major increase in the number of nuclei; it signals rather the onset of a morphological transition from spherulitic to highly oriented structures at early times. This is observed only when the applied strain is sufficiently large, suggesting a critical strain as the criterion for the onset of the transition. At a shear rate of 200 s-1 the critical strain is estimated to be in the range of 30 and 50; and since $t_{\mathrm{s}} = \gamma_{\mathrm{s}} / \dot{\gamma}_{\mathrm{s}}$, an equivalent criterion is a critical shearing time, which is between 0.15 s and 0.25 s. From a practical point of view, given such a short time scale, a morphological transition is inevitable for this polymer under industrial processing conditions.

This observation can also be interpreted as a result of the transformation of primary nuclei from point-like (or needlelike [64]) into threadlike precursors (or shish), on the basis that the former develop into spherulites (or slightly distorted spherulites) while the latter template the growth of row or highly oriented structures (cylindrulites or shish-kebabs). This interpretation is based on the phenomenological model introduced for non-nucleated polymers by Janeschitz-Kriegl *et al.* [23, 33] and later corroborated by Kornfield *et al.* [10, 34, 64]. However, the interpretation here differs slightly from those studies, which used pressure flow in a channel to generate shear. It is more straightforward and less unambiguous in the present study, as the shear rate, strain and stress are all uniform throughout the sample, in contrast to the nonlinear spatial variation of the flow field and the crystalline structures (*i.e.*, skin-core morphology) in pressure flow. In principle, the threadlike precursors are thought to be the product of growth or elongation of point-like nuclei [10, 23], which were formed by flow at an earlier time, during the continued deformation. A more elaborate model describing the formation of threadlike precursors using the concept of specific work, which departs from the previous work [23, 33], has recently been proposed by the first authors [6, 8, 65], and how well this model fits the present data is discussed in the subsequent chapter.

Importantly, it is postulated here that not all point-like nuclei are transformed into threadlike precursors at the instant the critical strain is exceeded, and, accordingly, that the entire sample is not abruptly converted into a highly oriented morphology. In fact, it has been shown recently [10, 34, 64] that the number and length of threadlike precursors depend on shearing time (or shear strain[*] here) and the availability of highly oriented chains. So at a shear rate of 200 s^{-1} and strain of 50, it is speculated that only a minute quantity of threadlike precursors have been developed from point-like nuclei, particularly those made up of chains in the upper end of the molecular weight distribution, and thus the sheared sample still consists mainly of point-like nuclei. This means that the resulting morphology would remain principally spherulitic and largely unchanged from that at a strain of 30. Consistent with this mechanistic interpretation, the late kinetic data show a very subtle difference between $|\eta^*|(t)/|\eta^*|_{q0}$ at a strain of 50 and that at 30 (Fig. 5.6b),

---

[*] Kumaraswamy *et al.* [64] stressed that the formation of threadlike precursors is not governed by the total strain, although it depends on the shearing time. In contrast to their pressure flow setup, the present study applied a constant shear rate, and thus shear strain is inseparably related to the shearing time by: $\gamma_s = \dot{\gamma}_s t_s$.

and had the growth kinetics been dominated otherwise by highly oriented structures, there would be a significant change in the rheological response, *i.e.*, the former would be shifted to much shorter times than the latter. Also in line with this interpretation is that the $I(t)/I(0)$ data at later times for a strain of 50 (Fig. 5.6a) indicate a smaller slope than those at a strain of 30.

To allow a more quantitative analysis, two additional characteristic times are introduced; $t_{0.5I}$ is the time at which $I(t)/I(0)$ drops to 50 %, and $t_{4\eta}$ is that at which $|\eta^*|(t)/|\eta^*|_{q0}$ increases to four. Widely used in other studies [34, 36, 54], $t_{0.5I}$ reveals growth kinetics of crystalline structures during early stages; whereas $t_{4\eta}$ represents the late kinetics and is selected such that the data are not affected by nonlinear viscoelasticity and correspond closely to the time at which $I(t)/I(0)$ approaches its minimum, when about half of the sample volume is estimated to be occupied by spherulites (see Section 4.4.3). Note that $t_{0.5I}$ also corresponds to the time at which $|\eta^*|(t)/|\eta^*|_{q0}$ reaches about 1.08 – 1.20. As will become clear later, the choice of characteristic time and type of plot, *i.e.*, whether γ_s, $\dot{\gamma}_s$ or t_s is used as the abscissa and whether the data are plotted on a logarithmic or linear scale, can influence the conclusions. In the following discussion, the present results will also be compared to those in the literature adopting Janeschitz-Kriegl's short-term shearing protocol [33]. To facilitate this comparison, Table 5.3 summarizes key points from selected references, of which most studied non-nucleated polymers, as there are very few data for nucleated polymers. Owing to the wide range of experimental design (*e.g.*, flow devices, measurement techniques, materials, flow and thermal conditions), a quantitative comparison is not possible, but it is clear that there are major discrepancies in both the observations and interpretations regarding saturation behavior and morphological transition (see Table 5.3).

Table 5.3. Shear-induced crystallization kinetics results from selected references.

Authors	Plot(s)	Findings and Interpretations
⊙ Janeschitz-Kriegl *et al.* [15, 23, 33]	log $t_{\lambda/2}$ vs. log t_s (at various extrapolated $\dot{\gamma}_w$)	-Power law: $t_{1/2} \propto t_s^n$, $n \le -1$ for nucleated polymers with melt-sensitive agent and non-nucleated polymers; $n = -2$ for degraded, non-nucleated polymers. No saturation behavior.
⊙ Kumaraswamy *et al.* [34]	log $t_{1/2}$ or log $t_{\lambda/2}$ vs. log t_s (at a given σ_w)	-For $t_s < t_{crit}$: $t_{1/2} \propto t_s^n$, where $-1 \le n \le -2$ -For $t_s > t_{crit}$: $t_{1/2}$ or $t_{\lambda/2}$ is constant (*i.e.*, saturation) -Saturation is associated with threadlike precursors. Transition to oriented growth occurs during saturation.
○ Somani *et al.* [66]	log $t_{1/2I_s}$ vs. $\dot{\gamma}_s$ (at a given γ_s)	-With increasing $\dot{\gamma}_s$, log $t_{1/2I_s}$ first decreases, and then saturates. -Results interpreted in terms of coil-stretch transition.
○ Fulchiron *et al.* [16, 62]	log $t_{1/2I_t}$ vs. $\dot{\gamma}_s$ (at various t_s)	-log $t_{1/2I_t}$ is essentially constant for low $\dot{\gamma}_s$ and decreases monotonically above a critical $\dot{\gamma}_s$. No saturation behavior.
○ Vleeshouwers and Meijer [55]	t_{onset} vs. t_s (at a given $\dot{\gamma}_s$)	-With increasing t_s, t_{onset} first decreases sharply, and then shows a short plateau, and finally decreases modestly.
○ Elmoumni and Winter [54]	$t_{1/2}$ vs. γ_s (at two Weissenberg numbers)	-With increasing γ_s, $t_{1/2}$ first decreases, and then appears to saturate at very large γ_s. The first decrease is associated with the increase in nuclei density, the transition to oriented structures occurs near the apparent saturation.
■ Baert *et al.* [36]	log $t_{1/2}$ vs. log γ_s or log $\dot{\gamma}_s$ (at various $\dot{\gamma}_s$ or γ_s)	-With increasing γ_s or $\dot{\gamma}_s$, log $t_{1/2}$ first decreases, then shows a plateau (sometimes less apparent), and finally decreases again (transition to oriented growth as indicated by upturn in birefringence).
○ Housmans *et al.* [67]	log $t_{1/2,\dot{\gamma}} / t_{1/2,Q}$ vs. t_s (at various $\dot{\gamma}_s$)	-With increasing t_s, log $t_{1/2,\dot{\gamma}} / t_{1/2,Q}$ first decreases (increase in point-like nuclei), then shows a plateau (saturation of nuclei), and finally decreases again (formation of oriented nuclei).

⊙: pressure flow; ○: rotational flow; ■: sliding plate; γ_s : shear strain; $\dot{\gamma}_s$: shear rate; $\dot{\gamma}_w$: wall shear rate; σ_w : wall shear stress; t_{crit} : critical shearing time for saturation to be observed; t_{onset} : onset crystallization time based on oscillatory shear measurement; t_s : shearing time; $t_{\lambda/2}$: time at which retardance is half of light wavelength; $t_{1/2}$: time at which total transmitted light intensity is half of its initial value; $t_{1/2I_s}$: time at which total SAXS intensity is half of its normalized value; $t_{1/2I_t}$: time at which transmitted light intensity through cross-polarizers is half of its normalized value; $t_{1/2,\dot{\gamma}}$: time at which storage modulus is half of its normalized value in shear-induced crystallization; $t_{1/2,Q}$: same as above, but in quiescent crystallization

The dependence of t_{ind}, $t_{0.5I}$ and $t_{4\eta}$ on strain γ_{s} at a shear rate of 200 s^{-1} is shown in Fig. 5.7a. In this semi-log plot, the onset of a morphological transition is most evident from the substantial slope change in t_{ind} at $\gamma_{\mathrm{s}} \approx 30$, whereas saturation behavior is marked by an apparent plateau that is especially noticeable in both $t_{0.5I}$ and $t_{4\eta}$ at large strains, *e.g.*, $\gamma_{\mathrm{s}} > 20$. Figure 5.7b shows results[*] at a higher shear rate of $\dot{\gamma}_{\mathrm{s}} = 500\ \mathrm{s}^{-1}$, which are found to be similar to those at 200 s^{-1} (Fig. 5.7a) but with slight variations. First, the morphological transition at 500 s^{-1} commences at a slightly lower critical strain, as indicated by the distinct change to a steeper slope in t_{ind} at $\gamma_{\mathrm{s}} \approx 20$. This shows that, rather than being invariant with shear rate, the critical strain is smaller at a larger shear rate. The other two slight variations can be seen in the $t_{0.5I}$ and $t_{4\eta}$ data at large γ_{s}, where $t_{0.5I}$ suggests no saturation and can be reasonably fitted by a single slope, and indicates a slope change at $\gamma_{\mathrm{s}} \approx 30$ after saturation at $\gamma_{\mathrm{s}} \approx 20$. These differences from the results at 200 s^{-1} can be explained using the earlier idea about the dependence of the number of the threadlike precursors on strain. In this context, at 500 s^{-1}, threadlike precursors, which only begin to form in very small quantity at $\gamma_{\mathrm{s}} \approx 20$, increase in concentration with increasing γ_{s}, and the resulting changes at much larger strains ($\gamma_{\mathrm{s}} > 20$) are reflected in the growth kinetics at later times by both $t_{0.5I}$ and $t_{4\eta}$. In contrast, at the lower shear rate of 200 s^{-1}, a similar effect on $t_{0.5I}$ and $t_{4\eta}$ would only be possible at much higher strains, *i.e.*, $\gamma_{\mathrm{s}} > 50$.

---

[*] The raw data for this and other shear rates are given in Appendix F.

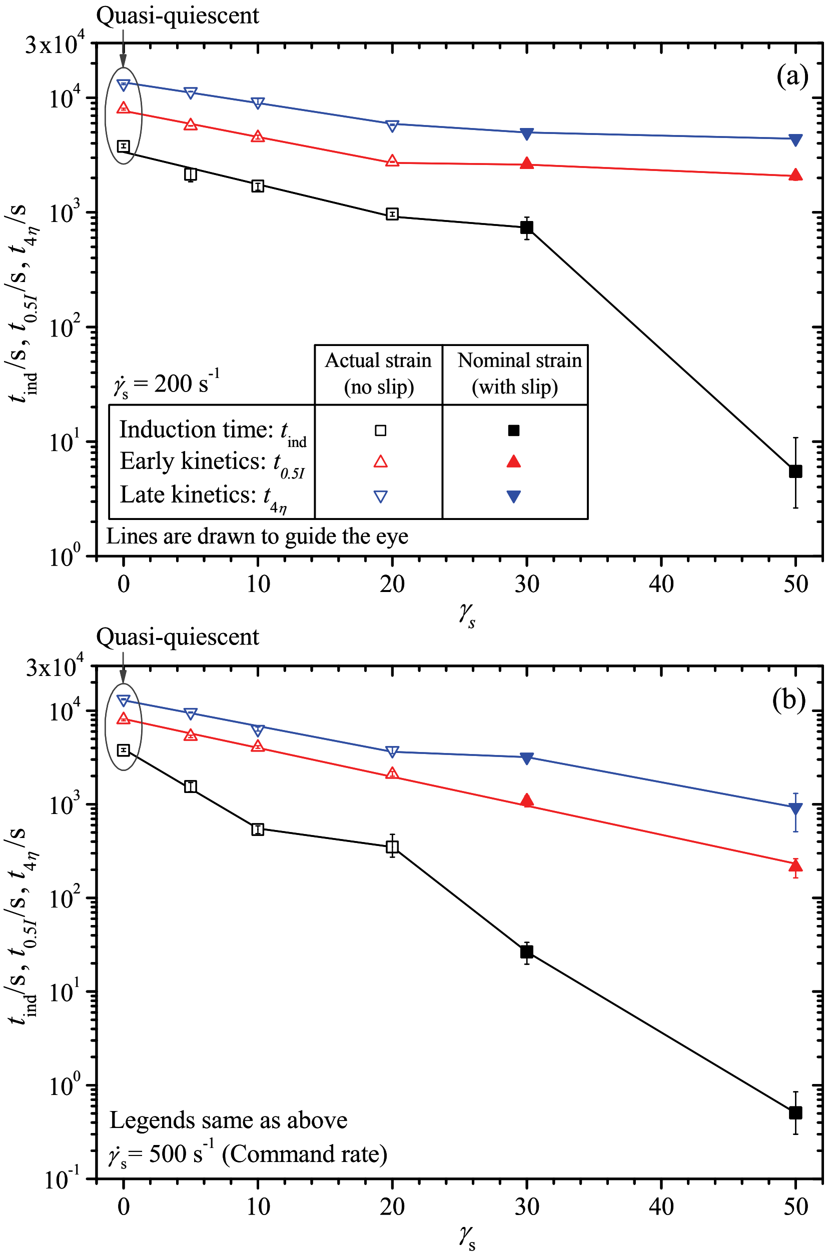

Figure 5.7. Dependence of characteristic crystallization times t_{ind}, $t_{0.5I}$ and $t_{4\eta}$ on strain for iPP1 at high shear rates: (a) 200 s^{-1}, and (b) 500 s^{-1}. A morphological transition is shown clearly by a marked slope change in t_{ind}, whereas saturation behavior is manifested as an apparent plateau, which is more evident in $t_{0.5I}$ and $t_{4\eta}$ at 200 s^{-1} at large strains. The large differences observed for t_{ind}, $t_{0.5I}$ and $t_{4\eta}$ at large strains are associated with the quantity of thread precursors (see text). Strains at 30 and 50 are nominal values due to slip. Data shown are averages and ranges for three measurements at 155.5 °C.

The appearance of a plateau followed by a second slope change (Figs. 5.7a and b) resembles qualitatively the recent observations of Housmans *et al.* [67] for some non-nucleated polypropylenes (see Table 5.3), although these authors used much lower shear rates ($\dot{\gamma}_s \leq 60$ s^{-1}) and plotted their data versus t_s (equivalent to γ_s here). These authors did not mention slip and attributed the existence of the plateau exclusively to the saturation of point-like nuclei. Their interpretation, as well as that by Baert *et al.* [36], who plotted in terms of log γ_s, of the second slope change as a consequence of a morphological transition is consistent with the present work.

Vleeshouwers and Meijer [55] reported a similar trend using a linear plot of a different characteristic time versus t_s, but observed no orientation in the solidified sheared samples (likely due to the low shear rates used, *viz.*, $\dot{\gamma}_s < 12$ s^{-1}). And curiously, they associated the observed acceleration in crystallization partly to mechanical degradation. In investigating the effect of strains, Elmoumni and Winter [54] found that a morphological transition only takes place at large strains ($\dot{\gamma}_s \geq 600$, although the shear rates used were low, $\dot{\gamma}_s < 20$ s^{-1}) , and contrary to the present study, they noted the transition happened near saturation rather than during the second slope change, which was however not reported (see Table 5.3). Upon examination of their data, it seems that the second slope change was overlooked for two reasons; first, they used a linear scale rather than a logarithmic scale for plotting the characteristic time, and second, the characteristic time chosen for analysis was inappropriate as it represents a much later crystallization time (*i.e.*, a fall in light intensity to 97 % rather than 50 % should be used). In fact, their results would match the present findings if these oversights were corrected.

Predictably, for the same range of strains, crystallization at much lower shear rates than those previously mentioned would not induce a morphological transition, as indicated by the absence of a distinct slope change in the data at 10 s^{-1} and 50 s^{-1} in Fig. 5.8. That the transition is not triggered if the shear rate is below a threshold value suggests a second criterion; thus, the initiation of highly oriented crystal growth requires shear flow that exceeds both a critical rate and a critical strain. This is, unsurprisingly, analogous to the requirement noted by Kumaraswamy *et al.* [34] regarding both a critical shear stress (or a critical strain rate in his recent review [11]) and a critical shearing time, based on results obtained using pressure flow in a slit.

Figure 5.8 also reveals the inadequacy of relying on a single characteristic time to describe shear-induced crystallization behavior. This is of lesser concern if a morphological transition is not involved, as the difference between characteristic times is small when the growth kinetics of spherulites is only modestly altered by flow. However, when there is a morphological change, a single time cannot adequately characterize the transition. For instance, the initial appearance of a small number of oriented structures is best detected by t_{ind}, but this can mislead us into thinking that the entire sample is highly oriented, even when the dominant structures are spherulites. On the other hand, a later time, $t_{0.5I}$ or $t_{4\eta}$, is better for characterizing the overall change associated with bulk morphology, but at the expense of overestimating the critical strain. A second problem of using only one characteristic time is that some features are either less or not evident at certain conditions, a prime example being the absence of saturation at 500 s^{-1} if $t_{0.5I}$ is used (Fig. 5.8b). Thirdly, the result of a quantitative analysis can be affected by the choice of characteristic time due to large differences in the magnitudes of change, as seen in the orders of magnitude of the data range: four for t_{ind} (Fig. 5.8a), two for $t_{0.5I}$ (Fig. 5.8b), and one and a half for $t_{4\eta}$ (Fig. 5.8c). To overcome these shortcomings, it is necessary to use at least two characteristic times to illuminate the underlying crystallization behavior, especially in cases when the sheared sample undergoes a morphological transition.

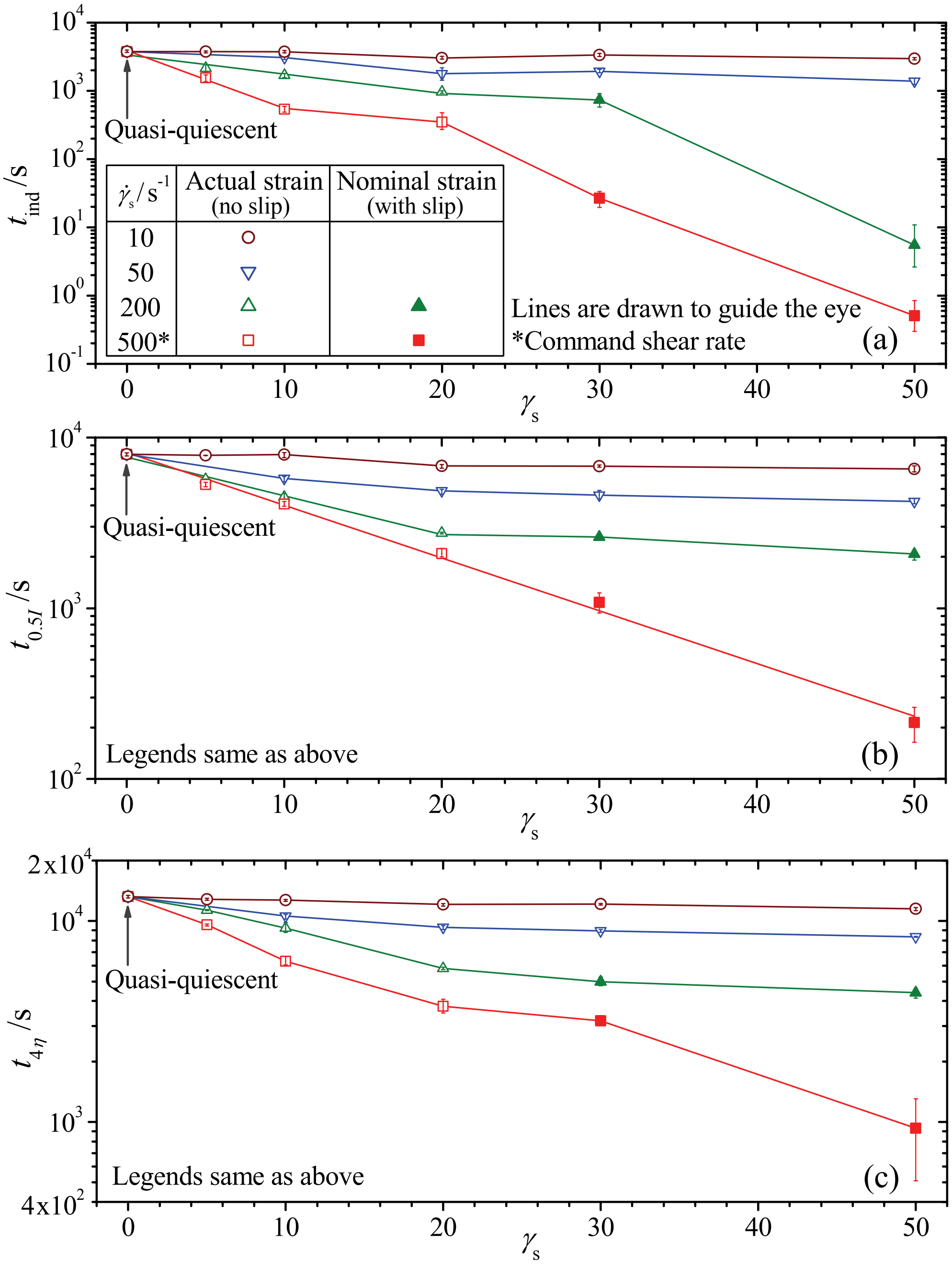

Figure 5.8. Dependence of characteristic crystallization times of iPP1 on shear strain at various shear rates during: (a) earliest stage using t_{ind} , (b) early kinetics using $t_{0.5I}$, and (c) late kinetics using $t_{4\eta}$ In comparison to 200 s^{-1} and 500 s^{-1}, a distinct slope change, indicative of a morphological transition, is not observed at low shear rates of 10 s^{-1} and 50 s^{-1}. The data also indicate that it is inadequate to use a single characteristic time to deduce the crystallization behavior (see text). Strains at 30 and 50 for shear rates of 200 s^{-1} and 500 s^{-1} are nominal values due to slip. Data shown are averages and ranges for three measurements at 155.5 °C.

Also widely used for kinetic analysis, particularly in the case of continuous shearing where strain is not a variable, as well as for testing of models [68, 69], is a double logarithmic plot of the characteristic crystallization time versus shear rate $\dot{\gamma}_{\mathrm{s}}$. Figure 5.9 shows such a plot for the largest strain studied, γ_{s} = 50, at shear rates in the range of 1 s^{-1} to 500 s^{-1}. The two important features mentioned earlier, a plateau indicative of saturation in point-like nuclei and a distinct slope change suggestive of a morphological transition, are not observed, especially in the $t_{0.5I}$ and $t_{4\eta}$ data. This is qualitatively consistent with what is generally reported [16, 62], where crystallization time remains essentially constant at low values of $\dot{\gamma}_{\mathrm{s}}$ and decreases monotonically at high values of $\dot{\gamma}_{\mathrm{s}}$, although some literature data [16, 62] showed very brief saturation behavior. Understandably, it is not unusual that the saturation behavior is not evident in the log-log plot, since this feature only manifests itself over a narrow range of $\dot{\gamma}_{\mathrm{s}}$, likely between 50 s^{-1} and 200 s^{-1} for the data in Fig. 5.9. And this provides some clues as to why a curve with a fairly smooth slope change (without a saturation plateau) is commonly used to fit data obtained at high shear rates under continuous shearing [37]. Saturation in the induction time under continuous shearing was observed by Sherwood et al. [2], but the shear rates used (≤ 60 s^{-1}) were not high enough to reveal the second decrease in the induction time that would follow saturation.

Two of the studies listed in Table 5.3 discussed in detail the plateau due to saturation of crystallization kinetics with $\dot{\gamma}_{\mathrm{s}}$. Based on observations of one distinct and two less apparent plateaus for three poly(1-butene) samples, Baert *et al.* [36] concluded that saturation behavior was arguable. On the other hand, with only three data points, Hsiao *et al.* [39, 66] interpreted saturation behavior in terms of a critical orientation molecular weight M^{*}. This parameter was adapted from Keller's model [9], developed on the basis of a coil-stretch transition (which was used by de Gennes for polymer solutions [70]), for describing shish-kebab formation in extensional-flow induced crystallization. These authors assumed that only chains having a molecular weight exceeding M^{*} can be oriented by flow to accelerate crystallization, and that M^* varies with $\dot{\gamma}_\mathrm{s}$ according to $M^* \propto \dot{\gamma}_\mathrm{s}^{-\alpha}$, where α is a temperature-dependent exponent (~ 0.15 for iPP at 140 °C). This power-law relationship suggests that M^* decreases sharply with increasing $\dot{\gamma}_\mathrm{s}$ at low values of $\dot{\gamma}_\mathrm{s}$ but becomes relatively insensitive to any increase in $\dot{\gamma}_\mathrm{s}$ at high values of $\dot{\gamma}_\mathrm{s}$, and this results in a saturation plateau. This simple model seems to describe their results, which were limited to a maximum shear rate of 102 s^{-1}, but it could not explain the second slope that is expected to commence at much higher shear rates (as shown by Baert *et al.* [36]), which were not tested in their experiment.

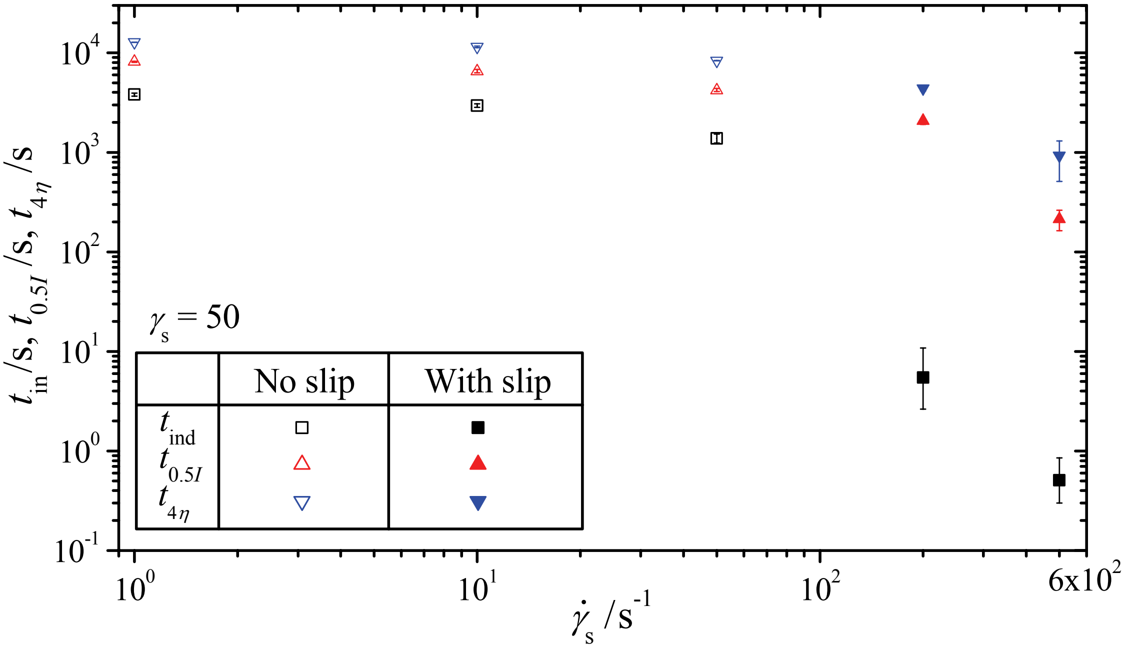

Figure 5.9. Dependence of characteristic crystallization times t_ind, $t_{0.5I}$ and $t_{4\eta}$ on shear rate at a strain of 50 for iPP1. A plateau indicative of saturation in crystallization kinetics and a distinct slope change indicative of a morphological transition are not evident in this plot. Due to slip, nominal values are used for shear rates of 200 s^{-1} and 500 s^{-1}. Data shown are averages and ranges for three measurements at 155.5 °C.

A double logarithmic plot of characteristic crystallization time versus shearing time t_{s} for various values of $\dot{\gamma}_{\mathrm{s}}$ is also commonly used [15, 23, 33, 34], and the resulting power-law exponents have served as the basis of an empirical model developed by Janeschitz-Kriegl *et al.* [15, 23, 33], which was later adopted in other models [68, 71, 72]. Figures 5.10a and b show such plots for t_{ind} and $t_{0.5I}$, respectively; $t_{4\eta}$ is not presented here, as its trend is similar to that of $t_{0.5I}$. As shown in the first plot, the morphological transition that occurs with increasing t_{s} at the two high shear rates of 200 s^{-1} and 500 s^{-1} is characterized by a marked change in slope, with the two power-law exponents changing from -0.6 and -1.1 to -8. The exponent for the second slope is an apparent value, as the data are affected by slip. Unlike that shown in an equivalent plot using γ_{s} as the abscissa (Fig. 5.7), the saturation behavior is masked by the logarithmic scale in Fig. 5.10. For the $t_{0.5I}$ data in the second plot, a distinct slope change indicative of the progress of the morphological transition is also observed at 500 s^{-1}, but the second slope has a smaller exponent of -2.5. As was said earlier, the choice of a characteristic time can affect the kinetic analysis, so the power-law exponent for the second slope at 500 s^{-1} (Figs. 5.10a and b) may have a value intermediate between -8 and -2.5 for any characteristic time chosen arbitrarily between t_{ind} and $t_{0.5I}$, *i.e.*, corresponding to a fall between 3 % and 50 % in $I(t)/I(0)$. It is also pertinent to consider whether there will be a plateau for t_{ind} after the second slope at longer shearing times, *i.e.*, $t_{\mathrm{s}} > 0.1$ s at $\dot{\gamma}_{\mathrm{s}} = 500$ s^{-1}. However, this cannot be determined, as the value of t_{ind} is about 0.5 s when $t_{\mathrm{s}} = 0.1$ s, meaning that any further increase in t_{s} would render t_{ind} meaningless, because its value would be smaller than t_{ind}, *i.e.*, crystallization would start during shearing.

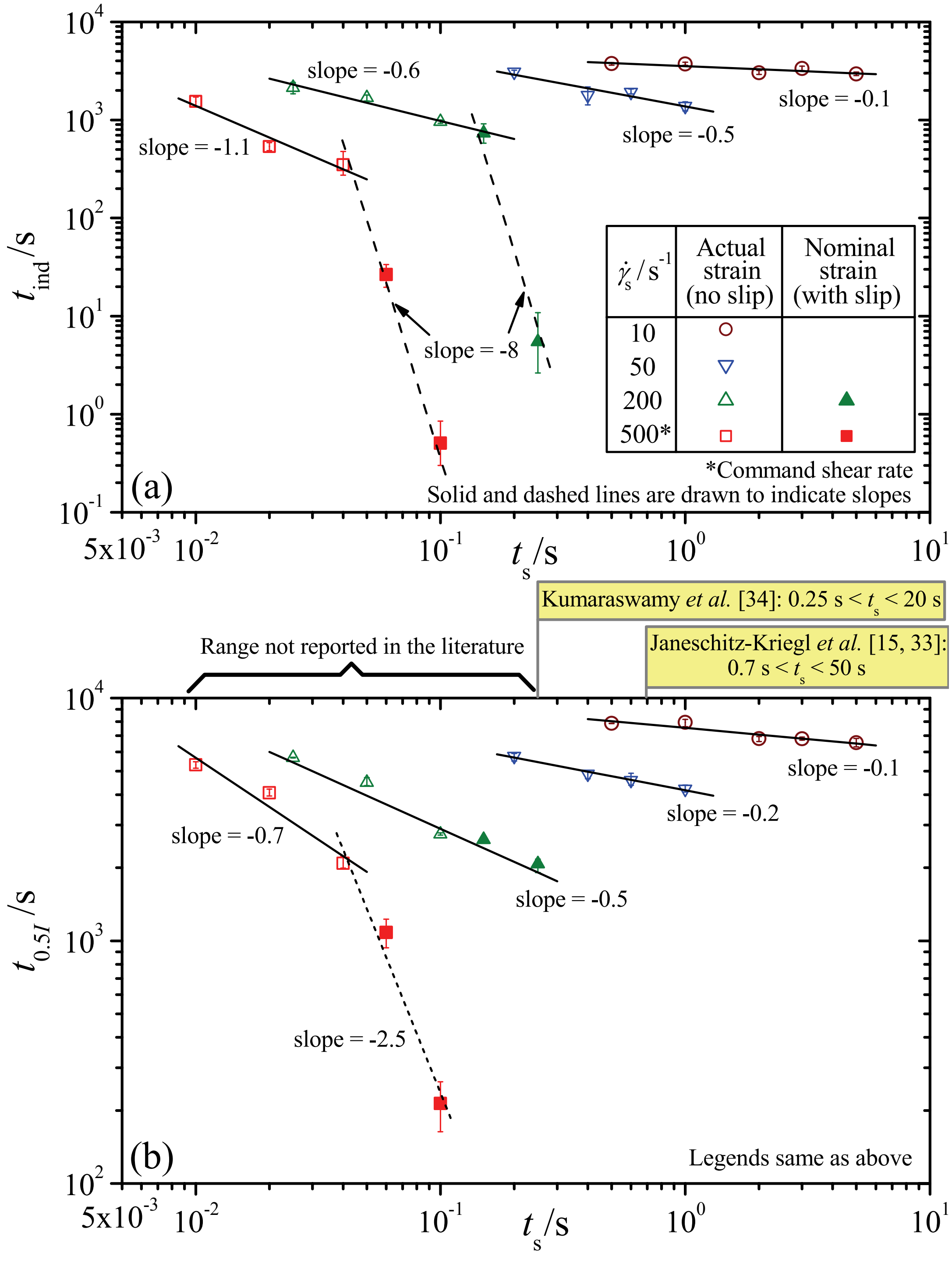

Figure 5.10. Dependence of characteristic crystallization times of iPP1 on shearing time at various shear rates in terms of (a) induction time t_{ind}, and (b) early kinetics using $t_{0.5I}$. A large slope change (dashed line) indicative of a morphological transition is observed at large shear rates (see text for details). Data shown are averages and ranges for three measurements at 155.5 °C.

There are serious discrepancies between the results shown in Figs. 5.10a and b and those reported by Kumaraswamy *et al.* [34] and Janeschitz-Kriegl *et al.* [15, 23, 33], notwithstanding differences in the values of t_s (*i.e.*, much smaller in this study compared to those investigated by the two groups, see Fig. 5.10b), the flow devices used (*i.e.*, sliding plate versus slit [34] and duct [33]) and other experimental conditions. The first authors [34] speculated that the observed saturation in the crystallization times, viz., the turbidity half-time $t_{1/2}$ and retardation half-time $t_{\lambda/2}$, was a consequence of the consumption of high-molecular weight chains in the formation of oriented structures or threadlike precursors; and this is different from the findings here, as well as those of Housmans *et al.* [67], where the saturation behavior (observed in semi-log plot using γ_s in Fig. 5.7) is associated with point-like nuclei and not threadlike precursors. Furthermore, these authors concluded that highly oriented structures only begin to form after $t_{1/2}$ and $t_{\lambda/2}$ indicate a plateau (based on Figs. 5 and 6 in [34]), but they did not report a slope change in these times accompanying the morphological transition; and this is contrary to what is demonstrated in the present work and in two recent studies [36, 67]. The discrepancies appear to arise largely from the authors' incorrect interpretation of their data, as a later report by the same group [10] mentioned that the formation of threadlike precursors commences at a much earlier shearing time (1 s $\leq t_s \leq$ 2 s, *i.e.*, during which $t_{1/2}$ decreases with increasing t_s, see Fig. 10 in [10]), well before the reported plateau (t_s > 5 s, *i.e.*, during which $t_{1/2}$ remains constant with increasing t_s). It seems that when analyzing their data the authors also overlooked a very brief plateau (0.5 s $\leq t_s \leq$ 0.75 s, Fig. 5 in [34]) that is probably associated with saturation in point-like nuclei. Within the range of parameters investigated, the present study did not find any evidence of saturation in kinetics associated with threadlike precursors.

Previously, Kumaraswamy *et al.* [34] discussed the differences between their results and those of Janeschitz-Kriegl *et al.* [15, 23, 33]. Intriguingly, neither a plateau nor a slope change was reported by the latter group, which is at odds with the present findings and others [36, 67] (based on plots of either t_s or the equivalent γ_s as the abscissa). Instead, Janeschitz-Kriegl *et al.* fitted all the data with straight lines using a power-law exponent of -1 for a nucleated sample containing a melt-sensitive agent as well as for several non-nucleated samples [15, 23] and an exponent of -2 for degraded, non-nucleated samples [33]. But, the fit was found to be incorrect, as an examination of their data revealed that the exponents were actually in the range of -0.4 to -0.9 for the nucleated samples. In brief, the empirical model formulated by these authors [15, 23, 33] relates t_s and $\dot{\gamma}_\mathrm{s}$ (or wall shear rate $\dot{\gamma}_\mathrm{w}$) to the number density of point-like nuclei, $N \propto \dot{\gamma}_\mathrm{s}^2 t_\mathrm{s}$, and the total length of the threadlike precursors per unit volume, $L_\mathrm{tot} \propto \dot{\gamma}_\mathrm{s}^2 t_s$ (for nucleated polymers) or $L_\mathrm{tot} \propto \dot{\gamma}_\mathrm{s}^4 t_s^2$ (for non-nucleated polymers). A primary basis of this model is that the power-law exponent is a constant of either -1 or -2, independent of $\dot{\gamma}_\mathrm{s}$. Obviously, this condition is not met by the actual fit of their data as well as the results shown in Figs. 5.10 a and b, which indicate that the power-law exponent varies from -0.1 to -1.1 for t_ind or from -0.1 to -0.7 for $t_{0.5I}$ (based on slopes of the solid lines in the figures) as $\dot{\gamma}_\mathrm{s}$ increases from 10 s^{-1} to 500 s^{-1}. Of interest is whether these deviations from the model are restricted specifically to nucleated polymers; it appears that literature data of non-nucleated polymers also indicate that the power-law exponent changes with $\dot{\gamma}_\mathrm{s}$ (based on slopes in plots of crystallization time versus t_s or γ_s [36, 67]). In addition, as already shown, the exponent also varies significantly with the choice of characteristic crystallization time in the case of a morphological transition, which, however, was also not accounted for in the model. Therefore, it is clear that if the data shown in Fig. 5.10 are to be used for the development of a new model, the dependence of the power-law exponent on shear rate and on the characteristic crystallization time must be taken into consideration.

5.4.4 Uniformity of Sheared Samples

Figure 5.11 shows top-view photographs of solidified samples of iPP1 taken following quasi-quiescent crystallization and shear-induced crystallization at various shearing conditions. Uniformity in the samples shown was evaluated based on the area of white domains relative to that of dark gray domains. The pictures were taken with samples placed on a black background, so the dark gray domains (*e.g.*, in Fig. 5.11g) are highly transparent whereas the white domains (Fig. 5.11a) are nearly opaque. These domains were visible to the naked eye, as their size was in the range of millimeters to centimeters. It is important to note that the non-uniformity associated with spatial variation in flow field reported in some literature (*e.g.*, skin-core morphology in pressure flow [33, 34]) is different from those shown below, because the flow field used in the present study was uniform.

As shown in Fig. 5.11a, white domains were found uniformly distributed in the quasi-quiescent sample, indicating a good dispersion of NA-11 particles in the polymer matrix. The white domains were made up of densely packed spherulites (see Fig. 5.3a). Uniform samples were also obtained following shear-induced crystallization with γ_s = 50 at $\dot{\gamma}_s$ = 10 s^{-1} and 50 s^{-1} (Figs. 5.11b and c). Lower strains, *i.e.*, γ_s < 50, at these two low shear rates and $\dot{\gamma}_s$ = 200 s^{-1} yielded similar samples (not shown due to indiscernible difference with Figs. 5.11b and c). As mentioned, growth of oriented structures in place of spherulitic structures takes place at high shear rates and large strains; as a result, non-uniform samples were obtained for $\dot{\gamma}_s$ = 200 s^{-1} (Fig. 5.11d) and 500 s^{-1} (Fig. 5.11h) with γ_s = 50.

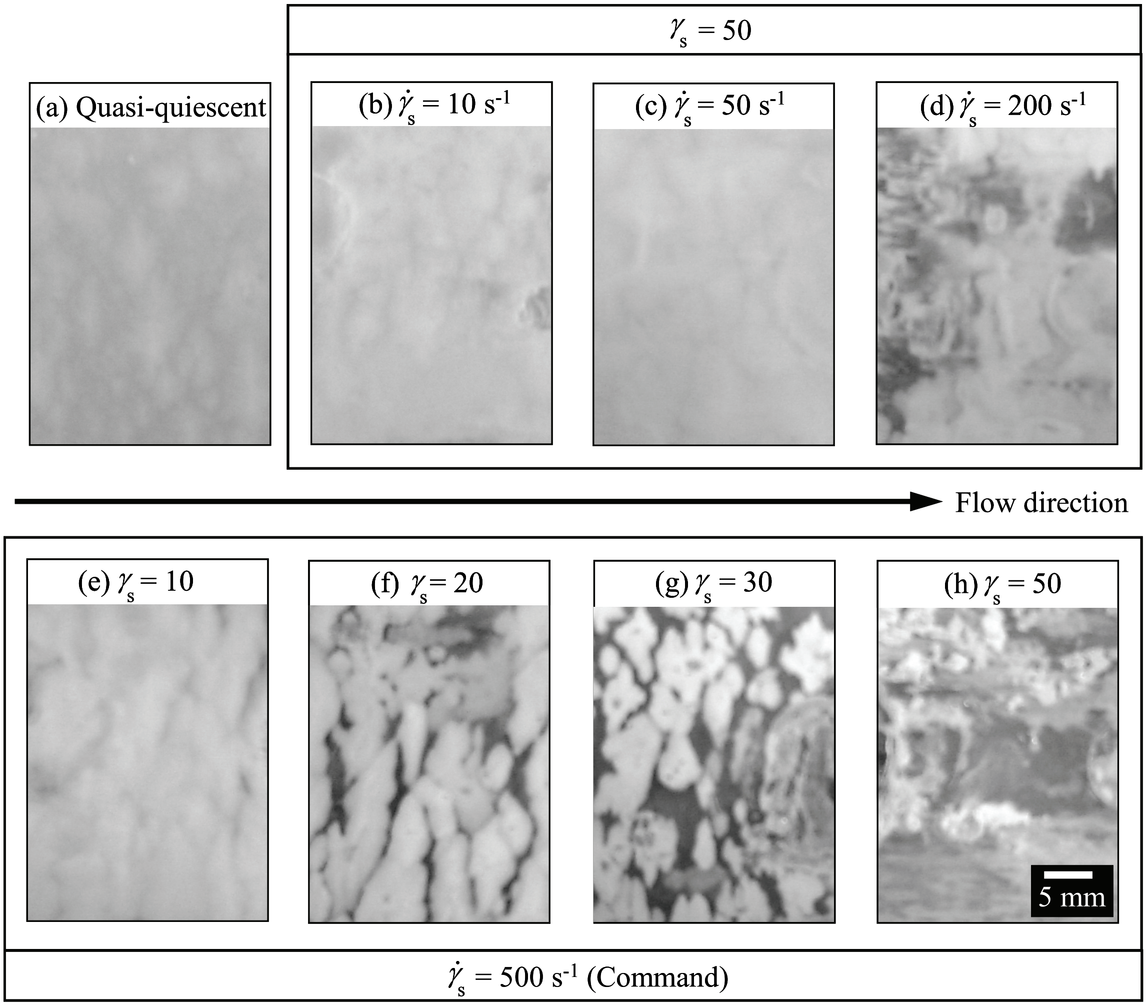

Figure 5.11. Top-view photographs of the solidified iPP1 samples obtained following various crystallization conditions at 155.5 °C: (a) Quasi-quiescent, (b) $\dot{\gamma}_s = 10\ s^{-1}$, $\gamma_s = 50$, (c) $\dot{\gamma}_s = 50\ s^{-1}$, $\gamma_s = 50$, (d) $\dot{\gamma}_s = 200\ s^{-1}$, $\gamma_s = 50$ (nominal), (e) Command $\dot{\gamma}_s = 500\ s^{-1}$, $\gamma_s = 10$, (f) Command $\dot{\gamma}_s = 500\ s^{-1}$, $\gamma_s = 20$, (g) $\dot{\gamma}_s = 500\ s^{-1}$, $\gamma_s = 30$ (nominal), and (h) $\dot{\gamma}_s = 500\ s^{-1}$, $\gamma_s = 50$ (nominal). Uniform samples were found under quasi-quiescent crystallization in (a) and mild shearing conditions in (b), (c) and (e). Segregation of crystalline structures (white agglomerates) was observed at large shear rates and moderate strains in (f) and (g). High shear rates and strains lead to morphological transition in (d) and (h). All pictures have the same scale bars as that displayed in (h).

Shearing at a command rate of $\dot{\gamma}_s$ = 500 s^{-1} with increasing γ_s reveals an interesting feature not found at lower rates. As mentioned, uniformly distributed white domains similar to those found in quasi-quiescent crystallization were observed at low strain, *i.e.*, γ_s = 10 (Fig. 5.11e), while non-uniformity was found at large strain, *i.e.*, γ_s = 50 (Fig. 5.11h). Interestingly, segregation of crystalline structures is found at intermediate strains, *i.e.*, γ_s = 20 and 30. Compared to Fig. 5.11h for γ_s = 50, the non-uniformity observed for γ_s = 20 in Fig. 5.11f is characterized by distinctly segregated white agglomerates and dark gray domains. As will be explained later, the segregation is thought to be due to the complex interaction between flow and the NA-11 particles in the polymer matrix. As γ_s increased to 30 (Fig. 5.11g), the sample became increasingly non-uniform as a result of two phenomena: segregation due to flow and NA-11, and growth of oriented structures. At a larger γ_s of 50 (Fig. 5.11h), the observed non-uniformity is dominated by oriented structures. The structures that make up the white agglomerates and dark gray domains are shown in Fig. 5.12. The white agglomerates shown in the photograph in Fig. 5.12a are packed with very fine spherulites (optical micrograph in Fig. 5.12c), whereas the dark gray domains contained few birefringent structures (optical micrograph in Fig. 5.12d). Structures that were oriented in the flow direction can be seen in the optical micrograph in Fig. 5.12e.

To further examine factors controlling segregation, pictures of the other three polymers obtained following the same shear-induced crystallization conditions of $\dot{\gamma}_s$ = 494 s^{-1} and γ_s = 20 are compared to that of iPP1 in Fig. 5.13. In contrast to iPP1 (Fig.5.13a), iPP2 was found to be uniform (Fig. 5.13b), suggesting the importance of molecular weight in inducing segregation. Neither iPP3 nor iPP4 showed any sign of segregation (Fig. 5.13c and d), implying that NA-11 plays a role. The kinetic analysis in Section 5.1 suggested that transition to oriented growth occurs in iPP4, thus explaining the non-uniformity shown in Fig. 5.13d, which resembles somewhat that shown in Fig. 5.11h for iPP1 at a larger γ_s.

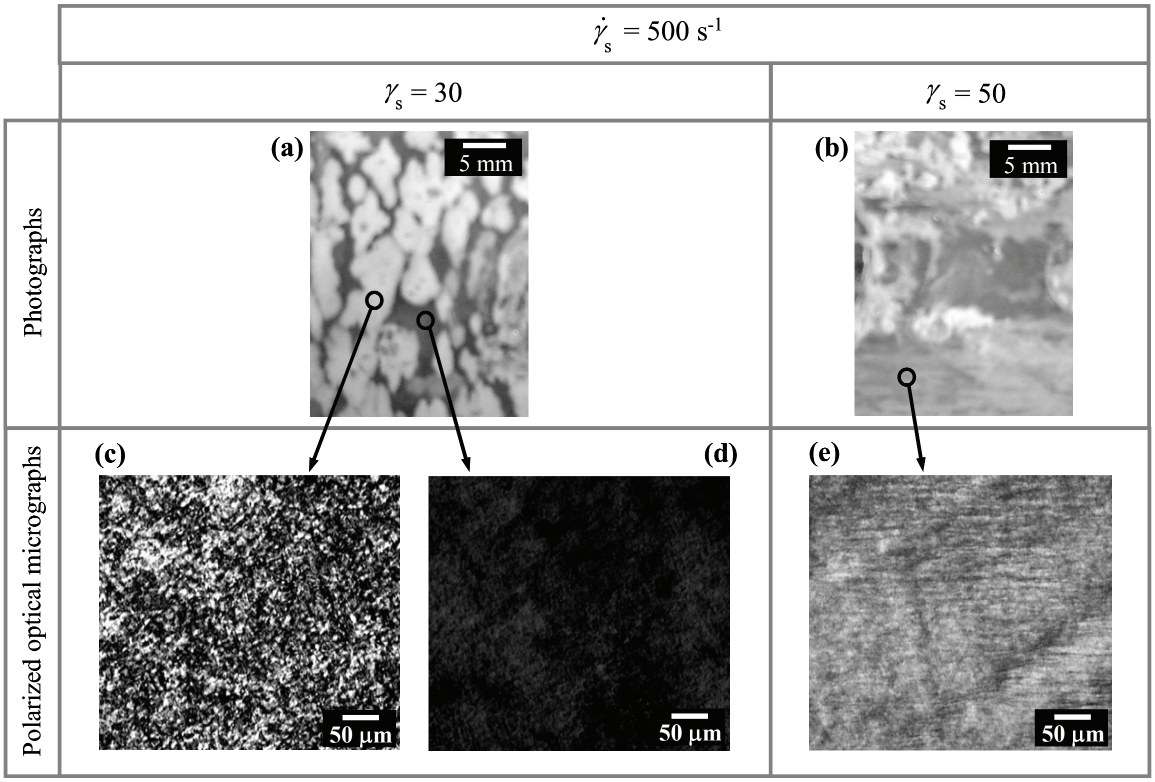

Figure 5.12. Morphological examination of the non-uniformities observed in the solidified iPP1 samples obtained following shear-induced crystallization at 155.5 °C. Top-view photographs show non-uniformities and polarized optical micrographs reveal morphology. (a) At $\dot{\gamma}_s = 500\ s^{-1}$, $\gamma_s = 30$ (nominal), distinctly segregated white agglomerates and dark gray domains were observed. (b) At $\dot{\gamma}_s = 500\ s^{-1}$, $\gamma_s = 50$ (nominal), morphological transition was observed. (c) The white agglomerates consist of fine, densely packed spherulites. (d) The dark gray domains contain few birefringent structures. (e) Oriented structures were found.

Little information is available in the literature with regard to the type of non-uniformity observed here, as earlier morphological analyses usually focused on structures with size ranges in micrometers or smaller. It is shown here that segregation can take place, and its occurrence depends on the presence of nucleating agent, the shearing conditions and molecular weight. The complex interactions between these variables deserve further investigation.

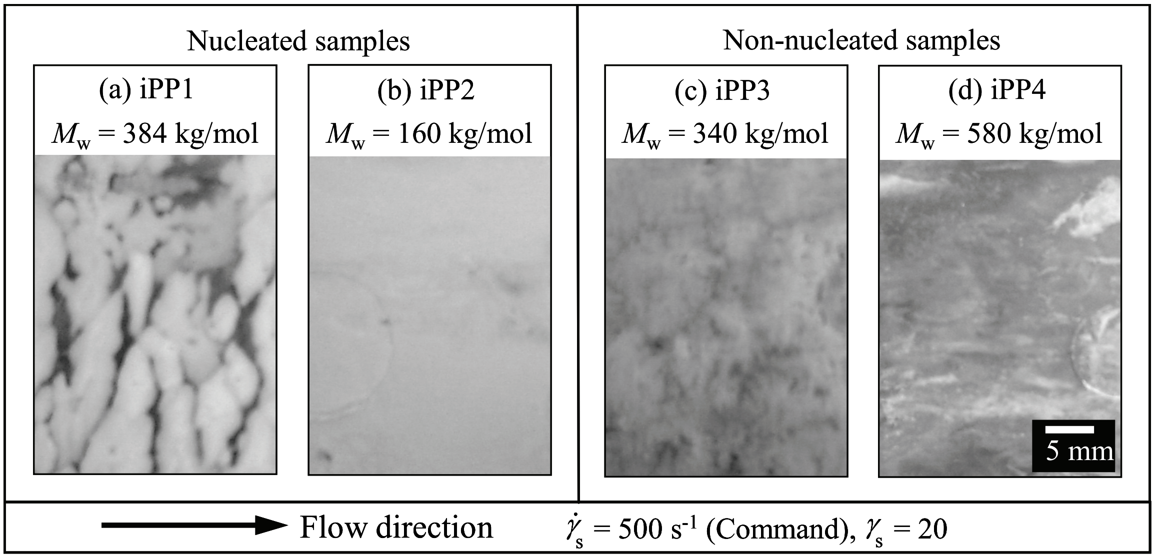

Figure 5.13. Top-view photographs of solidified samples obtained following shear-induced crystallization at $\dot{\gamma}_s = 500$ s^{-1} (command rate) and $\gamma_s = 20$ at 155.5 °C for different samples. (a) iPP1, (b) iPP2, (c) iPP3, and (d) iPP4. Only nucleated sample iPP1 at high shear rates was found to show segregation of crystalline structures. All pictures have the same scale bars as that displayed in (d).

5.5 Conclusions

Unlike that under quiescent conditions, the nucleation pathway of nucleated polymers after a brief, strong shear is not regulated by the nucleating agent. The effect of shear is primarily in inducing nucleation and is much less effective in altering the growth kinetics. If the shearing conditions are strong, molecular weight controls the nucleation kinetics, independent of the presence of a nucleating agent. Relative to quiescent crystallization, the induction time of non-nucleated polymers is more effectively reduced by shear than that of nucleated polymers. The effects of nucleating agent and shear on shortening the induction time are not additive. For low-molecular weight polymers, a nucleating agent is more effective than flow to enhance crystallization kinetics and decrease the spherulite size. With increasing shear rate or strain, crystallization first accelerates as a consequence of the increase in the number of point-like nuclei, then saturates due to either slip or the consumption of high-molecular weight components for the creation of point-like nuclei, and finally accelerates again at the onset of transition from spherulitic to oriented morphology. Within the range of conditions studied, saturation in kinetics associated with threadlike precursors was not found. Both a critical shear rate and a critical strain are required for a morphological transition to occur. The complex interactions between nucleating agent, shearing conditions and molecular weight can lead to segregation of crystalline structures, resulting in non-uniformity in the bulk samples.

5.6 References

1. Lagasse, R.R. and Maxwell, B. "An experimental study of the kinetics of polymer crystallization during shear flow" *Polym. Eng. Sci.* (1976) **16**, 189-199.
2. Sherwood, C.H., Price, F.P., and Stein, R.S. "Effect of shear on the crystallization kinetics of poly(ethylene oxide) and poly(ε-caprolactone) melts" *J. Polym. Sci., Polym. Symp.* (1978) **63**, 77-94.
3. Khanna, Y. "Rheological mechanism and overview of nucleated crystallization kinetics" *Macromolecules* (1993) **26**, 3639-3643.
4. Tribout, C., Monasse, B., and Haudin, J.M. "Experimental study of shear-induced crystallization of an impact polypropylene copolymer" *Colloid Polym. Sci.* (1996) **274**, 197-208.
5. Wolkowicz, M.D. "Nucleation and crystal growth in sheared poly(1-butene) melts" *J. Polym. Sci., Polym. Symp.* (1978) **63**, 365-382.
6. Janeschitz-Kriegl, H., Ratajski, E., and Stadlbauer, M. "Flow as an effective promotor of nucleation in polymer melts: A quantitative evaluation" *Rheol. Acta* (2003) **42**, 355-364 (2003) 42, 355-364.
7. Kurja, J. and Mehl, N. "Nucleating agents for semi-crystalline polymers", in *Plastics Additives Handbook*, H. Zweifel, R. D. Maier, M. Schiller, Eds., (Hanser Publishers, Munich, 2009), 967-990.
8. Janeschitz-Kriegl, H. *Crystallization Modalities in Polymer Melt Processing: Fundamental Aspects of Structure Formation* (SpringerWienNewYork, Germany, 2010).
9. Keller, A. and Kolnaar, H.W.H. "Flow-induced orientation and structure formation", in *Materials Science and Technology: A Comprehensive Treatment*, R. W. Cahn, P. Haasen, E. J. Kramer, Eds., Vol. 18, (Wiley-VCH, Weinheim, 1997), 189-268.
10. Kornfield, J.A., Kumaraswamy, G., and Issaian, A.M. "Recent advances in understanding flow effects on polymer crystallization" *Ind. Eng. Chem. Res.* (2002) **41**, 6383-6392.

11. Kumaraswamy, G. "Crystallization of polymers from stressed melts" *J. Macromol. Sci., Polym. Rev.* (2005) **45**, 375-397.
12. Somani, R.H., Yang, L., Zhu, L., and Hsiao, B.S. "Flow-induced shish-kebab precursor structures in entangled polymer melts" *Polymer* (2005) **46**, 8587-8623.
13. Fujiyama, M. and Wakino, T. "Structures and properties of injection moldings of crystallization nucleator-added polypropylenes. I. Structure-property relationships" *J. Appl. Polym. Sci.* (1991) **42**, 2739-2747.
14. Gahleitner, M., Wolfschwenger, J., Bachner, C., Bernreitner, K., and Neißl, W. "Crystallinity and mechanical properties of PP-homopolymers as influenced by molecular structure and nucleation" *J. Appl. Polym. Sci.* (1996) **61**, 649-657.
15. Jerschow, P. and Janeschitz-Kriegl, H. "The role of long molecules and nucleating agents in shear induced crystallization of isotactic polypropylenes" *Int. Polym. Process.* (1997) **12**, 72-77.
16. Naudy, S., David, L., Rochas, C., and Fulchiron, R. "Shear induced crystallization of poly(m-xylylene adipamide) with and without nucleating additives" *Polymer* (2007) **48**, 3273-3285.
17. Byelov, D., Panine, P., Remerie, K., Biemond, E., Alfonso, G.C., and de Jeu, W.H. "Crystallization under shear in isotactic polypropylene containing nucleators" *Polymer* (2008) **49**, 3076-3083.
18. Nogales, A., Mitchell, G.R., and Vaughan, A.S. "Anisotropic crystallization in polypropylene induced by deformation of a nucleating agent network" *Macromolecules* s (2003) **36**, 4898-4906.
19. Nogales, A. and Mitchell, G.R. "Development of highly oriented polymer crystals from row assemblies" *Polymer* (2005) **46**, 5615-5620.
20. Balzano, L., Portale, G., Peters, G.W.M., and Rastogi, S. "Thermoreversible DMDBS phase separation in iPP: The effects of flow on the morphology" *Macromolecules* s (2008) **41**, 5350-5355.
21. Balzano, L., Rastogi, S., and Peters, G.W.M. "Flow induced crystallization in isotactic polypropylene-1,3:2,4-bis(3,4-dimethylbenzylidene)sorbitol blends: Implications on morphology of shear and phase separation" *Macromolecules* s (2008) **41**, 399-408.
22. Huo, H., Jiang, S., An, L., and Feng, J. "Influence of shear on crystallization behavior of the β phase in isotactic polypropylene with β-nucleating agent" *Macromolecules* (2004) **37**, 2478-2483.
23. Eder, G. and Janeschitz-Kriegl, H. "Crystallization", in *Materials Science and Technology: A Comprehensive Treatment*, R. W. Cahn, P. Haasen, E. J. Kramer, Eds., Vol. 18, (Wiley-VCH, Weinheim, 1997), 269-342.

24. Yamazaki, S., Hikosaka, M., Toda, A., Wataoka, I., Yamada, K., and Tagashira, K. "Nucleation and morphology of polyethylene under shear flow" J. Macromol. Sci., Part B: Phys. (2003) **42B**, 499-514.
25. Zhu, P.W., Tung, J., Phillips, A., and Edward, G. "Morphological development of oriented isotactic polypropylene in the presence of a nucleating agent" *Macromolecules* (2006) **39**, 1821-1831.
26. Housmans, J.W., Gahleitner, M., Peters, G.W.M., and Meijer, H.E.H. "Structure-property relations in molded, nucleated isotactic polypropylene" *Polymer* (2009) **50**, 2304-2319.
27. Kelarakis, A., Yoon, K., Sics, I., Somani, R.H., Chen, X., Hsiao, B.S., and Chu, B. "Shear-induced orientation and structure development in isotactic polypropylene melt containing modified carbon nanofibers" *J. Macromol. Sci., Phys.* (2006) **45B**, 247-261.
28. García-Gutiérrez, M.C., Hernández, J.J., Nogales, A., Panine, P., Rueda, D.R., and Ezquerra, T.A. "Influence of shear on the templated crystallization of poly(butylene terephthalate)/single wall carbon nanotube nanocomposites" *Macromolecules* (2008) **41**, 844-851.
29. Mago, G., Fisher, F.T., and Kalyon, D.M. "Effects of multiwalled carbon nanotubes on the shear-induced crystallization behavior of poly(butylene terephthalate)" *Macromolecules* (2008) **41**, 8103-8113.
30. Lee Wo, D. and Tanner, R.I. "The impact of blue organic and inorganic pigments on the crystallization and rheological properties of isotactic polypropylene" *Rheol. Acta* (2010) **49**, 75-88.
31. Zhu, P.W., Tung, J., Edward, G., and Nichols, L. "Effects of different colorants on morphological development of sheared isotactic polypropylene: A study using synchrotron wide-angle x-ray scattering" *J. Appl. Phys.* (2008) **103**, 124906.
32. Kristiansen, M., Werner, M., Tervoort, T., Smith, P., Blomenhofer, M., and Schmidt, H.W. "The binary system isotactic polypropylene/bis(3,4-dimethylbenzylidene)sorbitol: Phase behavior, nucleation, and optical properties" *Macromolecules* (2003) **36**, 5150-5156.
33. Liedauer, S., Eder, G., Janeschitz-Kriegl, H., Jerschow, P., Geymayer, W., and Ingolic, E. "On the kinetics of shear-induced crystallization in polypropylene" *Int. Polym. Process.* (1993) **8**, 236-244.
34. Kumaraswamy, G., Issaian, A.M., and Kornfield, J.A. "Shear-enhanced crystallization in isotactic polypropylene. 1. Correspondence between in situ rheo-optics and ex situ structure determination" *Macromolecules* (1999) **32**, 7537-7547.

35. Langouche, F. “Orientation development during shear flow-induced crystallization of i-PP” *Macromolecules* (2006) **39**, 2568-2573.
36. Baert, J., Van Puyvelde, P., and Langouche, F. “Flow-induced crystallization of PB-1: From the low shear rate region up to processing rates” *Macromolecules* (2006) **39**, 9215-9222.
37. Hadinata, C., Gabriel, C., Ruellmann, M., Kao, N., and Laun, H.M. “Shear-induced crystallization of PB-1 up to processing-relevant shear rates” *Rheol. Acta* (2006) **45**, 539-546.
38. Duplay, C., Monasse, B., Haudin, J.M., and Costa, J.L. “Shear-induced crystallization of polypropylene: Influence of molecular weight” *J. Mater. Sci.* (2000) **35**, 6093-6103.
39. Nogales, A., Hsiao, B.S., Somani, R.H., Srinivas, S., Tsou, A.H., Balta-Calleja, F.J., and Ezquerra, T.A. “Shear-induced crystallization of isotactic polypropylene with different molecular weight distributions: In situ small- and wide-angle X-ray scattering studies” *Polymer* (2001) **42**, 5247-5256.
40. Seki, M., Thurman, D.W., Oberhauser, J.P., and Kornfield, J.A. “Shear-mediated crystallization of isotactic polypropylene: The role of long chain-long chain overlap” *Macromolecules* (2002) **35**, 2583-2594.
41. Acierno, S., Palomba, B., Winter, H.H., and Grizzuti, N. “Effect of molecular weight on the flow-induced crystallization of isotactic poly(1-butene)” *Rheol. Acta* (2003) **42**, 243-250.
42. Hadinata, C., Gabriel, C., Ruellman, M., and Laun, H.M. “Comparison of shear-induced crystallization behavior of PB-1 samples with different molecular weight distribution” *J. Rheol.* (2005) **49**, 327-349.
43. Acierno, S., Coppola, S., and Grizzuti, N. “Effects of molecular weight distribution on the flow-enhanced crystallization of poly(1-butene)” *J. Rheol.* (2008) **52**, 551-566.
44. Yoshimoto, S., Ueda, T., Yamanaka, K., Kawaguchi, A., Tobita, E., and Haruna, T. “Epitaxial act of sodium 2,2'-methylene-bis-(4,6-di-t-butylphenylene) phosphate on isotactic polypropylene” *Polymer* (2001) **42**, 9627-9631.
45. Nagasawa, S., Fujimori, A., Masuko, T., and Iguchi, M. “Crystallisation of polypropylene containing nucleators” *Polymer* (2005) **46**, 5241-5250.
46. Behrendt, N., Mohmeyer, N., Hillenbrand, J., Klaiber, M., Zhang, X., Sessler, G.M., Schmidt, H.W., and Altstädt, V. “Charge storage behavior of isotropic and biaxially-oriented polypropylene films containing α- and β- nucleating agents” *J. Appl. Polym. Sci.* (2006) **99**, 650-658.

47. Xu, J., Srinivas, S., Marand, H., and Agarwal, P. “Equilibrium melting temperature and undercooling dependence of the spherulitic growth rate of isotactic polypropylene” *Macromolecules* (1998) **31**, 8230-8242.
48. Haas, T.W. and Maxwell, B. “Effects of shear stress on the crystallization of linear polyethylene and poly-1-butene” *Polym. Eng. Sci.* (1969) **9**, 225-241.
49. Padden, F.J., Jr. and Keith, H.D. “Spherulific crystallization in polypropylene” *J. Appl. Phys.* (1959) **30**, 1479-1484.
50. Varga, J. “Supermolecular structure of isotactic polypropylene” *J. Mater. Sci.* (1992) **27**, 2557-2579.
51. Sawyer, L.C., Grubb, D.T., and Meyers, G.F. *Polymer Microscopy*, 3rd ed. (Springer, New York, 2008).
52. Somani, R.H., Yang, L., Sics, I., Hsiao, B.S., Pogodina, N.V., Winter, H.H., Agarwal, P., Fruitwala, H., and Tsou, A. “Orientation-induced crystallization in isotactic polypropylene melt by shear deformation” *Macromol. Symp.* (2002) **185**, 105-117.
53. Kumaraswamy, G., Kornfield, J.A., Yeh, F., and Hsiao, B.S. “Shear-enhanced crystallization in isotactic polypropylene. 3. Evidence for a kinetic pathway to nucleation” *Macromolecules* (2002) **35**, 1762-1769.
54. Elmoumni, A. and Winter, H.H. “Large strain requirements for shear-induced crystallization of isotactic polypropylene” *Rheol. Acta* (2006) **45**, 793-801.
55. Vleeshouwers, S. and Meijer, H.E.H. “A rheological study of shear induced crystallization” *Rheol. Acta* (1996) **35**, 391-399.
56. Jay, F., Haudin, J.M., and Monasse, B. “Shear-induced crystallization of polypropylenes: Effect of molecular weight” *J. Mater. Sci.* (1999) **34**, 2089-2102.
57. Elmoumni, A., Gonzalez-Ruiz, R.A., Coughlin, E.B., and Winter, H.H. “Isotactic poly(propylene) crystallization: Role of small fractions of high or low molecular weight polymer” *Macromol. Chem. Phys.* (2005) **206**, 125-134.
58. Baert, J. and Van Puyvelde, P. “Effect of molecular and processing parameters on the flow-induced crystallization of poly-1-butene. Part 1: Kinetics and morphology” *Polymer* (2006) **47**, 5871-5879.
59. Tavichai, O., Feng, L., and Kamal, M.R. “Crystalline spherulitic growth kinetics during shear for linear low-density polyethylene” *Polym. Eng. Sci.* (2006) **46**, 1468-1475.
60. Haudin, J.M., Duplay, C., Monasse, B., and Costa, J.L. “Shear-induced crystallization of polypropylene. Growth enhancement and rheology in the crystallization range” *Macromol. Symp.* (2002) **185**, 119-133.

61. Coccorullo, I., Pantani, R., and Titomanlio, G. “Spherulitic nucleation and growth rates in an iPP under continuous shear flow” *Macromolecules* (2008) **41**, 9214-9223.
62. Koscher, E. and Fulchiron, R. “Influence of shear on polypropylene crystallization: Morphology development and kinetics” *Polymer* (2002) **43**, 6931-6942.
63. Kimata, S., Sakurai, T., Nozue, Y., Kasahara, T., Yamaguchi, N., Karino, T., Shibayama, M., and Kornfield, J.A. “Molecular basis of the shish-kebab morphology in polymer crystallization” *Science* (2007) **316**, 1014-1017.
64. Kumaraswamy, G., Verma, R.K., Kornfield, J.A., Yeh, F., and Hsiao, B.S. “Shear-enhanced crystallization in isotactic polypropylene. In-situ synchrotron SAXS and WAXD” *Macromolecules* (2004) **37**, 9005-9017.
65. Janeschitz-Kriegl, H. and Ratajski, E. “Kinetics of polymer crystallization under processing conditions: Transformation of dormant nuclei by the action of flow” *Polymer* (2005) **46**, 3856-3870.
66. Somani, R.H., Hsiao, B.S., Nogales, A., Srinivas, S., Tsou, A.H., Sics, I., Balta-Calleja, F.J., and Ezquerra, T.A. “Structure development during shear flow-induced crystallization of i-PP: In-situ small-angle X-ray scattering study” *Macromolecules* (2000) **33**, 9385-9394.
67. Housmans, J.-W., Steenbakkers, R.J.A., Roozemond, P.C., Peters, G.W.M., and Meijer, H.E.H. “Saturation of pointlike nuclei and the transition to oriented structures in flow-induced crystallization of isotactic polypropylene” *Macromolecules* (2009) **42**, 5728-5740.
68. Zuidema, H., Peters, G.W.M., and Meijer, H.E.H. “Development and validation of a recoverable strain-based model for flow-induced crystallization of polymers” *Macromol. Theory Simul.* (2001) **10**, 447-460.
69. Coppola, S., Grizzuti, N., and Maffettone, P.L. “Microrheological modeling of flow-induced crystallization” *Macromolecules* (2001) **34**, 5030-5036..
70. de Gennes, P.G. “Coil-stretch transition of dilute flexible polymers under ultrahigh velocity gradients” *J. Chem. Phys.* (1974) **60**, 5030-5042.
71. Zheng, R. and Kennedy, P.K. “A model for post-flow induced crystallization: General equations and predictions” *J. Rheol.* (2004) **48**, 823-842.
72. Tanner, R.I. and Qi, F. “Stretching, shearing and solidification” *Chem. Eng. Sci.* (2009) **64**, 4576-4579.

Chapter 6: Parameters Characterizing Shear-Induced Crystallization

6.1 Introduction

A number of parameters have been reported to be useful for characterizing acceleration in crystallization and/or the onset of morphological transition, but there is no agreement as to which is the most appropriate. How well some of these describe the results presented in the previous chapter is examined below.

6.2 Product of Shear Rate and Strain

The idea of using the product of shear rate and strain, $\dot{\gamma}_{\mathrm{s}}\gamma_{\mathrm{s}}$ or $\dot{\gamma}_{\mathrm{s}}^{2}t_{\mathrm{s}}$, came from personal communication with Prof. Hermann Janeschitz-Kriegl at Johannes Kepler University in Linz, Austria. In an early study [1], his group used an equivalent parameter of $\dot{\gamma}_{\mathrm{w}}^{2}t_{\mathrm{s}}$ to plot data obtained from pressure flow experiments, but recently [2-4], they have switched to using specific work. Rather than $\dot{\gamma}_{\mathrm{s}}$, the extrapolated wall shear rate $\dot{\gamma}_{\mathrm{w}}$ was used due to non-uniformity in pressure flow. Additionally, the authors [1] argued that a power of two was used for $\dot{\gamma}_{\mathrm{w}}$ because crystallization should not depend on the direction of shearing. As there is no other literature regarding use of $\dot{\gamma}_{\mathrm{s}}\gamma_{\mathrm{s}}$ for representing crystallization data, the applicability of this parameter remains to be verified.

Figure 6.1 shows double logarithmic plot of characteristic crystallization times versus $\dot{\gamma}_{\mathrm{s}}\gamma_{\mathrm{s}}$ for data obtained in the ranges of $1\ \mathrm{s}^{-1} \leq \dot{\gamma}_{\mathrm{s}} \leq 500\ \mathrm{s}^{-1}$ and $5 \leq \gamma_{\mathrm{s}} \leq 50$ for nucleated sample iPP1. The inset shows the data on a semi-log scale. Excluding those indicating morphological transition, the data shown for each characteristic time can be reasonably represented by a single curve. Compared to t_{ind}, both $t_{0.5I}$ and $t_{4\eta}$ appear to give better correlation for data with values of $\dot{\gamma}_{\mathrm{s}}\gamma_{\mathrm{s}} > 10\,000$. This is because these two crystallization times are less sensitive than t_{ind} in reflecting changes in kinetics that occur at the onset of a morphological transition. The good correlation of the data at moderate values of $\dot{\gamma}_\mathrm{s}\gamma_\mathrm{s}$ (*i.e.*, 50 $< \dot{\gamma}_\mathrm{s}\gamma_\mathrm{s} <$ 10 000) thus suggests that $\dot{\gamma}_\mathrm{s}\gamma_\mathrm{s}$ is an appropriate parameter for representing the effect of shear on crystallization kinetics that is associated with the increase in the number of point-like nuclei.

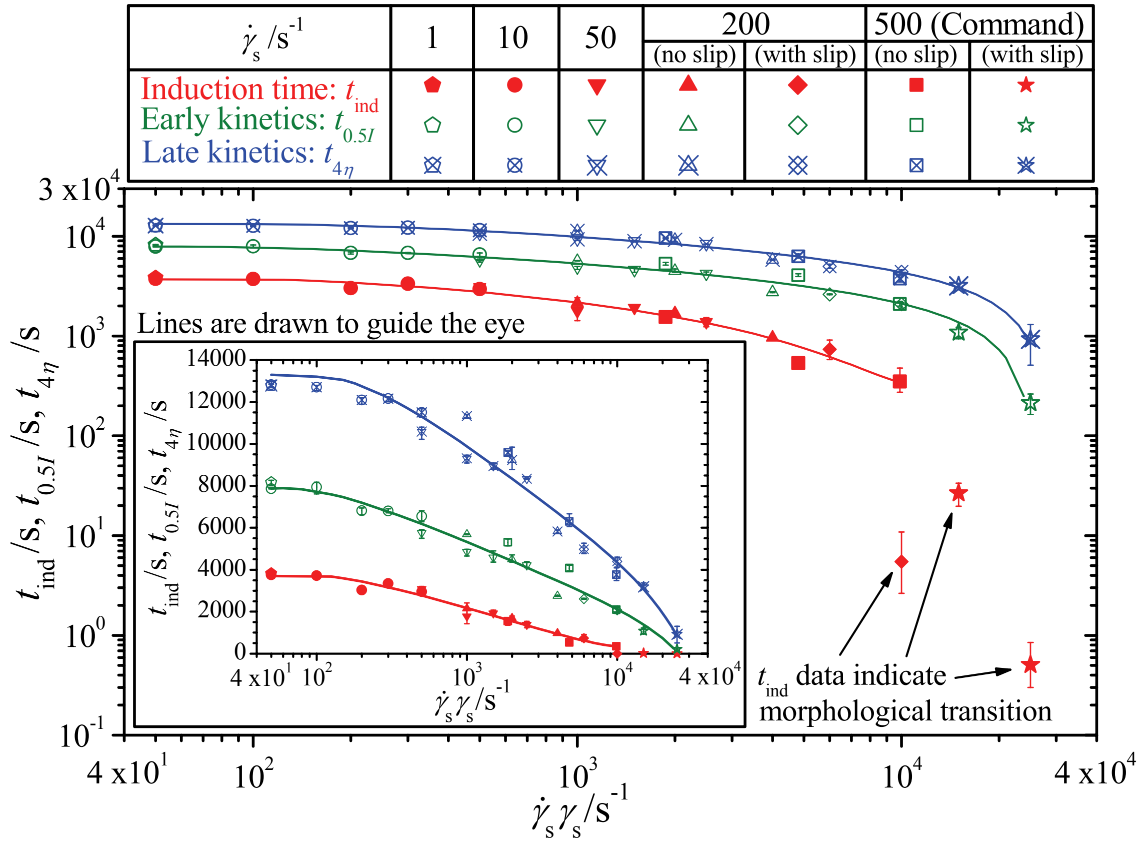

Figure 6.1. Dependence of characteristic crystallization times on the product of shear rate and strain for nucleated sample iPP1. The inset shows the data on a semi-log scale. The good correlation found for the data shown (excluding those indicating a morphological transition) implies that the product of shear rate and strain is able to describe satisfactorily the effect of shear on the increase in crystallization kinetics. Nominal values were used for shearing conditions involving slip. Data shown are averages and ranges for three measurements at 155.5 °C.

The less satisfactory correlation of the t_{ind} data at large values of $\dot{\gamma}_{\mathrm{s}}$ and γ_{s} (*i.e.*, $\dot{\gamma}_{\mathrm{s}}\gamma_{\mathrm{s}}$ > 10 000) implies that $\dot{\gamma}_{\mathrm{s}}\gamma_{\mathrm{s}}$ is less effective in representing the more complicated changes in kinetics that occur with morphological transition. As mentioned earlier, oriented structures only begin to form if $\dot{\gamma}_{\mathrm{s}}$ and γ_{s} both exceed some critical values. Because the dependence of these two critical values is highly nonlinear, it is not surprising that $\dot{\gamma}_{\mathrm{s}}\gamma_{\mathrm{s}}$ is inadequate to represent these complicated changes. Note that slip might have also affected the correlation for data with $\dot{\gamma}_{\mathrm{s}}\gamma_{\mathrm{s}} > 10\,000$, as nominal values of $\dot{\gamma}_{\mathrm{s}}$ and γ_{s} were used. If slip was absent, actual values of $\dot{\gamma}_{\mathrm{s}}\gamma_{\mathrm{s}}$ would be larger and t_{ind} would be lower.

Using a double logarithmic plot of the product of the characteristic optical retardation time $t_{\lambda/2}$ and growth rate G versus $\dot{\gamma}_{\mathrm{w}}^2 t_{\mathrm{s}}$ (or $\dot{\gamma}_{\mathrm{w}}\gamma_{\mathrm{w}}$), Janeschitz-Kriegl *et al.* [1] found that a straight line with a constant slope of -2 fit all their data. This is in sharp contrast to a monotonically decreasing curve with a slope that varies with $\dot{\gamma}_{\mathrm{s}}\gamma_{\mathrm{s}}$ for the t_{ind} data shown in Fig. 6.1, *viz.*, a slope of $>$-1/4 at small $\dot{\gamma}_{\mathrm{s}}\gamma_{\mathrm{s}}$ and increasing steepness with a value of $<$-4 at large $\dot{\gamma}_{\mathrm{s}}\gamma_{\mathrm{s}}$. Several issues make it difficult to ascertain the main cause of these discrepancies. First, the experiments in the present study applied a constant shear rate, *i.e.*, $\dot{\gamma}_{\mathrm{s}}$ does not vary with t_{s}, whereas those in these authors' study applied a constant pressure drop or wall shear stress σ_{w}, *i.e.*, $\dot{\gamma}_{\mathrm{w}}$ varies with t_{s} before reaching a steady flow. It is a crude approximation to represent $\dot{\gamma}_{\mathrm{w}}$ as a constant, although the authors [5] noted that a strain of five units would be adequate for the applied flow condition to become steady and that their experiments used strains much greater than this minimum strain. Strictly speaking, this means that $\dot{\gamma}_{\mathrm{w}}^2 t_{\mathrm{s}}$ is not an accurate parameter describing the flow history of their measurements; in fact, it would seem more appropriate to use σ_{w} since it is the controlled variable in pressure flow. Thus, despite the apparent similarity between $\dot{\gamma}_{\mathrm{w}}^2 t_{\mathrm{s}}$ and $\dot{\gamma}_{\mathrm{s}}\gamma_{\mathrm{s}}$, the validity of the comparison becomes unclear as the flow histories are not the same. Second, the ordinates used are different:

$t_{\lambda/2}G$ was used by Janeschitz-Kriegl *et al.* whereas t_{ind} was selected here. Multiplication of $t_{\lambda/2}$ by G should not affect the comparison, because a constant growth rate was assumed. The difference in sensitivity between $t_{\lambda/2}$ and t_{ind} might contribute to the differences in the values of the slope (on a log-log plot), but this cannot be the reason for the difference between a straight line and a monotonically decreasing curve. Third, the data obtained by these authors appear to represent only the crystallization kinetics of the highly oriented structures at the skin layer. For the data presented, skin-core morphology was found due to non-uniformity in stress and shear rate in pressure flow. No data were provided in the case when oriented structures was not observed; or in other words, it is not known from their results how crystallization kinetics would change with $\dot{\gamma}_{\mathrm{w}}^{2}t_{\mathrm{s}}$ if the effect of shear is only in increasing the number of point-like nuclei. This contrasts with the present study, which showed that $\dot{\gamma}_{\mathrm{s}}\gamma_{\mathrm{s}}$ is more useful for representing the kinetics associated with enhancement in point-like nuclei than that accompanying the formation of oriented structures. Fourth, it is uncertain if the use of non-nucleated, degraded samples in their study might contribute to the discrepancies.

In a later study [6], these authors used a different set of samples, of which two were nucleated with a melt-sensitive sorbitol compound. Instead of -2, a slope of -1 based on plots of $t_{\lambda/2}$ versus t_{s} was reported for nucleated and non-nucleated samples. The results given for one of the nucleated samples (Fig. 6 in [6]) are presented here in Fig. 6.2a using $\dot{\gamma}_{\mathrm{w}}\gamma_{\mathrm{w}}$ as the abscissa. Considering the wide range of strains studied ($35 \le \gamma_{\mathrm{w}} \le 870$), the correlation is considered acceptable, although a slope of -1 is only a fair fit. Highly oriented structures (see Fig. 10 in [6]) were associated with these data. It is puzzling why $\dot{\gamma}_{\mathrm{w}}\gamma_{\mathrm{w}}$ seems to describe the highly oriented growth quite well in their study while the correlation with $\dot{\gamma}_{\mathrm{s}}\gamma_{\mathrm{s}}$ in the present work was found to be poor when morphological transition is induced.

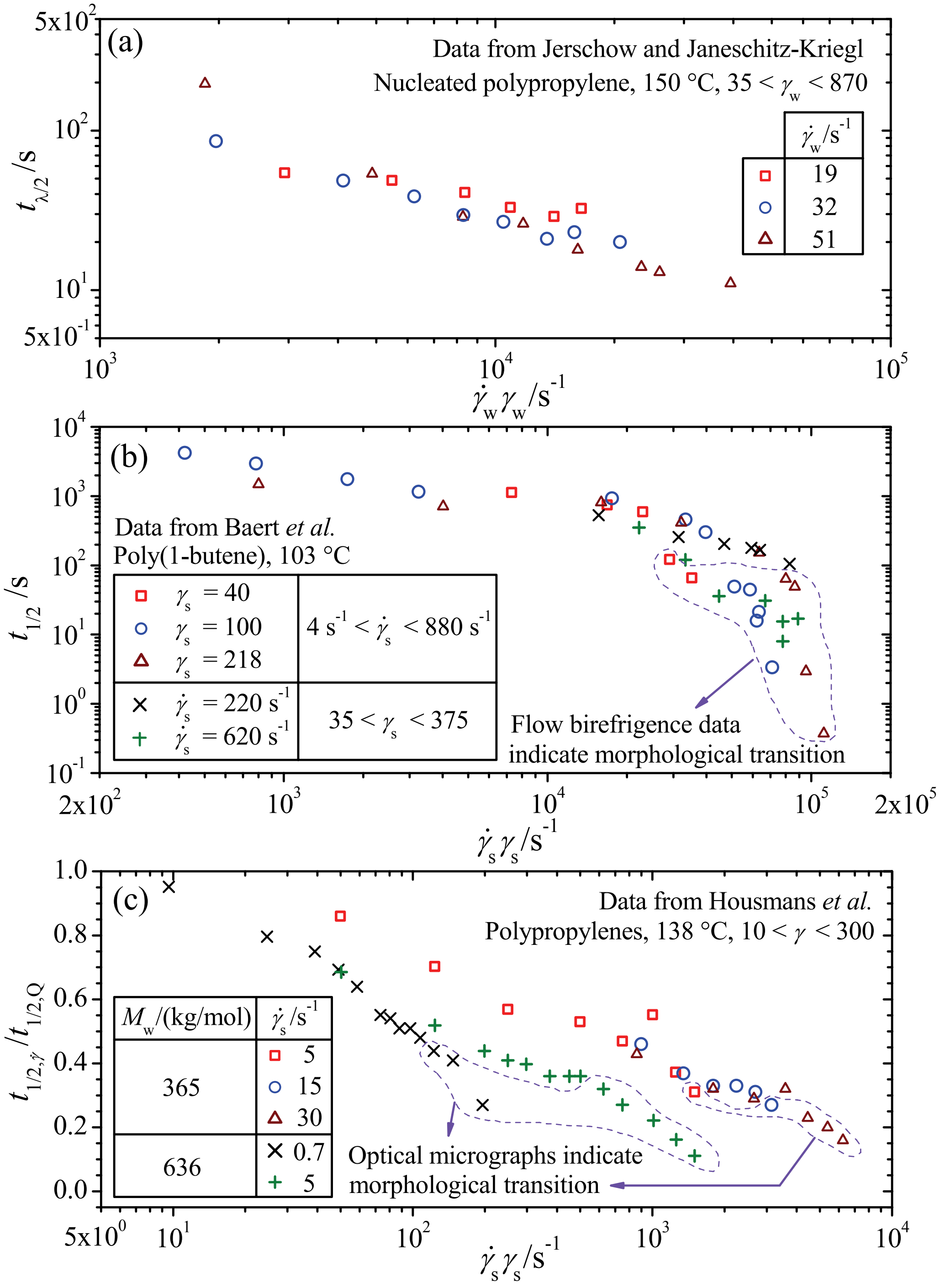

Figure 6.2. Crystallization characteristic time (see Table 5.3 for definitions) versus the product of shear rate and strain for data taken from selected references: (a) Jerschow and Janeschitz-Kriegl [6], (b) Baert *et al.* [7], and (c) Housmans *et al.* [8]. The good correlation of these data (excluding those indicating a morphological transition) confirms the applicability of the product of shear rate and strain for describing shear-induced crystallization kinetics.

No other group has plotted their data using $\dot{\gamma}_s\gamma_s$. In order to verify the applicability of this parameter, data taken from recent publications of two groups [7, 8] are plotted versus $\dot{\gamma}_s\gamma_s$ in Figs. 6.2b and c. Previously, analysis of these data was carried out using only plots of t_s, $\dot{\gamma}_s$ and γ_s. Definitions of the characteristic crystallization times shown in these figures, *i.e.*, $t_{1/2}$ and $t_{1/2,\dot{\gamma}} / t_{1/2,Q}$, were given in Table 5.3. A sliding plate device [7] and a rotational rheometer [8] were used, thus complications associated with the use of pressure flow were eliminated. The samples studied were non-nucleated poly(1-butene) and polypropylene. Figure 6.2b shows the data of Baert *et al.* (Figs. 8 and 9 in [7]) obtained for a wide range of shear rates and strains ($4\ \text{s}^{-1} \leq \dot{\gamma}_s \leq 880\ \text{s}^{-1}$, $35 \leq \gamma_s \leq 375$). Excluding those indicating morphological transition (within the region marked with dash line), the data shown correlate very well with $\dot{\gamma}_s\gamma_s$. Figure 6.2c shows the data of Housmans *et al.* (Figs. 7 and 8 in [8]) obtained for two polypropylenes of different molecular weights. The shear rates used were quite low ($0.7\ \text{s}^{-1} \leq \dot{\gamma}_s \leq 30\ \text{s}^{-1}$), although the strains were large ($10 \leq \gamma_s \leq 300$). Similarly, a fair correlation with $\dot{\gamma}_s\gamma_s$ was found for data that indicate no morphological transition for each sample. As no material property is accounted for by $\dot{\gamma}_s\gamma_s$, data between samples of different M_w are not expected to overlap. This is illustrated in Fig. 6.2c, wherein data of the high-molecular weight sample are found at lower values than those of the low-molecular weight sample at comparable $\dot{\gamma}_s\gamma_s$. Clearly, the results presented in Figs. 6.2b and c support the present findings that $\dot{\gamma}_s\gamma_s$ is more suitable for representing crystallization kinetics associated with point-like nuclei than for characterizing morphological changes. And importantly, the results also confirm the applicability of this empirical parameter not only for nucleated and non-nucleated polymers but also for a very broad range of shear rates and strains, *i.e.*, at least two orders of magnitude.

The feasibility of relating crystallization time to $\dot{\gamma}_s\gamma_s$ implies that shear rate and strain are equally effective in enhancing the number of point-like nuclei that lead to acceleration in crystallization. In other words, a reduction in the crystallization time, before reaching saturation and inducing morphological transition, can be accomplished by increasing either $\dot{\gamma}_{\mathrm{s}}$ or γ_{s} by the same proportion at comparable $\dot{\gamma}_{\mathrm{s}}\gamma_{\mathrm{s}}$. Somani *et al.* [9] investigated the relative importance of $\dot{\gamma}_{\mathrm{s}}$ and γ_{s} using a rotational flow device by small-angle X-ray scattering and wide-angle X-ray diffraction measurements, and concluded that the effect of $\dot{\gamma}_{\mathrm{s}}$ is much stronger than that of γ_{s} at comparable values of $\dot{\gamma}_{\mathrm{s}}\gamma_{\mathrm{s}}$. However, their study only considered two pairs of measurements using a rather narrow range of shear rates, *i.e.*, $30\ \mathrm{s}^{-1} \leq \dot{\gamma}_{\mathrm{s}} \leq 60\ \mathrm{s}^{-1}$. Additionally, the differences in the published X-ray images (Fig. 3 in [9]) do not seem to be as significant as described by these authors. In contrast, the conclusion made here was based on results for a much broader range of shearing conditions ($1\ \mathrm{s}^{-1} \leq \dot{\gamma}_{\mathrm{s}} \leq 500\ \mathrm{s}^{-1}$ and $5 \leq \gamma_{\mathrm{s}} \leq 50$ in this work, see Fig. 6.2 for shearing conditions used in other studies). Hence, in cases when morphological transition does not take place, it is reasonable to accept the notion of an equal importance of $\dot{\gamma}_{\mathrm{s}}$ and γ_{s}.

6.3 Product of Characteristic Relaxation Time and $\dot{\gamma}_{\mathrm{s}}\gamma_{\mathrm{s}}$

It is very desirable to have a parameter that also accounts for the effect of molecular weight. A practical approach is to multiply $\dot{\gamma}_{\mathrm{s}}\gamma_{\mathrm{s}}$ by a rheological quantity that is related to M_{w}. Either a viscosity or a characteristic relaxation time seems a sensible choice. The product of a viscosity and $\dot{\gamma}_{\mathrm{s}}\gamma_{\mathrm{s}}$ is analogous to specific work [4], which is discussed later. On the other hand, multiplying $\dot{\gamma}_{\mathrm{s}}\gamma_{\mathrm{s}}$ by a characteristic relaxation time renders the resulting parameter dimensionless. Obviously, this approach assumes that an average relaxation time is adequate in representing the overall relaxation dynamics. Several options are available for this time (see Chapter 3), thus the selection of one that is most relevant is not straightforward.

The reptation time τ_{d} and the weight-average relaxation time τ_{w} were evaluated by comparing data for nucleated sample iPP1 with those for the other three samples using plots of t_{ind} versus $\tau_{\mathrm{d}}\dot{\gamma}_{\mathrm{s}}\gamma_{\mathrm{s}}$ (Fig. 6.3) and versus $\tau_{\mathrm{w}}\dot{\gamma}_{\mathrm{s}}\gamma_{\mathrm{s}}$ (inset). The values of τ_{d} and τ_{w} are given in Table 3.1. Only the t_{ind} data are shown because this time has been shown to best reflect the effect of shear on crystallization kinetics and is very sensitive to M_{w} (inset in Fig. 5.4a). Comparing the data shown in Fig. 6.3 with those in the inset reveals that $\tau_{\mathrm{d}}\dot{\gamma}_{\mathrm{s}}\gamma_{\mathrm{s}}$ gives a slightly better correlation than $\tau_{\mathrm{w}}\dot{\gamma}_{\mathrm{s}}\gamma_{\mathrm{s}}$. The values of τ_{d} and τ_{w} differ by two orders of magnitude (see Table 3.1), but the main difference between these two times is that τ_{w} is more sensitive to the breadth of the molecular weight distribution. Results comparable to those of τ_{d} would be obtained if either the number-average relaxation time τ_{n} or simply the zero-shear viscosity η_0 were used (due to the proportional relationships between these three quantities, see Chapter 3). It should be mentioned that only when the plateau moduli G_{N}^{0} are different that the results obtained with τ_{d} and those with η_0 do not scaled proportionally.

Because τ_{c} is much easier to measure than τ_{d} and τ_{w}, this characteristic relaxation time, which is the inverse of the frequency at which the storage and loss moduli cross has been used in some work [10]. However, this time has only been used to form a Weissenberg number for characterizing the onset of a morphological transition, and there has been no report of its use with $\dot{\gamma}_{\mathrm{s}}\gamma_{\mathrm{s}}$. Results comparable to those shown in Fig. 6.3 were obtained when τ_{d} was replaced by τ_{c} , and this is expected because of the approximate proportionality between these two times for the four samples studied (see values in Table 3.1). A relaxation time reflecting the high-molecular weight components, in conjunction with the Weisssenberg number (sometimes denoted incorrectly as the Deborah number), has also been used to classify shear-induced crystallization behavior [8, 11]. The justification for this is that long chains can be much more easily stretched and relax much more slowly than short ones in a polydisperse sample, and they are therefore thought to be more important in inducing an oriented morphology. But this idea has been criticized by Janeschitz-Kriegl [4] as being not realistic. Additionally, there is no reliable method to estimate such a relaxation time*. For these reasons, this time was not considered in the present study.

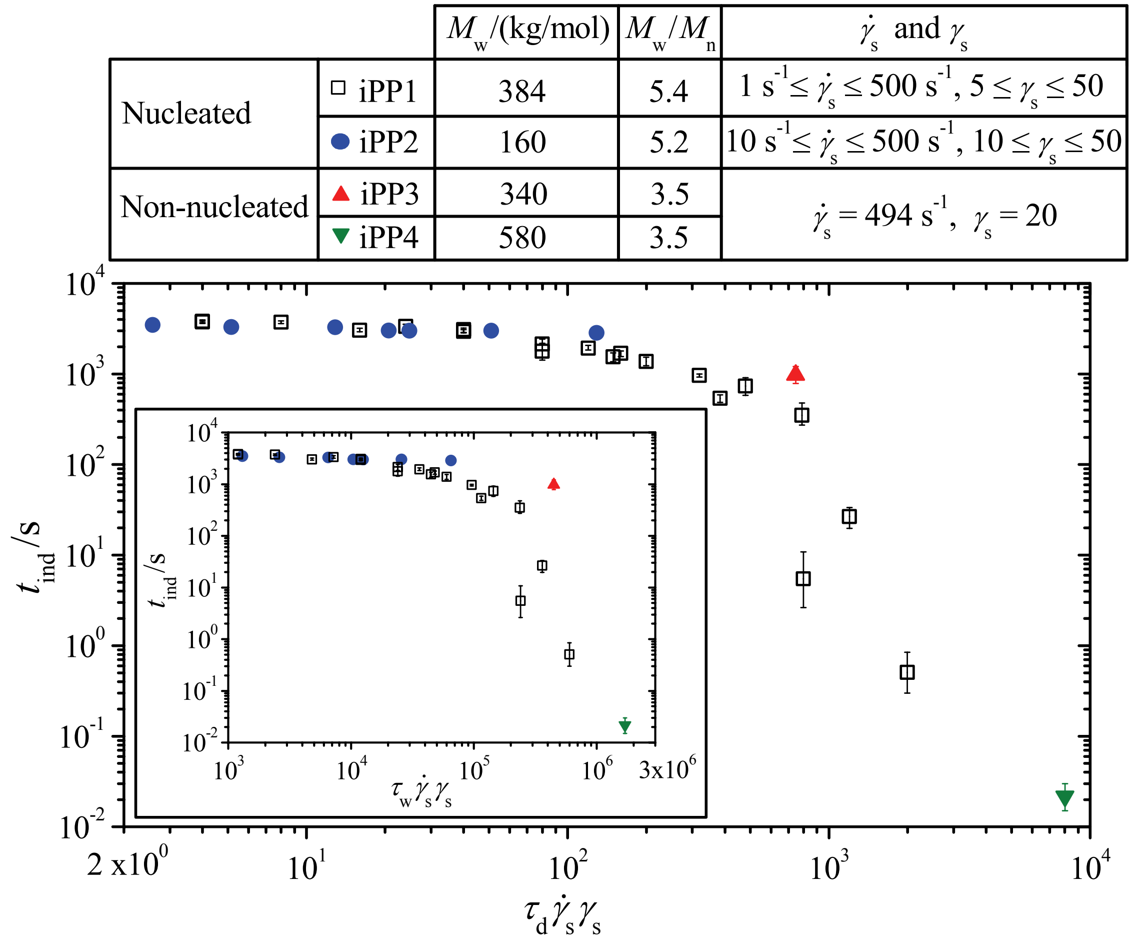

		M_w/(kg/mol)	M_w/M_n	$\dot{\gamma}_s$ and γ_s
Nucleated	□ iPP1	384	5.4	$1\ s^{-1} \le \dot{\gamma}_s \le 500\ s^{-1}$, $5 \le \gamma_s \le 50$
	● iPP2	160	5.2	$10\ s^{-1} \le \dot{\gamma}_s \le 500\ s^{-1}$, $10 \le \gamma_s \le 50$
Non-nucleated	▲ iPP3	340	3.5	$\dot{\gamma}_s = 494\ s^{-1}$, $\gamma_s = 20$
	▼ iPP4	580	3.5	

Figure 6.3. Dependence of induction time on the product of reptation time, shear rate and strain for the four samples studied. The inset shows the results obtained using the weight-average relaxation time in place of the reptation time. The reptation time appears to be useful to account for the effect of molecular weight (see text). The effect of molecular weight Nominal values were used for shearing conditions involving slip (see Fig. 6.1). Data shown are averages and ranges for three measurements at 155.5 °C.

---

* The presently available methods [11] are still considered unsatisfactory, because the criteria used are somewhat arbitrary. For example, there is uncertainty in determining the longest, discrete relaxation time using a Maxwell model since the relaxation strength decreases monotonically with the relaxation time (see Fig. 3.6a). Furthermore, the high-molecular weight components do not act individually and a critical concentration is needed.

If a relaxation time were not used, iPP2 would have a much longer t_{ind} than iPP1 at large values of $\dot{\gamma}_{\mathrm{s}}\gamma_{\mathrm{s}}$ (*e.g.*, at $\dot{\gamma}_{\mathrm{s}}\gamma_{\mathrm{s}}$ = 9880, t_{ind} = 3000 s for iPP2 and t_{ind} = 350 s for iPP1), meaning that the data for iPP2 would be much higher than those for iPP1 at comparable values of $\dot{\gamma}_{\mathrm{s}}\gamma_{\mathrm{s}}$. This difference can be accounted for by the use of $\tau_{\mathrm{d}}\dot{\gamma}_{\mathrm{s}}\gamma_{\mathrm{s}}$ in Fig. 6.3, since the value of τ_{d} of iPP2 is about one order of magnitude smaller than that of iPP1.

Not much can be said for iPP3 and iPP4, as only two data points are available (Fig. 6.3). Experiments at low $\dot{\gamma}_{\mathrm{s}}$ and γ_{s} were not performed, but due to the absence of nucleating agent, the t_{ind} data for these two samples are expected to be much larger than those of iPP1 and iPP2. This difference cannot be accounted for by the use of $\tau_{\mathrm{d}}\dot{\gamma}_{\mathrm{s}}\gamma_{\mathrm{s}}$ alone. A procedure that can be used to produce comparable results for all the four samples at low $\dot{\gamma}_{\mathrm{s}}\gamma_{\mathrm{s}}$ is to normalize the data to the t_{ind} value in quasi-quiescent crystallization. This procedure has been used in some studies [8, 12-14] but for different purposes. However, the normalization will also shift the t_{ind} data at large $\dot{\gamma}_{\mathrm{s}}\gamma_{\mathrm{s}}$ to lower values. Hence, it is not possible to use a single parameter to represent the dominant influence of nucleating agent at low $\dot{\gamma}_{\mathrm{s}}\gamma_{\mathrm{s}}$ and the strong effect of M_{w} at large $\dot{\gamma}_{\mathrm{s}}\gamma_{\mathrm{s}}$.

Some groups have used an apparently similar parameter for correlating data obtained for non-nucleated polymers [12, 14]. Hadinata *et al.* [14] demonstrated the feasibility of using $\tau_{\mathrm{w}}^{0.5}\dot{\gamma}t_{\mathrm{onset,q}}^{0.5}$ to superpose data obtained at three temperatures for three poly(1-butene) samples, where $t_{\mathrm{onset,q}}$ was defined as the onset crystallization time based on an upturn in viscosity at a shear rate sufficiently low ($\dot{\gamma}$ = 0.0001 s^{-1}) that the crystallization kinetics was comparable to that under quiescent conditions. They used a "characteristic retardation time" τ_{w}, because their samples had very broad molecular weight distributions (5.7 $\leq M_{\mathrm{w}}/M_{\mathrm{n}} \leq$ 19.6). In their experiments, shearing was applied continuously, so $\dot{\gamma}$ rather than $\dot{\gamma}_{\mathrm{s}}$ is used here to denote shear rate. The effect of $\dot{\gamma}$ on crystallization kinetics was studied at low shear rates ($\dot{\gamma} \leq 0.3\ \mathrm{s}^{-1}$), but the range was extended to $10^{-4}\ \mathrm{s}^{-1} \leq \dot{\gamma} \leq 500\ \mathrm{s}^{-1}$ in a later study [15]. In justifying the use of $\tau_{\mathrm{w}}^{0.5}\dot{\gamma}t_{\mathrm{onset,q}}^{0.5}$, these authors explained that $\dot{\gamma}t_{\mathrm{onset,q}}^{0.5}$ would be equivalent to $\dot{\gamma}_{\mathrm{s}}^{2}t_{\mathrm{s}}$ in Janeschitz-Kriegl's model [1, 5, 6] if $\dot{\gamma}t_{\mathrm{onset,q}}^{0.5}$ were squared, and this analogy is also noted in Janeschitz-Kriegl's new book [4]. On close inspection, the analogy does not seem to be well founded, because t_{s} and $t_{\mathrm{onset,q}}$ are totally unrelated quantities; t_{s} denotes a short duration of shearing and can vary with $\dot{\gamma}_{\mathrm{s}}$, whereas $t_{\mathrm{onset,q}}$ represents the typically long crystallization time measured under quiescent conditions and is invariant with $\dot{\gamma}$.

On the other hand, Baert and van Puyvelde [12] used $\tau_{\mathrm{d}}\dot{\gamma}_{\mathrm{s}}t_{1/2,\mathrm{q}}^{0.5}$ to represent data obtained at three temperatures for three poly(1-butene) samples, of which two were the same used by Hadinata *et al.* [14]. These authors used the short-term shearing protocol, thus allowing direct comparison with the present work. Unlike the parameters used in the present study and by Hadinata *et al.* [14], $\tau_{\mathrm{d}}\dot{\gamma}_{\mathrm{s}}t_{1/2,\mathrm{q}}^{0.5}$ is not dimensionless and has a non-integer dimension. More importantly, instead of t_{s} or γ_{s}, the turbidity half-time observed under quiescent crystallization $t_{1/2,\mathrm{q}}$ was used. For the same reason as $t_{\mathrm{onset,q}}$, $t_{1/2,\mathrm{q}}$ is used to compensate for the differences in quiescent crystallization kinetics due to temperature and molecular weight, but its relevance in shear-induced crystallization is questionable, since it is simply a constant that does not vary with shearing conditions. Obviously, the parameter $\tau_{\mathrm{d}}\dot{\gamma}_{\mathrm{s}}t_{1/2,\mathrm{q}}^{0.5}$ omits the influence of shearing time or strain. As a result, rather than showing one curve for data at various $\dot{\gamma}_{\mathrm{s}}$ and γ_{s}, the published data [12] show separate curves for various values of γ_{s}. It should be mentioned that in the studies of Baert and van Puyvelde [12] and Hadinata *et al.* [14], the measured crystallization time in shear-induced crystallization was normalized by that under quiescent crystallization, *i.e.*, $t_{1/2,\mathrm{q}}$ or $t_{\mathrm{onset,q}}$. As mentioned earlier, this normalization step facilitates the correlation of data at low $\dot{\gamma}_\mathrm{s}$ and γ_s. In short, while $\tau_\mathrm{w}^{0.5}\dot{\gamma}t_\mathrm{onset,q}^{0.5}$ and $\tau_\mathrm{d}\dot{\gamma}_\mathrm{s}t_\mathrm{1/2,q}^{0.5}$ have been reported to give good correlations [12, 14], the effect of γ_s or t_s is omitted, making these parameters unsuitable for general application.

6.4 Specific Work

In view of the limitations of their model based on $\dot{\gamma}_\mathrm{s}^2 t_\mathrm{s}$ [1, 5, 6], Janeschitz-Kriegl *et al.* [2-4] recently recommended that $\dot{\gamma}_\mathrm{s}^2 t_\mathrm{s}$ be replaced by specific work w, which is the total mechanical work per unit volume applied over the duration of shearing. Their new approach differs significantly from their earlier work [1, 5, 6] in two main aspects: first, the number density of nuclei determined by counting the spherulites in the solidified samples, rather than crystallization time inferred from optical retardation measurements, is used to correlate with specific work; and second, a sliding plate device designed for shearing at a constant stress, rather than pressure flow, is used. In justifying the use of specific work, Janeschitz-Kriegl [4] explained that the rate of this quantity is the product of shear stress and shear rate, and that shear stress is a measure of chain orientation, whereas shear rate represents the probability of an encounter between oriented chains. The definition of specific work is given by Eq. 6.1, but this equation is not used in most studies. As given below for comparison (Eqs. 6.2–6.4), expressions resulting from various assumptions are more commonly used [2, 8, 16, 17].

$$w \equiv \int_0^{t_\mathrm{s}} \sigma(t)\,\dot{\gamma}_\mathrm{s}(t)\,\mathrm{d}t \tag{6.1}$$

$$w = \bar{\eta}\int_0^{t_\mathrm{s}} \dot{\gamma}_\mathrm{s}^2(t)\,\mathrm{d}t \tag{6.2}$$

$$w = \int_0^{t_\mathrm{s}} \eta(\dot{\gamma})\,\dot{\gamma}_\mathrm{s}^2(t)\,\mathrm{d}t = \int_0^{t_\mathrm{s}} \left|\eta^*(\omega)\right|\dot{\gamma}_\mathrm{s}^2(t)\,\mathrm{d}t = \int_0^{t_\mathrm{s}} \left[\frac{\eta_1}{1+\left(\omega/\omega_1\right)^{\alpha_1}} + \eta_2\right]\dot{\gamma}_\mathrm{s}^2(t)\,\mathrm{d}t \tag{6.3}$$

$$w = \eta(\dot{\gamma})\,\dot{\gamma}_\mathrm{s}^2 t_\mathrm{s} = \left|\eta^*(\omega)\right|\dot{\gamma}_\mathrm{s}^2 t_\mathrm{s} = \left[\frac{\eta_0}{1+\left(K\omega\right)^{1-m}}\right]\dot{\gamma}_\mathrm{s}^2 t_\mathrm{s} \tag{6.4}$$

where σ is shear stress, η is viscosity, $\overline{\eta}$ is the "viscosity averaged over the shear rates experienced" [2], η_0 is zero-shear viscosity, $\left|\eta^*(\omega)\right|$ is the magnitude of the complex viscosity, ω is the frequency in small-amplitude oscillatory shear, η_1, η_2, ω_1, α_1, K and m are fitting parameters.

Plots of characteristic crystallization times versus specific work for iPP1 are shown on a semi-log scale in Fig. 6.4 and on a linear scale in the inset. Specific work was calculated according to Eq. 6.1, and the integral was evaluated only for the transient stress measured during shearing (see Section 3.5.5), since $\dot{\gamma}_\mathrm{s}$ does not vary with t_s. Nominal values are given for specific work when data indicate slip. Particularly for those indicating no morphological transition, the data shown in Fig. 6.4 do not seem to correlate well with specific work. In stark contrast to the good correlation found with $\dot{\gamma}_\mathrm{s}\gamma_\mathrm{s}$ in Fig. 6.1, the large spread of the data shown in Fig. 6.4 suggests that specific work is much less satisfactory than $\dot{\gamma}_\mathrm{s}\gamma_\mathrm{s}$ for representing the effect of shear on crystallization kinetics. In other words, the transient stress does not appear to be a relevant rheological quantity. A double logarithmic plot was also used by Janeschitz-Kriegl *et al.* [2], but even if this is used, the correlation is still not as good as that based on $\dot{\gamma}_\mathrm{s}\gamma_\mathrm{s}$.

Instead of using the exact equation for specific work, Janeschitz-Kriegl *et al.* [2] used Eq. 6.2 in their calculation. Unlike the present work, their study used creep experiments with shear stresses in the range of 25 kPa $\le \sigma \le$ 85 kPa (extended to 250 kPa in a later study [3]). As both shear rate and viscosity vary with time during the start-up period, they assumed an average viscosity over the duration of shearing; and in some cases [4], they further assumed a constant shear rate and calculated specific work using $\eta\dot{\gamma}_\mathrm{s}^2 t_\mathrm{s}$. Interestingly, they found that the number density of nuclei and specific work yielded a straight line on a double logarithmic plot, with a temperature-dependent slope having a value between three and four for iPP. More simply put, $N \propto w^n \propto \left(\eta\dot{\gamma}_\mathrm{s}^2 t_\mathrm{s}\right)^n$ with $3 \le n \le 4$

for temperature range from 140 °C to 160 °C. They also reported that specific work can be used as a universal parameter to analyze the results obtained from both shear- and extension-induced crystallizations. By extrapolating the straight lines at various temperatures to the results from an earlier study using pressure flow, they estimated that the transition from point-like nuclei to threadlike precursors occurs at a critical specific work of 25 MPa [4].

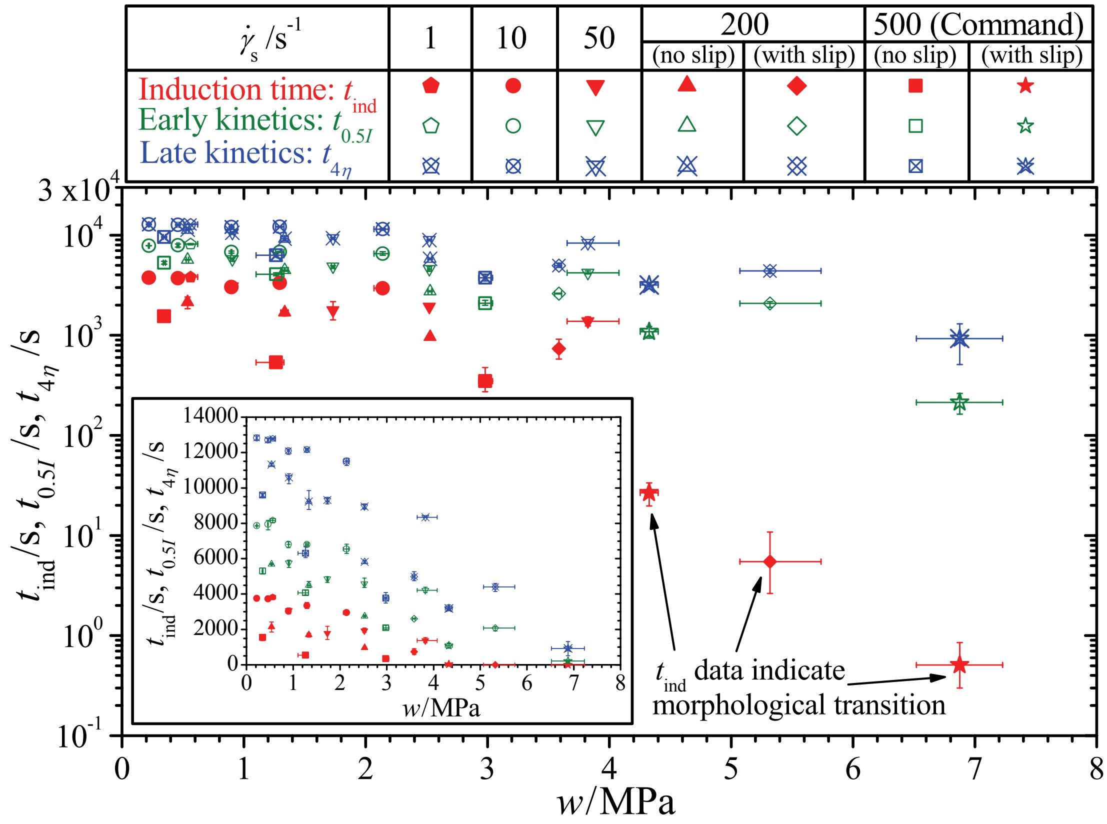

Figure 6.4. Dependence of characteristic crystallization times on specific work for iPP1. The inset shows the data on a linear scale. The poor correlation of the data suggests that specific work is less satisfactory than the product of shear rate and strain to describe shear-induced crystallization kinetics. Nominal values were used for shearing conditions involving slip. Data shown are averages and ranges for three measurements at 155.5 °C.

There are two major discrepancies between their results and the present findings. First, the poor correlation of the data with specific work shown in Fig. 6.4 is in sharp contrast to the good power-law relationship found by those authors. In the correlation, data based on crystallization times were used in the present work, whereas those based on the number density of nuclei were used in their study; but this should not cause a discrepancy, since these two quantities are proportionately related, *i.e.*, a shorter induction time corresponds to a larger number density of nuclei. It is not clear whether difference in the flow history, *i.e.*, constant σ in their study versus constant $\dot{\gamma}_{\mathrm{s}}$ in the present work, might be the source of the discrepancy. No other work has experimentally confirmed the reported $N \propto w^n$ relationship. Thus, it is not possible to establish the cause of the discrepancy. Second, the critical specific work at which morphological transition commences is estimated to be in the range of 3.5 MPa to 4.5 MPa for iPP1 (nominal value, based on Fig. 6.4), whereas a much larger value of 25 MPa was reported in their study [4]. Additionally, as mentioned in the previous chapter, growth of oriented structures was also found for non-nucleated sample iPP4 after being sheared at $\dot{\gamma}_{\mathrm{s}}$ = 498 s^{-1} and γ_{s} = 20. At these conditions, the specific work was (5.6 ± 0.6) MPa, which is also much lower than the suggested threshold of 25 MPa.

Specific work was also used recently by Mykhaylyk *et al.* [16] and Housmans *et al.* [8] to analyze their data. Both groups used rotational flow devices, *viz.*, a Linkam shear cell and a rotational rheometer. Parallel-plate fixtures were used, and shear rate was thus not uniform but varied with radius. In the calculation of specific work, they both neglected the transient stress change during the start-up period, and assumed a constant viscosity, and then applied the so-called Cox-Merz rule [18, 19], *i.e.*, $\eta(\dot{\gamma}) = \left|\eta^*(\omega)\right|$ with $\dot{\gamma} = \omega$. The empirical equations used for fitting the $\left|\eta^*(\omega)\right|$ data were different; Mykhaylyk *et al.* [16] used Eq. 6.3 whereas Housmans *et al.* [8] used Eq. 6.4. A pertinent question is whether these approximations would affect the correlation. Figure 6.5 compares results obtained using the exact definition (Eq. 6.1) and those based on a simplified equation

$w = |\eta^*(\omega)|\dot{\gamma}_\mathrm{s}\gamma_\mathrm{s}$ (*i.e.*, with the assumptions of steady flow and the Cox-Merz rule), where the values of $|\eta^*(\omega)|$ used for calculations were taken from the data shown in Fig. 3.1. The comparison indicates that the simplified equation provides a fair approximation of the specific work, with a maximum error of 16 % relative to the calculations based on Eq. 6.1. This implies that the assumptions used by Mykhaylyk *et al.* [16] and Housmans *et al.* [8] were quite reasonable.

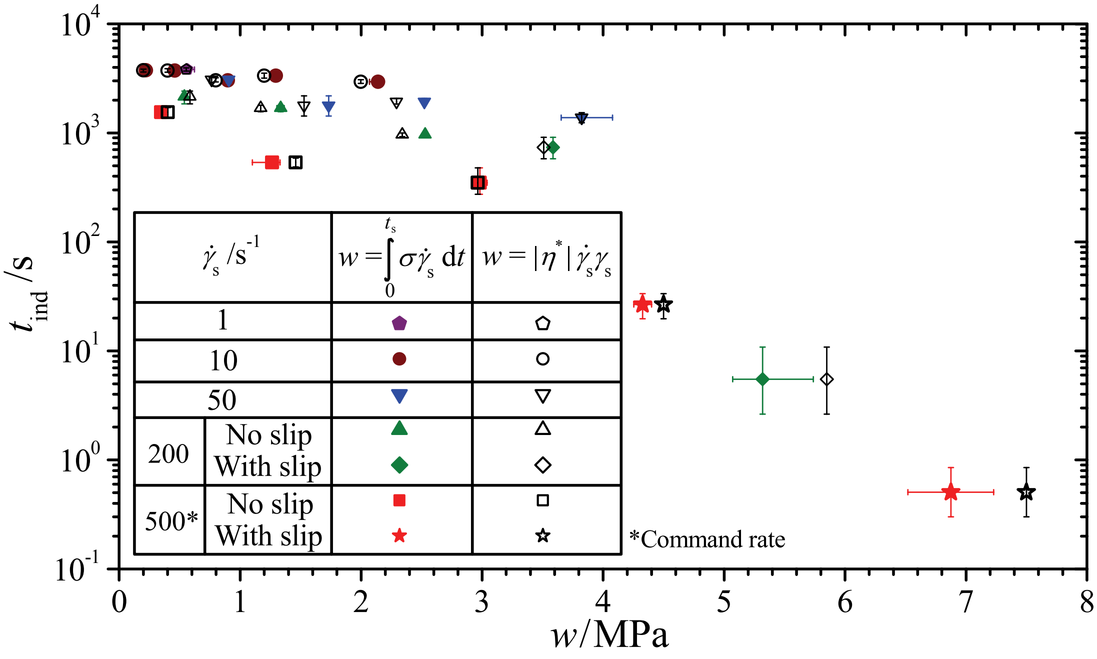

Figure 6.5. Comparison of the correlation results based on induction time for specific work calculated using the exact definition and that calculated using a simplified equation. Nominal values were used for shearing conditions involving slip. Data shown are averages and ranges for three measurements for iPP1 at 155.5 °C.

Mykhaylyk *et al.* [16] correlated the morphology observed by *ex-situ* small-angle X-ray scattering and optical birefringence with specific work. They found that the critical specific work for morphological transition for the three blends of hydrogenated polybutadienes studied varied from 0.8 MPa to 7.8 MPa, depending on fraction of the high-molecular weight components (*viz.*, a smaller value for a larger fraction). Also, they reported that the critical specific work does not vary with shear rate, provided that the shear rate is above a value that can stretch the chains, namely the inverse of the Rouse time. Crystallization kinetics, however, was not measured. Thus, it is not possible to relate their results to the present findings. It should be mentioned that specific work appears to serve different purposes; these authors used it solely for identifying the critical value for the onset of morphological transition, whereas Janeschitz-Kriegl *et al.* [2] used it primarily for correlating the number density of nuclei.

On the other hand, the data of Housmans *et al.* [8] support the present findings, despite some differences in the interpretation of data. They used two types of data for correlation with specific work: the normalized characteristic crystallization time $t_{1/2,\dot{\gamma}} / t_{1/2,\mathrm{Q}}$ obtained by oscillatory shear measurements (definition given in Table 5.3), and the number density of nuclei. First, the $t_{1/2,\dot{\gamma}} / t_{1/2,\mathrm{Q}}$ data do not overlap for different shear rates (Figs. 10–12 in [8]), indicating a poor correlation with specific work. In fact, as shown earlier in Fig. 6.2c, their data are much better correlated with $\dot{\gamma}_\mathrm{s}\gamma_\mathrm{s}$. Thus, their results are in agreement with the conclusion of the present study that $\dot{\gamma}_\mathrm{s}\gamma_\mathrm{s}$ is a better parameter than specific work to represent the effect of shear on crystallization kinetics. Second, the critical specific work for morphological transition reported for the two of the three polypropylenes studied were in the range of 2 MPa and 5.5 MPa (larger value for lower molecular weight). The range of 3.5 MPa to 4.5 MPa found in this study for iPP1 is within their range. This agreement is very promising, after taking consideration the large differences in the values of $\dot{\gamma}_\mathrm{s}$ and γ_s used in their study (Fig. 6.2c) and those in the present work (Fig. 5.8). But, they also noted that one of their samples did not show a morphological transition even when the specific work was above 12 MPa, and attributed this to the shear rate being too low. Third, a plot of the number density of nuclei versus specific work (Fig. 17 in [8]) did not yield the $N \propto w^n$ relationship found by Janeschitz-Kriegl *et al.* [2]. Rather, a plateau associated with saturation of point-like nuclei was reported.

However, it should be mentioned that Housmans *et al.* did not measure the number density of nuclei. Instead, they used the Avrami equation and an empirical expression that relates time evolution of the storage modulus to the volume of material crystallized ("space filling" [8]) to calculate this quantity. The accuracy of this calculation remains to be validated experimentally.

Using a multipass rheometer, Scelsi *et al.* [17] found that the onset of crystallization based on flow birefringence measurements correlated well with a simulated critical work of 9 MPa to 11 MPa for a polyethylene. In their numerical simulation, a multimode Pom-Pom model was used as the constitutive equation in Eq. 6.1.

It should be mentioned that before the reports of Janeschitz-Kriegl *et al.* [2-4], some groups [20, 21] used specific work to analyze data obtained in continuous shearing. Tan and Gogos [20] measured the induction time based on an upturn in shear stress and proposed a linear relationship between the nucleation rate and specific work. However, their analysis is questionable, because the induction time did not seem to be well-defined, as the tabulated values did not match the upturn in the plotted stress (Fig. 2 in [20]). Using a capillary apparatus, Titomanlio and Marrucci [21] correlated the temperature at which crystallization occurs, as detected by the build-up in stress, with specific work. However, no kinetic data were reported.

In summary, compared to $\dot{\gamma}_s \gamma_s$, specific work is a poor parameter for representing shear-induced crystallization kinetics associated with the increase in point-like nuclei. On the other hand, the usefulness of specific work for characterizing the onset of morphological transition remains an open question, as critical values reported in the literature are somewhat inconsistent (see Table 6.1). Also, as mentioned, two studies [8, 16] have shown that a critical specific work alone is inadequate for initiating a morphological transition and that a critical shear rate is needed.

Table 6.1. Literature values of critical specific work.

Authors	Polymer	T / °C	w_{critical} / MPa
Janeschitz-Kriegl [4]	Isotactic polypropylene	140 to 160	25
Mykhaylyk *et al.* [16]	Blends of hydrogenated polybutadiene	115	0.8 to 7.8
Housmans *et al.*[8]	Isotactic polypropylene	138	2 to 5.5
Scelsi *et al.* [17]	High-density polyethylene	125	9 to 11
This study	Isotactic polypropylene (nucleated)	155.5	3.5 to 4.5 (nominal)

It should be mentioned that shear stress and specific work have the same dimensions; and Kumaraswamy *et al.* [22] found that a critical shear stress (~ 0.047 MPa for the sample studied) and a critical shearing time (~ 5 s) are the criteria for a morphological transition. For the three data points that showed a morphological transition (Fig. 6.1), the measured stresses (see Figs. 3.9b and c) exceeded the reported 0.047 MPa [22], but the shearing times were much shorter, *viz.*, 0.12 s for 200 s^{-1} and 0.05 s for 500 s^{-1}. It is thus clear that the dependence of critical stress and critical shearing time is highly nonlinear, thus making these two criteria unsuitable for characterizing morphological transition.

6.5 The Weissenberg Number

The Weissenberg number Wi, as given by Eq. 6.5 [19] for simple shear flow, has been used in many studies to characterize the onset of: 1) a change in crystallization kinetics relative to quiescent crystallization; 2) a transition from spherulitic to highly oriented morphology.

$$\mathrm{Wi} \equiv \dot{\gamma}_{\mathrm{s}} \tau \tag{6.5}$$

Various characteristic relaxation times have been used [8, 10-13, 15, 23-29]. The Weissenberg number is sometimes incorrectly called the Deborah number [7, 11, 15, 23-

25, 27], which is given as follows in the case where t_s is characteristic duration of the deformation, not its rate:

$$\mathrm{De} \equiv \tau / t_s \tag{6.6}$$

By means of Eqs. 6.5 and 6.6, the product of a relaxation time and $\dot{\gamma}_s \gamma_s$ discussed earlier can be represented as $\mathrm{Wi} \cdot \gamma_s$ or $\mathrm{De} \cdot \gamma_s^2$.

There is no agreement with regard to the values for the Weissenberg number at which kinetic and/or morphological changes begin. A classification of the effect of flow on crystallization into four regimes has been proposed by van Meerveld *et al.* [11]. According to these authors, for two of the regimes, Wi > 1 based on τ_d is needed to produce chain orientation and change crystallization kinetics, whereas Wi > 1 based on τ_s is required to generate chain stretching and initiate morphological transition. If the first criterion was applied to the results obtained here, the critical shear rates necessary to change the crystallization kinetics of iPP1, iPP2, iPP3 and iPP4 would be 12.5 s^{-1}, 194 s^{-1}, 13.0 s^{-1} and 1.2 s^{-1}, respectively. The value of 12.5 s^{-1} is a reasonable estimate for iPP1, as it is in good agreement with Fig. 5.9, in which the data for γ_s = 50 indicate that the onset of an appreciable change in t_{ind} begins at a value of $\dot{\gamma}_s$ between 10 s^{-1} and 50 s^{-1}. On the other hand, the value of 194 s^{-1} is underestimated for iPP2 as the data shown in Fig. 5.2 for an even higher shear rate ($\dot{\gamma}_s$ = 494 s^{-1}) indicate only a marginal change in kinetics relative to quasi-quiescent crystallization. As for iPP3 and iPP4, acceleration of crystallization was found at $\dot{\gamma}_s$ = 494 s^{-1} with γ_s = 20; but only the data at this $\dot{\gamma}_s$ were available, and this rate clearly exceeds the estimates of 13.0 s^{-1} and 1.2 s^{-1}. On the other hand, the second criterion is not evaluated as determination of τ_s remains unclear for polydisperse melts, although some procedure has been proposed [11].

Compared to the parameters mentioned above, which contain both $\dot{\gamma}_s$ and γ_s , the Weissenberg number involves only $\dot{\gamma}_s$. As evidenced in this study and previous work

[22], both a critical $\dot{\gamma}_s$ (or σ) and a critical γ_s (or t_s) are necessary for morphological transition to occur. This implies that use of the Weissenberg number alone is limited only to flow with large γ_s or t_s, notably in continuous shearing. In other words, the Weissenberg number cannot predict the onset of morphological transition in experiments involving small γ_s or t_s. This point is supported by the data of Elmoumni and Winter [10]. They showed that the criterion of Wi = 1 alone is not adequate for the initiation of a morphological transition, as a large strain, *i.e.*, $\gamma_s > 600$, which is much greater than that is required to reach steady flow ($\gamma_s \sim 40$), is also necessary. However, it should also be mentioned that it is not necessary for the stress in start-up flow to become steady to initiate changes in crystallization kinetics and morphology; for example, a steady stress was not reached for the shearing conditions shown in Figs. 3.9b and c but a morphological transition was found in Fig. 6.1.

It should be mentioned that in his new book [4] Janeschitz-Kriegl explicitly criticizes the use of this number. He argues that rather than the relaxation time of the melt, it is that of the structures induced during flow (*i.e.*, precursors) that is more relevant in crystallization. This is also partly because the relaxation time of the precursor is much longer than any relaxation time of the melt [30]. He notes that the Weissenberg number is only "a measure of readiness of association" [4].

6.6 Conclusions

The product of shear rate and strain is a much more useful parameter than specific work for describing shear-induced crystallization kinetics associated with the increase in the point-like nuclei. It is, however, less useful for characterizing morphological transition. This quantity reveals the equal importance of shear rate and strain, and multiplication by a suitable relaxation time seems adequate to account for the strong influence of molecular weight at high shear rates. A critical specific work appears to be a promising parameter for identifying the transition from spherulitic to oriented morphology, but its usefulness is limited by two issues: lack of a consistent range of values and the apparent requirement for a minimum shear rate. The Weissenberg number is inadequate as it does not take strain into account.

6.7 References

1. Liedauer, S., Eder, G., Janeschitz-Kriegl, H., Jerschow, P., Geymayer, W., and Ingolic, E. “On the kinetics of shear-induced crystallization in polypropylene” *Int. Polym. Process.* (1993) **8**, 236-244.
2. Janeschitz-Kriegl, H., Ratajski, E., and Stadlbauer, M. “Flow as an effective promotor of nucleation in polymer melts: A quantitative evaluation” *Rheol. Acta* (2003) **42**, 355-364.
3. Janeschitz-Kriegl, H. and Ratajski, E. “Kinetics of polymer crystallization under processing conditions: Transformation of dormant nuclei by the action of flow” *Polymer* (2005) **46**, 3856-3870.
4. Janeschitz-Kriegl, H. *Crystallization Modalities in Polymer Melt Processing: Fundamental Aspects of Structure Formation* (SpringerWienNewYork, Germany, 2010).
5. Eder, G. and Janeschitz-Kriegl, H. “Crystallization”, in *Materials Science and Technology: A Comprehensive Treatment*, R. W. Cahn, P. Haasen, E. J. Kramer, Eds., Vol. 18, (Wiley-VCH, Weinheim, 1997), 269-342.
6. Jerschow, P. and Janeschitz-Kriegl, H. “The role of long molecules and nucleating agents in shear induced crystallization of isotactic polypropylenes” *Int. Polym. Process.* (1997) **12**, 72-77.
7. Baert, J., Van Puyvelde, P., and Langouche, F. “Flow-induced crystallization of PB-1: From the low shear rate region up to processing rates” *Macromolecules* (2006) **39**, 9215-9222.
8. Housmans, J.-W., Steenbakkers, R.J.A., Roozemond, P.C., Peters, G.W.M., and Meijer, H.E.H. “Saturation of pointlike nuclei and the transition to oriented structures in flow-induced crystallization of isotactic polypropylene” *Macromolecules* (2009) **42**, 5728-5740.
9. Somani, R.H., Yang, L., Hsiao, B.S., Sun, T., Pogodina, N.V., and Lustiger, A. “Shear-induced molecular orientation and crystallization in isotactic polypropylene: Effects of the deformation rate and strain” *Macromolecules* (2005) **38**, 1244-1255.

10. Elmoumni, A. and Winter, H.H. “Large strain requirements for shear-induced crystallization of isotactic polypropylene” *Rheol. Acta* (2006) **45**, 793-801.
11. van Meerveld, J., Peters, G.W.M., and Hütter, M. “Towards a rheological classification of flow induced crystallization experiments of polymer melts” *Rheol. Acta* (2004) **44**, 119-134.
12. Baert, J. and Van Puyvelde, P. “Effect of molecular and processing parameters on the flow-induced crystallization of poly-1-butene. Part 1: Kinetics and morphology” *Polymer* (2006) **47**, 5871-5879.
13. Acierno, S., Palomba, B., Winter, H.H., and Grizzuti, N. “Effect of molecular weight on the flow-induced crystallization of isotactic poly(1-butene)” *Rheol. Acta* (2003) **42**, 243-250.
14. Hadinata, C., Gabriel, C., Ruellman, M., and Laun, H.M. “Comparison of shear-induced crystallization behavior of PB-1 samples with different molecular weight distribution” *J. Rheol.* (2005) **49**, 327-349.
15. Hadinata, C., Gabriel, C., Ruellmann, M., Kao, N., and Laun, H.M. “Shear-induced crystallization of PB-1 up to processing-relevant shear rates” *Rheol. Acta* (2006) **45**, 539-546.
16. Mykhaylyk, O.O., Chambon, P., Graham, R.S., Fairclough, J.P.A., Olmsted, P.D., and Ryan, A.J. “The specific work of flow as a criterion for orientation in polymer crystallization” *Macromolecules* s (2008) **41**, 1901-1904.
17. Scelsi, L., Mackley, M.R., Klein, H., Olmsted, P.D., Graham, R.S., Harlen, O.G., and McLeish, T.C.B. “Experimental observations and matching viscoelastic specific work predictions of flow-induced crystallization for molten polyethylene within two flow geometries” *J. Rheol.* (2009) **53**, 859-876.
18. Cox, W.P. and Merz, E.H. “Correlation of dynamic and steady flow viscosities” *J. Polym. Sci.* (1958) **28**, 619-622.
19. Dealy, J.M. and Larson, R.G. *Structure and Rheology of Molten Polymers: From Structure to Flow Behavior and Back Again* (Hanser Publishers, Munich, 2006).
20. Tan, V. and Gogos, C.G. “Flow-induced crystallization of linear polyethylene above its normal melting point” *Polym. Eng. Sci.* (1976) **16**, 512-525.
21. Titomanlio, G. and Marrucci, G. “Capillary experiments of flow induced crystallization of HDPE” *AIChE J.* (1990) **36**, 13-18.
22. Kumaraswamy, G., Issaian, A.M., and Kornfield, J.A. “Shear-enhanced crystallization in isotactic polypropylene. 1. Correspondence between in situ rheo-optics and ex situ structure determination” *Macromolecules* (1999) **32**, 7537-7547.

23. Van der Beek, M.H.E., Peters, G.W.M., and Meijer, H.E.H. “Classifying the combined influence of shear rate, temperature, and pressure on crystalline morphology and specific volume of isotactic (poly)propylene” *Macromolecules* (2006) **39**, 9278-9284.
24. Coppola, S., Grizzuti, N., and Maffettone, P.L. “Microrheological modeling of flow-induced crystallization” *Macromolecules* (2001) **34**, 5030-5036.
25. Coppola, S., Balzano, L., Gioffredi, E., Maffettone, P.L., and Grizzuti, N. “Effects of the degree of undercooling on flow induced crystallization in polymer melts” *Polymer* (2004) **45**, 3249-3256.
26. Heeley, E.L., Fernyhough, C.M., Graham, R.S., Olmsted, P.D., Inkson, N.J., Embery, J., Groves, D.J., McLeish, T.C.B., Morgovan, A.C., Meneau, F., Bras, W., and Ryan, A.J. “Shear-induced crystallization in blends of model linear and long-chain branched hydrogenated polybutadienes” *Macromolecules* (2006) **39**, 5058-5071.
27. Chen, Q., Fan, Y., and Zheng, Q. “Rheological scaling and modeling of shear-enhanced crystallization rate of polypropylene” *Rheol. Acta* (2006) **46**, 305-316.
28. Bustos, F., Cassagnau, P., and Fulchiron, R. “Effect of molecular architecture on quiescent and shear-induced crystallization of polyethylene” *J. Polym. Sci., Part B: Polym. Phys.* (2006) **44**, 1597-1607.
29. Somani, R.H., Yang, L., Zhu, L., and Hsiao, B.S. “Flow-induced shish-kebab precursor structures in entangled polymer melts” *Polymer* (2005) **46**, 8587-8623.
30. Janeschitz-Kriegl, H. and Eder, G. “Shear induced crystallization, a relaxation phenomenon in polymer melts: A re-collection” *J. Macromol. Sci., Part B: Phys.* (2007) **46B**, 591-601.

Chapter 7: Conclusions

1. Light intensity and oscillatory shear measurements have comparable capabilities in detecting nascent crystalline structures, but the former is more suitable for tracking changes during early kinetics, whereas the latter is more useful for monitoring the late stages.
2. The gel point is not reached during the early stages of crystallization but most likely when about half of the sample volume is occupied by the spherulites.
3. The crystallization of nucleated polymers after a brief, strong shear is not governed by a nucleating agent, in contrast with behavior under quiescent conditions.
4. The strong effect of shear is chiefly in inducing nucleation and is much less significant in altering growth kinetics.
5. Provided that shearing conditions are strong, molecular weight governs nucleation kinetics, regardless of whether a sample is nucleated or not.
6. Based on the comparison with quiescent crystallization, the induction time of non-nucleated polymers is more effectively reduced by shear than that of nucleated polymers.
7. The presence of a nucleating agent and shear act to shorten the induction time, but these effects are not additive.
8. With increasing shear rate or strain, crystallization first accelerates as a result of the increase in the number of point-like nuclei, then saturates due to either slip or consumption of high-molecular weight components for the creation of nuclei, and finally accelerates again at the onset of the transition from spherulitic to oriented morphology.
9. Both a critical shear rate and a critical strain are required to induce a morphological transition.
10. The product of shear rate and strain is a more useful parameter than specific work for describing the effect of shear on crystallization kinetics associated with the

increase in the point-like nuclei. But, it is less useful for characterizing a morphological transition.

11. The importance of this product reveals the equal importance of shear rate and strain, and multiplication by a suitable relaxation time appears to account for the effect of molecular weight.
12. A critical specific work appears to be a promising parameter for characterizing a morphological transition, but its usefulness is limited by the lack of a consistent range of values and the need for a minimum shear rate.
13. The Weissenberg number is not a useful parameter, since it does not take strain into account.
14. The complex interactions between nucleating agent, shearing conditions and molecular weight can lead to segregation of crystalline structures, resulting in non-uniformity in the bulk samples.

Chapter 8: Original Contributions to Knowledge

1. Developed a technique for tracking shear-induced crystallization kinetics simultaneously by rheology and light intensity.
2. Devised an optical fiber probe for use in a sliding plate rheometer.
3. Determined and elucidated the relative influence of the nucleating agent, molecular weight, shear rate, and strain in shear-induced crystallization at high shear rates.
4. Confirmed that the nucleation pathway of nucleated polymers after strong shear is not regulated by the nucleating agent.
5. Corroborated the requirement of a critical shear rate and a critical strain for initiating a morphological transition.
6. Demonstrated the usefulness of the product of shear rate and strain for describing the effect of shear on crystallization kinetics.
7. Proved the inadequacy of specific work and the Weissenberg number for characterizing kinetic and morphological changes.
8. Found non-uniformity in bulk samples resulting from segregation of crystalline structures.

Appendix A: Instrument Specifications

Tables A.1, A.2 and A.3 provide detailed information about the sliding plate rheometer, the optical system, as well as the data acquisition and instrument control hardware, respectively.

Table A.1. Sliding plate rheometer.

Component	Manufacturer & Model/ Part No.	Details
Moving plate	Custom made	• Stainless steel AISI 420, 63 microinch surface finish • 10.5" length x 4" width x 3/16" depth • A pair of Teflon® siderails • Width for sample loading: 4.7 cm • 10 holes at edges for mounting to the linear bearing table with screws
Stationary plate	Custom made	• Stainless steel AISI 420, 63 microinch surface finish • 10.0" length x 5.3" width x 0.72" depth • 0.3975" drilled hole for mounting shear stress transducer • 3/8" diameter x 0.6" thickness hole for mounting thermocouple 1 • 15.5 mm diameter x 2.5 mm thickness hole for mounting sapphire window • Eight tapped holes of 0.344" diameter on left and right edges for fastening plate to support frame with shoulder screws and nuts • Equipped with hinges at bottom side ends and two handles at the middle for ease of opening
Spacers	Custom made	• Stainless steel AISI 420, 63 microinch surface finish, available thicknesses in millimeters: 0.2, 0.3, 0.4, 1.0, 1.5 (machined to tolerances of ± 0.005 mm)
Linear bearing table	Custom made Roller bearing from Schneeberger, Switzerland Model: R 9 300	• 300 mm length • 4 tracks, 2 roller cages with 15 rollers each

Table A.1. continued on next page ...

Component	**Manufacturer & Model/ Part no.**	**Details**
Support frame	Custom made	• 18.8" length x 5.3" width, a channel at center for mounting linear bearing table • 14 oval holes drilled in frame for improved heat transfer
Load frame	Shore Western, Monrovia, CA Model: 302.2 (modified)	• Two-column symmetrical, fixed platen, movable crosshead • 100 kN force rating
Heavy-duty hydraulic pump	MTS Systems Corporation, Eden Prairie, MN Model: 506.02	• 22.7 L/min flow capacity • 76 L reservoir capacity • Hydraulic oil Shell Tellus 46
Linear hydraulic actuator	MTS Systems Corporation, Eden Prairie, MN Model: 244.11	• 15 kN force rating • 150 mm stroke length
Servovalve	MTS Systems Corporation, Eden Prairie, MN Model: 252.23C	• 37 L/min full-flow rating for 1000 psi pressure drop
Linear variable differential transformer	Trans-Tek Inc., Ellington, CT Model: 0219-0000	• Stroke length: 76.2 mm (full), 96.5 mm (max.) • Non-linearity: ≤ ± 0.25 % full scale • Sensitivity: 0.50 V/V ± 10 % at full scale
Capacitance proximity probe	Capacitec, Inc., Ayer, MA Model: HPT-40	• Linear range: 0.508 mm, ± 0.2 % full scale • Sensor outer diameter: 1.016 mm • Threaded case outer diameter: 4.750 mm
Force convection oven	Applied Test Systems, Butler, PA Model: 3710	• 425 °C maximum temperature • 14" length x 14" width x 24" height
Heating elements (two units)	Hotwatt, Danvers, MA Part no.: FS14	• Ceramic insulated finned strip heater • Power: 1650 W at 240 V
Thermocouple 1	Omega Engineering, Inc., Stamford, CT Part no.: BTH-090-J-2 1/4-60-1	• Type J, spring-loaded bayonet style assembly, 2.25" probe tip, 60" length
Thermocouples 2, 3 and 4	Omega Engineering, Inc., Stamford, CT Part no.: 5TC-TT-E-36-72	• Type E, fast-response, 0.005" diameter, PFA-insulated, 72" length
High-temperature grease	DuPont, Wilmington, DE Part no.: Krytox® GPL-226	• Maximum temperature: 260 °C

Table A.2. Optical system.

Component	Manufacturer & Model/ Part no.	Details
Helium-Neon laser	Optikon Corp., Waterloo, ON Model: LGK 7672	• 632.8 nm, 5 mW, random polarization • Mounting accessories (Thorlabs): V-clamp (VC3), post (TR2), post holder (PH1.5-ST), mounting base (BA1)
Amplified photodiodes (two units)	Thorlabs, Newton, NJ Part no.: PDA100A	• Large surface area, switchable-gain (8 settings: 0 dB to 70 dB), silicon detector, 400 nm to 1100 nm wavelength, output voltage: 0 V to 10 V • Accessories: SM1 to SMA fiber connector adapter plate (SM1SMA), posts (TR2), post holders (PH1.5-PT), mounting bases (BA1)
Non-polarizing beam splitter	Thorlabs, Newton, NJ Part no.: BS010	• 10 mm x 10 mm x 10 mm cube, 400 nm to 700 nm wavelength, 50/50 split • Accessories: Kinematic prism mount (KM100P), clamping arm (PM1), post (TR2), post holder (PH1.5-ST), mounting base (BA1)
Neutral density filter	Thorlabs, Newton, NJ Part no.: NDC-25C-4M	• 380 nm to 1200 nm wavelength, 0 to 4.0 adjustable optical density • Accessories: Post (TR2), post holder (PH1.5-ST), mounting base (BA1)
Broadband dielectric mirrors (two units)	Thorlabs, Newton, NJ Part no.: BB05-E02	• 400 nm to 750 nm wavelength • Accessories: Kinematic mirror mounts (KS05), posts (TR2), post holders (PH1.5-ST), mounting bases (BA1)
Fiber coupler	Thorlabs, Newton, NJ Part no.: KT110	• SMA fiber termination • Aspheric lens (C230TM-B) with 4.5 mm focal length, 0.55 numerical aperture
Optical breadboard	Thorlabs, Newton, NJ Part no.: PBH11103	• 36" length x 12" width x 2.4" thickness
Optical fibers	Edmund Optics, Barrington, NJ Part no.: NT57-068	• Fused silica core, multimode, step-indexed, polyimide buffer, 200 nm to 800 nm wavelength, 0.22 numerical aperture, 6 mm bend radius, 200 µm core diameter, 220 µm clad diameter
Sapphire window	Edmund Optics, Barrington, NJ Part no.: NT43-367	• 15 mm diameter, 2 mm thickness, transmittance: >85 % at 632.8 nm, random axis orientation, no coating
High-temperature epoxy	Epoxy Technology, Billerica, MA Model: EPO-TEK 353ND	• Maximum operating temperature: 250 °C (continuous), 350 °C (intermittent)

Table A.3. Data acquisition and instrument control hardware.

Component	Manufacturer & Model/ Part no.	Details
PCI data acquisition board (LabVIEW™ desktop)	National Instruments, Austin, TX Part no.: PCI-6221	• Multifunction input/output, PCI interface • 16-bit, 250 000 samples/s, 8 differential input channels, 2 analog output channels
PCI data acquisition board (WinTEST® desktop)	Keithley Instruments, Inc., Cleveland, OH Part no.: KP-3108	• Multifunction input/output, PCI interface • 16-bit, 100 000 samples/s, 8 differential input channels, 2 analog output channels
Signal conditioning modules	National Instruments, Austin, TX Connector block part no.: SC-2345 (777458-02)	• Shielded connector block, connected to PCI card via shielded cable (SHC68-68-EPM) • Modules: feedthrough modules (SCC-FT01), isolated analog input module with low pass filter (SCC-AI02)
Capacitec® amplifier	Capacitec, Inc., Ayer, MA Rack model: 4004-P115	• Available for 4 channels • Clock driver card (4100C), amplifier cards with adjustable offset and gain settings (4100, 4100-L) • Analog DC output: 10 V
LVDT signal conditioner	Analog Devices, Inc., Norwood, MA Part no.: AD598	• 20 kHz to 20 kHz excitation frequency, ± 11 V output, 0.05 % linearity
WinTEST® PCI Series controller	Bose Corporation – EnduraTEC Systems Group, Minnetonka, MN Model: PCI 41	• 4 input and 2 control channels
USB temperature conditioning module	Measurement Computing Corporation, Norton, MA Part no.: USB-TEMP	• 24-bit, 2 samples/second/channel, 8 differential channels • USB interface, accepts thermocouples, RTDs, thermistors and semiconductor sensors
Power controller	Applied Test Systems, Butler, PA Model: PC20-LC	• Zero-crossover proportional SCR power control, 120/240 V, 20 A

Appendix B: Data Acquisition and Control Program

The main features of the graphical user interface program or *virtual instrument* (VI), developed in LabVIEW^{TM} 8.0, for use with the data acquisition and instrument control scheme shown in Fig. 2.9 are given below. The program is implemented on a desktop computer running Windows XP SP3.

B.1. Interactive User Interface (Front Panel)

Figure B.1 shows a screenshot of the interactive user interface, or *front panel*. The top left table displays temperatures acquired by various thermocouples. The bottom table contains user input parameters for temperature control, *e.g.*, the set point temperature, and the proportional-integral-differential control settings. An option of switching from an automatic control to a manual setting is available. The three waveform charts on the right show the voltage measurements acquired by the shear stress transducer, photodiode 1, and photodiode 2, respectively. The three files containing the timing, temperature, and voltage data can be saved for analysis.

B.2. Source Code (Block Diagram)

Figure B.2 shows the source code, or *block diagram*, that supports the program execution. A description of the programming details is beyond the scope of this thesis. The various components (built-in functions, subVIs, indicators, controls, while loops, case structures, *etc.*) are neatly organized and wired, users with some experience in LabVIEW^{TM} programming should have no difficulty understanding the dataflow. Important comments have also been appropriately documented in the block diagram.

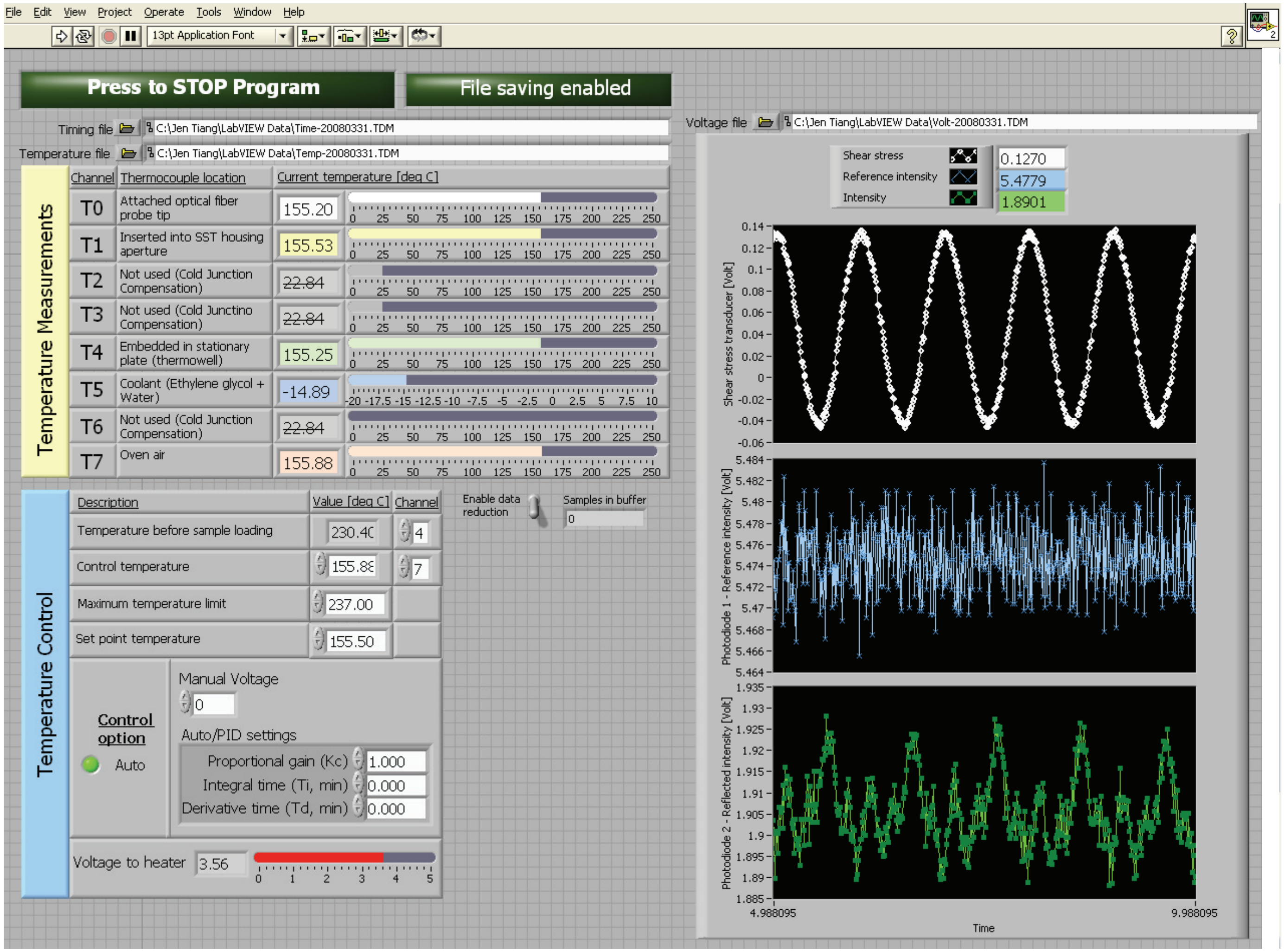

Timing file C:\Jen Tiang\LabVIEW Data\Time-20080331.TDM

Temperature file C:\Jen Tiang\LabVIEW Data\Temp-20080331.TDM

Voltage file C:\Jen Tiang\LabVIEW Data\Volt-20080331.TDM

Channel	Thermocouple location	Current temperature [deg C]
T0	Attached optical fiber probe tip	155.20
T1	Inserted into SST housing aperture	155.53
T2	Not used (Cold Junction Compensation)	22.84
T3	Not used (Cold Junctino Compensation)	22.84
T4	Embedded in stationary plate (thermowell)	155.25
T5	Coolant (Ethylene glycol + Water)	-14.89
T6	Not used (Cold Junction Compensation)	22.84
T7	Oven air	155.88

Description	Value [deg C]	Channel
Temperature before sample loading	230.4C	4
Control temperature	155.8E	7
Maximum temperature limit	237.00	
Set point temperature	155.50	

Enable data reduction

Samples in buffer 0

Control option

● Auto

Manual Voltage 0

Auto/PID settings

Proportional gain (Kc) 1.000

Integral time (Ti, min) 0.000

Derivative time (Td, min) 0.000

Voltage to heater 3.56

Shear stress	0.1270
Reference intensity	5.4779
Intensity	1.8901

Figure B.1. Screenshot of the interactive user interface (*front panel*) of the LabVIEW^{TM} program used.

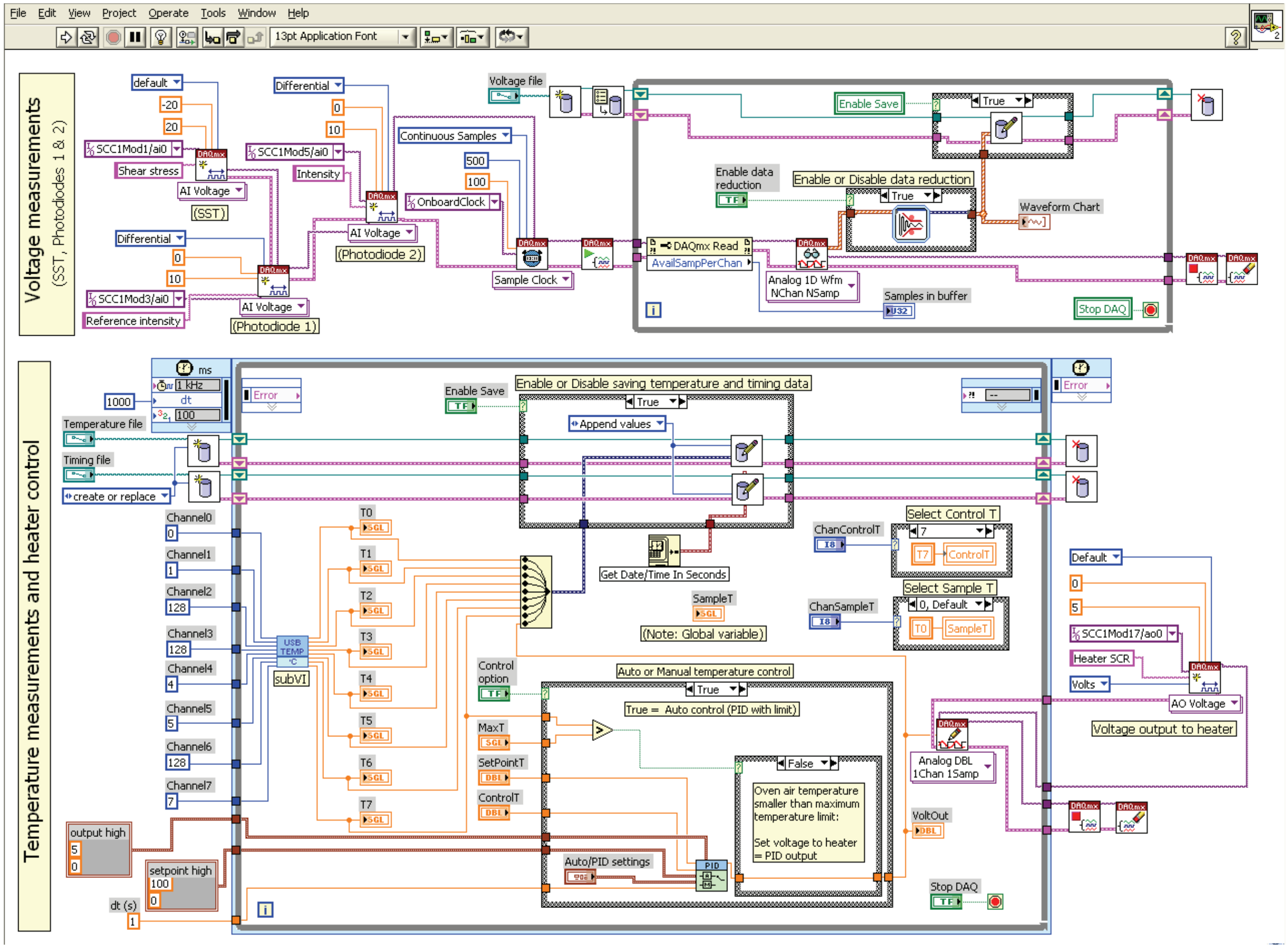

Figure B.2. Screenshot of the source code (*block diagram*) of the LabVIEW^{TM} program used.

Appendix C: SPR Strain Sweep and Data Conversion

C.1. Strain Sweep

Figure C.1 shows strain sweep results obtained using the sliding plate rheometer at a frequency of 1 Hz at 155.5 °C. Based on the plots of storage modulus and stress amplitude versus strain amplitude shown, a strain amplitude of 20 % was selected for use in crystallization studies of iPP1, iPP2 and iPP3, whereas a lower value of 10 % was used for iPP4. These values were within the linear viscoelastic regime indicated on the figure.

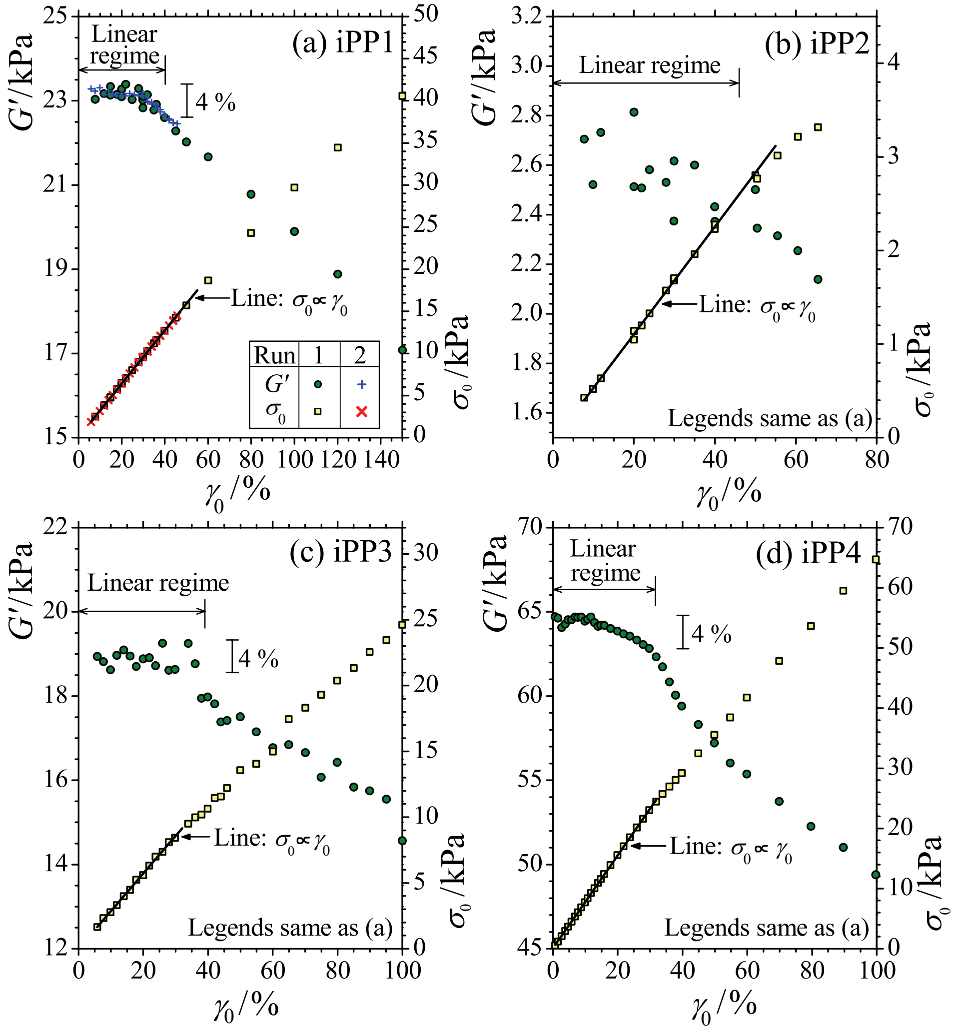

Figure C.1. SPR strain sweeps measured at a frequency of 1 Hz at 155.5 °C for (a) iPP1, (b) iPP2, (c) iPP3, and (d) iPP4. The linear regime is marked.

C.2. Conversion of Waveforms from Time Domain into Frequency Domain

The stress $\sigma(t)$ and strain $\gamma(t)$ waveforms acquired in crystallization experiments were converted into frequency domain using a built-in function (*Extract single tone information.vi*) in LabVIEW^{TM}. The calculation was based on a fast Fourier transform algorithm with a Hann window using successive blocks of data from three to five cycles. As shown in Fig. C.2, the results calculated from this method are in good agreement with the raw waveforms.

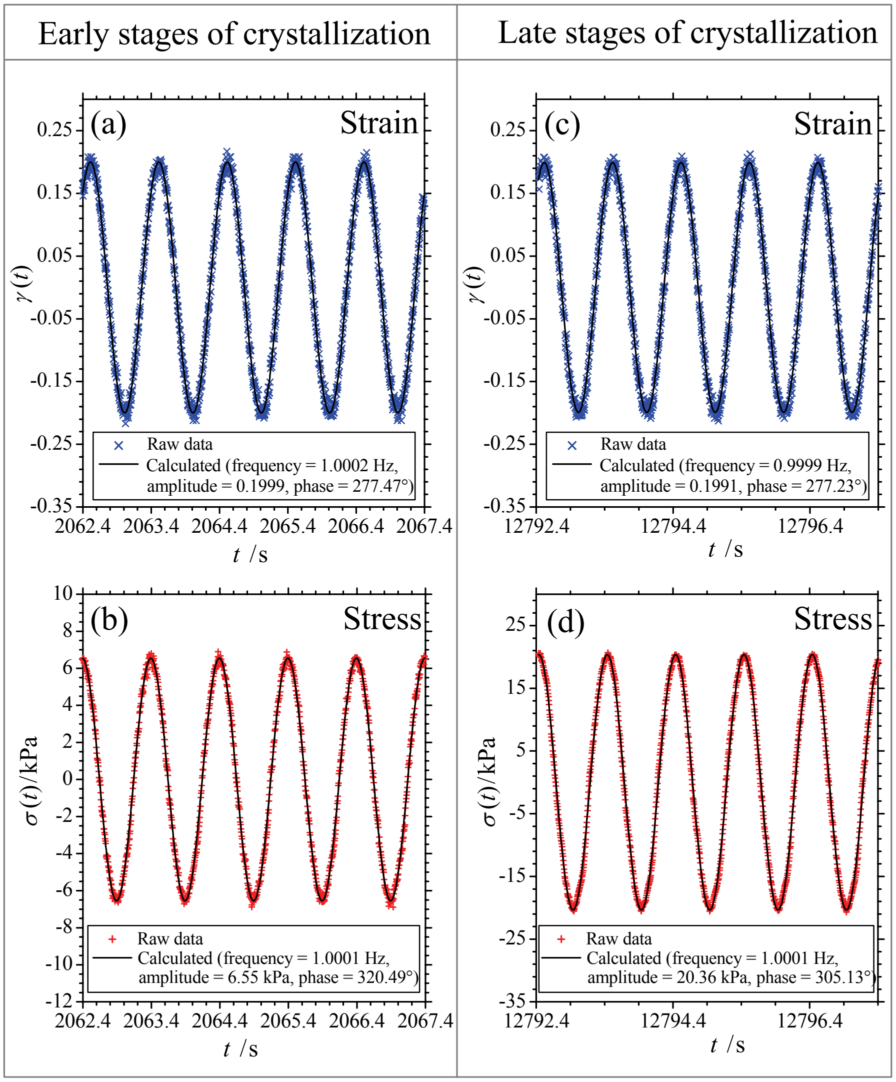

Figure C.2. Demonstration of a satisfactory conversion of raw waveforms into frequency data using the method described. Strain and stress data during early kinetics are shown in (a) and (b), whereas those during late kinetics are shown in (c) and (d). Quasi-quiescent crystallization data of iPP1 at 155.5 °C are shown.

Appendix D: ARES Strain Sweep Results

The following table shows the strain amplitudes, obtained from strain sweep experiments of which the values were found within the linear viscoelastic limit, used in the frequency sweep tests at 155.5 °C. Note that a range of values were used at low frequencies. This is because the stress signal was very small for the lower end of the frequency range (*i.e.*, 0.01 rad/s), and thus a large strain was needed; and to avoid nonlinear response due to the use of a large strain amplitude at the upper end of the frequency range (*i.e.*, 0.1 rad/s), different values of strain amplitudes were judiciously selected.

Table D.1. Strain (%) selected for use in frequency sweep tests.

Sample	Frequency, ω /(rad/s)			
	500 – 100	100 – 1	1 – 0.1	0.1 – 0.01
iPP1	0.15	1	4	8 – 40
iPP2	1	6	8-50	50 – 300
iPP3	0.2	1	3	8 – 65
iPP4	0.1	0.25	0.6	4

Appendix E: Differential Scanning Calorimetry Calibration and Data Correction

E.1. Temperature and Enthalpy Calibration

The calibration described below was performed in accordance with the recommendations in an IUPAC report[*] [1], in addition to the procedure prescribed in the DSC manufacturer's manual. It was done in both the heating and cooling modes using an indium standard[†] with purity of 99.999 %, a melting or fusion temperature T_{fus} of 156.60 °C and an enthalpy of fusion $\Delta_{\text{fus}}h$ of 28.45 J/g. The mass of the indium was 5.4611 mg.

Figure E.1a shows the temperature calibration results in the heating mode on a plot of the extrapolated peak onset temperature T_{e} versus scanning rate β. Linear extrapolation to zero heating rate was carried out to determine $T_{\text{e}}(\beta = 0)$, and subtraction of this value from T_{fus} gives the temperature correction term [1]: $\Delta T_{\text{corr}}(\beta = 0) = T_{\text{fus}} - T_{\text{e}}(\beta = 0)$ = 0.31 °C. The slope $\Delta T_{\text{e}}/\Delta\beta$ was 0.02110 °C/min. The results shown were determined based on the measured signals plotted in terms of the heat-flow rate Φ_{meas} versus temperature T_{meas} in Figs. E.1b to e for various heating rates. The value of T_{e} is given by the intersection of the interpolated baseline and the tangent line drawn to the ascending section of the melting endotherm [2].

---

[*] Due to time and resource limitations, not all of the recommendations in the IUPAC report (*e.g.*, heat-flow rate calibration, number of calibration substances) were followed. However, the procedures applied here are deemed adequate for the purpose of this study.

[†] The indium standard was obtained from the instrument manufacturer (P/N: 0319-0033, PerkinElmer, Waltham, MA). Its thermal properties are within the uncertainties specified by the U.S. National Institute for Standards and Technology: T_{fus} = (156.5985 ± 0.00034) °C and $\Delta_{\text{fus}}h$ = (28.51 ± 0.19) J/g [1].

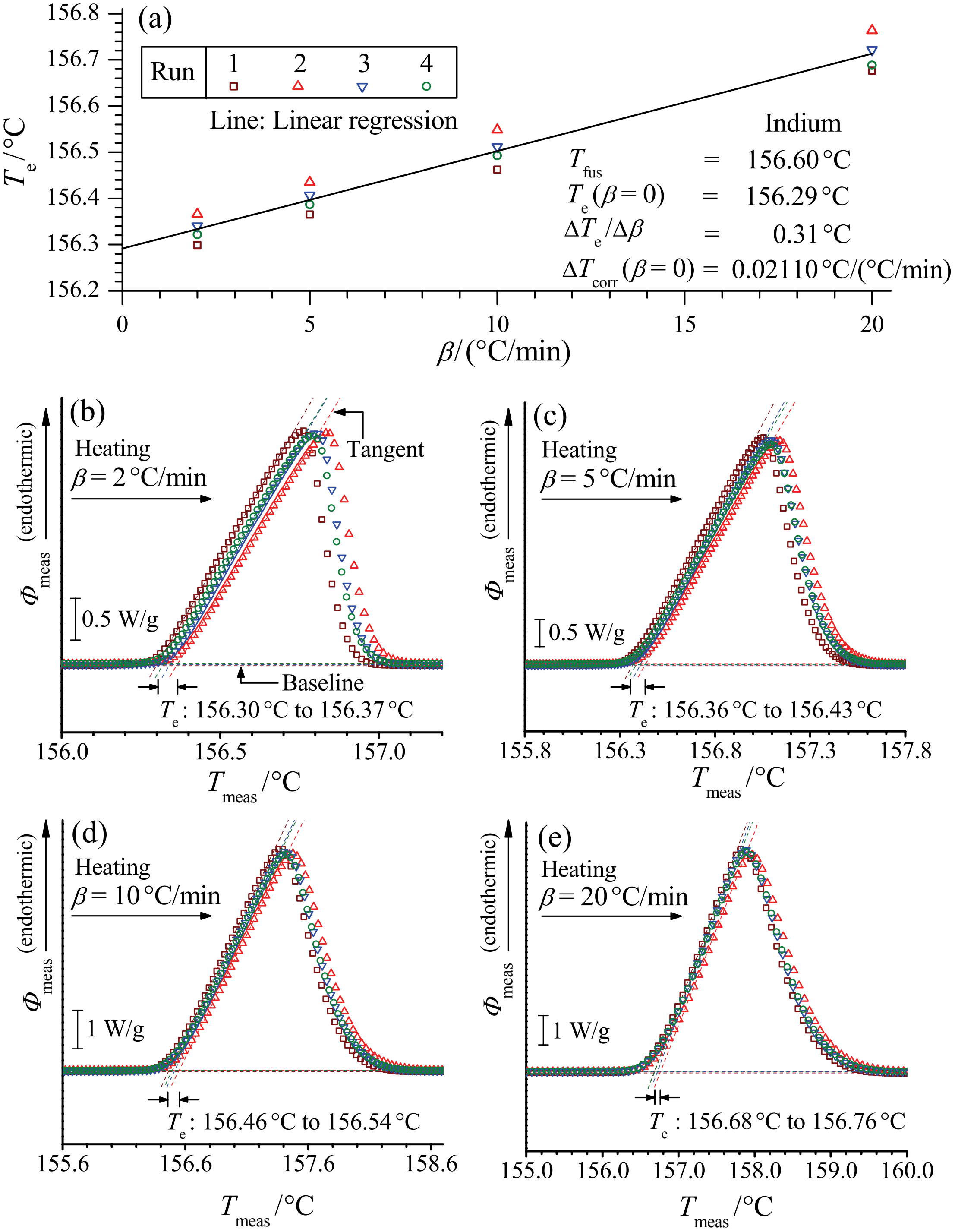

Figure E.1. DSC temperature calibration results in the heating mode using an indium standard. (a) By means of a linear extrapolation, the plot of extrapolated peak onset temperature versus scanning rate yields a temperature correction term of 0.31 °C at zero heating rate. Results shown in (a) were determined based on plots of measured heat-flow rate versus measured temperature at various scanning rates: (b) 2 °C/min, (c) 5 °C/min, (d) 10 °C/min, and (e) 20 °C/min. Data are for four runs.

Temperature calibration in the cooling mode is less reproducible and is only used for checking symmetry of the temperature scale [1]. Taking into consideration of a possible supercooling effect of 2 °C for indium [2], the calibration results shown in Fig. E.2a are deemed acceptable. The results shown were determined based on the measured signals given in Figs. E.2b to e for various cooling rates.

The enthalpy calibration factor K_{H} is defined [1] as the ratio of $\Delta_{\mathrm{fus}}h$ to the peak area A of the measured curves (*i.e.*, those shown in Figs. E.1b to e and Figs. E.2b to e). As shown in Fig. E.3, the results indicate a negligible difference (< 0.7 %) between $\Delta_{\mathrm{fus}}h$ and A, and an insignificant dependence of K_{H} on the scanning rate in the range of -20 °C/min to 20 °C/min.

E.2. Data Correction

The measured curves were processed and analyzed according to the recommendations by Höhne *et al.*[*] [2]. First, T_{meas} was corrected to the true temperature T using the temperature calibration results obtained from Fig. E.1a by means of the following equations:

$$T = T_{\mathrm{meas}} + \Delta T_{\mathrm{corr}}(\beta) \tag{E1.1}$$

$$\Delta T_{\mathrm{corr}}(\beta) = \Delta T_{\mathrm{corr}}(\beta = 0) - \beta \frac{\Delta T_{\mathrm{e}}}{\Delta \beta} \tag{E1.2}$$

Since heat-flow rate calibration was not done, correction of the measured heat-flow rate Φ_{meas} to the true heat-flow rate Φ cannot be made. Nonetheless, the enthalpy calibration results (Fig. E.3) suggest a reasonably good approximation of $\Phi \approx \Phi_{\mathrm{meas}}$. In the subsequent step, contribution of the sample pan to the measured curve was accounted for by deducting the zero line Φ_{zero} (*i.e.*, from tests carried out with empty pans). A linear baseline was used in the evaluation of the peak area.

---

[*] The deconvolution or desmearing procedure described by Höhne *et al.* [2] is rather rigorous, only the steps deemed important for the purpose of this study were used.

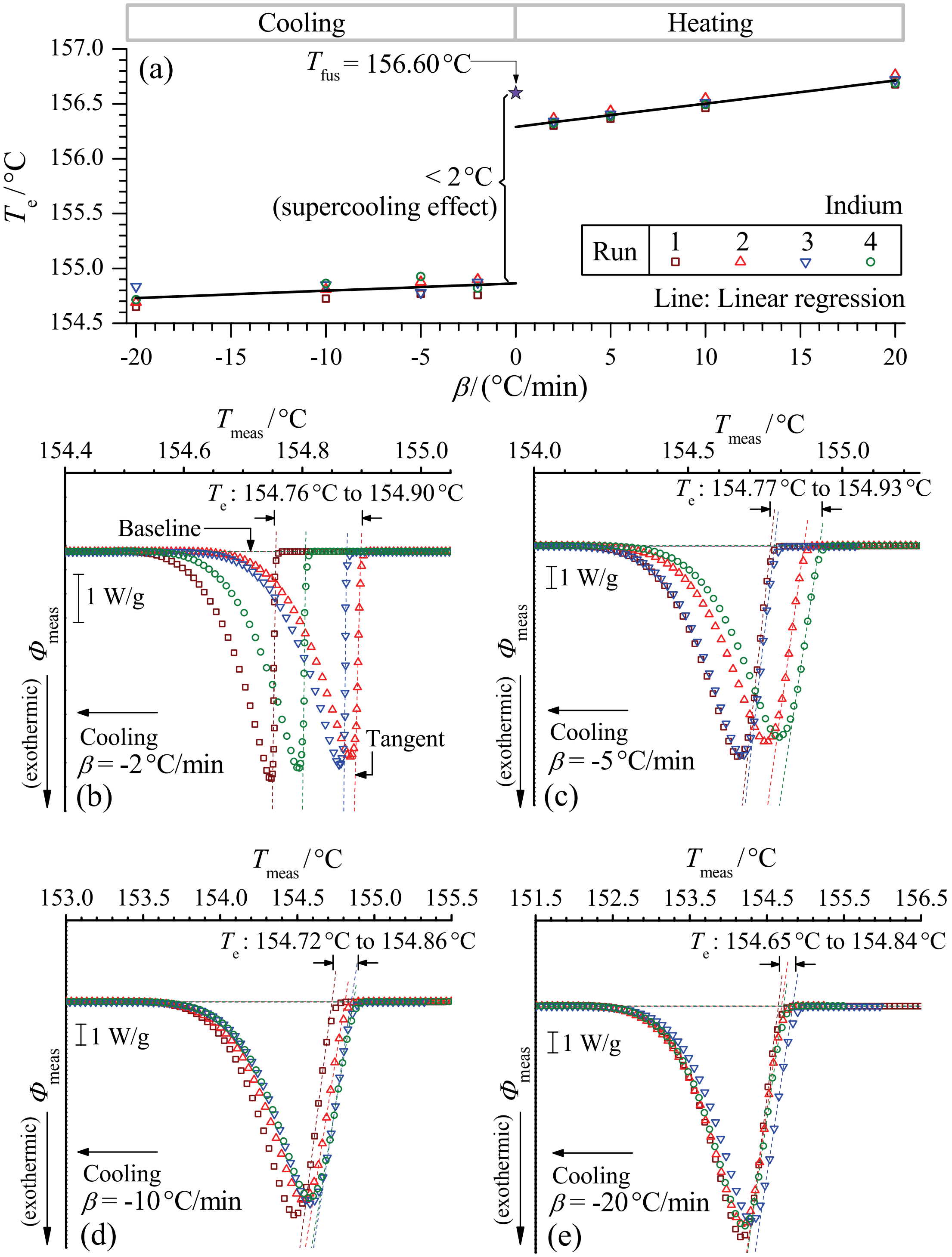

Figure E.2. DSC temperature calibration results in the cooling mode using an indium standard. (a) Taking the supercooling effect into account, the symmetry of the instrument is deemed acceptable. Results shown in (a) were determined based on plots of measured heat-flow rate versus measured temperature at various scanning rates: (b) -2 °C/min, (c) -5 °C/min, (d) -10 °C/min, and (e) -20 °C/min. Data shown are for four runs.

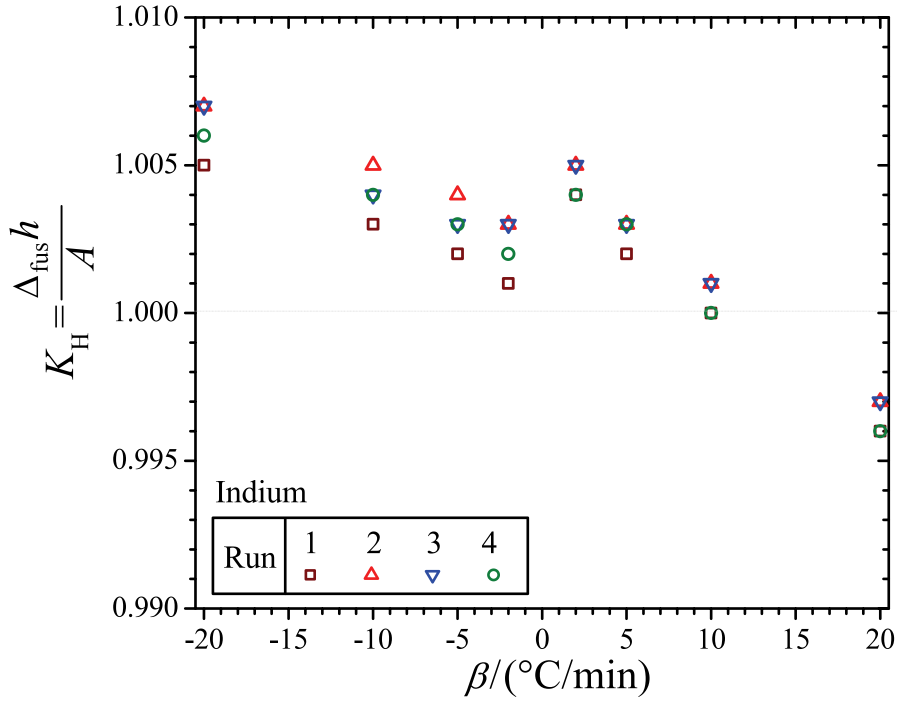

Figure E.3. Plot of enthalpy calibration factor versus scanning rate shows a deviation of less than 0.7 % between the enthalpy of fusion of an indium standard and the measured peak area. Data shown are for four runs.

E.3. References

1. Della Gatta, G.; Richardson, M.J.; Sarge, S.M., and Stølen, S. “Standards, calibration, and guidelines in microcalorimetry. Part 2. Calibration for differential scanning calorimetry (IUPAC Technical Report)” *Pure Appl. Chem.* (2006) **78**, 1455-1476.
2. Höhne, G.W.H.; Hemminger, W.F., and Flammersheim, H.-J. *Differential Scanning Calorimetry*, 2nd ed. (Springer, Berlin, 2003).

Appendix F: Supplementary Shear-Induced Crystallization Data

Data not presented in Chapter 5 are shown below.

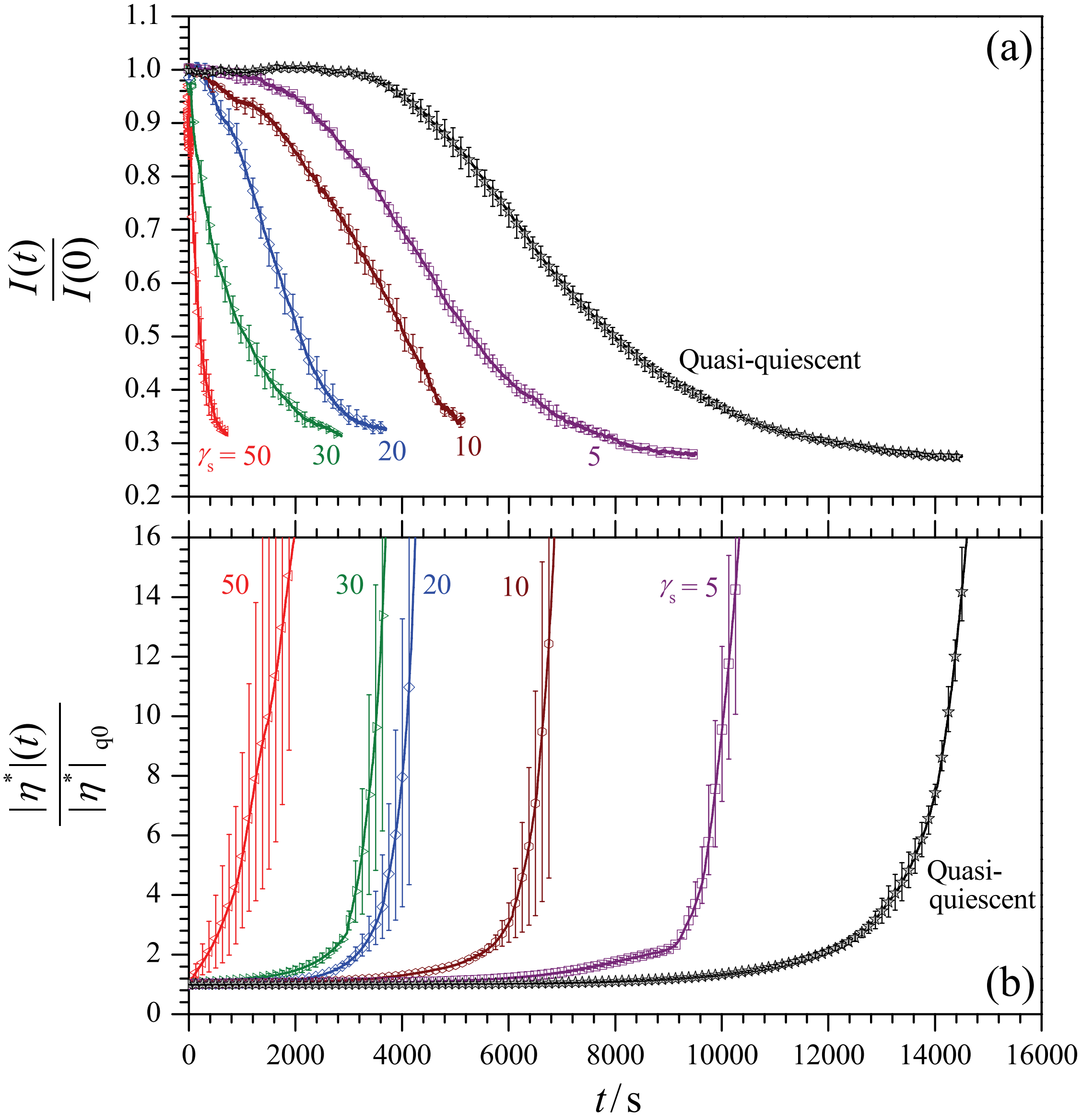

Figure F.1. Crystallization of iPP1 following shearing at a command shear rate of 500 s^{-1} with various strains in comparison to quasi-quiescent crystallization at 155.5 °C. (a) The normalized light intensity describes early kinetics, and (b) the normalized magnitude of the complex viscosity describes late kinetics. Data shown are averages and ranges for three measurements.

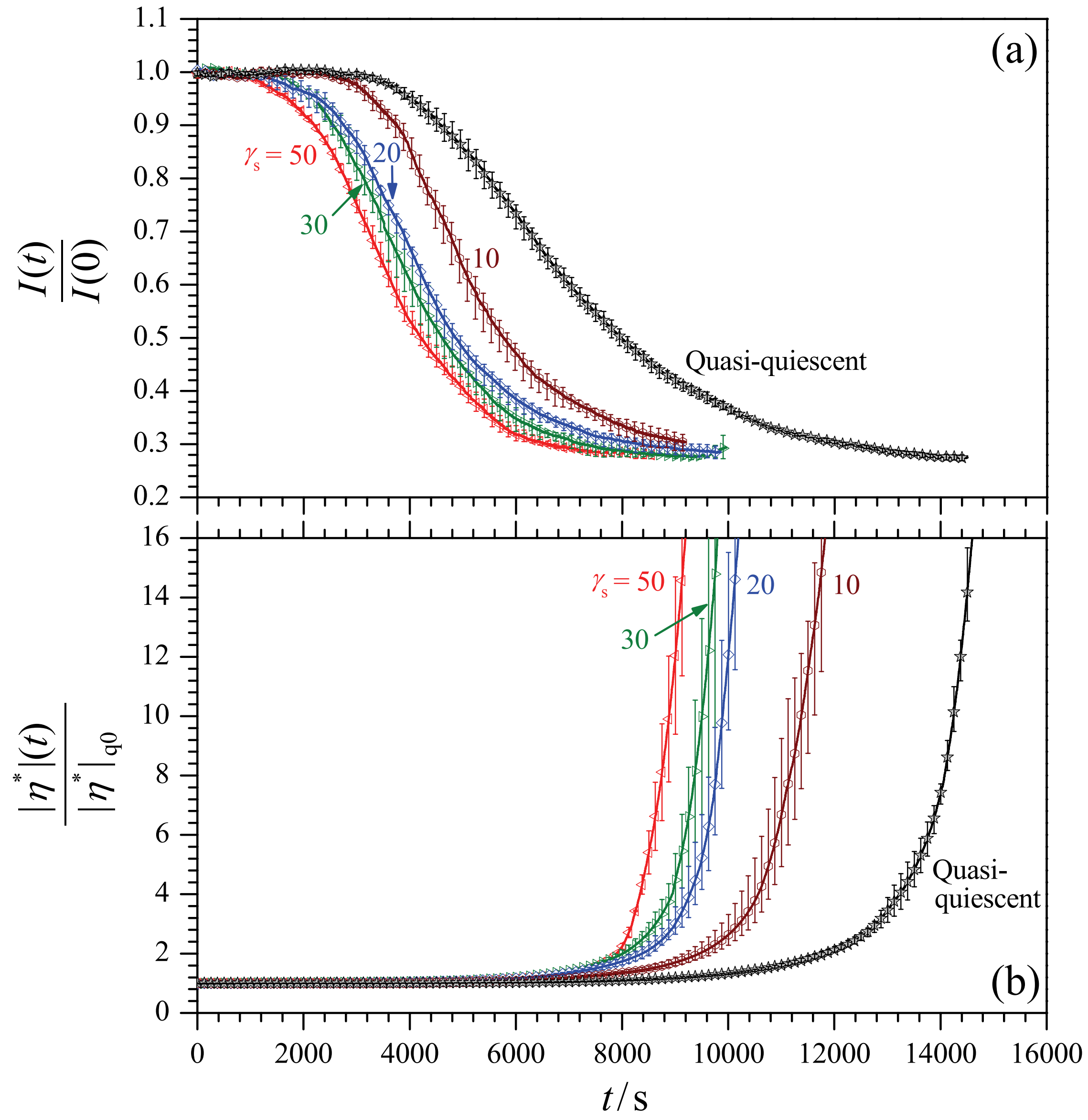

Figure F.2. Crystallization of iPP1 following shearing at a shear rate of 50 s^{-1} with various strains in comparison to quasi-quiescent crystallization at 155.5 °C. (a) The normalized light intensity describes early kinetics, and (b) the normalized magnitude of the complex viscosity describes late kinetics. Data shown are averages and ranges for three measurements.

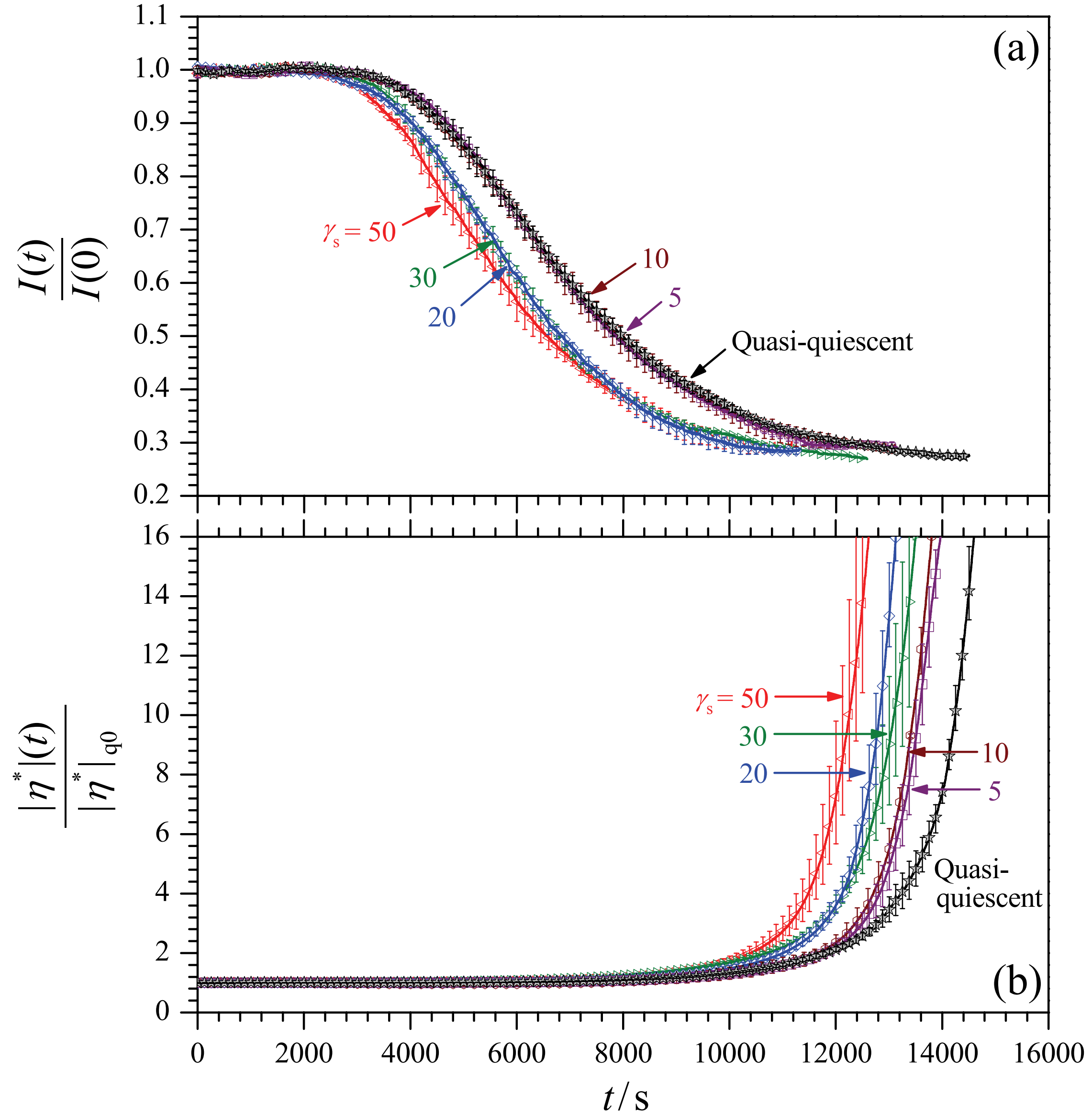

Figure F.3. Crystallization of iPP1 following shearing at a shear rate of 10 s^{-1} with various strains in comparison to quasi-quiescent crystallization at 155.5 °C. (a) The normalized light intensity describes early kinetics, and (b) the normalized magnitude of the complex viscosity describes late kinetics. Data shown are averages and ranges for three measurements.